United States
Environmental Protection
Agency

Industrial Environmental Research
Laboratory
Research Triangle Park NC 27711

EPA-600/7-79-003
January 1979

EPA

Influence of Aerodynamic Phenomena on Pollutant Formation in Combustion (Phase II. Liquid Fuels)

Interagency Energy/Environment R&D Program Report

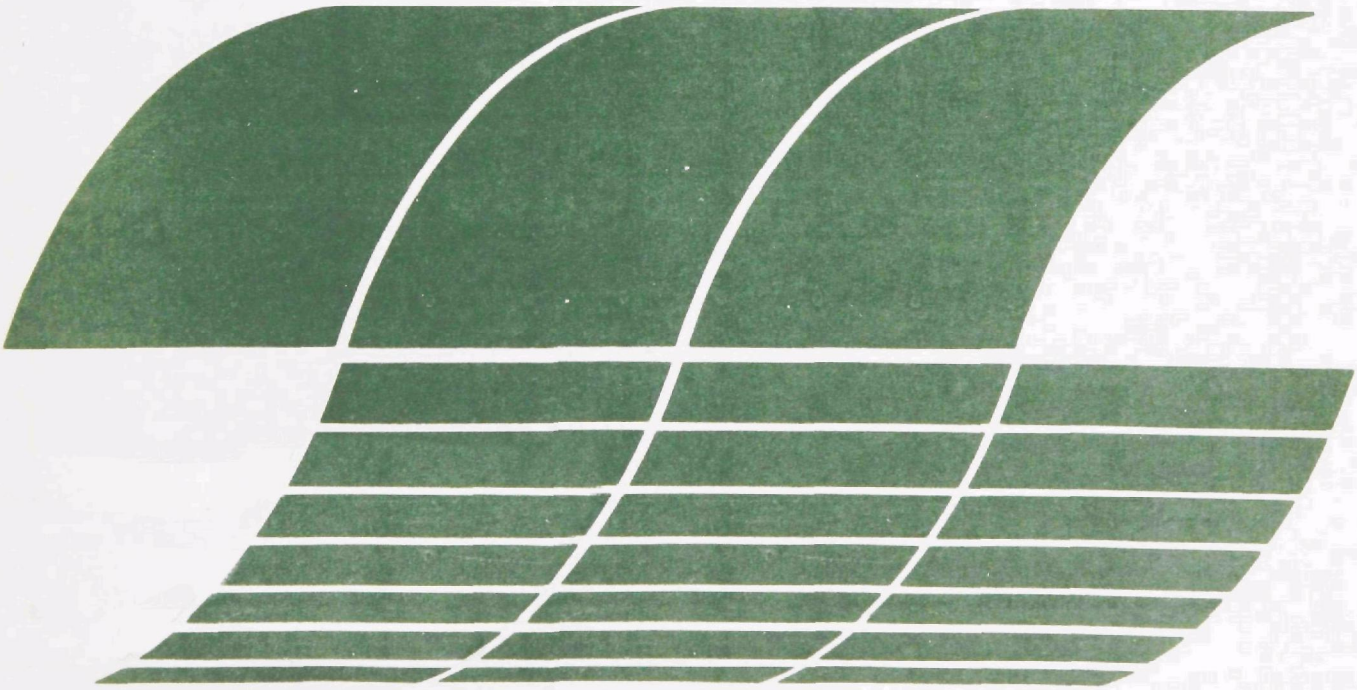

RESEARCH REPORTING SERIES

Research reports of the Office of Research and Development, U.S. Environmental Protection Agency, have been grouped into nine series. These nine broad categories were established to facilitate further development and application of environmental technology. Elimination of traditional grouping was consciously planned to foster technology transfer and a maximum interface in related fields. The nine series are:

1. Environmental Health Effects Research
2. Environmental Protection Technology
3. Ecological Research
4. Environmental Monitoring
5. Socioeconomic Environmental Studies
6. Scientific and Technical Assessment Reports (STAR)
7. Interagency Energy-Environment Research and Development
8. "Special" Reports
9. Miscellaneous Reports

This report has been assigned to the INTERAGENCY ENERGY-ENVIRONMENT RESEARCH AND DEVELOPMENT series. Reports in this series result from the effort funded under the 17-agency Federal Energy/Environment Research and Development Program. These studies relate to EPA's mission to protect the public health and welfare from adverse effects of pollutants associated with energy systems. The goal of the Program is to assure the rapid development of domestic energy supplies in an environmentally-compatible manner by providing the necessary environmental data and control technology. Investigations include analyses of the transport of energy-related pollutants and their health and ecological effects; assessments of, and development of, control technologies for energy systems; and integrated assessments of a wide range of energy-related environmental issues.

EPA REVIEW NOTICE

This report has been reviewed by the participating Federal Agencies, and approved for publication. Approval does not signify that the contents necessarily reflect the views and policies of the Government, nor does mention of trade names or commercial products constitute endorsement or recommendation for use.

This document is available to the public through the National Technical Information Service, Springfield, Virginia 22161.

EPA-600/7-79-003

January 1979

Influence of Aerodynamic Phenomena on Pollutant Formation in Combustion (Phase II. Liquid Fuels)

by

L.J. Spadaccini, John McVey, Jan Kennedy, A.S. Kesten,
F.K. Owen, and C.T. Bowman

United Technologies Research Center
300 Main Street
East Hartford, Connecticut 06108

Contract No. 68-02-1873
Program Element No. EHE624A

EPA Project Officer: W. Steven Lanier

Industrial Environmental Research Laboratory
Office of Energy, Minerals, and Industry
Research Triangle Park, NC 27711

Prepared for

U.S. ENVIRONMENTAL PROTECTION AGENCY
Office of Research and Development
Washington, DC 20460

Influence of Aerodynamic Phenomena on Pollutant Formation in Combustion (Phase II - Liquid Fuels)

TABLE OF CONTENTS

TABLE OF CONTENTS (Cont'd)

ABSTRACT

An experimental investigation of the effects of the interaction between physical and chemical processes on pollutant formation and destruction in a liquid fuel turbulent diffusion flame burner has been carried out. In this investigation, the effects of fuel type, inlet air swirl, inlet air temperature and combustor pressure on the spray characteristics and the time-mean and fluctuating flow field structure have been determined using probing and optical techniques. Changes in the spray and flow field structure have been correlated with changes in pollutant emissions from the burner. The results of this investigation show that variation of these operating parameters produce major changes in spray dynamics and vaporization rates and in the time-averaged fuel/air distribution within the burner which significantly influence energy release rates and pollutant formation and destruction. In addition, it was found that there are significant differences between the mean velocities of the gas and fuel droplets which likely influence droplet vaporization rates and mixing of the vaporized fuel and air.

LIST OF FIGURES

ACKNOWLEDGMENTS

A number of individuals at UTRC made significant contributions to the experimental investigation. Dr. M. F. Zabielski and Mr. G. L. Dodge designed the gas sampling system used in the investigation and developed the calibration procedures employed in the gas sampling portion of the experiments. Mr. T. A. Murrin assisted throughout the experimental program and was responsible for operation of the combustor and for reduction of much of the experimental data. The high-speed motion pictures of the reacting flows were made by Mr. R. J. Haas. Ms. B. B. Johnson assisted in reduction and compilation of the experimental data and in the preparation of the final report. Mr. P. Raber of the Norden Division of United Technologies Corporation assisted with the laser holographic measurements. Mr. Eugene Brull designed the hydrocarbon analyzer used in conjunction with a phase-discriminating probe.

This research program was carried out under the sponsorship of the Environmental Protection Agency, EPA Contract 68-02-1873, Research Triangle Park, North Carolina, under the direction of Mr. W. S. Lanier, Project Officer. A special debt of gratitude is owed to Mr. Lanier for asking the critical question and questioning the critical answers.

SECTION 1

INTRODUCTION

A large number of continuous combustion devices, including furnaces and gas turbines, operate on liquid fuels. Investigations of pollutant emissions from these devices indicate that changes in injector design which change the droplet size distribution in the spray and variations in air inlet conditions which alter the interaction between the fuel spray and the surrounding gas stream (Refs. 1-6) can have a significant effect on pollutant formation and destruction. Norster and Lefebvre (Ref. 1) found that atomization techniques can affect pollutant emissions, particularly exhaust smoke, in a gas turbine combustor. Grobman (Ref. 2) reported that improving fuel atomization reduces hydrocarbon and carbon monoxide emissions during idle in a wide range of conventional and experimental gas turbine combustors. Mellor and his co-workers (Refs. 3,5) and Pompei and Heywood (Ref. 4) have attributed changes in carbon monoxide and nitric oxide emissions from gas turbine combustion with fuel injection pressures to changes in fuel atomization and vaporization rates. Inlet air temperature and swirl, combustor pressure and combustor reference velocity* significantly influence hydrocarbon, carbon monoxide and nitrogen oxide emissions (Refs. 1-3,6). Hence, it appears that appropriate modifications of fuel atomization techniques and combustor inlet conditions can result in significant reductions in the emissions of most pollutant species from continuous combustion devices.

The combustion of liquid fuel sprays is a complex process involving simultaneous heat, mass and momentum transfer and chemical reaction which are influenced by the fuel characteristics, the droplet size distribution and number density, the relative velocity between the droplets and surrounding gas and the ambient gas temperature and composition. Although qualitative models and empirical correlations of pollutant emissions from liquid-fueled combustors have been developed (see, for example, Refs. 7 and 8), our present understanding of spray burning is insufficient to permit quantitative predictions of the effects of changes in fuel injection techniques and operating conditions on pollutant emissions. Investigations of burning sprays have been hampered by difficulties associated with measuring the characteristics of the spray and with determining the interaction of the spray with the surrounding gas stream. However, recently-developed optical and probing techniques appear to be promising diagnostic tools for measurements on burning sprays.

*The combustor reference velocity, V_{ref}, is a measure of combustor residence time and is defined by $V_{ref} \equiv \dot{M}_{air}/\rho_{air}A_{max}$ where $\dot{M}_{air}$ = air flow rate, ρ_{air} = inlet air density and A_{max} = maximum combustor cross-sectional area.

The present report documents the results of an experimental investigation, sponsored by EPA under Contract 68-02-1873, of the effects of several operating parameters on the spray characteristics and flow field structure in a liquid-fuel turbulent diffusion flame burner and the subsequent effects on pollutant formation and destruction.

SECTION II

EXPERIMENTAL APPARATUS AND INSTRUMENTATION

The experimental apparatus and approach used in this study are similar to those employed previously to study pollutant formation and energy release in gaseous-fuel turbulent diffusion flames (Ref. 9). The only significant change in the combustor configuration is the fuel injector modification required for liquid fuel operation. A schematic diagram of the water-cooled combustion system is presented in Figure 1. It consists of an electric resistance-type air heater, a 12.2 cm-dia water-cooled cylindrical combustor section having a centrally located pressure-atomizing fuel injector and an extension section which contained an exhaust probe rake and a water-cooled orifice plate which can be installed to increase the combustor pressure. As in the gaseous fuel study, flame stabilization in the high velocity flows investigated was achieved by producing a recirculation zone in the initial region of the combustor by imparting a swirl component to the airflow. Swirl was imparted by inserting replaceable sets of straight swirl vanes into the annular passage which surrounds the fuel injector. The trailing edges of the swirl vanes are located upstream of the injector exit plane to permit measurement of the airflow characteristics entering the combustor. The combustor was designed to permit independent variation of each of three operating parameters -- inlet air swirl, combustor pressure and air preheat -- which are known to significantly influence emissions from liquid-fuel combustors.

In the present study, three fuels were investigated -- liquid propane, iso-octane, and No. 2 distillate fuel. These fuels provide an orderly progression in complexity of molecular structure and distillation characteristics and permit an evaluation of the effects of chemical and physical properties of fuels on pollutant formation and energy release. Typical liquid fuel properties and the results of limited quantitative fuel analyses are given in Appendix E. The injector assembly was water-cooled so that the fuel was not heated by the high-temperature inlet air, and fuel injector design and injection pressure were chosen to ensure liquid injection. A conventional pressure-atomizing swirl-type nozzle which produced a nominal 60 deg hollow-cone spray with a nominal droplet Sauter mean diameter of 100 μm in quiescent air at atmospheric pressure was used for iso-octane and No. 2 distillate fuel. This type of nozzle proved unsuitable for propane since vaporization occured internally due to expansion in the nozzle swirl chamber. Therefore, a tangential-feed, pressure-atomizing nozzle in which the full pressure drop occurred across the exit orifice was used to maintain the propane liquid to the point of injection. The direction of rotation imparted by the swirlers to both the fuel and the air streams were identical for each of the configurations tested. The fuel injectors, air swirl vane designs, and the fuel injector assembly are shown in Appendix A.

SCHEMATIC DIAGRAM OF AXISYMMETRIC COMBUSTION FACILITY

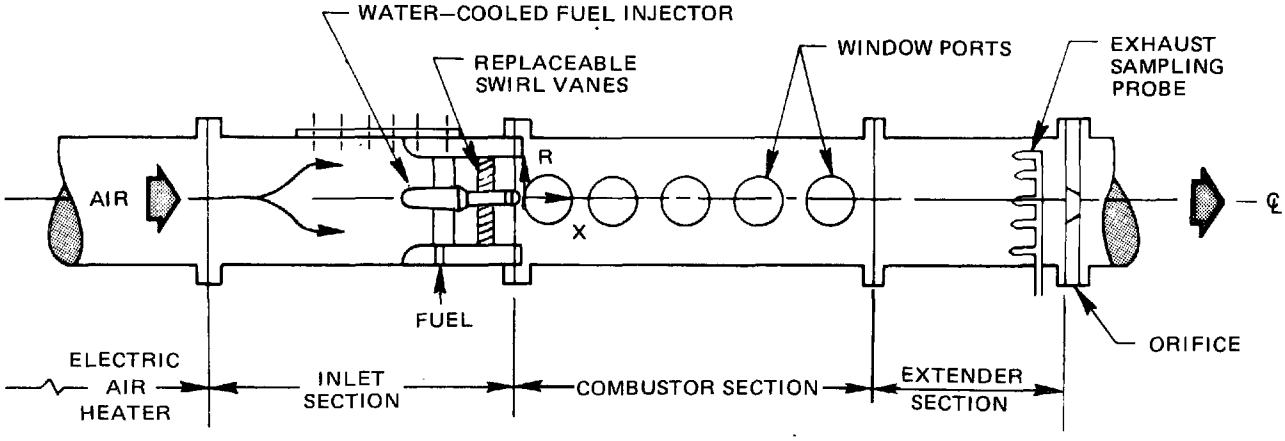

Measurements in the combusting flow were made through 6.4-cm dia window ports in the combustor sections (Fig. 1). A pair of window ports 180 deg apart are present at each location and permit the use of optical measurement techniques (e.g., laser velocimetry and laser holography). The location of a port directly downstream of the injector exit plane allowed an unhindered view of the flame in the vicinity of the fuel injector and permitted acquisition of flow field data close to the injection plane. The combustor probing devices are compatible with all window ports and may replace a quartz window or water-cooled plug in any given port. In addition, the entry section was designed to permit axial relocation of the fuel injector between tests, thereby increasing the number of axial locations at which radial traverse can be made. A porous-metal disc installed in the air entry section serves to provide a uniform inlet flow, which was verified by laser velocimeter measurements, and the combustor wall temperature was maintained at a constant value ($\sim 500^{\circ}K$) along the entire 100 cm length by regulating the coolant flow rates.

The concentration of nitrogen oxides (NO, NO_2), oxygen (O_2), carbon monoxide (CO), carbon dioxide (CO_2), and unburned hydrocarbons (THC) within the combustor were measured using cooled traversing sampling probes coupled to on-line analytical instrumentation. Nondispersive infrared analyzers were used to measure the CO and CO_2 concentrations in the gas sample and a para-magnetic analyzer was used to measure O_2 concentrations. The NO and NO_2 concentrations were measured using a chemiluminescence analyzer. An exhaust probe rake was used to aspirate gas samples from equal annuli for determination of the average concentrations of pollutant species in the exhaust flow. The inlet flow into the gas sampling probes was maintained choked, resulting in aerodynamic cooling of the sample by means of a rapid internal expansion. The combined effects of expansion and wall-cooling served to quench further chemical reactions. A liquid-vapor phase-discriminating sampling probe and a heated flame ionization detector were used to measure the total hydrocarbon (i.e., liquid plus vapor) and gaseous-hydrocarbon concentrations. The flow was sampled isokinetically and phase separation was achieved within the probe by aspirating a portion of the flow into a perpendicularly-oriented vapor-only sampling tube. Temperature distributions at the exhaust plane and within the combustor were obtained using a traversing calibrated-heat-loss thermocouple probe. Although conventional thermocouple materials are limited to temperatures below $2000^{\circ}K$, cooling the exposed junction by conduction extends the range of thermocouple utilization to gas temperatures above the melting point of the material to the $2000\text{-}2500^{\circ}K$ range. In order to obtain the local stream temperature, the measured stream thermocouple temperature must be corrected for conduction and radiation heat losses; therefore, calibration data were acquired simultaneously with the required temperature measurement. Mean and rms gas and droplet velocities were measured using a dual-beam, frequency-offset laser velocimeter and single-particle time-domain signal processing. This velocity measurement technique

removes directional ambiguity errors which arise in recirculating flows. The laser velocimeter also provided a qualitative measure of droplet number densities in the burning spray which could be used to establish the spray trajectory. Selective seeding of the airstream with micron-sized phenolic resin particles was used to obtain a sufficient signal-to-noise ratio in regions of low fuel droplet number density to permit measurements of the local gas velocity. The number density, trajectory and mean diameter of droplets in nonburning and burning liquid fuel sprays were determined using an off-axis, transmitted-light type laser holography system. Fringe patterns were produced on a holographic plate by the interaction of an object beam, directed through the combustor section, and a reference beam, directed around the combustor section. Reconstruction of the holograms was accomplished with a second optical system and the data were reduced manually using a 12-power loupe. High-speed color motion pictures (500 frames per second) of the flame in the vicinity of the injector were obtained to assist in the interpretation of the test results. Detailed descriptions of the sampling probes and associated instrumentation are given in Appendix A.

SECTION III

EXPERIMENTAL RESULTS

Description of Experiments

The principal objective of the experimental program was to investigate the interaction of physical and chemical processses in heterogeneous combustion on pollutant formation and destruction. This was accomplished by (1) determining the effects of combustor operating conditions on pollutant emissions, (2) obtaining detailed maps of the combustor flow field, and information on fuel spray characteristics and liquid-vapor concentration distributions for a range of operating conditions, and (3) correlating changes in flow field structure with changes in pollutant formation and energy release. The experimental results will be used to assist in assessing the validity of various models for turbulent transport and droplet burning.

The combustor was designed so that it would be amenable to analytical modeling and yet would exhibit many of the essential features of practical burners. Ultimately, it is intended that the information obtained from the experimental and complementary theoretical studies will be utilized for evaluating potential emission control strategies.

The experimental program comprised two different types of tests: (1) input-output tests to establish the relationship of liquid fuel and air input conditions to average exhaust species concentrations, and (2) flow-field mapping tests to obtain radial and axial distributions of temperature, species concentration and mean and rms gas and droplet velocities within the combustor and to evaluate fuel spray characteristics. The matrix of combustor operating conditions for tests conducted using iso-octane, No. 2 fuel oil and propane is presented in Table 1. These conditions were selected to encompass variations in operating parameters which, based on the results of Refs. 9 and 11, are believed to have the greatest influence on pollutant emissions. Tests were conducted at nominal combustor pressures of 1 atm and 3.3 atm, inlet air temperatures of 533K, 644K, and 755K, and for fuel-air equivalence ratios in the range 0.9 to 0.5 (10 to 100 percent excess air). The inlet airflow rate was held constant at a nominal value of 0.137 kg/sec and the swirl number was varied from low (S = 0.3) to moderate (S = 0.6) by interchanging swirl vanes. (Swirl number is defined in Table 1.) In the input-output tests, measurements were made at the exit of the combustor extender section (see Fig. 1), while in the mapping experiments detailed measurements were made within the combustor at a minimum of four axial locations. Variations in the average exhaust concentrations with overall fuel-air equivalence ratio and detailed flow field maps describing the effects of inlet air swirl, combustor pressure and air preheat are summarized below.

TABLE 1. NOMINAL TEST CONDITIONS

Fuel	Swirl No.*	Press. (atm)	T_{AIR} (K)	$\dot{M}_{AIR}$ (kg/sec)	Equiv. Ratio	Input-Output	Mapping
Iso-Octane	0.3	1.0	533	0.137	0.5-0.9	x	
	0.3	1.0	533	0.137	0.65	x	x
	0.3	1.0	644	0.137	0.65	x	
	0.3	1.0	750	0.137	0.65	x	
	0.3	3.3	533	0.137	0.65	x	x
	0.6	1.0	533	0.137	0.65	x	x
No. 2 Oil	0.3	1.0	533	0.137	0.5-0.9	x	
	0.3	1.0	533	0.137	0.65	x	x
	0.3	1.0	644	0.137	0.65	x	
	0.3	1.0	750	0.137	0.65	x	x
	0.3	3.3	533	0.137	0.65	x	
	0.6	1.0	533	0.137	0.65	x	
Propane	0.3	1.0	533	0.137	0.5-0.9	x	
	0.3	1.0	533	0.137	0.65	x	x
	0.3	1.0	644	0.137	0.65	x	
	0.3	1.0	750	0.137	0.65	x	
	0.3	3.3	533	0.137	0.65	x	
	0.6	1.0	533	0.137	0.65	x	

*As defined in Ref. 11:

$$S = \frac{1}{3}\frac{(1-Z^3)}{(1-Z^2)^{1.5}} \tan \eta$$

where Z = hub-to-tip ratio
η = angle of vanes

Input-Output Tests Results

Emissions data showing the effects of fuel type, inlet air swirl, combustor pressure, and air preheat at equivalence ratio 0.65 are summarized in Table 2. A complete tabulation of all (input-output and mapping) species concentration data is given in Appendix I. Because neither the Total Hydrocarbon Analyzer nor the sample transfer line were heated to prevent condensation of high molecular weight hydrocarbon species, exhaust THC concentration measurements were obtained only for tests in which propane fuel was used. However, use of the phase-discriminating sampling probe and the discrete-sampling heated hydrocarbon analyzer for the flow-field mapping tests permitted determinations of the total hydrocarbon (i.e., liquid plus vapor) and gaseous hydrocarbon concentrations within the combustor. These measurements are discussed in subsequent sections of the report. The high concentrations of oxygen (compared to equilibrium) measured with the exhaust rake and the low exhaust CO_2 concentrations, particularly for propane and iso-octane, are not indicative of incomplete combustion but rather of a sampling problem. It is likely that the problem was caused in part by the limited number of ports sampling a flow stream with sharp concentration gradients and the potential for blocking of some of these ports by particulates generated during combustion. Significant particulate loading was noted for propane (because of the narrow angle fuel injector employed) and for iso-octane. NO, NO_2 and CO concentrations are presented in Table 2 as measured and also corrected by the ratio of measured oxygen used to equilibrium oxygen used. Variations in the corrected exhaust concentrations of NO, NO_2 and CO with overall fuel-air equivalence ratio are illustrated in Figs. 2-4.

Tests conducted at fixed inlet conditions using each of the three fuels resulted in similar trends in exhaust emissions with increasing overall fuel-air equivalence ratio -- NO, CO and CO_2 exhaust concentrations increased while the exhaust concentration of O_2 decreased. These general trends are similar to what would be predicted for gas-phase premixed combustion. Calculated equilibrium exhaust concentrations for premixed, adiabatic combustion are presented in Table 2 for comparison. As would be expected for finite residence times, measured CO levels exceed equilibrium levels and measured NO_x levels are far below equilibrium levels.

Comparison of the emissions data obtained for each of the fuels tested indicates a dependence of exhaust emission on fuel type. These trends reflect in part the different carbon/hydrogen ratios of the fuel but also suggest that differences in the atomization, vaporization and mixing characteristics of the three fuels can affect pollutant formation and destruction. Detailed data describing the influence of fuel spray characteristics on the combustor flow field are discussed in subsequent sections of this report.

The influence of inlet air swirl on exhaust species concentration levels was evaluated using each of the three fuels at a combustion pressure of 1 atm. The

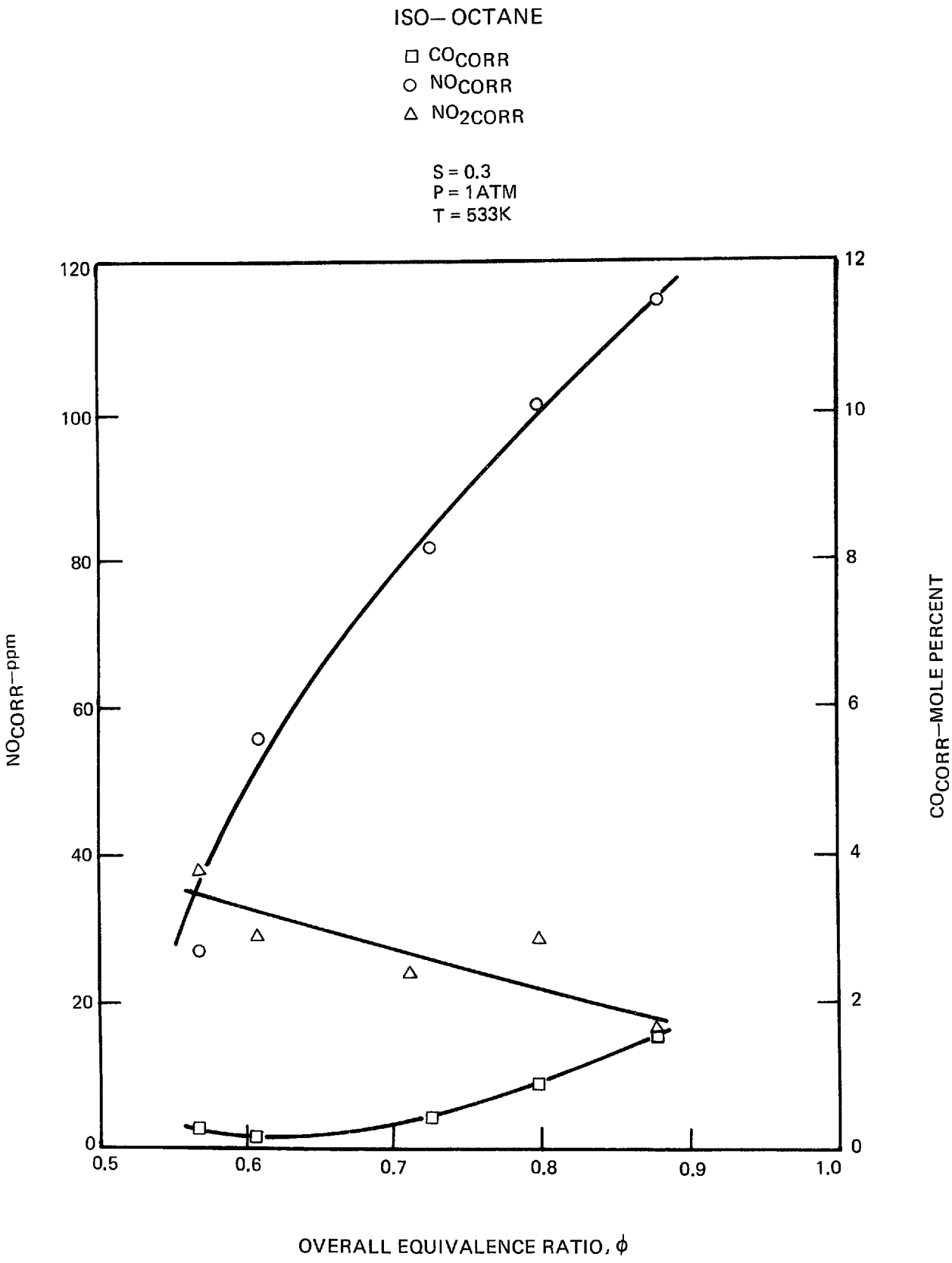
ISO– OCTANE
□ CO_{CORR}
○ NO_{CORR}
△ NO_{2CORR}
S = 0.3
P = 1ATM
T = 533K
120
100
80
60
40
20
0
12
10
8
6
4
2
0
0.5
0.6
0.7
0.8
0.9
1.0
NO_{CORR}–ppm
CO_{CORR}–MOLE PERCENT
OVERALL EQUIVALENCE RATIO, ϕ

FIG. 3

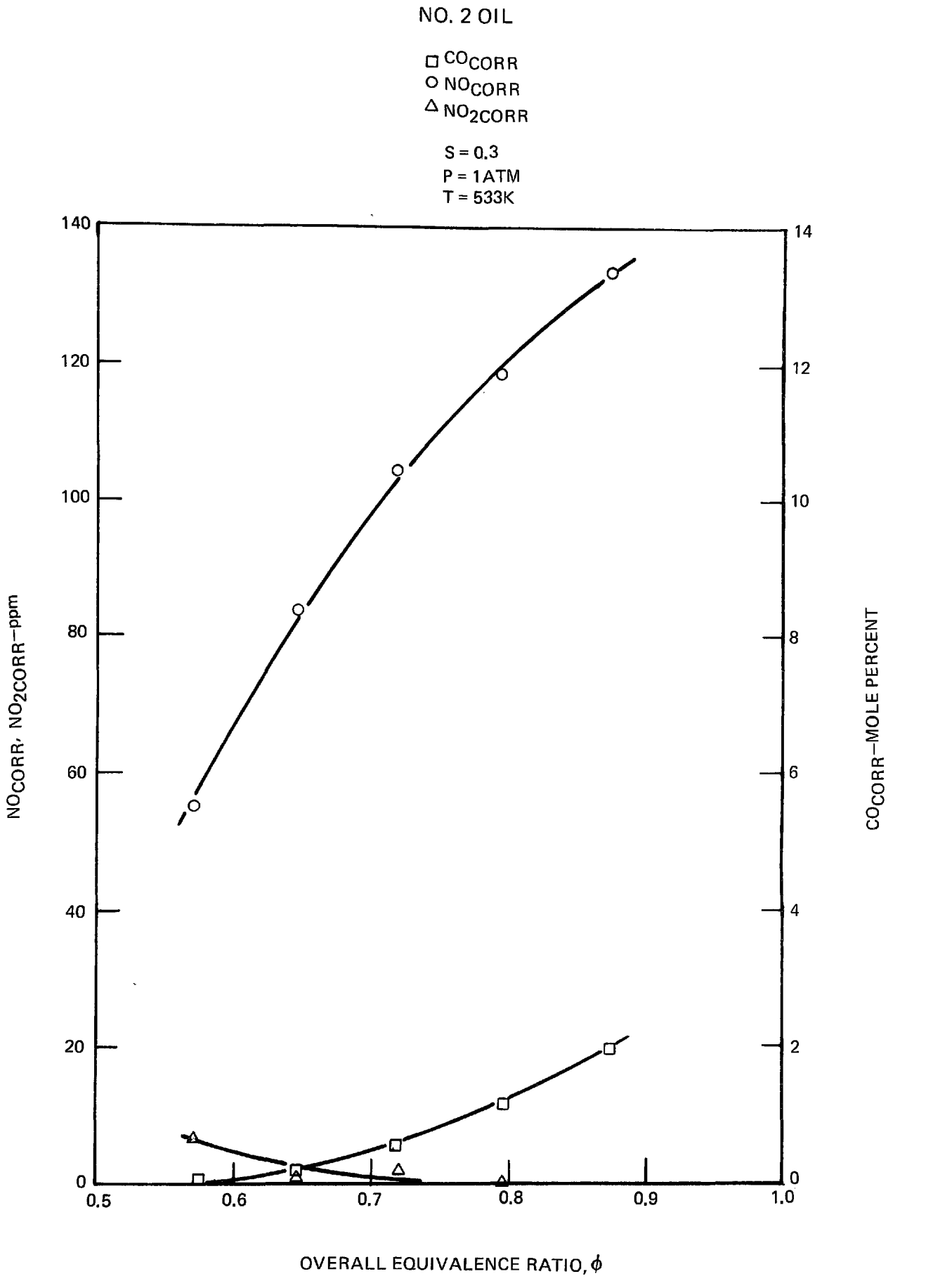

77-08-174-3

FIG. 4

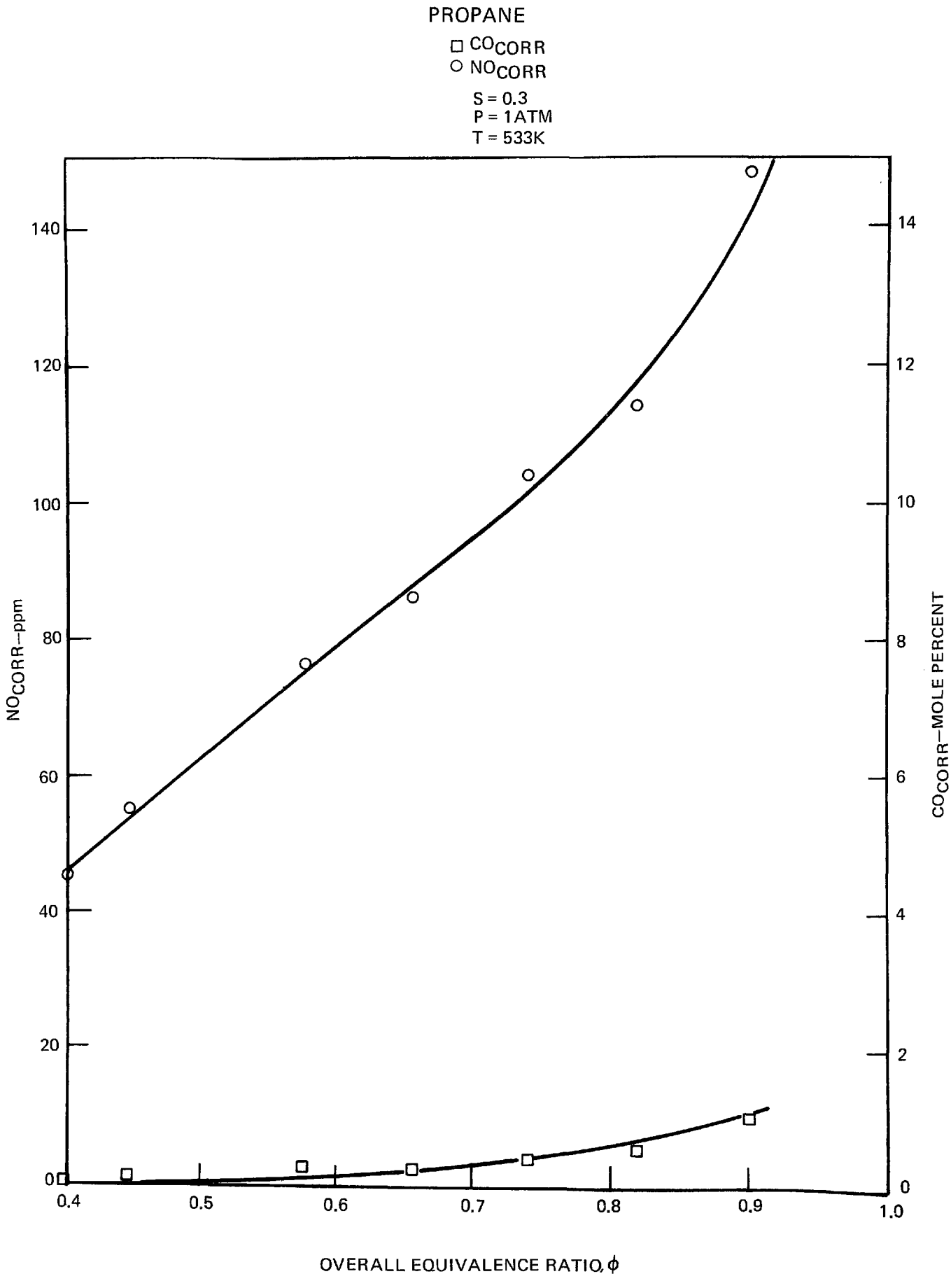

77–08–174–4

TABLE 2. EXHAUST SPECIES CONCENTRATIONS*

Test No.	Swirl	Press. (atm)	T_{air} K	Equiv. Ratio	O_2 Mole%	CO_2 Mole%	CO Mole%	$CO_{corr.}$** Mole%	NO ppm	$NO_{corr.}$** ppm	NO_x+ ppm	$NO_{x_{corr.}}$	THC ppm,C	$C_{Balance}$ %deficient at exhaust
							$i\text{-}C_8H_{18}$							
1	0.3	1.0	527	0.65	8.6	8.15	0.22	0.24	58	64	82	90	---	8.6
2	0.3	1.0	637	0.647	9.4	8.0	0.15	0.18	92	107	118	138	---	10.6
3	0.3	1.0	747	0.65	9.4	8.0	0.10	0.12	148	174	185	217	---	11.6
4	0.3	3.3	532	0.652	10.2	7.5	0.25	0.31	39	49	47	59	---	15.6
5	0.6	1.0	530	0.651	10.9	6.67	0.30	0.40	46	62	52	70	---	24.0
	Equil.	1.0	533	0.65	7.5	9.2	0.022		4410				0	
							No. 2 Oil							
6	0.3	1.0	532	0.65	7.7	8.6	0.20	0.20	86	88	87	89	---	10.4
7	0.3	1.0	644	0.655	8.8	-	0.08	0.09	120	135	121	136	---	---
8	0.3	1.0	748	0.644	7.7	8.98	0.041	0.041	166	169	167	170	---	7.3
9	0.3	3.3	533	0.655	6.8	10.4	0.06	0.06	116	112	116	112	---	-5.6
10	0.6	1.0	530	0.655	7.7	8.9	0.0075	0.0078	66	69	72	75	---	9.9
	Equil.	1.0	755	0.65	7.27	9.71	0.014		6883				0	
							C_3H_8							
11	0.3	1.0	533	0.65	11.3	7.3	0.26	0.36	62	87	62	87	461	12.0
12	0.3	1.0	644	0.655	10.9	7.65	0.18	0.24	89	121	89	121	336	9.7
13	0.3	1.0	750	0.655	11.5	7.1	0.08	0.12	110	160	113	164	241	17.3
14	0.3	3.3	533	0.655	8.11	7.3	0.025	0.027	94	100	94	100	186	15.7
15	0.6	1.0	539	0.66	10.9	6.8	0.15	0.20	82	112	82	112	---	20.8
	Equil.	1.0	533	0.65	7.56	8.56	0.028		4322				0	

*Expressed as measured on a dry basis

+NO_x = NO + NO_2

**Corrected by the ratio of measured oxygen used to equilibrium oxygen used.

emissions data, summarized in Table 2, indicate significant changes in concentration levels as a result of increasing swirl. In addition, variations in the trends of the exhaust composition data were observed for different fuels suggesting that there are differences in the structure of the flow fields which affect the pollutant formation and destruction. These differences were explored in greater detail in the mapping tests discussed in the following sections. Increasing the inlet air swirl from S = 0.3 to S = 0.6 resulted in increased exhaust concentration of NO_x in the liquid propane tests but in decreased NO_x concentrations in the iso-octane and No. 2 fuel oil tests. The trends observed for liquid propane are in agreement with those previously reported for gaseous propane and natural gas and are characteristic of a flow field having high fuel concentrations near the centerline (Refs. 9 and 11). Visual observations of the combustion process in the vicinity of the injector revealed that liquid propane was being injected in a concentrated stream having a very narrow spreading angle. The opposite trends observed in tests conducted with iso-octane and with No. 2 fuel oil probably are due to differences in the fuel/air distribution in the combustor. The effects of swirl on the combustor flow field are discussed later on in the report.

Input-output tests were also conducted to determine the effect of combustor pressure on exhaust species concentrations. Increasing the combustor pressure while maintaining constant inlet mass flow and temperature results in longer residence times and generally higher temperatures and reaction rates which produce increased NO emissions and decreased hydrocarbon emissions. These trends were found for liquid propane (cf., Tests 11 and 14) and No. 2 fuel oil (cf., Tests 6 and 9). However, the iso-octane tests show opposite trends with combustor pressure (cf., Tests 1 and 4). The measured exhaust NO concentration level decreased significantly and the exhaust CO concentration increased for combustion of iso-octane at 3.3 atm, suggesting a change in the fuel spray characteristics or fuel/air distributions at elevated pressure for this fuel. For the 3.3 atm iso-octane test, the exhaust gas temperature levels decreased and high concentrations of particulate carbon were observed, indicating a reduced combustion efficiency. The effects of pressure on mixing and vaporization are discussed later in the report.

A final series of input-output tests was conducted to determine the effect of inlet air temperature on pollutant emissions. Increased inlet air temperature should result in higher combustion temperatures and more rapid oxidation of fuel and CO and more rapid NO formation. The combustor temperature distributions (discussed in the following section) and the exhaust emissions data presented in Table 2 indicate that an increase in inlet air temperature from 533K to 750K resulted in a significant increase in the exhaust NO concentration and reduced UHC and CO concentrations. Other investigators (Ref. 12) have reported similar emissions trends with inlet air temperture, and similar increases in NO emissions levels were measured in previous natural gas combustion tests (Ref. 11).

Flow Field Mapping Results

Examination of the results of the input-output tests indicates that pollutant emissions levels are particularly sensitive to inlet air swirl, combustor pressure and inlet air temperature. Variations in these parameters produced some experimental trends which cannot be predicted on the basis of thermochemistry alone, suggesting that there is significant coupling between the fluid dynamic and chemical processes in the combustor. Such a coupling was observed in the previous gaseous fuel tests (Ref. 9). Therefore, detailed maps of the flow field and holograms of the fuel spray were obtained for the six test conditions listed in Table 1. These conditions were selected to encompass variations in combustor operating conditions which have the greatest influence on pollutant emissions, as determined from the input-output tests.

As in the gaseous fuel tests referenced above, the combustor mapping data were reduced to isopleth form to permit visualization of the radial and axial variation of individual flow field parameters and to facilitate comparisons between these parameters for each of the flow configurations investigated. However, since the radial distributions of mean flow properties were determined at a discrete number of axial locations within the combustor, some interpolation between stations was required. Typically a radial traverse consisted of 9 to 15 measurements spaced approximately uniformly across the combustor diameter. A complete tabulation of the experimental data is presented in Appendices G-I.

High-Speed Motion Pictures

High-speed (500 frames/sec) color motion pictures of the reacting flow in the vicinity of the fuel injector were obtained for each of the six test conditions. With the exception of the test using liquid propane, the fuel spray was visible for all test conditions. For the time resolution of the film, the fuel spray appeared steady; however, as will be seen later, the laser velocimeter data indicate that there are fluctuations in the droplet velocities. These films also showed that there were large-scale fluctuations in flame luminosity for all test conditions. These luminosity fluctuations were somewhat smaller in scale than the fluctuations observed in the gaseous fuel tests with low air/fuel velocity ratios (Ref. 9). These visual observations of the flame structure support the conclusions drawn later from laser velocimeter data regarding the fluctuations of the flow in the initial mixing regions. Analysis of the transient pressure data, discussed below, and limited laser velocimeter data obtained using the frequency tracker indicate that for the conditions investigated there were no significant resonant pressure or velocity fluctuations. Hence, the observed fluctuations are primarily fluid dynamic in origin and are not the result of coupling of the combustion process with the acoustic properties of the combustor or mechanical properties of the fuel injection system.

Transient Pressure Measurements

The results of gaseous-fuel combustion tests, conducted in earlier phases of this program (Ref. 9) have indicated the possibility of the occurrence of combustion instabilities during operation at 1 atm and near stoichiometric mixture ratios. Pressure oscillations having a frequency of approximately 120 Hz and amplitudes of up to $\pm$ 6 percent were reported. The present liquid-fuel combustion studies were initiated with a series of screening tests to evaluate the stability characteristics of the combustor, in order to insure that the configurations and test conditions selected for detailed mapping would be essentially free of combustion instabilities. The amplitude and frequency of the pressure fluctuations occurring for each of the mapping experiments were determined by analyzing the output signal of a close-coupled pressure transducer installed in the combustor window port nearest the injector.

As in the gaseous-fuel tests, a pressure fluctuation having a frequency of approximately 120 Hz (the fundamental acoustic mode of the combustor duct) was measured for tests conducted at 1 atm, S = 0.3 and equivalence ratios in the range $0.5 \leq \phi \leq 0.9$. Although the frequency of the oscillations was relatively insensitive to changes in the overall equivalence ratio, the amplitude decreased rapidly as the equivalence ratio decreased and was less than $\pm$ 0.5 percent for $\phi \leq 0.7$. The use of an orifice plate to increase the combustor pressure changed the acoustic characteristics of the duct and significantly reduced the natural frequency and the amplitude of the oscillations. Based on results from these tests, an overall fuel/air equivalence ratio of 0.65 was selected for the mapping tests.

The Effect of Swirl on Flow Field Structure and NO Formation

When a gaseous fuel is injected axially into a swirling air flow the primary mode of dispersion of the gaseous fuel is turbulent transport and the primary effects of increasing swirl are to increase local mixing rates and to increase radial and axial pressure gradients. Previous tests with natural gas (Ref. 9) have confirmed that energy release rates increase with increased swirl. However, liquid fuels of low volatility injected with a radial component of velocity may penetrate the airstream primarily as a result of droplet inertia. In this case, swirl would influence relative velocities between fuel droplets and air and would affect droplet vaporization and burning rates.

The input-output tests indicate that the effects of swirl are very different for the three fuels tested. For propane, increasing swirl results in a decrease in CO levels and an increase in NO_x. Here, propane behaves like a gaseous fuel and combustion rates are enhanced by increased turbulent transport rates. However, it is found that with iso-octane, CO levels increase and NO_x levels decrease with increased swirl. This result suggests that insufficient vaporization occurs close

to the injector to achieve the rapid air/vapor fuel mixing allowed at higher swirl number with an entirely vaporized fuel. In addition the effect of increased swirl is to shift air flow radially outward and increase the radial pressure gradient; this would tend to retard the penetration of small, partially vaporized fuel droplets. Since shear levels decay rapidly with axial distance, vaporized fuel introduced further downstream into the annular airstream does not burn rapidly.

For No. 2 fuel oil, increasing swirl results in a decrease in both CO and NO_x levels. Temperature and composition profiles presented later on in this report indicate that radial droplet penetration was the dominant mode of dispersion of this fuel. Once the fuel is dispersed across the airstream, the droplet combustion rates are probably increased with increasing swirl by higher relative velocities and turbulence levels. More rapid combustion and smaller flame standoff distances in burning droplets or droplet arrays would result in lower levels of both CO and NO_x.

Flow field mapping tests conducted with iso-octane confirm the results of the input-output tests and allow some tentative conclusions to be made about the interactions of swirl with fuels of moderate volatility. The time-mean temperature distributions obtained for iso-octane/air combustion at one atmosphere pressure and for inlet air swirl levels of 0.3 and 0.6, respectively, are presented in Fig. 5. An initial examination of the data reveals the similarity of the flow field structure obtained for each of these liquid-fuel test configurations and a general correspondence with the flow fields obtained previously using gaseous fuel (Ref. 9) i.e., the characteristic shape usually associated with axisymmetric, turbulent diffusion flames. The contours are characterized by peak temperatures occurring off the centerline in an annular region. Variations in liquid fuel and air inlet conditions altered the relative rates at which heat was released within the combustor, and specific trends resulting from these variations are evident with more detailed analysis of the data.

The temperature contours are not symmetric about the combustor centerline, but instead are displaced slightly toward negative values of R/R_o. Since the uniformity of the inlet flow was verified by laser velocimeter measurements and by temperature measurements in the inlet section, the apparatus was eliminated as the source of this asymmetry. Furthermore, the species concentration distributions appear symmetric about the combustor centerline. Therefore, the asymmetry must be the result of blockage introduced into the flow by traversing the comparatively large thermocouple probe (see Appendix A) from the positive to negative radial direction.

Specific trends resulting from systematic variation of the inlet swirl are evident from the temperature data. For example, increasing the swirl level from 0.3 to 0.6 results in an initial increase in the axial rate of heat release ($X/D<2$), followed by a gradual decrease in the axial rate of heat release ($X/D>2$).

TIME–AVERAGED TEMPERATURE DISTRIBUTIONS

ISO–OCTANE/AIR, 1 ATM, T_{AIR} = 533 °K, ϕ = 0.65

(A) SWIRL = 0.3

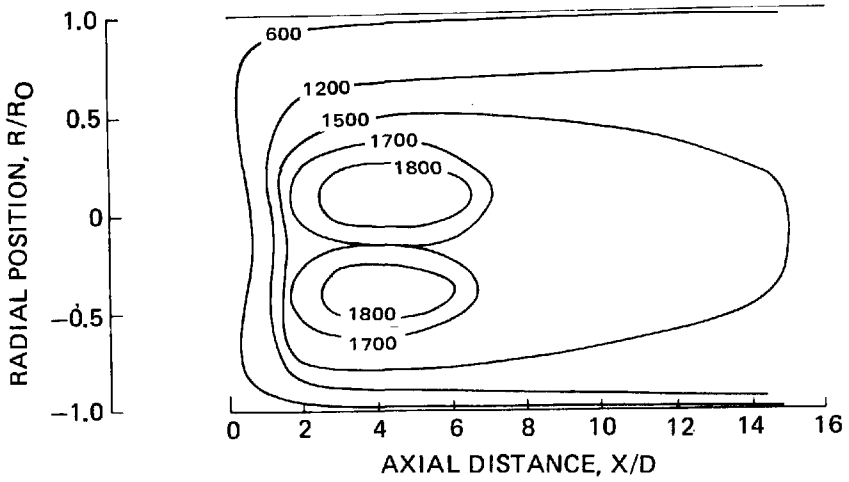

(B) SWIRL = 0.6

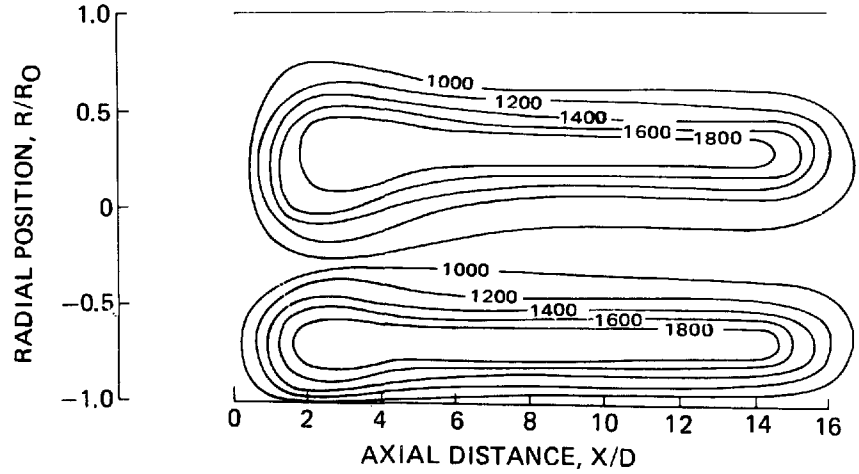

This initial increase of heat release rate is attributed to more rapid mixing of the vapor fraction. However, insufficient initial penetration of fuel droplets leads to an extended flame as indicated by the radial temperature gradients which remain steeper for a greater axial distance. For the case of 0.3 swirl, the greater part of the available chemical energy was released within an axial distance of approximately six combustor diameters (X/D = 6) and the downstream temperature distributions are relatively flat. Isotherms corresponding to S = 0.6, on the other hand, indicate a larger flame length, as evidenced by peak temperatures extending the full length of the combustor (X/D = 14).

Mean axial gas- and droplet-velocity contours obtained for iso-octane/air combustion at one atmosphere pressure are presented in Figs. 6 and 7. Differences between the local gas and droplet velocities are apparent near the injector, as are areas of flow recirculation. Also, some unsteadiness of the flow was indicated by fluctuations in the droplet velocity measurements. Farther downstream (X/D>1.0), droplet sizes and concentrations are reduced by evaporation and combustion and droplets are convected at the local gas velocity. At S = 0.3, it was not possible to distinguish between local fuel droplet and gas velocities in the vicinity of the spray near the centerline because of the high droplet concentration. Consequently, no gas flow recirculation is shown; however, the existence of a recirculation zone may be inferred from the droplet velocity data, Fig. 7a. Gas velocity measurements were possible at S = 0.6 and a torroidal-shaped recirculation zone was identified (Fig. 6). A primary effect of increasing the inlet air swirl from 0.3 to 0.6 was to shift the regions of droplet recirculation closer to the injector, thereby influencing flame stabilization and energy release in the initial region of the combustor.

The local time-mean axial velocities are somewhat higher at S = 0.6 and the diffusion-flame-like flow field structure persists for a greater axial distance. The insensitivity of the fuel droplet axial velocities to the level of inlet air swirl is also apparent from the similar appearance of the droplet velocity distributions in the initial mixing regions; however, at S = 0.6, high droplet velocities persist farther downstream. Spray trajectories, as determined from laser velocimetry and laser holography measurements are also shown in Fig. 7 and are in good agreement with the nominal spray angle of 60 degrees. The persistence of droplet velocity and the higher gas velocities at S = 0.6 are associated with the increase in recirculation zone size and consequent increase in mass flux density outside the recirculation zone. This increase in mass flux density was enhanced by the confined geometry of the combustion facility.

Gas composition contours for low (S = 0.3), and moderately (S = 0.6) swirling flows, discussed above, are shown in Figs. 8, 9 and 10. These data indicate the tendency of increased swirl to suppress mixing beyond a zone of rapid initial mixing near the injector. Radial concentration gradients are sharper with increased swirl and CO burnout is slower. Further insight into the effect of swirl on

MEAN AND RMS GAS VELOCITY DISTRIBUTIONS

ISO–OCTANE/AIR, 1 ATM, T_{AIR} = 533°K, ϕ = 0.65

RECIRCULATION ZONE

U_{RMS} >10 M/SEC

(A) SWIRL=0.3

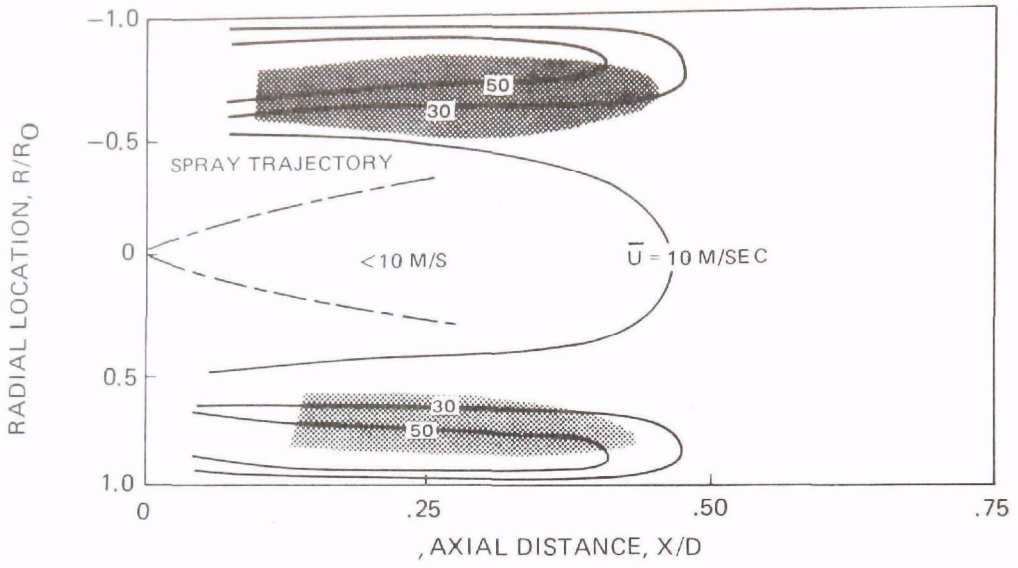

(B) SWIRL=0.6

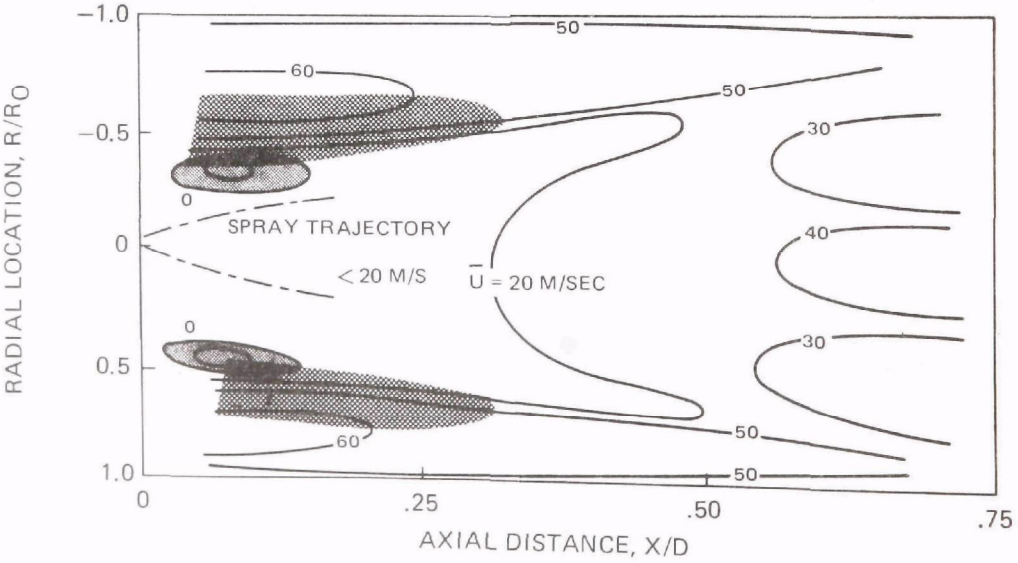

MEAN AND RMS DROPLET VELOCITY DISTRIBUTIONS

ISO OCTANE/AIR, 1 ATM, T_{AIR} 533°K, ϕ 0.65

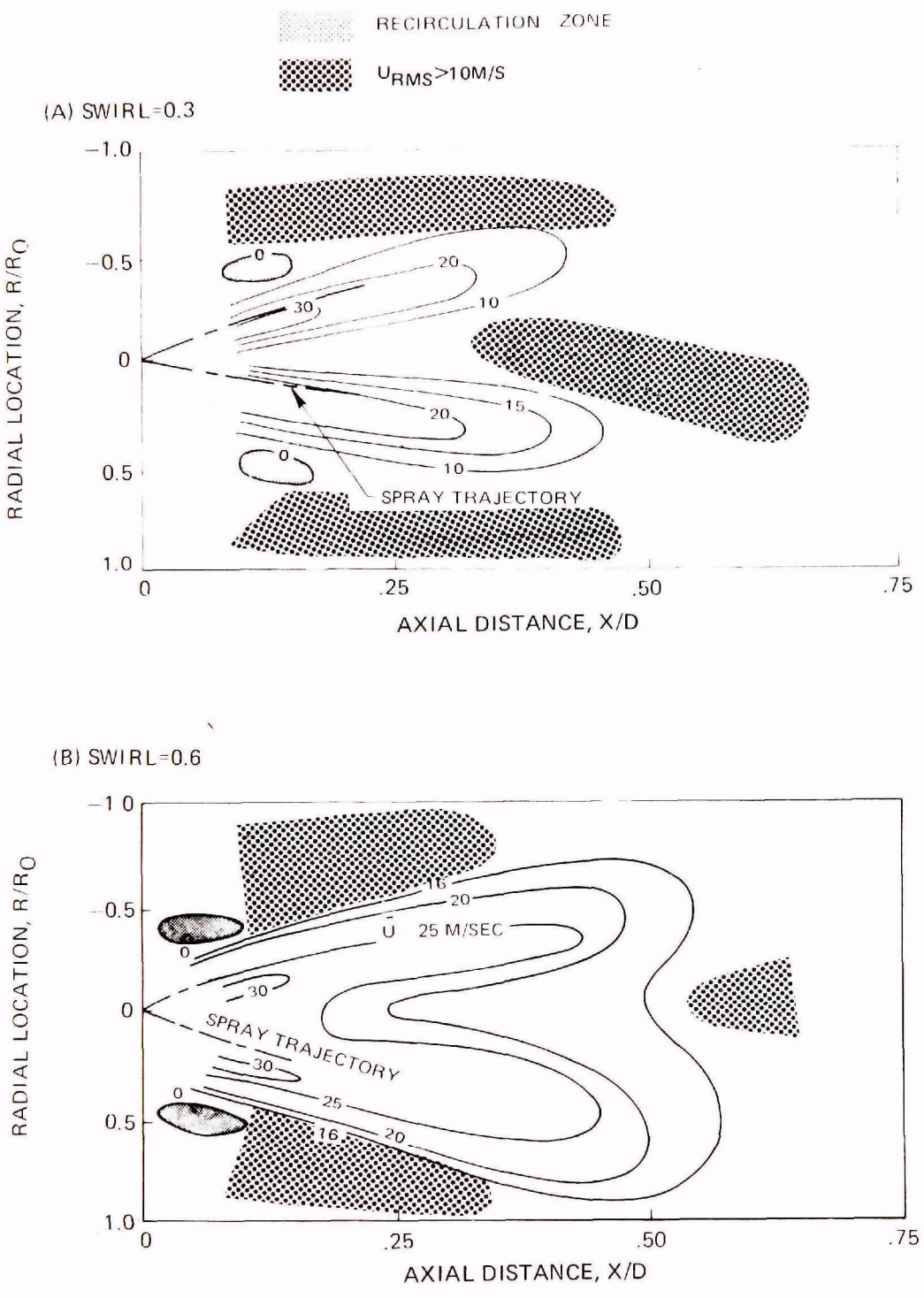

FIG. 8

TIME–AVERAGED O_2 DISTRIBUTIONS

ISO–OCTANE/AIR, 1ATM, $T_{AIR} = 533^{o}K$, $\phi = 0.65$

(A) SWIRL=0.3

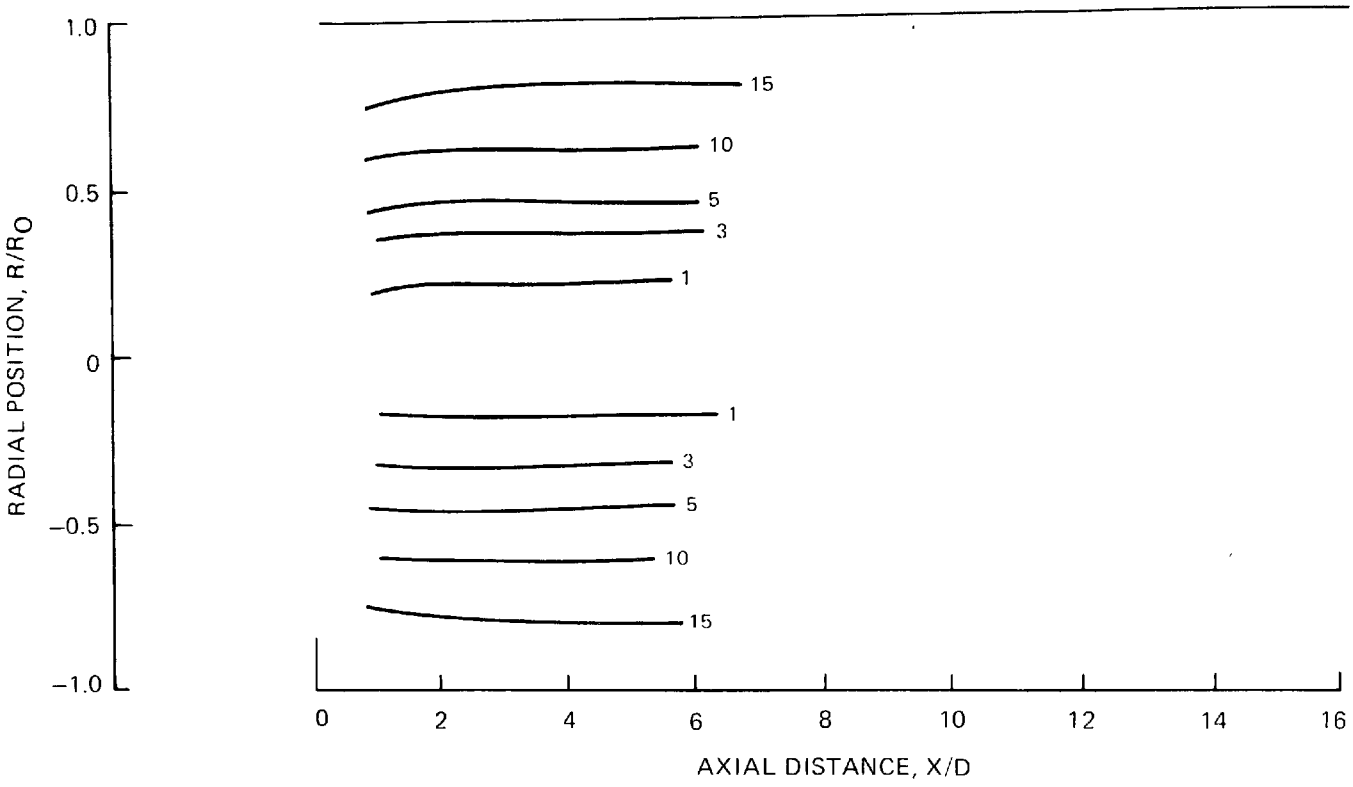

(B) SWIRL=0.6

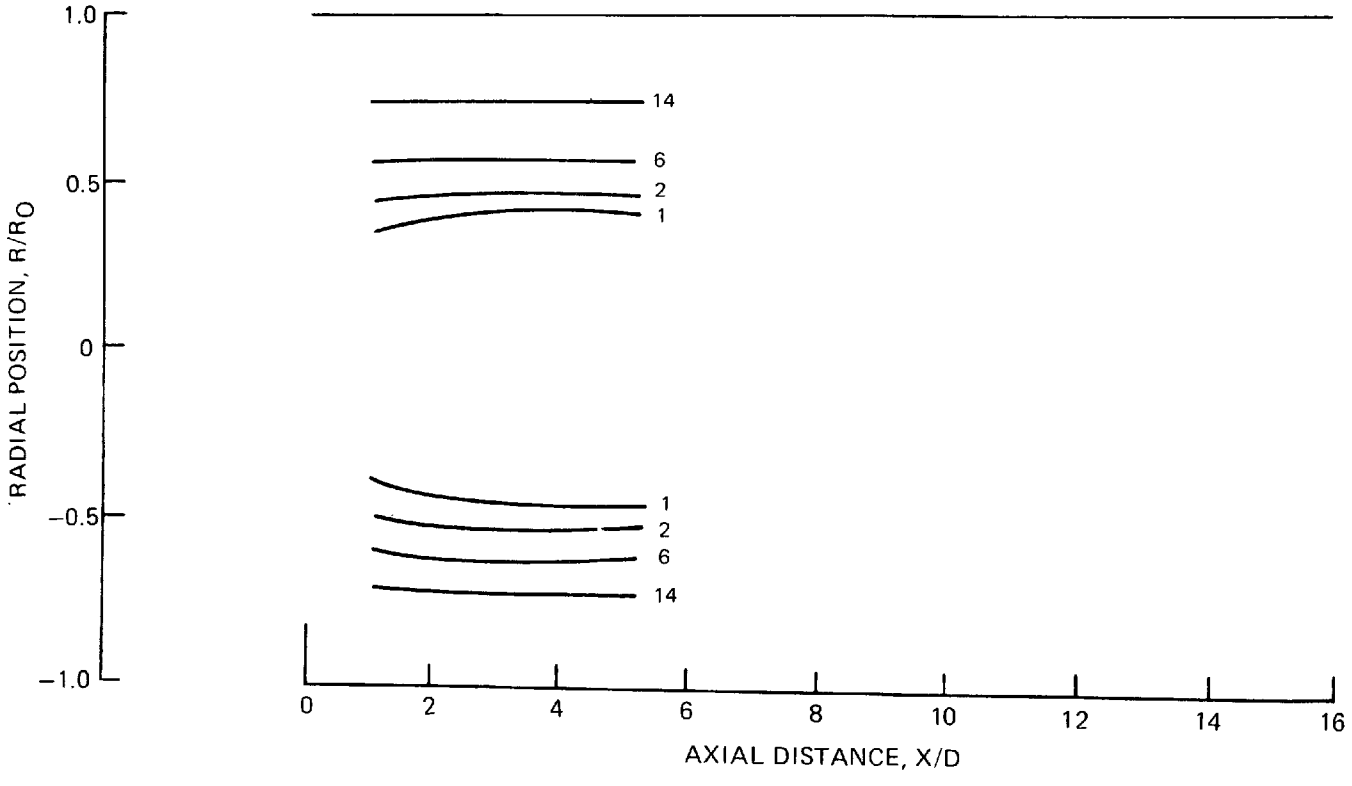

FIG. 9

TIME–AVERAGED CO DISTRIBUTIONS

ISO–OCTANE/AIR, 1 ATM, $T_{AIR} = 533^{o}K$, $\phi = 0.65$

(A) SWIRL=0.3

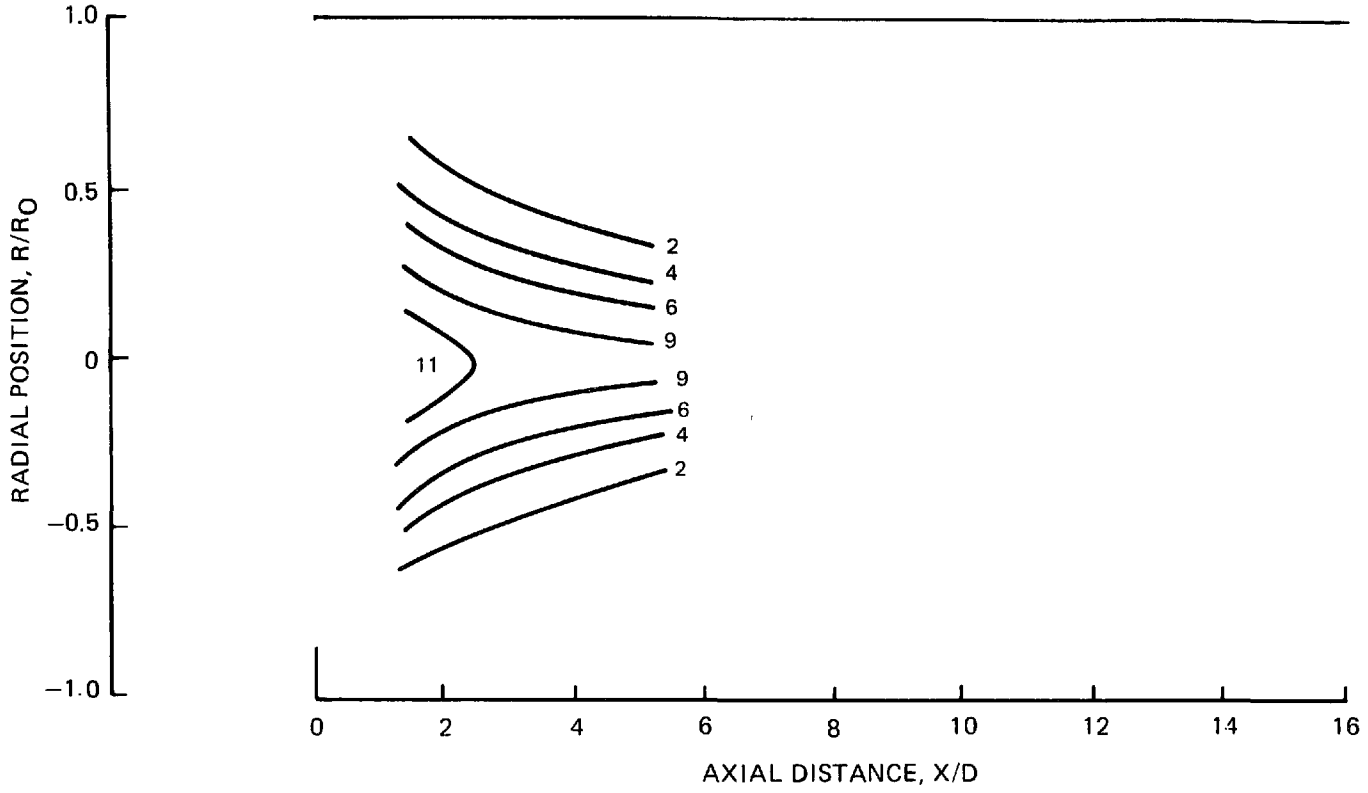

(B) SWIRL=0.6

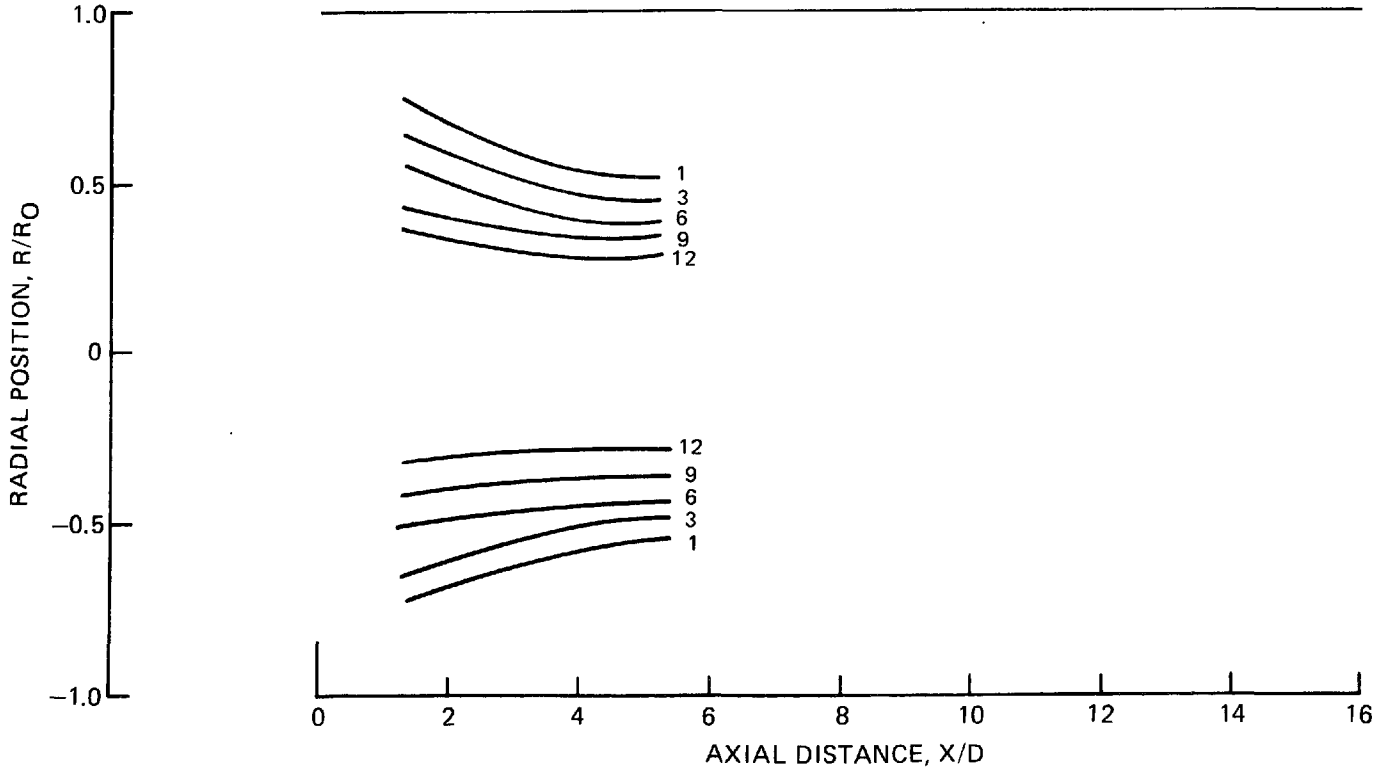

FIG. 10

TIME–AVERAGED CO_2 DISTRIBUTIONS

ISO–OCTANE/AIR, 1 ATM, $T_{AIR} = 533^{o}K$ $\phi = 0.65$

(A) SWIRL=0.3

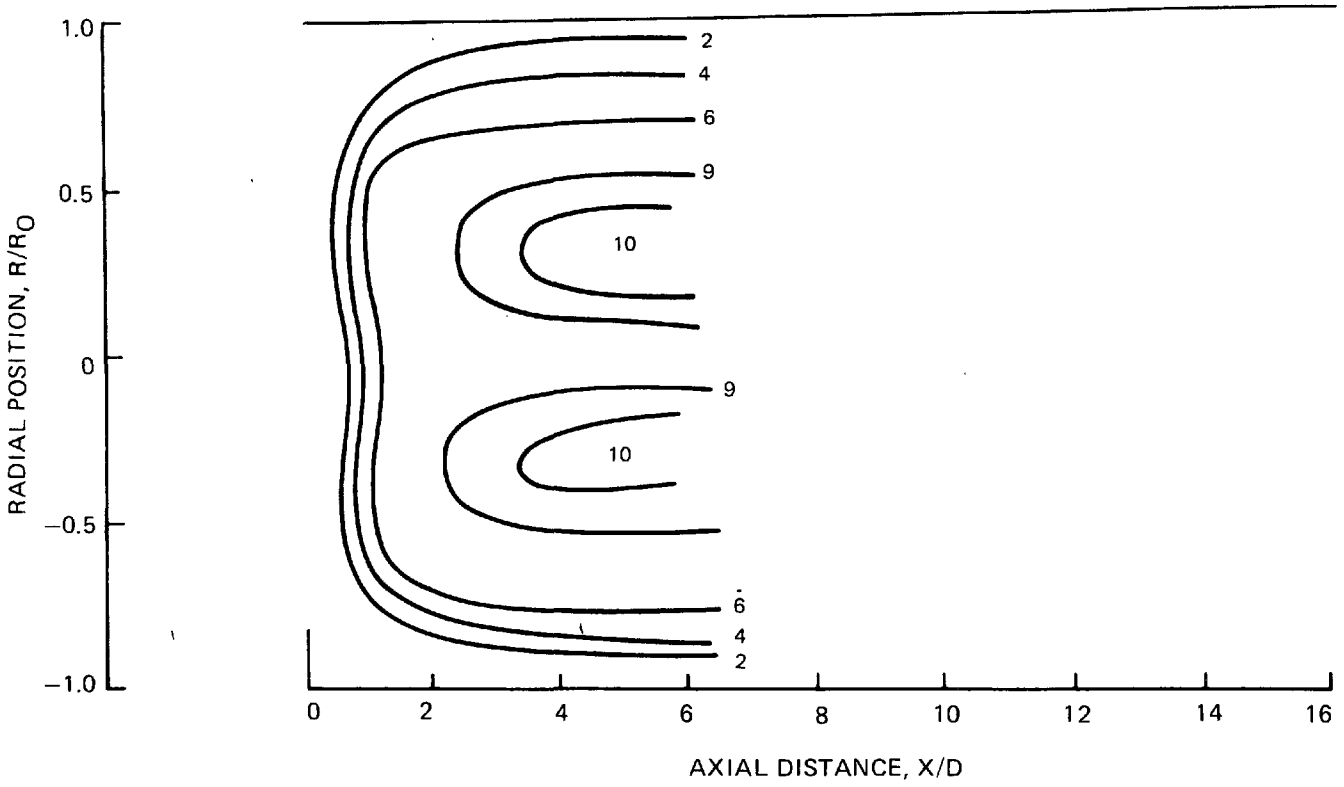

(B) SWIRL=0.6

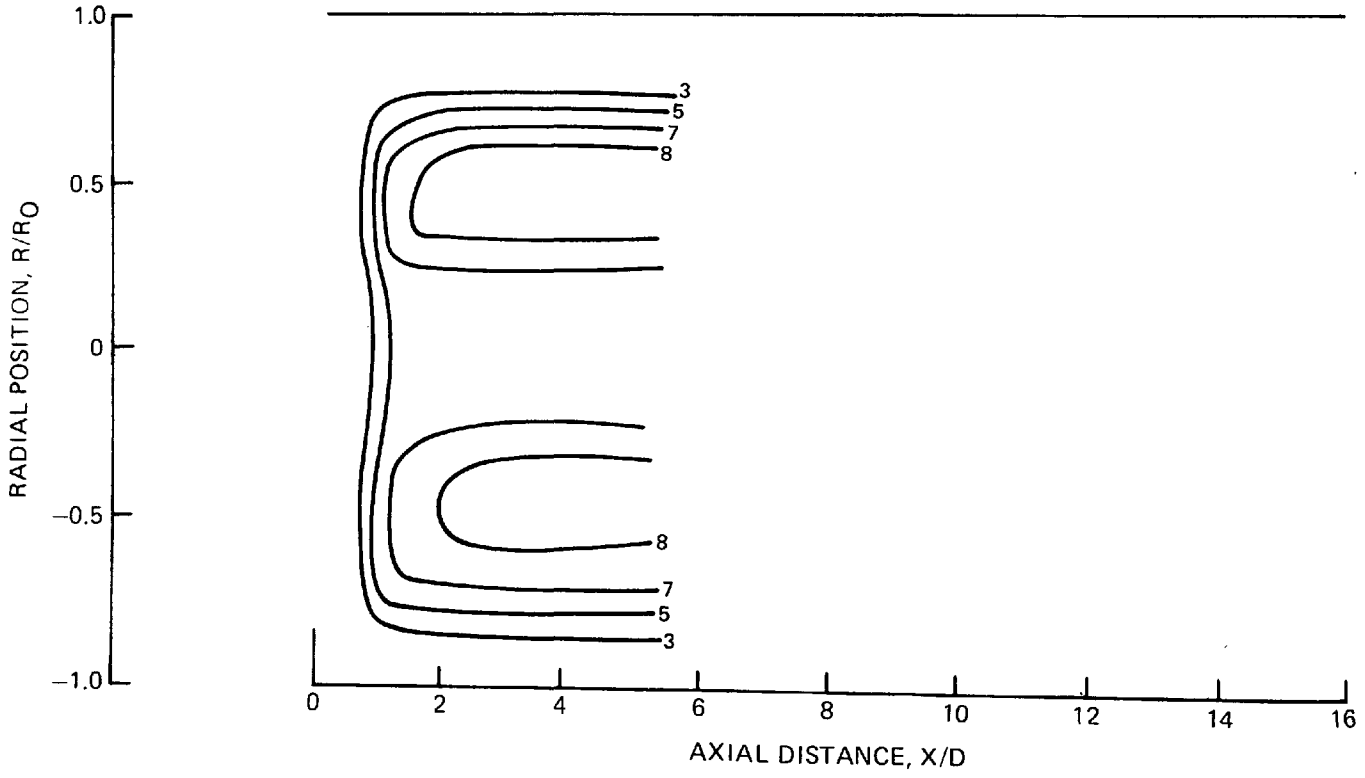

iso-octane vaporization and combustion is obtained from comparisons of total hydrocarbon concentration distributions (Fig. 11) together with profiles of the percentage of hydrocarbons vaporized (Fig. 12). In the upstream section of the combustor, total hydrocarbon concentrations are higher for the lower swirl number (Fig. 11), while the concentrations of unvaporized fuel (computed from the product of total hydrocarbon concentration from Fig. 11 and 1 minus the fraction vaporized from Fig. 12) are about the same. In this upstream region increased swirl promotes mixing of vaporized fuel. However, for the higher swirl number unvaporized fuel persists further downstream and the total hydrocarbon concentrations are greater in the downstream sections even after the fuel has vaporized. It is likely that this is a result of reduced droplet penetration into the airstream with increased swirl and the rapid decay of swirl (shear) induced mixing with axial distance.

NO concentration distributions are shown in Fig. 13. The regions of high NO concentration within the combustor are coincident with the regions of locally high temperature. At low swirl, higher concentrations of NO were measured close to the combustor centerline and in the vicinity of the injector. In contrast, at moderate swirl the reaction zone is moved rapidly outward and closer to the injector, and NO formation occurs in a narrow annular region. The combined effect of low oxygen concentration and low temperature result in a reduced rate of NO formation and, therefore, lower NO exhaust emissions levels at S = 0.6.

The mapping data indicate that, in the present combustor configuration, increasing swirl from 0.3 to 0.6 increases mixing of partially vaporized fuel with air in the initial region of the flow, resulting in increased energy release rates. Hence, increased swirl tends to move the region of flame stabilization closer to the fuel injector. Beyond this initial region, increasing swirl appears to suppress vaporization of the liquid fuel and subsequent mixing of the vaporized fuel with air. At sufficiently high swirl numbers, the radial pressure gradients reduce penetration of partially vaporized droplets into the airstream, resulting in a relatively cold fuel-rich region on the combustor centerline. The reduced vaporization rates result in an extended mixing region. In addition, axial decay of swirl-induced shear levels tends to reduce mixing rates downstream from the injector. Reduced mixing rates result in generally slower fuel oxidation and CO burnout rates and in lower NO formation rates.

Effect of Pressure On Flow Field Structure and NO Formation

Previous tests (Ref. 9) with natural gas have demonstrated several effects of pressure on exhaust emissions at constant mass flow rate. Increasing pressure from 1 to 3 atmospheres decreased CO levels and increased exhaust NO levels principally because combustor residence time increases with pressure. However, the local rate of energy release decreased indicating that mixing rate was suppressed at higher pressure. This would be expected since shear levels decrease

FIG. 11

TIME–AVERAGED DISTRIBUTIONS OF UNBURNED HYDROCARBONS

ISO–OCTANE/AIR, 1 ATM, T_{AIR}=533°K, ϕ =0.65

(A) SWIRL=0.3

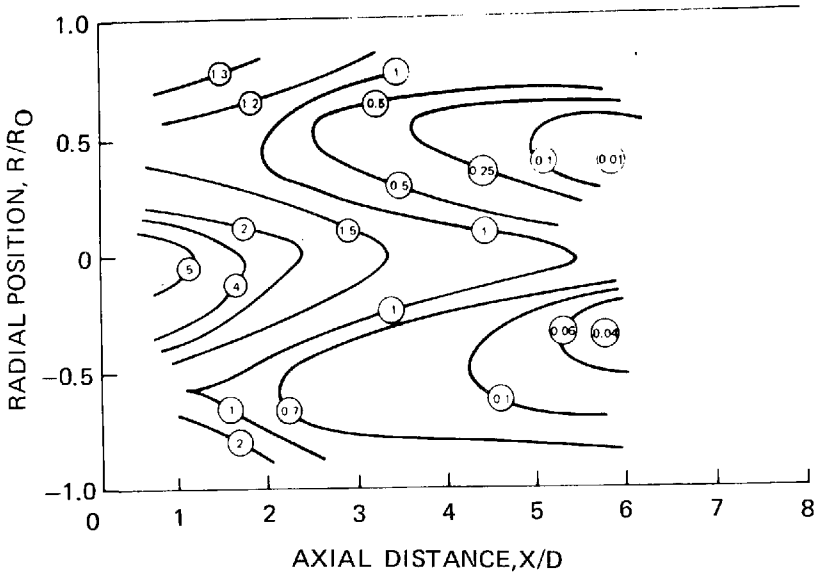

(B) SWIRL=0.6

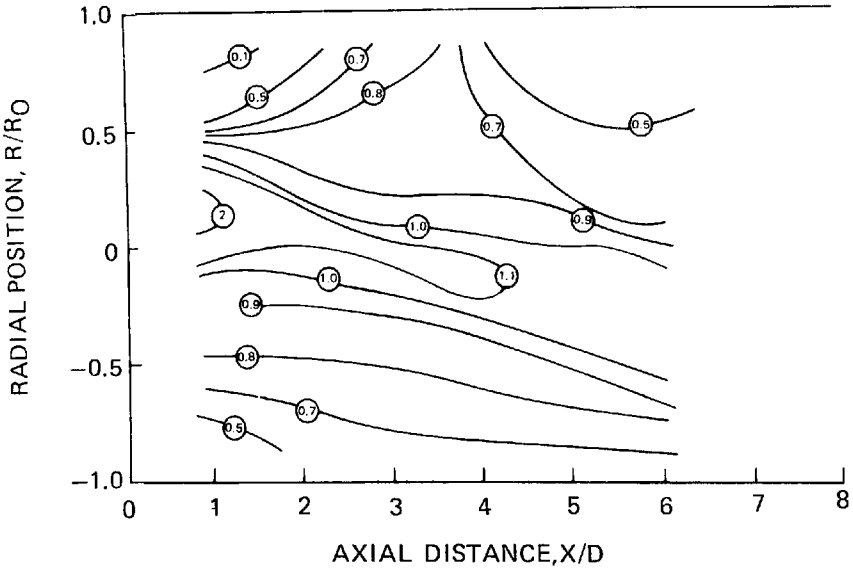

FIG.12

TIME–AVERAGED PERCENTAGE OF HYDROCARBONS VAPORIZED

ISO–OCTANE/AIR,1 ATM,T_{AIR}=533°K,ϕ=0.65

(A) SWIRL=0.3

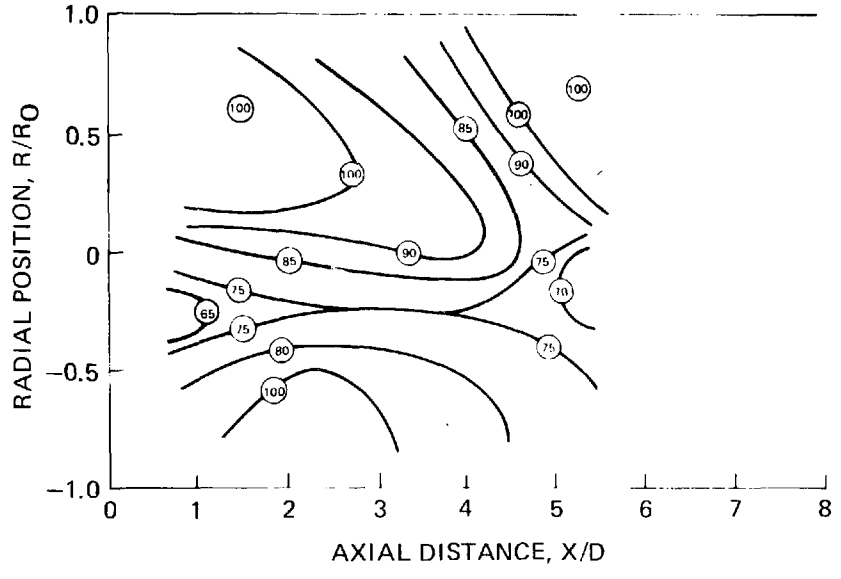

(B) SWIRL=0.6

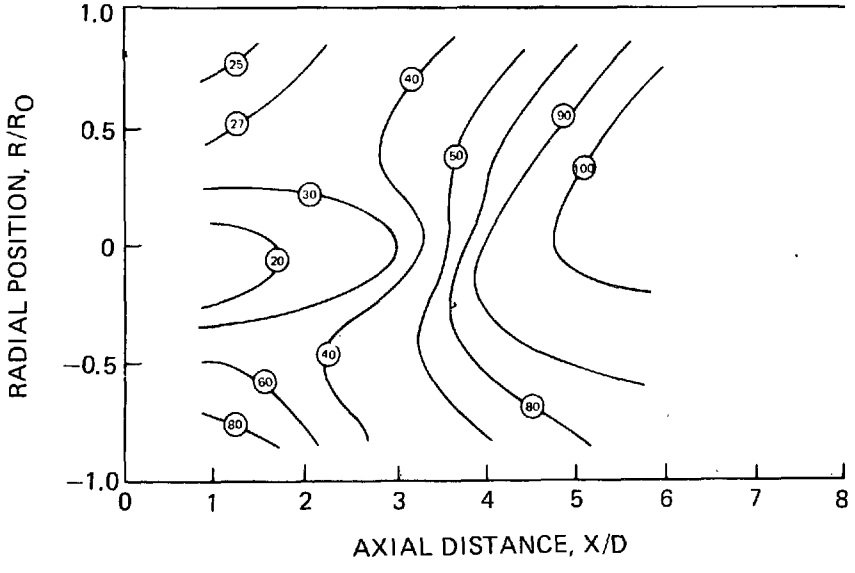

TIME–AVERAGED NO DISTRIBUTIONS

ISO–OCTANE/AIR, 1 ATM, $T_{AIR} = 533^{o}K$, ϕ=0.65

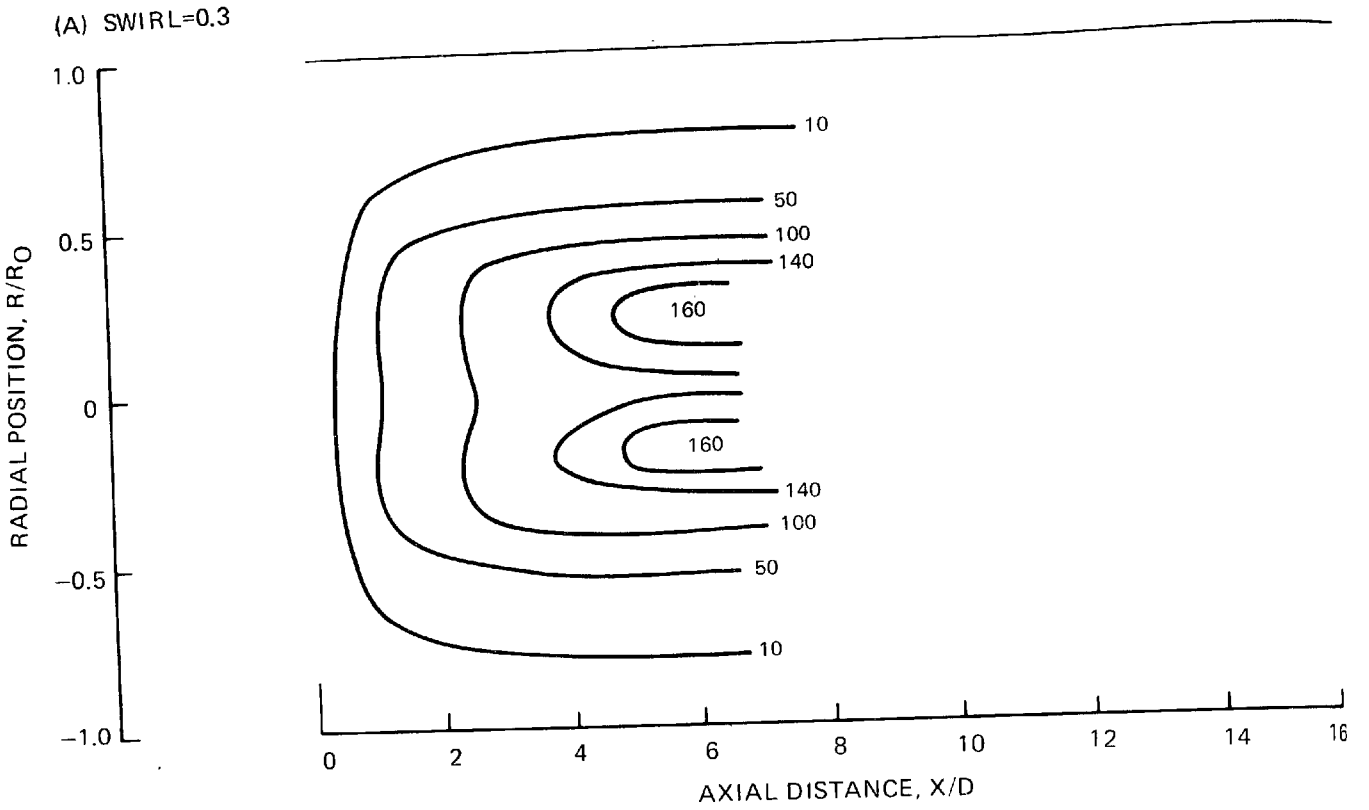

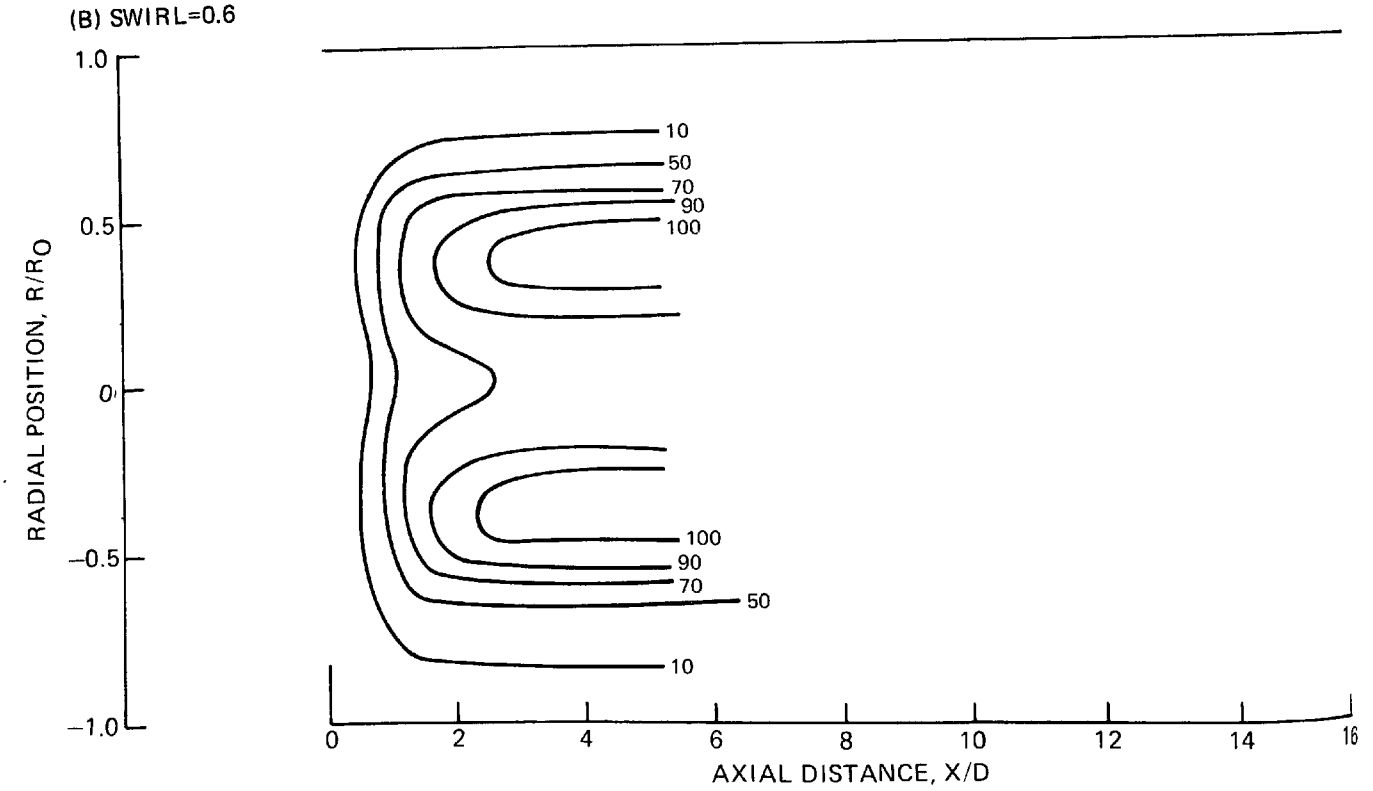

with decreasing velocity. This conclusion is supported by the fact that at even higher pressure, 7 atm, exhaust hydrocarbon levels increased despite the increased residence time.

For two of the liquid fuels investigated, No. 2 distillate oil and propane, increasing pressure from 1 to 3.3 atmospheres decreased CO levels and increased NO levels. However, when iso-octane was used as a fuel, CO levels increased and NO emission decreased as the pressure was increased from 1 to 3.3 atmospheres. The flow field mapping tests conducted using iso-octane confirm the results of the input-output tests and indicate the effect of pressure on the flow field structure and pollutant formation.

The time-mean temperature distributions, Fig. 14, indicate that longer flames are obtained at higher pressure. Furthermore, peak temperatures are lower at higher pressure suggesting lower energy release rates. Examination of the species concentration distributions obtained for iso-octane/air combustion at elevated pressure are consistent with the temperature data. Examination of Fig. 15 reveals that at 3.3 atm pressure, the O_2 cencentrations near the combustor centerline are lower, indicating a reduced mixing rate. Similarly, initial breakdown of the fuel to CO and oxidation of CO to CO_2 is slower at 3.3 atm (cf., Figs. 16 and 17). Figure 18 shows that NO is formed in an annular region close to the injector at approximately the same radial location as the peak temperature. There are steep radial gradients and low NO concentration levels at the combustor centerline. Peak NO concentrations at the elevated pressure are much lower than were observed at atmospheric pressure. An increase in pressure from 1.0 atm to 3.3 atm results in a significant decrease in NO emissions which may be attributed in part to lower temperatures.

One possible explanation for the different effect of pressure on flow field structure for iso-octane in comparison with natural gas, propane and No. 2 distillate oil is as follows: The propane rapidly vaporizes on injection into the combustor. Hence, both natural gas and propane may be considered gaseous fuels. In spite of reduced mixing rates resulting from the reduced shear levels associated with the lower air velocities, combustion is enhanced and NO emissions increase due to increased residence time and increased reaction rates. In contrast, No. 2 distillate oil burns largely inhomogeneously since vaporization rates are relatively low due to higher boiling points. Increased droplet penetration at higher pressure partially offsets the effect of reduced mixing due to shear and combustion goes to completion because of increased residence time. Iso-octane is more volatile than No. 2 distillate oil, and droplet vaporization tends to limit droplet penetration. With relatively little penetration of iso-octane liquid, combustion efficiency would be governed largely by droplet vaporization rates. But the droplet vaporization rate is a function of droplet boundary layer thickness, which in turn is a function of the product of gas density and relative velocity between droplets and air. For air moving at a velocity higher than the droplet velocity, as pressure increases the relative velocity might well be reduced far

TIME–AVERAGED TEMPERATURE DISTRIBUTIONS

ISO–OCTANE/AIR, $T_{AIR} = 533\ ^{o}K, \phi = 0.65$

(A) SWIRL = 0.3, 1 ATM

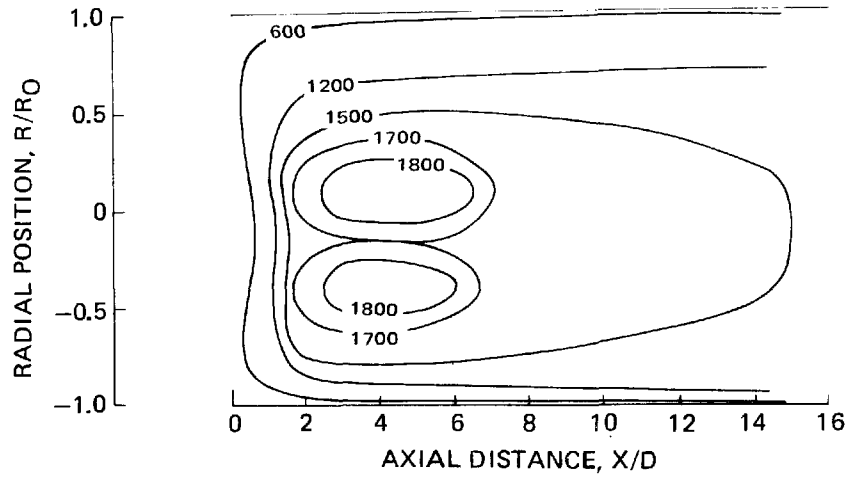

(B) SWIRL = 0.3, 3.3 ATM

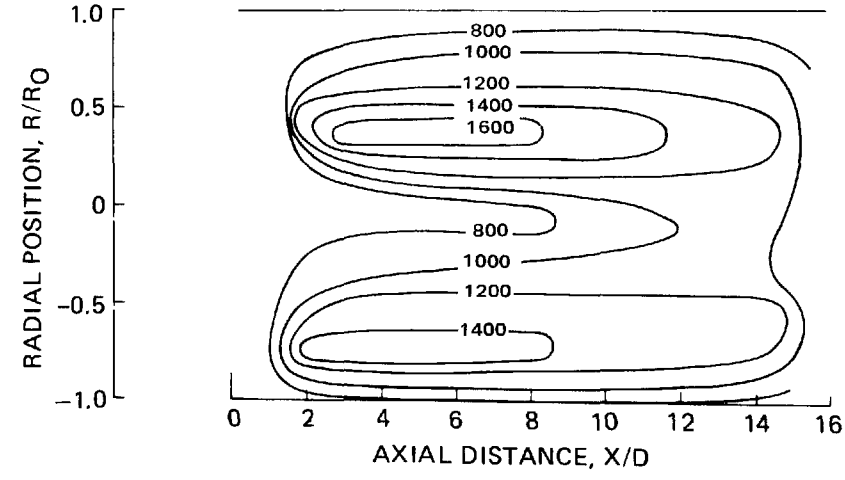

FIG. 15

TIME–AVERAGED O_2 DISTRIBUTIONS

ISO–OCTANE/AIR, 1 ATM, T_{AIR} = 533°K, ϕ = 0.65

(A) SWIRL=0.3, 1 ATM

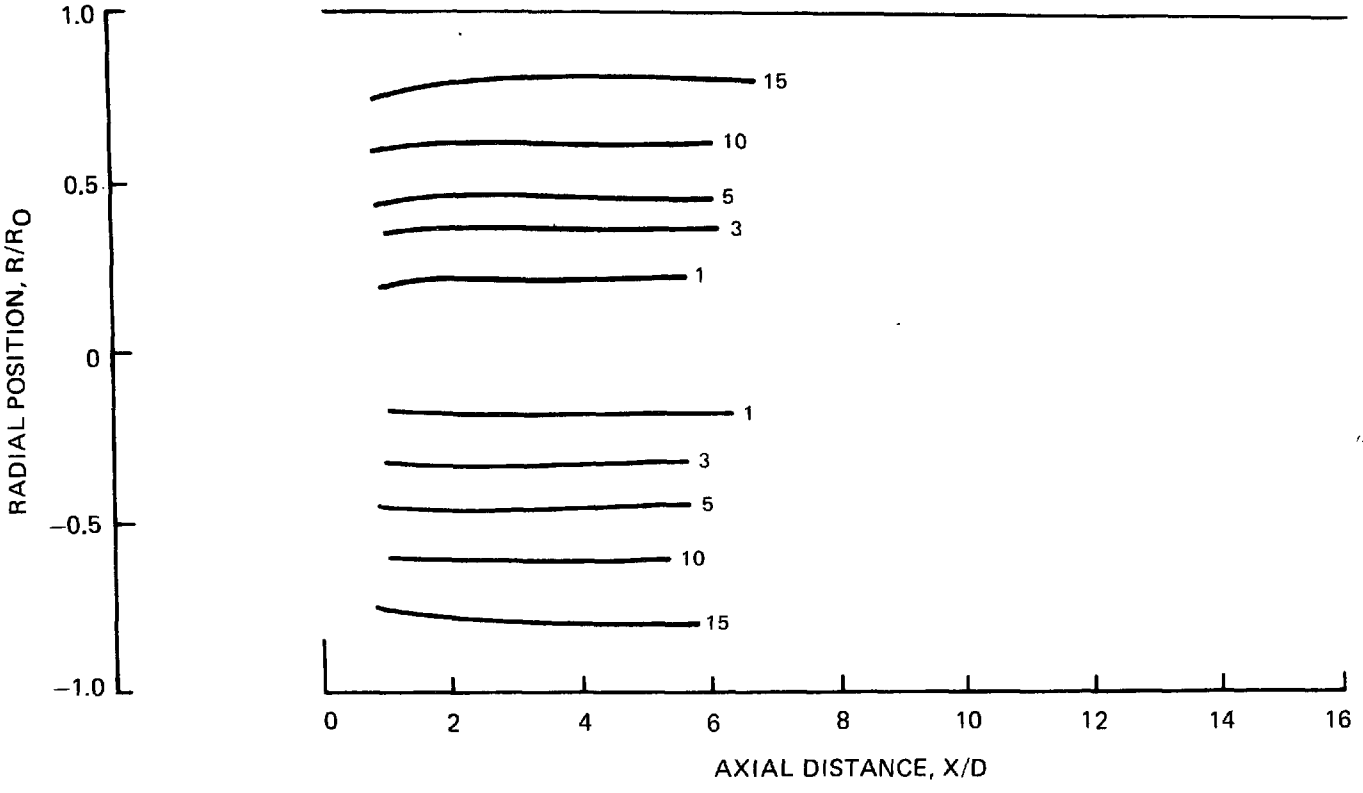

(B) SWIRL=0.3, 3.3 ATM

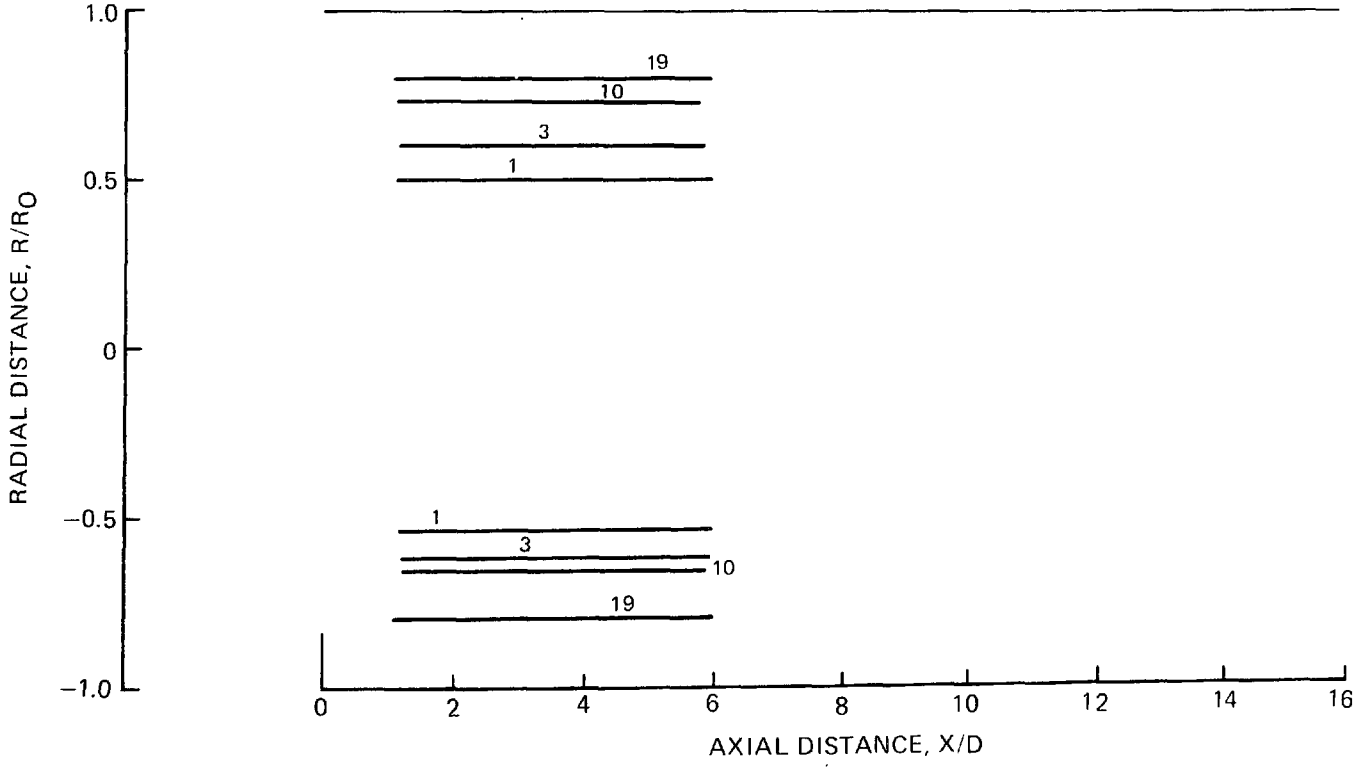

TIME–AVERAGED CO DISTRIBUTIONS

ISO–OCTANE/AIR, T_{AIR} = 533°K, ϕ = 0.65

(A) SWIRL = 0.3, 1 ATM

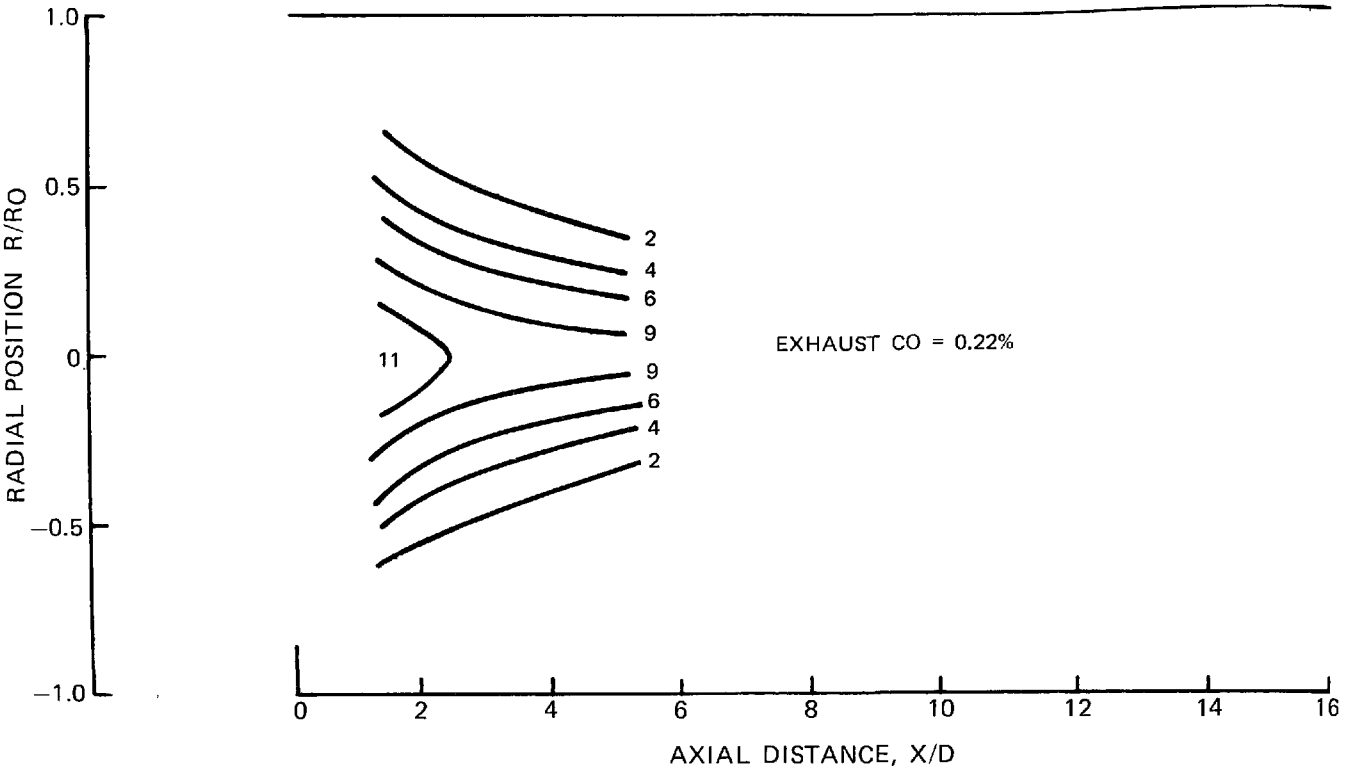

(B) SWIRL = 0.3, 3.3 ATM

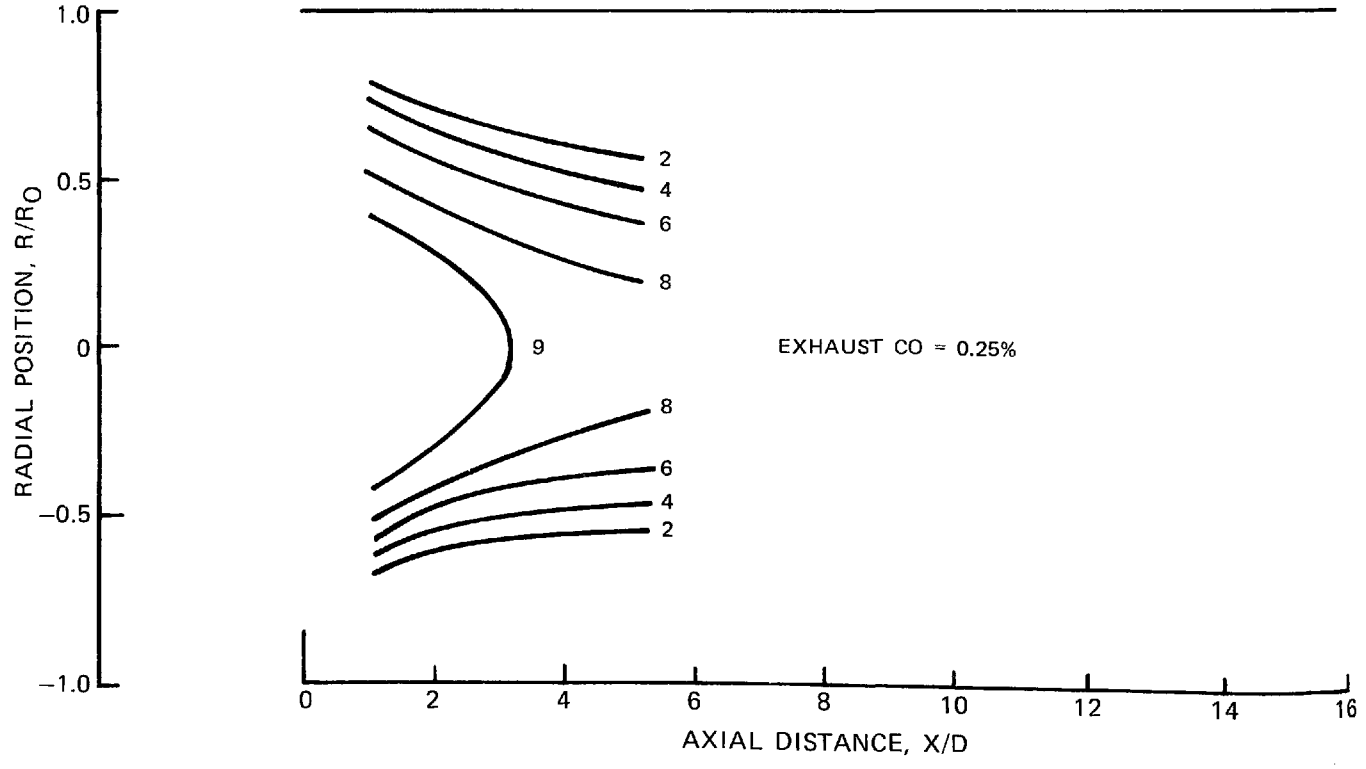

TIME–AVERAGED CO_2 DISTRIBUTIONS

ISO–OCTANE/AIR, T_{AIR} = 533°K, ϕ = 0.65

(A) SWIRL = 0.3, 1 ATM

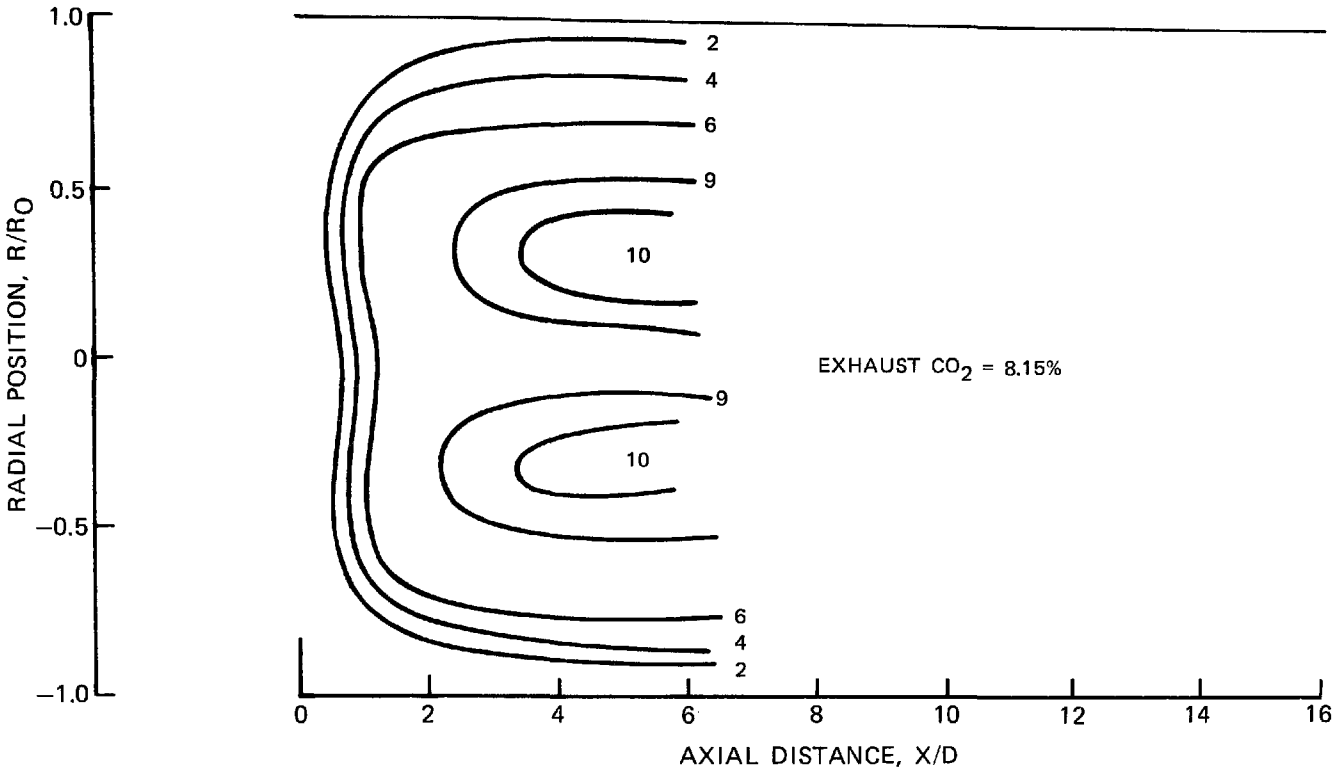

(B) SWIRL = 0.3, 3.3 ATM

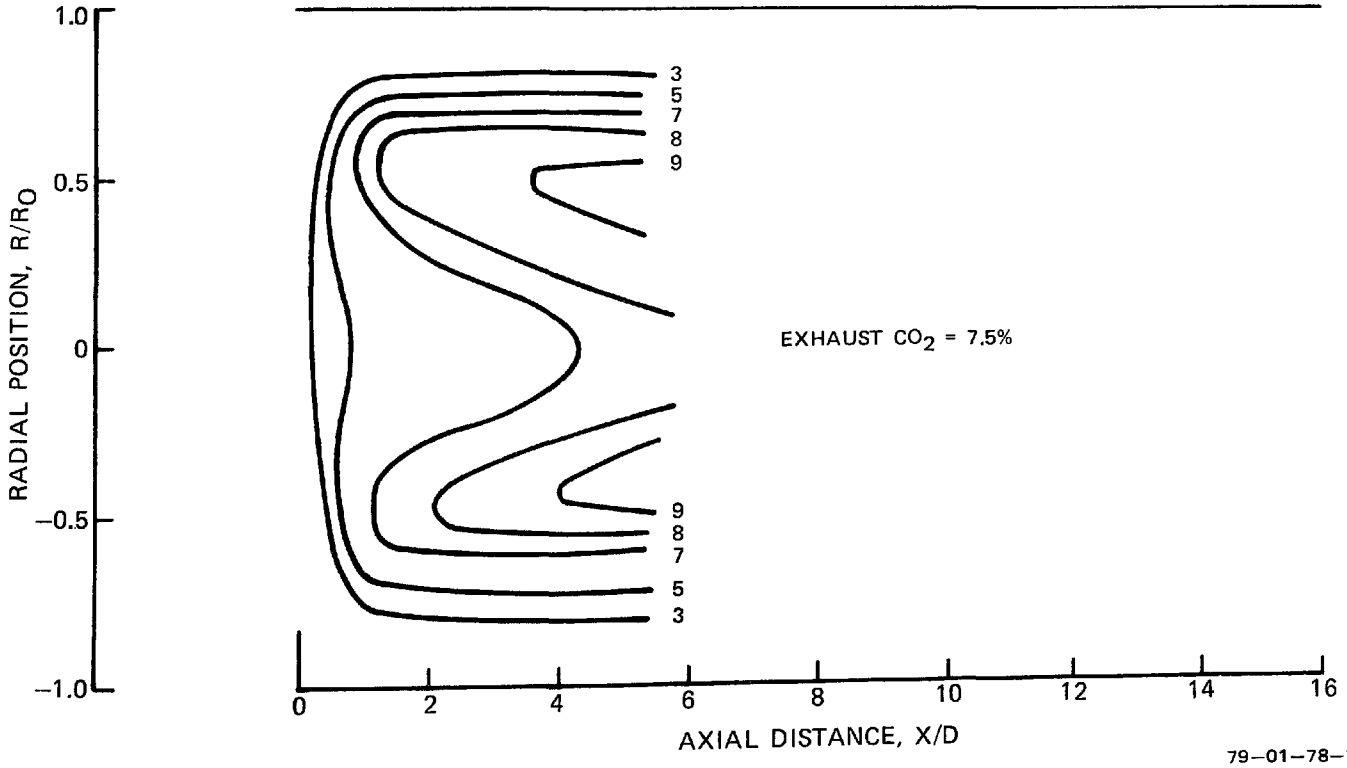

79–01–78–1

TIME–AVERAGED NO DISTRIBUTIONS

ISO–OCTANE/AIR , T_{AIR} - 533°K , ϕ = 0.65

(A) SWIRL=0.3,1ATM

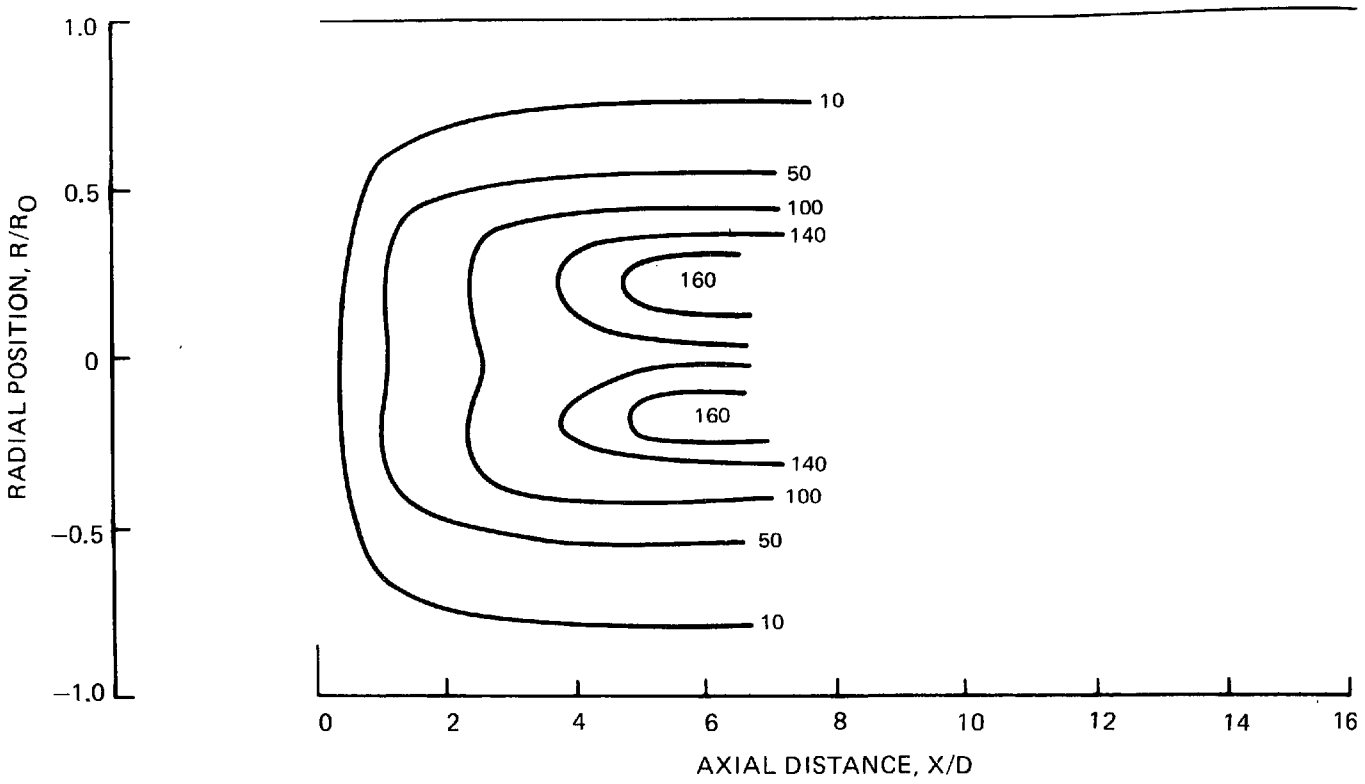

(B) SWIRL=0.3,3.3 ATM

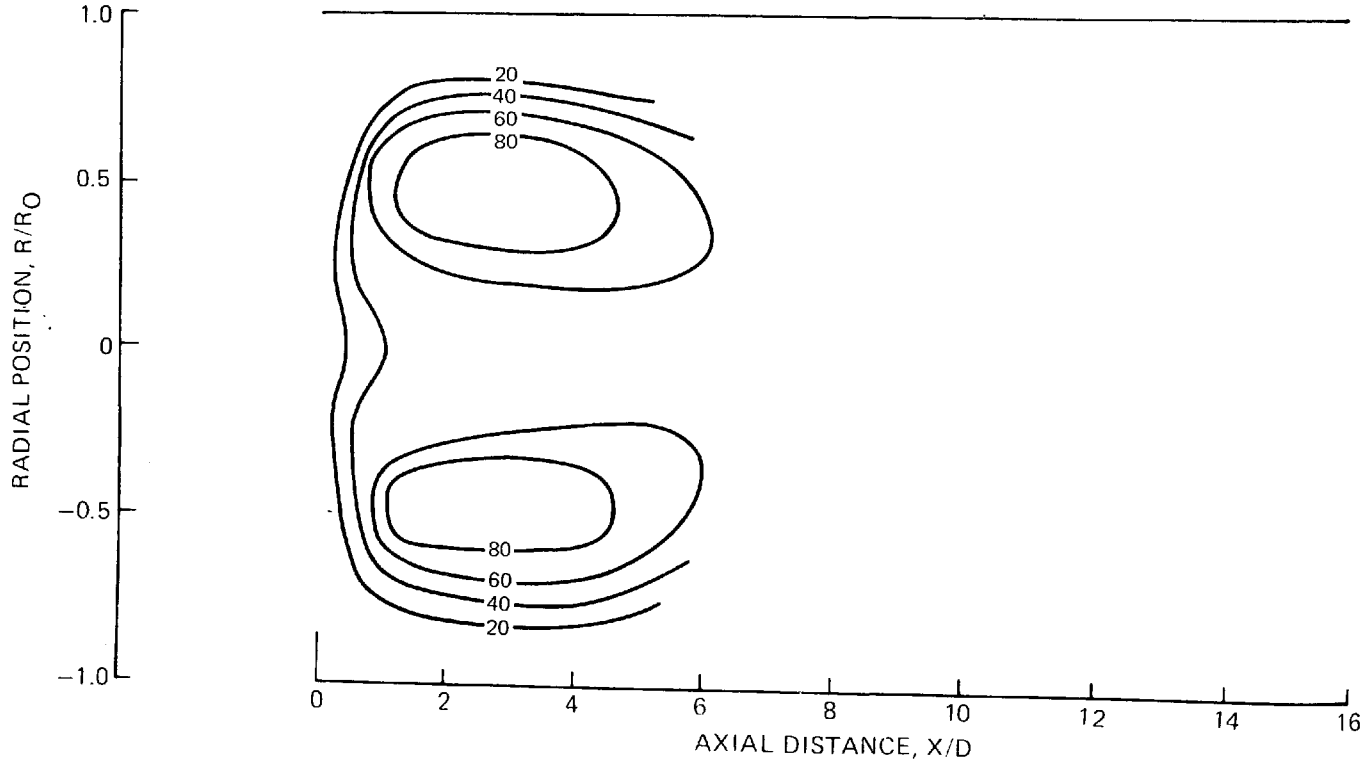

more than the density is increased. This could reduce vaporization rate with increasing pressure. Increasing boiling points with higher pressure would also tend to reduce the heat transfer rate with vaporizing fuel which is proportional to the difference between the ambient temperature and the boiling point temperature. Increased reaction rates due to increased pressure and increased residence time do not compensate for reduced shear levels, poorer penetration and lower vaporization rates and a significant amount of fuel vaporized prior to burning.

Effect of Fuel Type On Flow Field Structure and NO Formation

Liquid propane, iso-octane and No. 2 fuel oil differ widely in the physical properties which influence the atomization and vaporization (velocity, surface tension, heat capacity, latent heat of vaporization, vapor pressure). The energy added to the airstream by combustion at a given equivalence ratio is of similar magnitude for each of the three fuels; thus little difference in flow field structure or emission levels can be expected on the basis of equilibrium thermodynamic considerations. Also, the amount of fuel-bound nitrogen found in all of the fuels is quite small, and thus this factor is not believed to contribute significantly to the overall level of nitric oxide production. Typical properties of the liquid fuels and the results of limited quantitative fuel analyses are given in Appendix E.

Significant differences existed between the temperature patterns observed in the burner when using liquid propane as compared to patterns produced when using iso-octane or fuel oil -- see Fig. 19. This difference in pattern is due largely to the difference in the fuel distributions achieved when injecting propane. These fuel pattern differences are illustrated in Fig. 20 which presents levels of total unburned hydrocarbons within the combustor as determined by use of the phase-discriminating probe. Most of the propane was found to be concentrated near the centerline of the combustor; this fuel distribution is believed to have resulted from flashing of the liquid propane within the injector with the result that a conical spray was not achieved. Because of the initial fuel distribution, combustion was slow and peak temperatures were not achieved in the initial regions of the combustor (Fig. 19a). In the case of the iso-octane and fuel oil, spray patterns were similar and fuel penetrated to the outer combustor radii within two test section diameters (see section on Spray Characteristics). Temperature patterns produced were also qualitatively similar (Figs. 19b and 19c), the most significant difference being the higher temperatures at the outer radii of the combustor in the case of the fuel oil. Combustion appears to be more intense in the case of the iso-octane spray resulitng in slightly higher peak temperatures and steeper temperature gradients. The lower volumetric heat release rates in the case of the fuel oil are probably associated with the fuel oil droplet characteristics. The fuel oil droplets were somewhat larger than the iso-octane droplets initially and the fuel oil vaporizes less rapidly than iso-octane. Thus, although the distribution of unburned fuel in the initial region of the combustor is qualitatively

FIG. 19

TIME–AVERAGED TEMPERATURE DISTRIBUTIONS

S =0.3,1 ATM, T_{AIR}=533° K, ϕ=0.65

(A) PROPANE

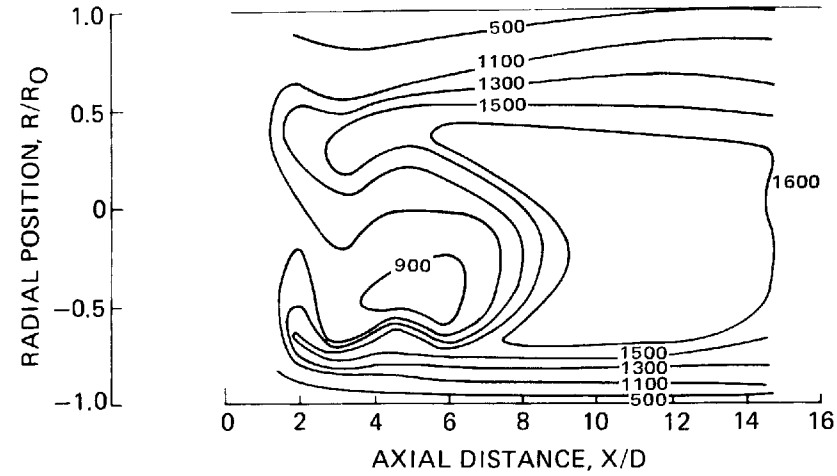

(B) ISO–OCTANE

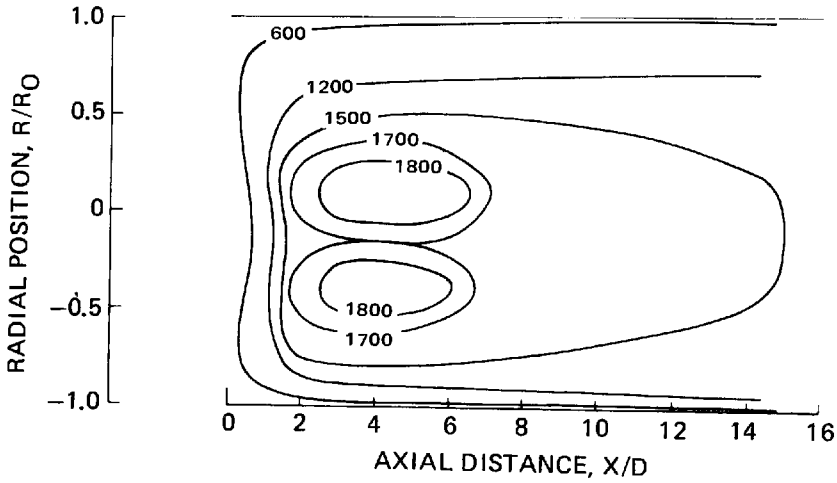

(C) NO.2 FUEL OIL

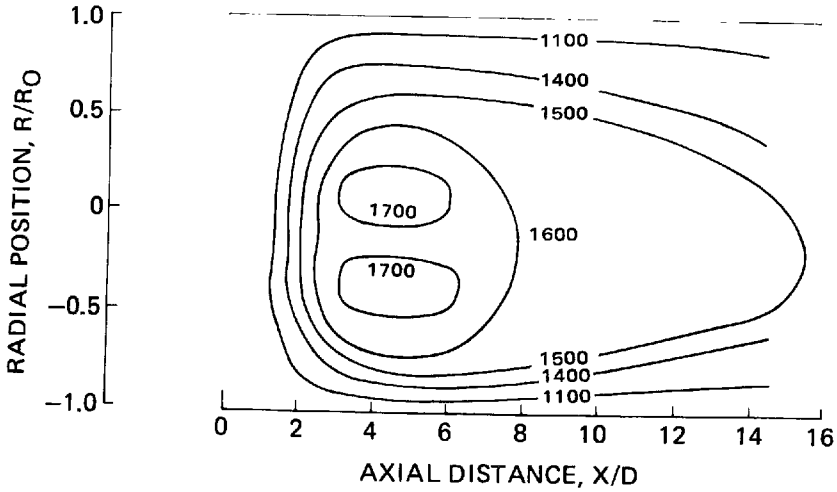

FIG. 20

TIME–AVERAGED DISTRIBUTIONS OF TOTAL UNBURNED HYDROCARBONS

S=0.3, 1 ATM, T_{AIR}=533°K, ϕ=0.65

(A) PROPANE

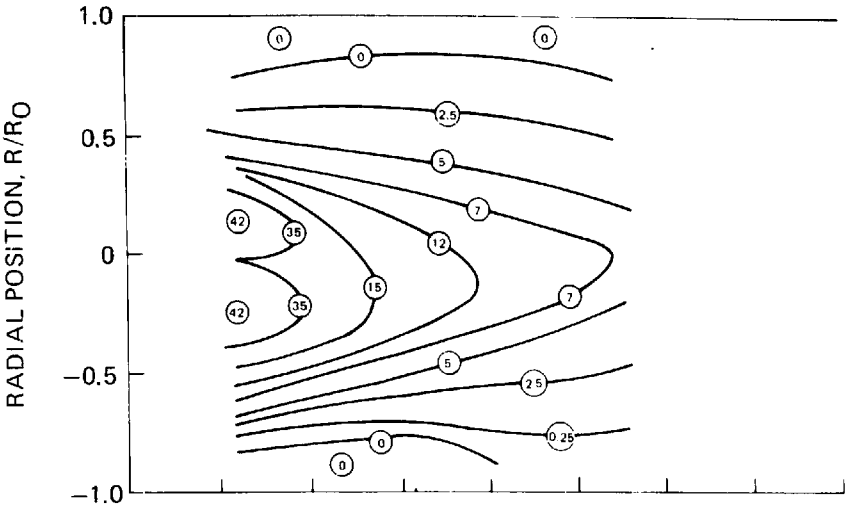

(B) ISO–OCTANE

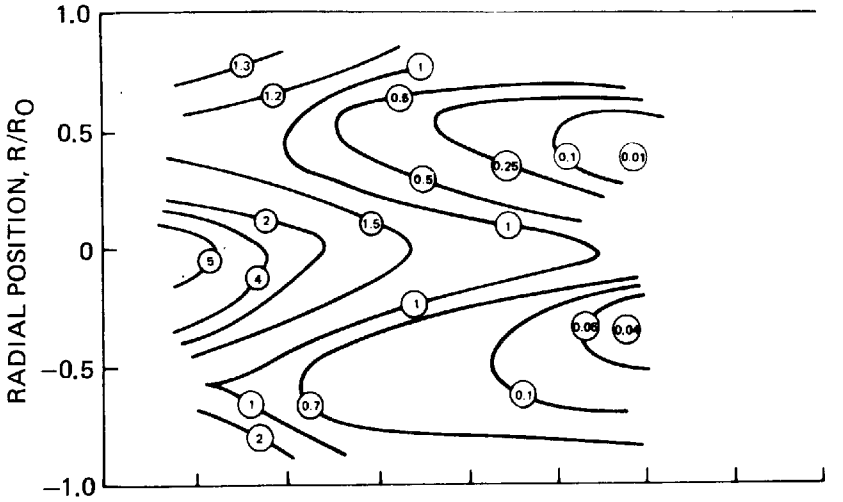

(C) NO.2 FUEL OIL

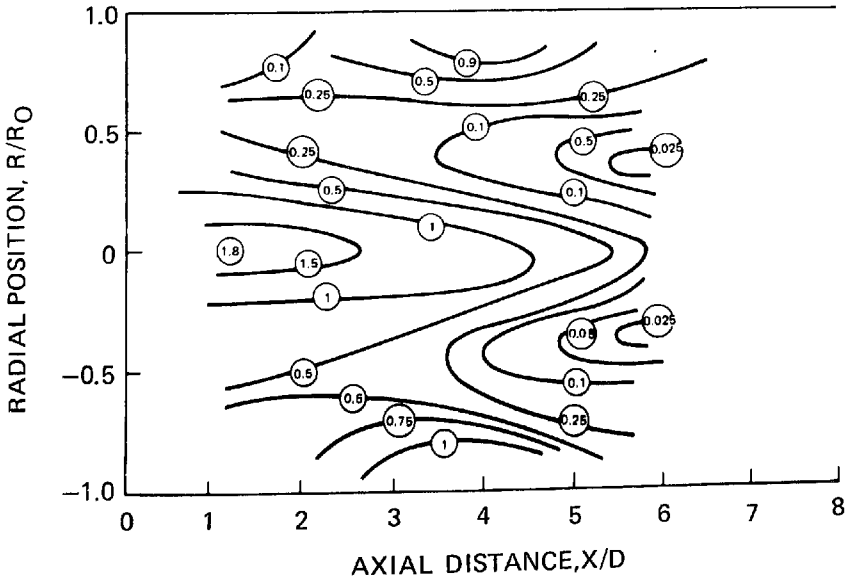

similar for the fuel oil and the iso-octane (Figs. 20b and 20c), the fuel oil droplets were larger and required greater time, and hence, distance to burn completely. The fact that a greater amount of reaction took place in the outer radii in the case of the fuel oil is confirmed by measurement of the oxygen concentration which shows that lower oxygen concentrations were found in this region (Fig. 21).

Effect of Air Preheat On Flow Field Structure and NO Formation

An increase in the inlet air temperature will influence flow field characteristics by affecting flow velocities, chemical reaction rates, and heat transfer rates. With all other conditions held constant, an increase in temperature will result in correspondingly higher temperatures throughout the combustor and will create higher flow velocities. These higher flow velocities will have the primary effect of decreasing the residence time of the combustor gases. The diminished time available for completion of the chemical kinetic processes is in most cases more than offset by the strong temperature dependence of individual reaction rates. Decreased time available for the droplet vaporization will be compensated for by the increased heat transfer rate associated with the greater temperature difference between the gas and the droplets.

Examination of the temperature patterns (Fig. 22) obtained for the case where the entrance temperature was increased by 220K (a 40 percent increase) shows that the combined effect is primarily to increase the temperature levels -- qualitatively, the temperature pattern did not change significantly. Correspondingly, the inlet temperature change resulted in only small changes in the unburned fuel pattern (Figs. 23a and 23b). As would be expected, the fraction of the unburned fuel existing in the vapor state was greater for the increased temperature level case (Figs. 23c and 23d).

The rate of formation of nitric oxide is very sensitive to local temperature and accordingly, the increased temperature levels resulted in an approximate doubling of the local NO concentration ratios (Fig. 24). This dramatic increase occurred over the complete equivalence ratio range tested in the input-output experiments. Emissions of CO would be expected to decrease with increased preheat level because of the increased rate of CO oxidation and higher temperature levels, and this, indeed, was found to be the case.

In conclusion, the effect of the increased preheat level was primarily to increase the temperature levels throughout the combustor and thereby to increase the production of nitric oxide; temperature patterns and composition patterns remain relatively unchanged.

FIG. 21

TIME–AVERAGED O_2 DISTRIBUTIONS

S= 0.3, 1 ATM, T_{AIR} = 533°K, ϕ = 0.65

(A) ISO–OCTANE

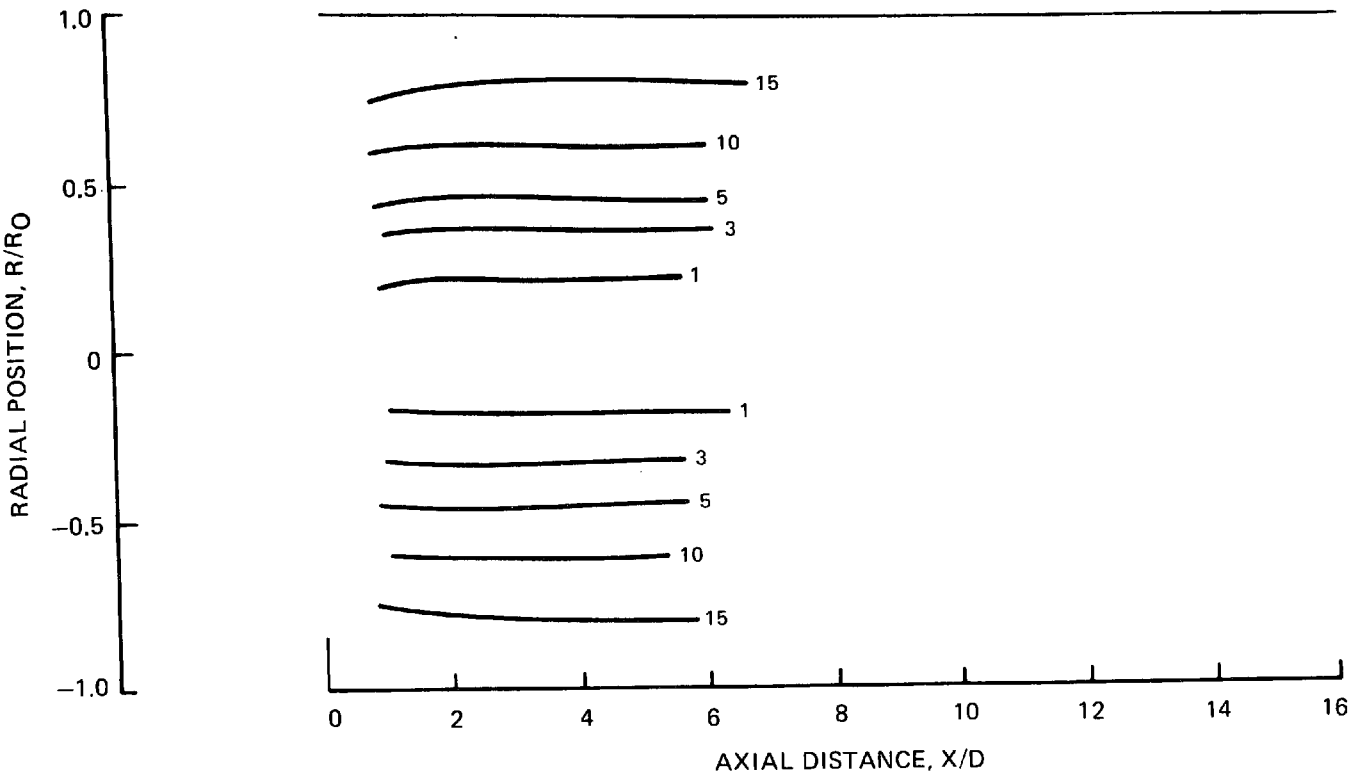

(B) NO.2 FUEL OIL

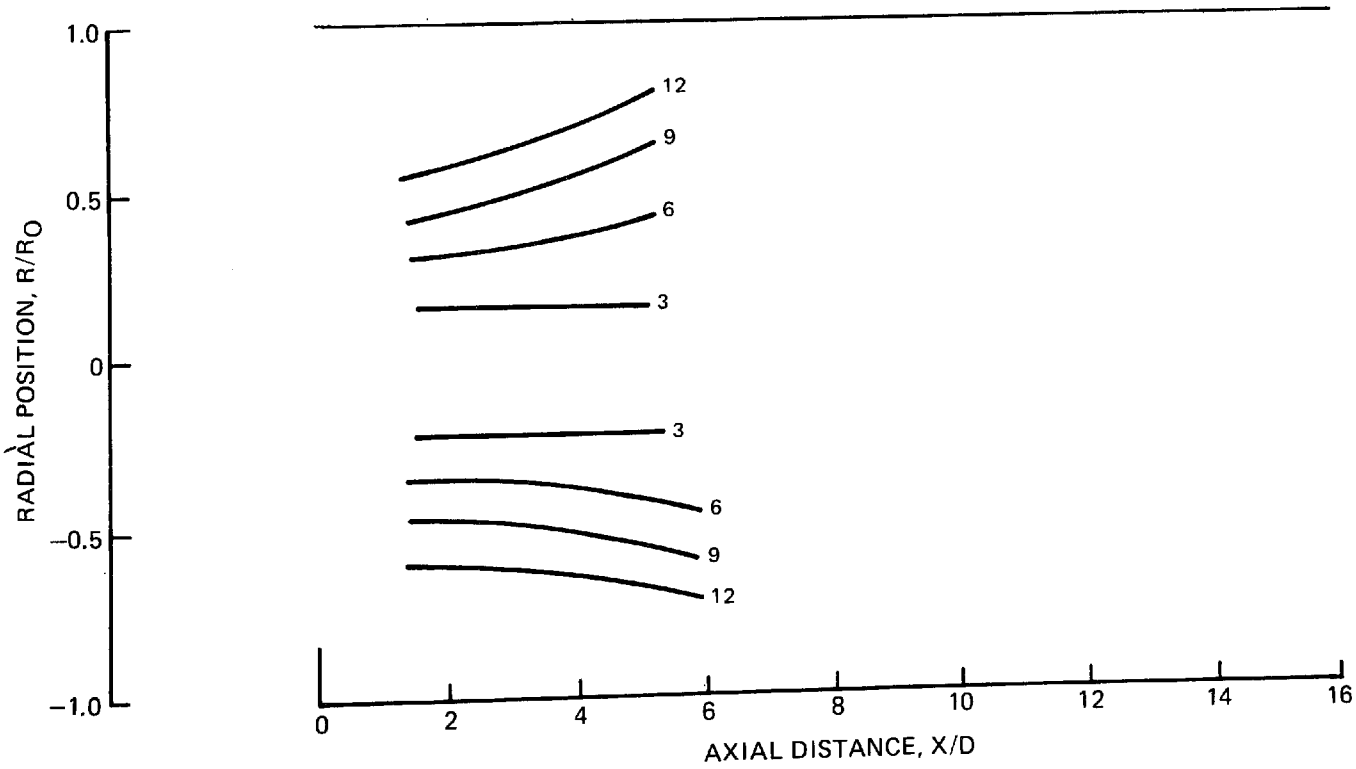

TIME–AVERAGED TEMPERATURE DISTRIBUTIONS

NO.2 FUEL OIL/AIR, $S = 0.3$, 1 ATM, $\phi = 0.65$

(A) $T_{AIR} = 533\ ^{o}K$

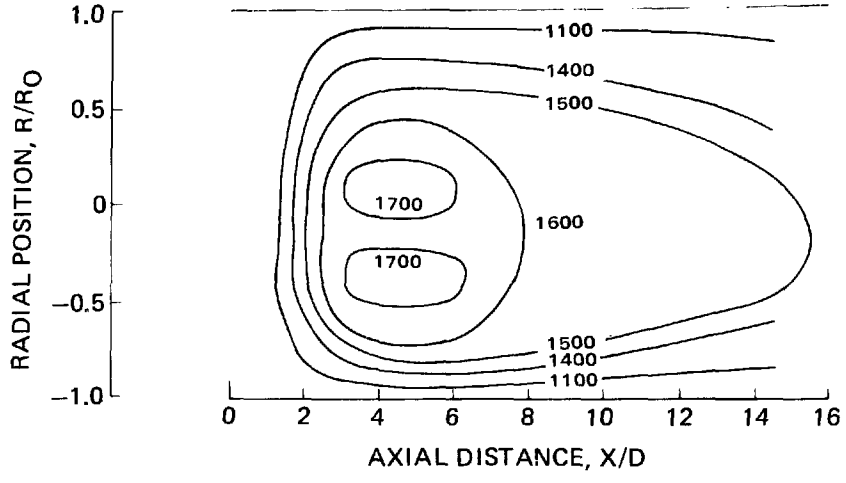

(B) $T_{AIR} = 750\ ^{o}K$

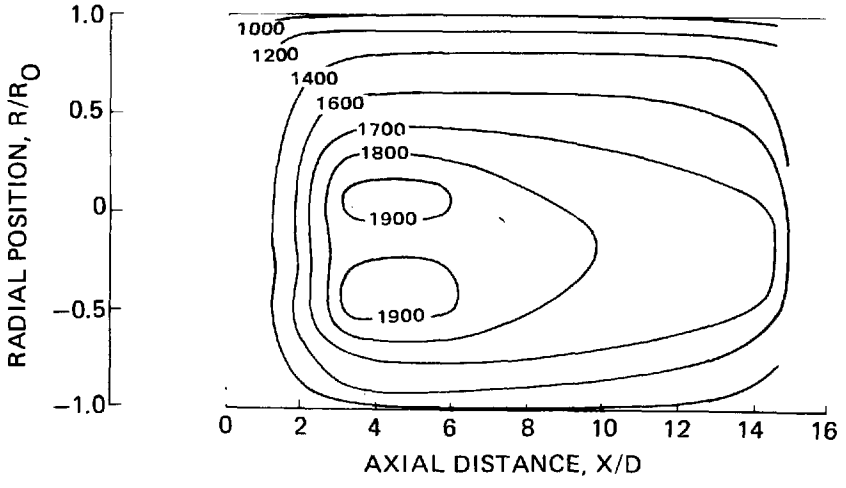

TIME–AVERAGED DISTRIBUTIONS OF UNBURNED HYDROCARBONS

NO.2 FUEL OIL/AIR, 1 ATM, S = 0.3

(A) PERCENT CARBON–TOTAL SAMPLE, T_{AIR}=533°K

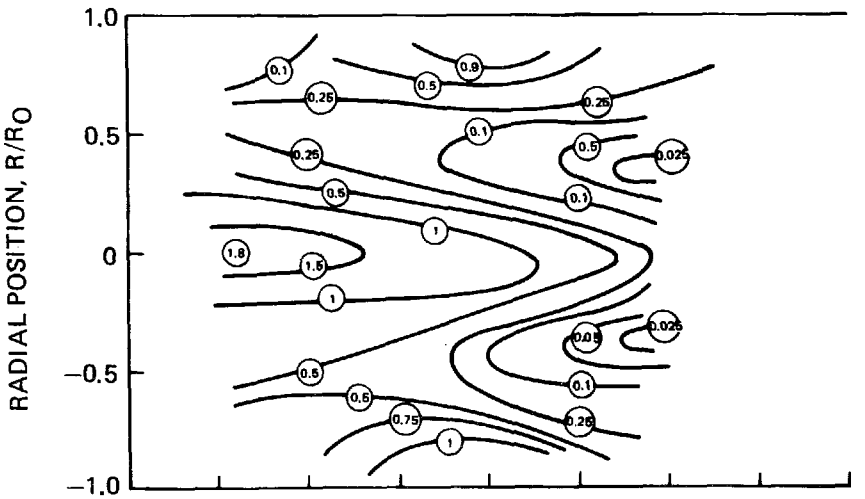

(B) PERCENT CARBON–TOTAL SAMPLE, T_{AIR}=750°K

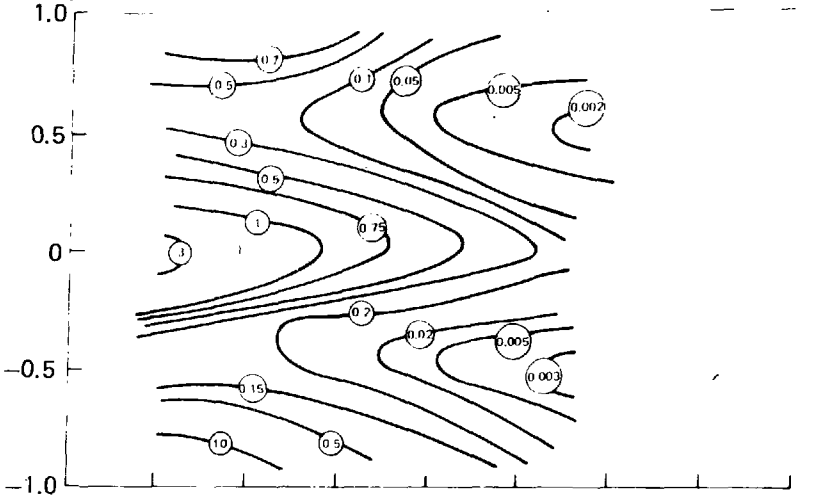

(C) PERCENTAGE OF HYDROCARBONS VAPORIZED, T_{AIR}=533°K

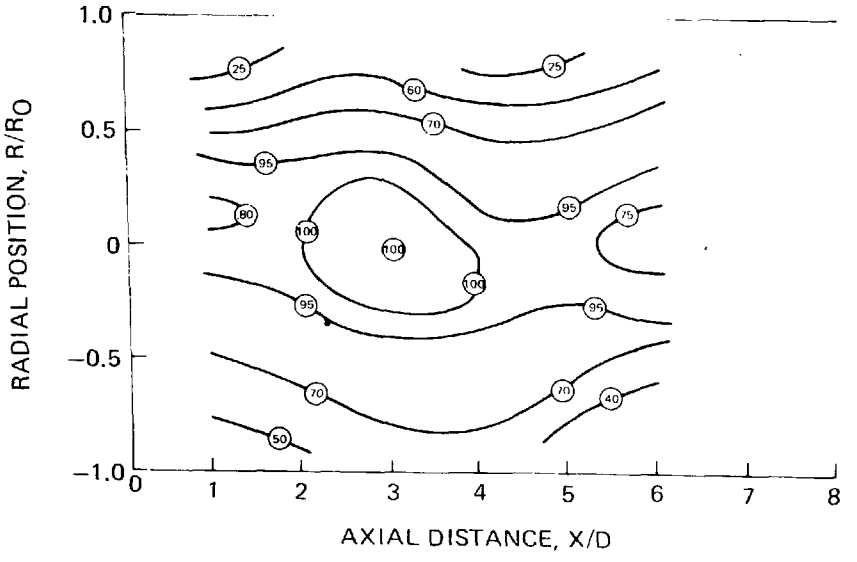

(D) PERCENTAGE OF HYDROCARBONS VAPORIZED, T_{AIR}=750°K

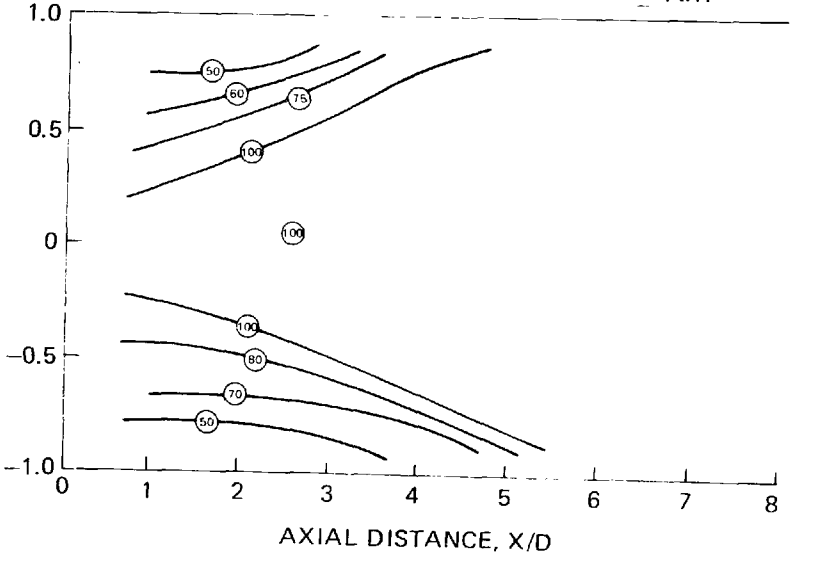

FIG. 23

FIG. 24

TIME–AVERAGED NO DISTRIBUTIONS

NO.2 FUEL OIL/AIR, S= 0.3 , 1 ATM, ϕ = 0.65

(A) T_{AIR}=533K

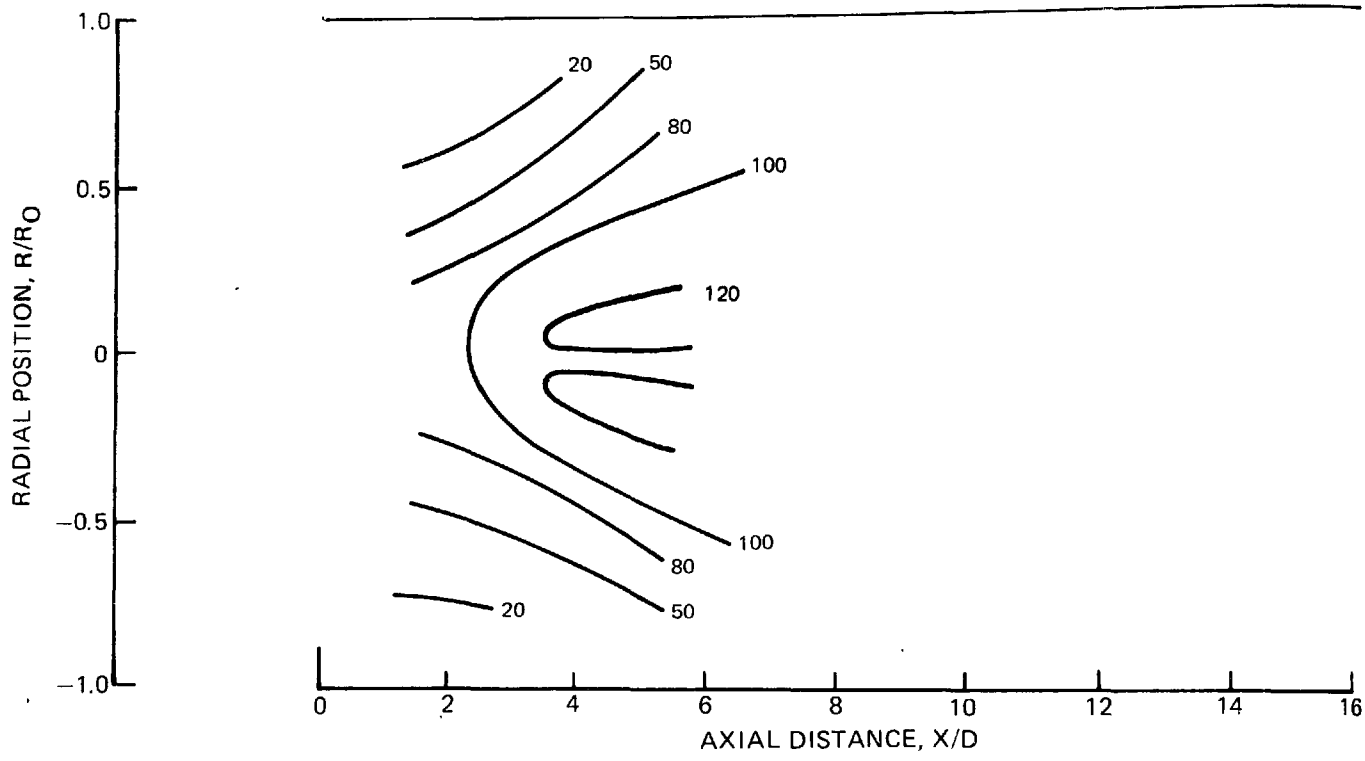

(B) T_{AIR}=750K

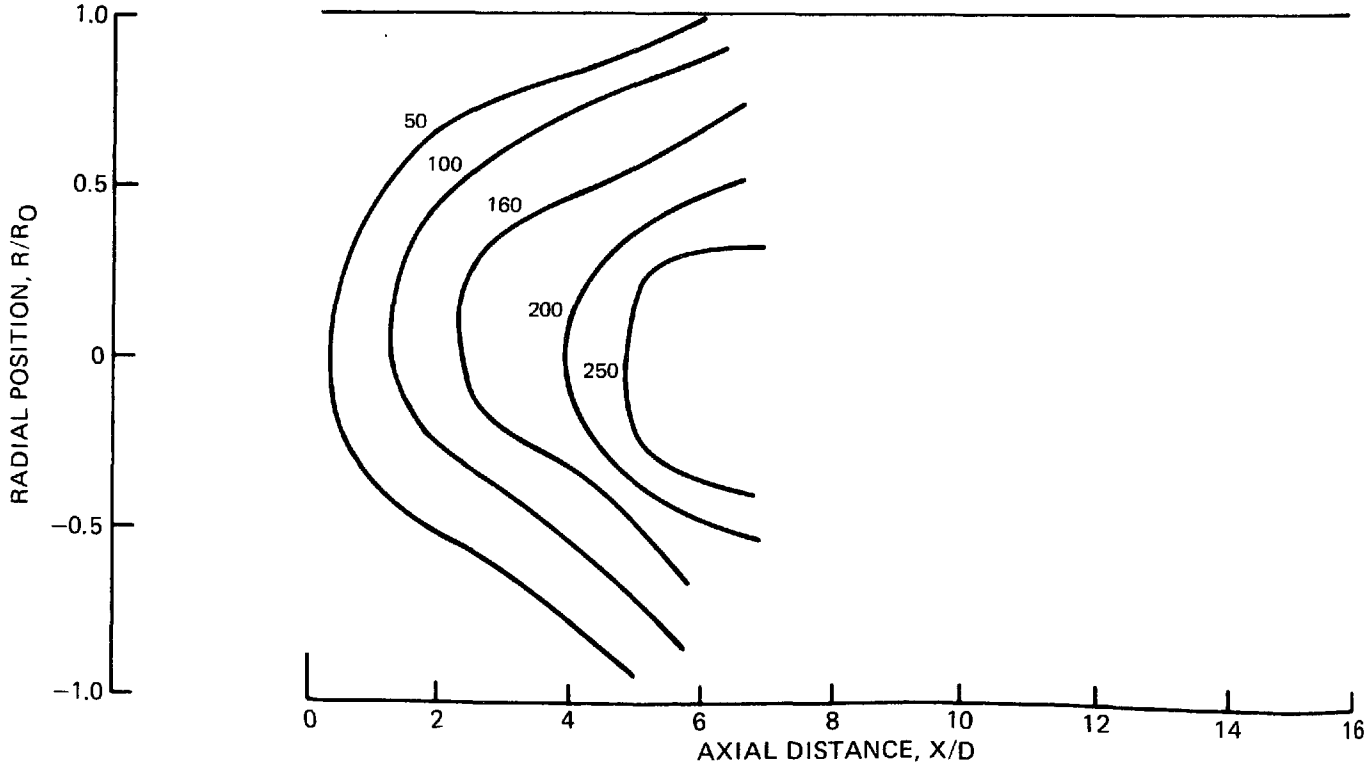

Spray Characteristics

As noted previously, the characteristics of the fuel spray play a determining role in establishing the emission characteristics of a spray combustion device. From the standpoint of achieving low emissions of nitrogen oxides and carbon monoxide it is desireable to obtain a homogeneous mixture of gaseous fuel and air where the local stoichiometry is everywhere lean such that the resulting flame temperature is low enough to reduce the NO formation rate but high enough to promote complete oxidation of CO. This implies that the injection device must distribute the fuel throughout an appropriate volume of air, and must finely atomize the fuel to obtain high surface to volume ratios such that the liquid fuel will quickly vaporize and diffuse through the surrounding oxidizing atmosphere. Attainment of a high degree of atomization is crucial to the attainment of rapid vaporization; in addition, however, high vaporization rates also may be obtained by the use of high volatility fuels, high air temperatures, high turbulence levels, and by flow situations where large differences exist between the mean fuel velocity and the mean air velocity. The combustor pressure level affects vaporization rate by changing the velocity and by raising the temperature at which droplet boiling occurs. In the current program many of the aforementioned parameters were varied and the influence on the spray pattern, the state of vaporization, and the production of nitric oxide was observed. In the following paragraphs these observations are reported and comparisons between observed behavior and anticipated behavior are drawn.

The pressure-atomizing swirl type injector (Fig. A-1) used in this program imparts a tangential velocity component to the liquid with the result that a hollow-cone spray is formed. When such an injector is employed, it is important that the cone angle be sufficiently large that the fuel is spread throughout the surrounding air but not so large that the fuel impinges on the combustor walls. Measurements of the spray cone angle for various operating conditions in these tests were obtained from both the laser velocimeter data and the holographic data. In the case of the laser velocimetry system, spray surface coordinates were taken to be those coordinates where the data rate was highest in the case of unseeded flows (see Appendix C). The spray cone angle was determined by plotting these coordinates as measured in a horizontal plane as a function of axial location and measuring the angle between lines faired through the data points (Fig. 25). In the case of the holographic system, the spray angle was determined from the best fit between the surface coordinates obtained from a reconstructed image of the spray and surface coordinates of a right circular cone (Appendix K). Tabulated data giving the spray cone angle under both burning and nonburning conditions is given in Table 3. The estimated error in the derived cone angle as obtained from these measurements was approximately two to three degrees for most of the cases examined. Excellent agreement between measurements made with both systems was obtained. Examination of the data indicates that the spray cone angle varied between 64 and 69 degrees for both iso-octane and No. 2 distillate oil at the

MEAN SPRAY TRAJECTORIES
OBTAINED BY LASER VELOCIMETRY

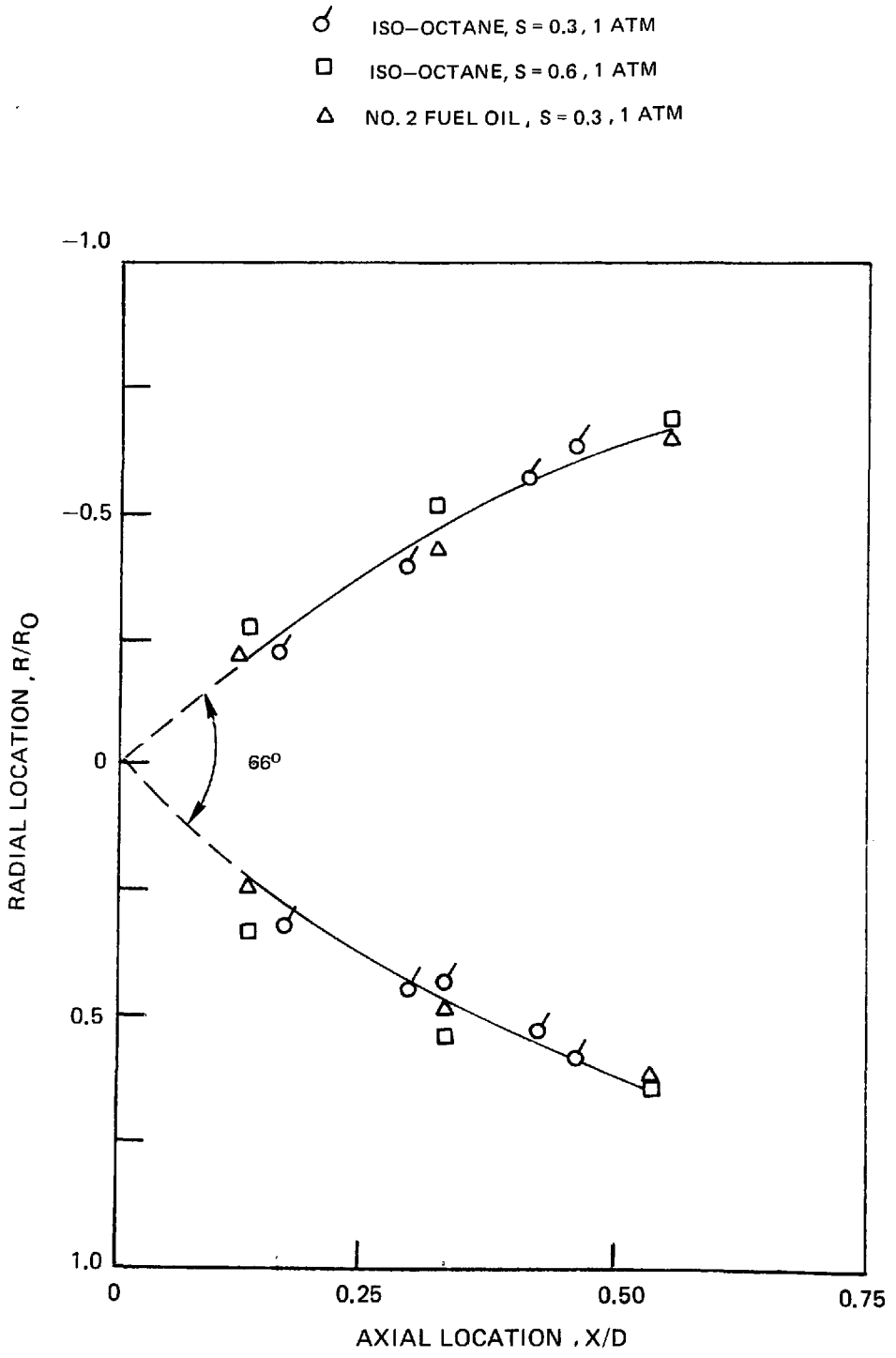

TABLE 3. SUMMARY OF SPRAY DATA OBTAINED USING HOLOGRAPHIC SYSTEM

Run	Combustion	Fuel	Pressure (atm)	Temperature (°K)	Swirl No.	Cone Angle degrees	Mean Drop - SMD dia. (μ)
129-8	No	Iso-octane	1.0	576	0.3	81	118
129-7	Yes	Iso-octane	1.0	574	0.3	69	105
130-3	No	No. 2 Oil	1.0	739	0.3	68	144
130-4	Yes	No. 2 Oil	1.0	758	0.3	57	138
130-7	No	No. 2 Oil	1.0	523	0.3	75	N/A
130-8	Yes	No. 2 Oil	1.0	532	0.3	65	140
133-1	No	Iso-Octane	1.0	541	0.6	71	128
133-3	Yes	Iso-Octane	1.0	537	0.6	64	120
132-2	No	Iso-Octane	3.1	551	0.3	N/A	N/A
132-4	Yes	Iso-Octane	3.1	528	0.3	67	105
131-4	No	Propane	1.0	532	0.3	-	-
131-5	Yes	Propane	1.0	532	0.3	-	-

low inlet temperature condition. A change in the air swirl had no discernible effect on the spray trajectory in the region where these measurements were made ($0 < X/D < 0.6$). A change in pressure level within the combustor from one to three atmospheres did not appear to have a significant effect on spray distribution. A noticeable change in spray angle occurred only in the case when the inlet air temperature was raised from 520K to 760K or when making a transition from a noncombusting flow condition to a combusting flow condition. No firmly documented explanation for the influence of inlet temperature is available. A possible explanation for this observation is that in higher temperature or combusting flows the dynamic pressure of the gases (ρV^2) is greater and therefore the increased drag forces tend to produce a somewhat flatter droplet trajectory, resulting in a narrower cone angle. The most dramatic change in the character of the spray occurred when liquid propane was used as the injectant. In this case the spray emerged from the injector as a columnar jet; no droplets were discernible within this jet. This behavior is probably associated with the flashing of the propane fuel as the fuel pressure decreases from the injector pressure to the combustor pressure.

The value of the mean droplets size (Sauter mean diameter) within the spray was determined by measuring the diameters of individual particles in the image of the reconstructed holograms. The mean droplet diameters were found to range from 100 to 150 microns. The results indicate that only the fuel type had a significant influence on droplet diameter; mean droplet sizes evaluated for the iso-octane sprays ranged from 105 to 128 microns, whereas the size range for No. 2 fuel oil sprays was from 138 to 144 microns (Table 3). Mean droplet size data were obtained both under combusting and noncombusting flow conditions; the droplet size in the combusting flow cases was found to be slightly smaller than for the non-combusting flow cases but the measured size difference is too small to be considered significant. Qualitative information on the distribution of droplet sizes within the spray cone are available from the laser velocimetry data. Because the strength of the signal received from the spray increases monotonically with the size of the scattering particles (particle visibility) it is possible to obtain size information by signal strength threshold level below which returned signals are rejected by the data acquisition system. Size information obtained in this manner is given in Fig. 26. As can be seen in this figure, at high threshold levels, where only the velocity of the large droplets are recorded, two major peaks (which correspond to the time-average spray location) are recorded as the combustor diameter is traversed. When the threshold level is reduced such that signals from the smaller droplets are accepted, the maximum droplet number densities are significantly higher and double peaks appear which suggest that there are large numbers (clouds) of smaller droplets surrounding the main trajectory. The existence of these smaller droplets adjacent to the main spray trajectory is consistent with the fact that the smaller droplets can be affected by the turbulent gas velocity fluctuations and therefore will tend to spread more rapidly into the surrounding gas than will the larger droplets.

EFFECT OF SIGNAL THRESHOLD LEVEL ON DROPLET NUMBER DENSITY PROFILE

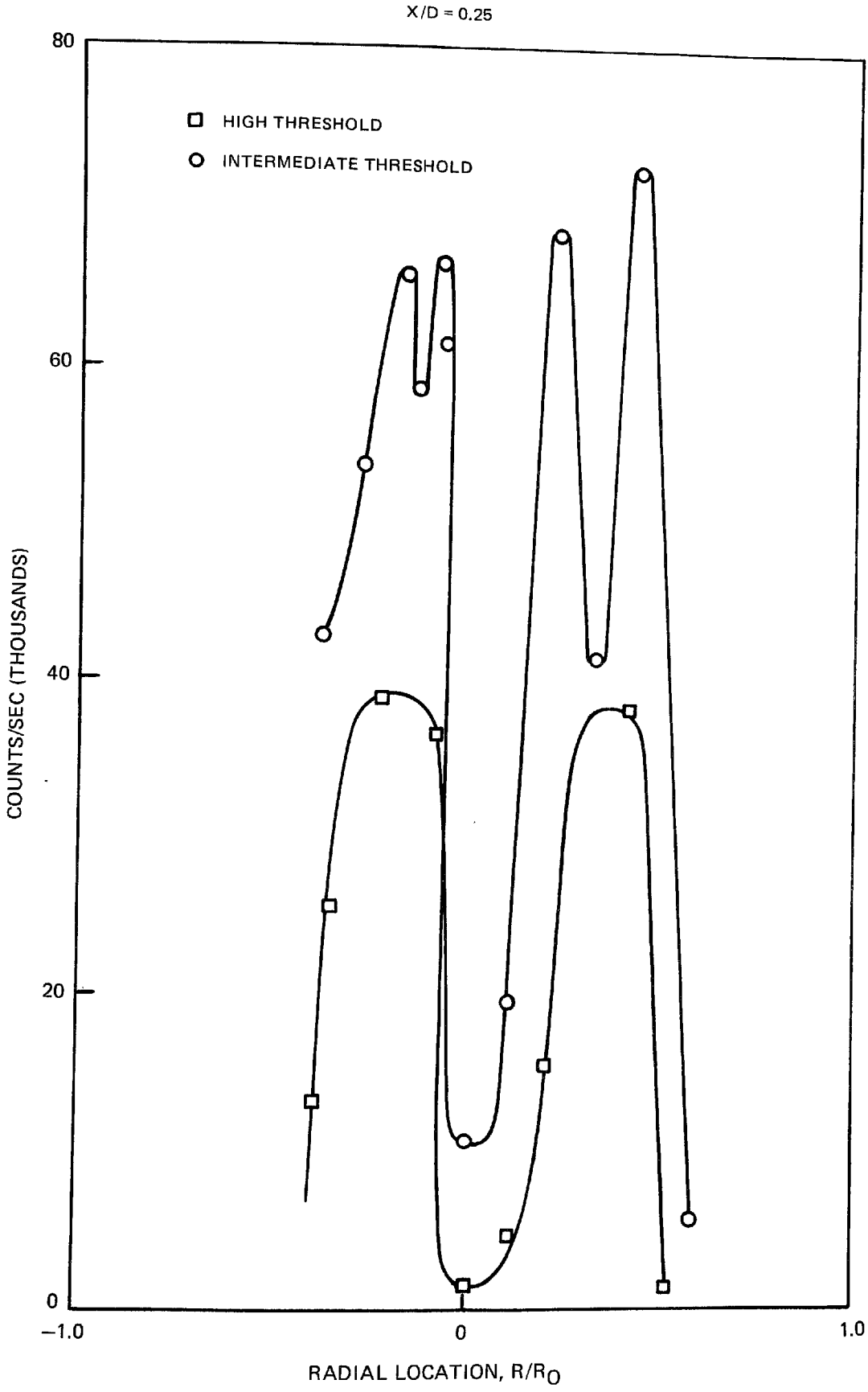

77−05−310−1

With respect to the vaporization of the sprays, it is anticipated that the fuel oil sprays will persist for a longer period of time or, equivalently, throughout a greater spatial extent of the combustor than will the iso-octane sprays because of the lower volatility of fuel oil. This expectation is confirmed by both the laser velocimetry data and the phase-discriminating probe data. Comparison of the 10 mps contours constructed from the LV data for the fuel oil (Fig. 27b) and the iso-octane (Fig. 28b) sprays shows the greater spatial extent of the fuel oil spray. Because the gas phase velocity profiles for these two tests (Figs. 27a and 28a) are quite similar and because the initial liquid velocities were nearly the same, it can be argued that it is the decreased rate of vaporization of fuel oil which is responsible for the greater contour dimension. With respect to the phase discriminating probe data, comparison of the data presented in Fig. 29 in the region to which the spray cone penetrates (R/R_o = 1.0, -1.0; X/D = 1.0) indicates greater concentrations of iso-octane were found than No. 2 fuel oil, but that the iso-octane exists in the gaseous form whereas significant amounts of liquid fuel oil persists (Fig. 30).

The fact that detectable amounts of liquid hydrocarbons were measured in the vicinity of the combustor wall raises the question as to whether the spray persists for a sufficient period of time that appreciable quantities of liquid fuel penetrate to the wall. The magnitudes of the percent carbon in the total samples as determined from the phase-discriminating probe indicate that this was not the case. Noting that the level of unburned hydrocarbon in the liquid phase can be determined by multiplying the total percentage of unburned hydrocarbons (e.g., Fig. 29b), by the percentage unvaporized (Fig. 30b), it is determined that the largest value of the percent carbon (0.5) due to the existence of liquid fuel is found downstream of the anticipated point of impingement as predicted from spray trajectory data and is small in magnitude compared to that value corresponding to stoichiometric mixtures (13.2 for iso-octane). Furthermore, no buildup of carbonaceous material on the cooled combustor wall was detected nor was any evidence of streaking or staining of the combustor walls noted during the periodic inspections of the test apparatus.

As noted above, the results of the phase-discriminating probe tests indicate that liquid fuel exists in the downstream region of the combustor; that is, downstream of the region associated with the spray cone itself. Existence of liquid fuel in this region is expected since the largest droplets require long burning times and will thus travel significant distances before being consumed. Again, one would expect to find more liquid fuel in the case of the tests conducted with fuel oil than in the case of tests with the more volatile iso-octane. Comparisons of the unburned hydrocarbon data for the two different fuels (Fig. 29) indicate that no major differences in the spatial pattern of the total (liquid plus vapor) unburned hydrocarbons exists and, surprisingly, somewhat higher levels of unburned hydrocarbons exist for iso-octane than for fuel oil. This may well be due to the differences in reaction rates associated with differences in liquid fuel penetration into the air stream. According to expectations, the fraction of the unburned

MEAN AXIAL VELOCITY DISTRIBUTIONS

NO. 2 FUEL OIL/AIR, SWIRL = 0.3, 1 ATM, $T_{AIR} = 533^{o}K$, $\phi = 0.65$

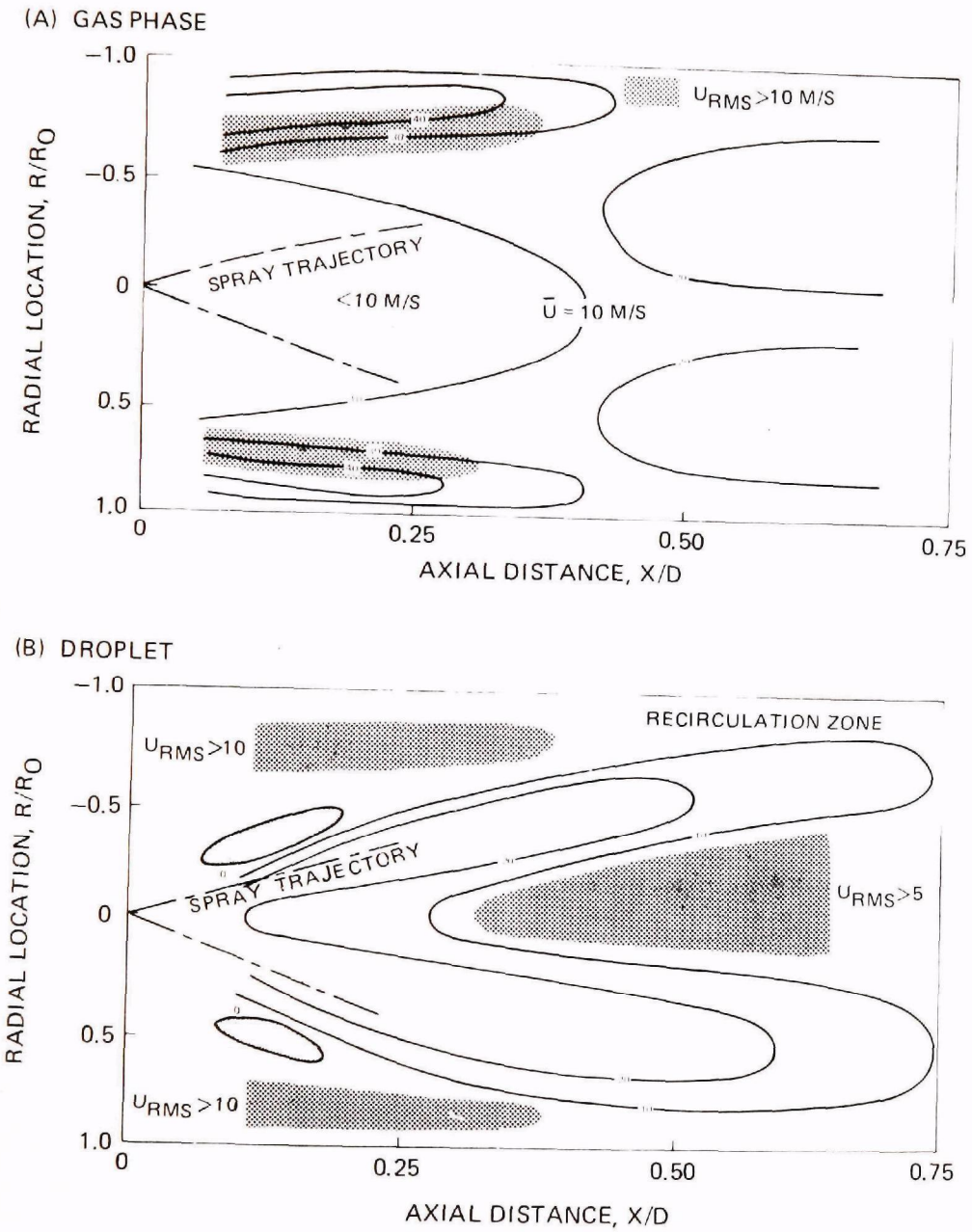

MEAN AND RMS AXIAL VELOCITY DISTRIBUTIONS

ISO–OCTANE/AIR, S = 0.3, 1 ATM, T_{AIR} = 533°K, ϕ = 0.65

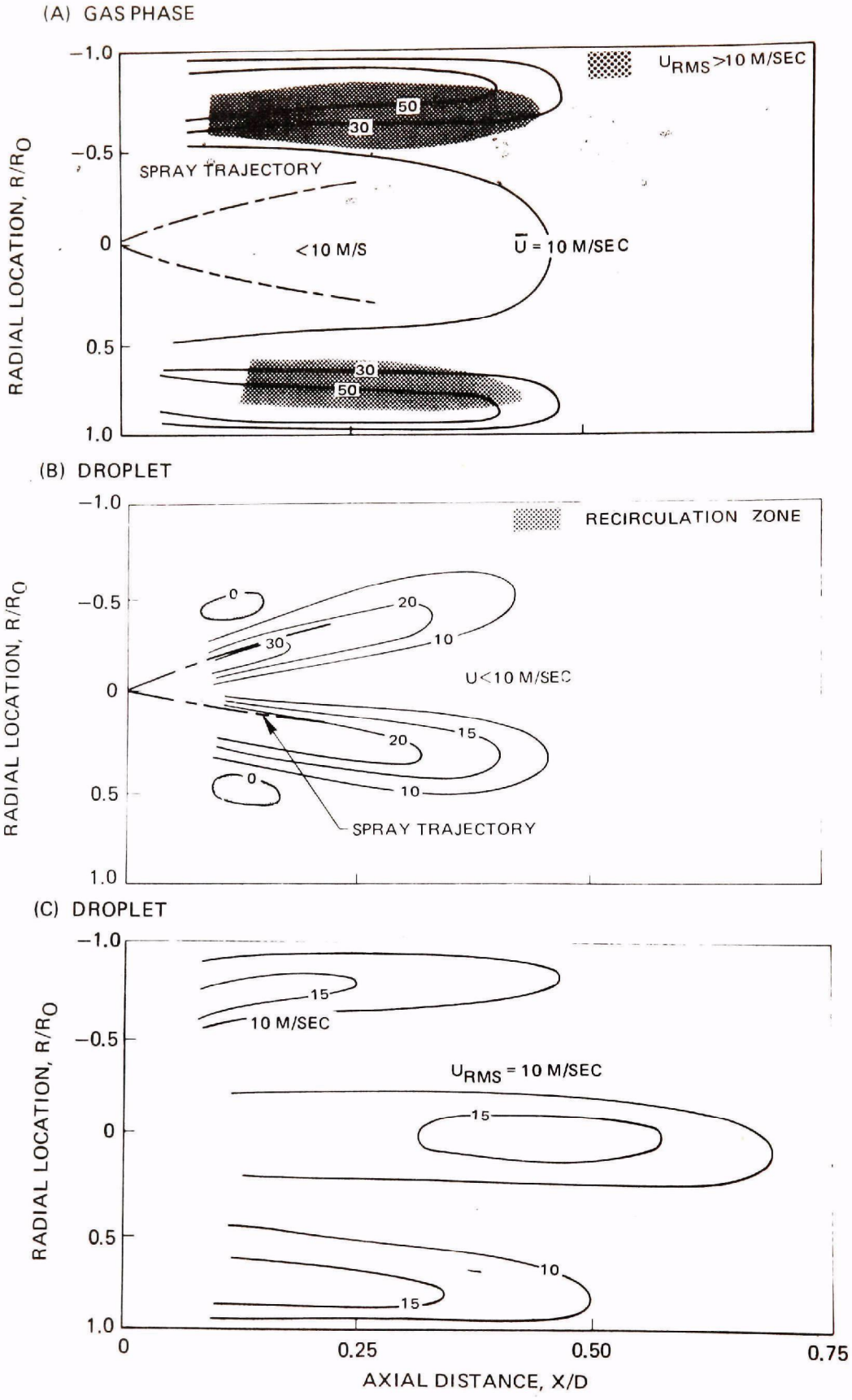

TIME–AVERAGED DISTRIBUTIONS OF TOTAL UNBURNED HYDROCARBONS

S = 0.3, 1 ATM, T_{AIR} = 533°K

(A) ISO–OCTANE

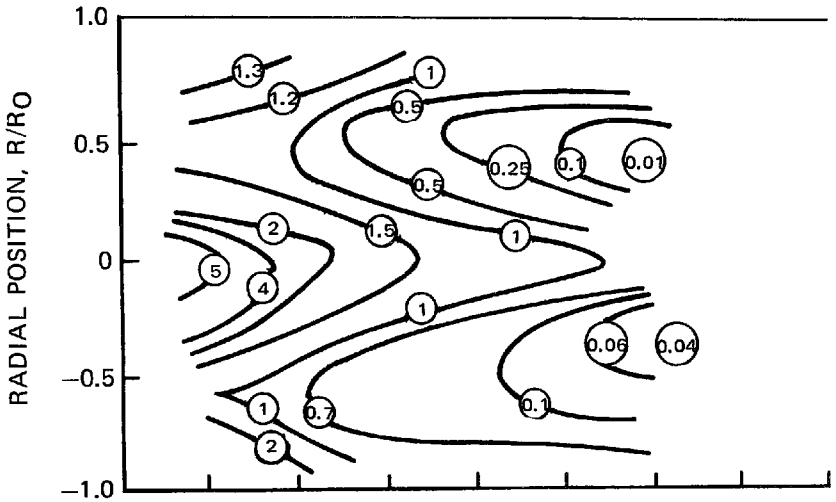

(B) NO.2 FUEL OIL

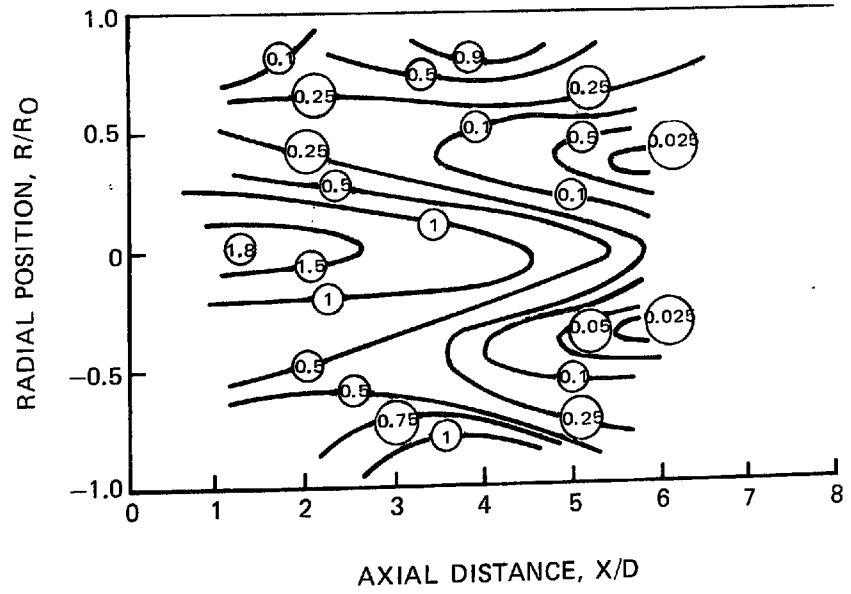

TIME–AVERAGED PERCENTAGE OF HYDROCARBONS VAPORIZED

$S = 0.3$, 1 ATM, $T_{AIR} = 533^{o}K$

(A) ISO–OCTANE

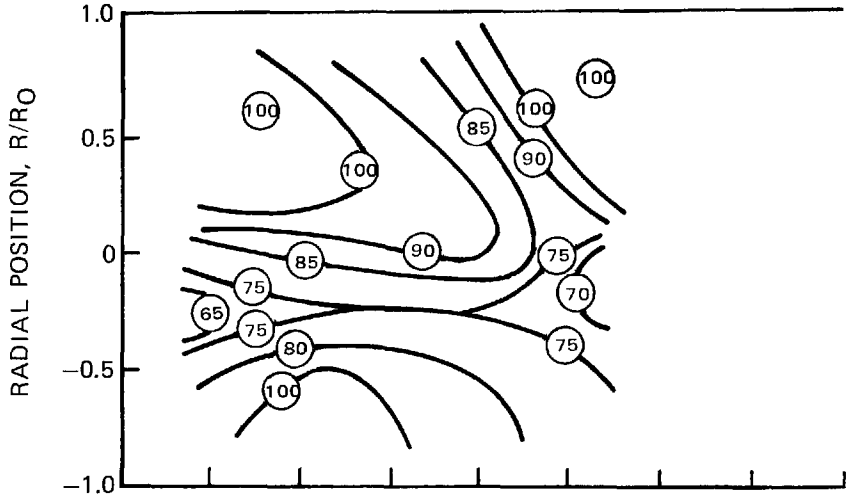

(B) NO.2 FUEL OIL

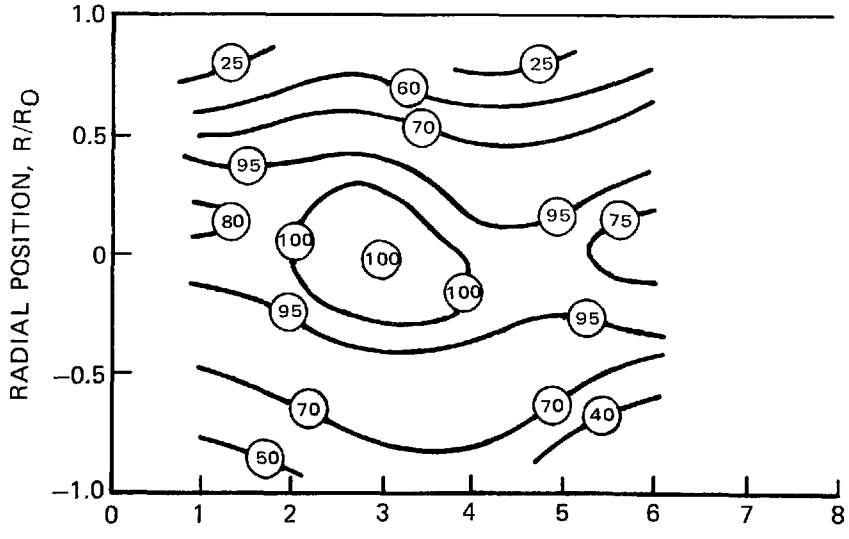

fuel that is in the liquid state is indeed higher for the fuel oil case than in the iso-octane case (Fig. 30).

Data obtained for propane, Fig. 31, show extremely high levels of unburned hydrocarbons near the combustor axis which is a result of aforementioned poor fuel distribution obtained with propane. The existence of significant amounts of liquid propane in the downstream region is indicative of the fact that the high fuel concentrations cause a reduction in the local gas temperature which precludes further vaporization until sufficient aerodynamic entrainment of the hot surrounding flow occurs.

The effect of a change in inlet temperature from 530K to 750K on the distribution of hydrocarbons is illustrated by the contour patterns in Figs. 29b, 30b, and 32. Again, it can be seen that no major change in the pattern of unburned hydrocarbons occurred; however, as expected, the fraction vaporized was somewhat higher in the higher temperature case.

Another feature of the fuel spray which bears comment is the location of the spray relative to the locations of the low velocity regions which act as flame stabilization sites. In highly stable combustion systems employing pressure atomizing fuel nozzles, the fuel is injected directly into large regions of recirculatory gas flow located on the combustor axis downstream of the fuel injector (Ref. 13). Typically, the bulk of the injected spray passes through the recirculating flow while a fraction of the smaller droplets remain in the recirculating flow and combine with entrained oxidizer thereby maintaining a hot gas core which serves as a flame stabilization region. As was discussed previously, particle visibility problems precluded velocity measurements in the vicinity of the spray at low swirl and, consequently, no time-mean recirculating flow is shown. However, a torroidal-shaped recirculating flow was detected in the high swirl case and positive gas velocities existed at all points on the combustor axis (see Figs. 28 and 33). Curiously, local regions of negative mean droplet velocity existed in the low swirl case (as well as in the high swirl case) even though the time-mean gas velocity was everywhere positive (see Figs. 27b and 28b). It is also noted that very large fluctuations in the velocity of the droplets occur within this device under both the moderate and low swirl conditions (Figs. 28c and 33c). These observations together with the previously reported transient pressure and luminosity fluctuations confirm that transient aerodynamic phenomena are influencing the behavior of the flow in the vicinity of the injector and that the application of the frequency tracking laser velocimetry techniques will be required to gain a thorough understanding of the detailed time-dependent flow processes.

The laser velocimetry system was also used to measure the tangential components of the gas velocity and of the fuel velocity (see Fig. 34). The fact that the sense of rotation of the air (solid symbols) is the same as that of the fuel (open symbols) is evident in the figure; also evident is the increased tangential velocity component of the gas in the moderate swirl case. Note that in the

TIME-AVERAGED DISTRIBUTIONS OF UNBURNED HYDROCARBONS

PROPANE,1 ATM, T_{AIR}=533°K, S= 0.3

(A) PERCENT CARBON–TOTAL SAMPLE

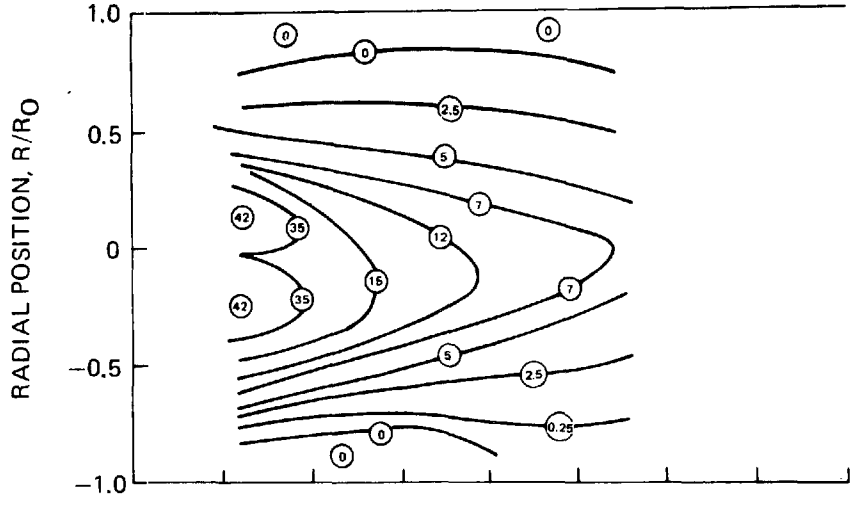

(B) PERCENTAGE OF HYDROCARBONS VAPORIZED

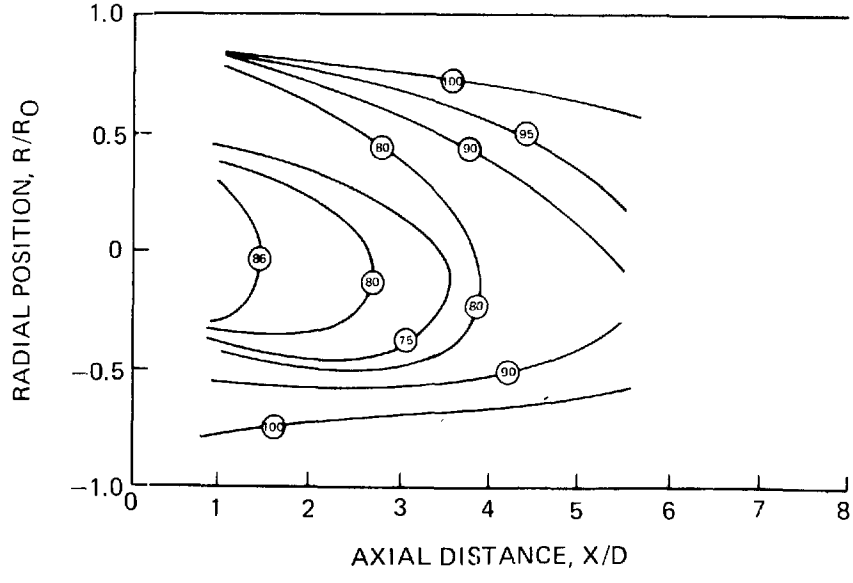

TIME–AVERAGED DISTRIBUTIONS OF UNBURNED HYDROCARBONS

Fig. 32

NO. 2 FUEL OIL, 1 ATM, T_{AIR} = 750° K, S = 0.3

(A) PERCENT CARBON–TOTAL SAMPLE

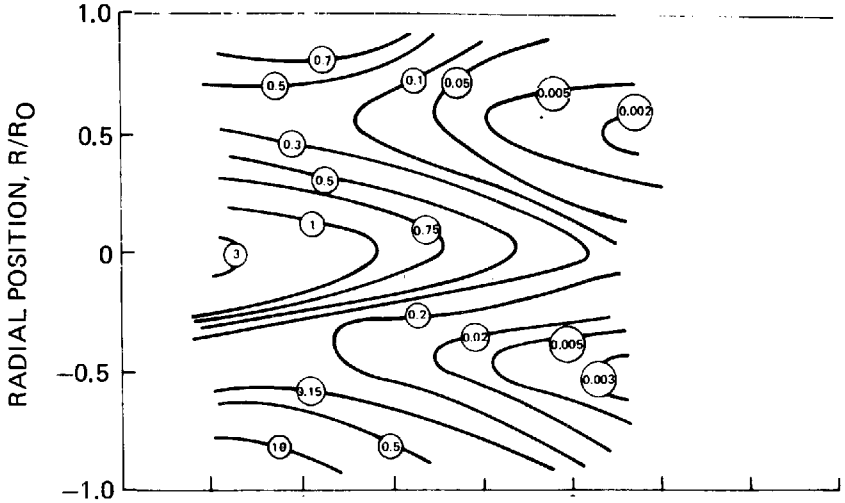

(B) PERCENTAGE OF HYDROCARBONS VAPORIZED

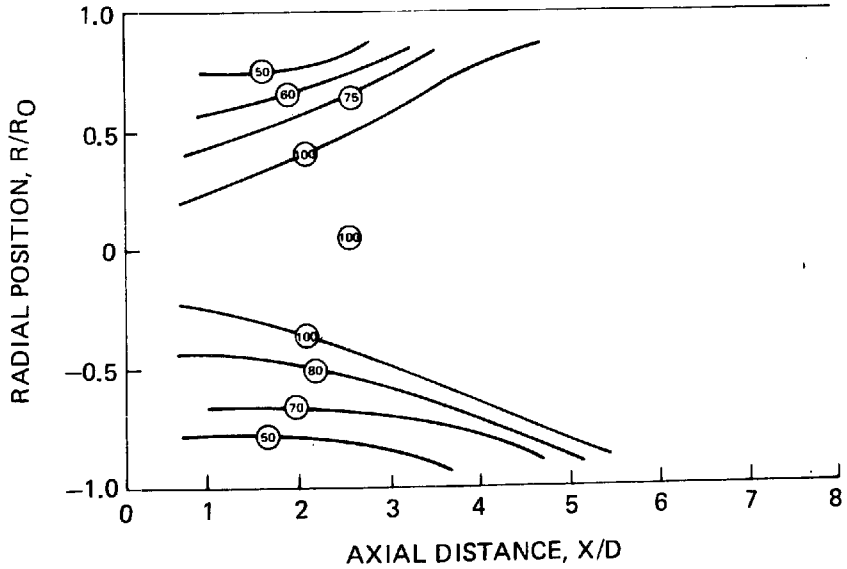

MEAN AND RMS AXIAL VELOCITY DISTRIBUTIONS

ISO-OCTANE/AIR, S = 0.6, 1 ATM, T_{AIR} = 533°K, ϕ = 0.65

RECIRCULATION ZONE

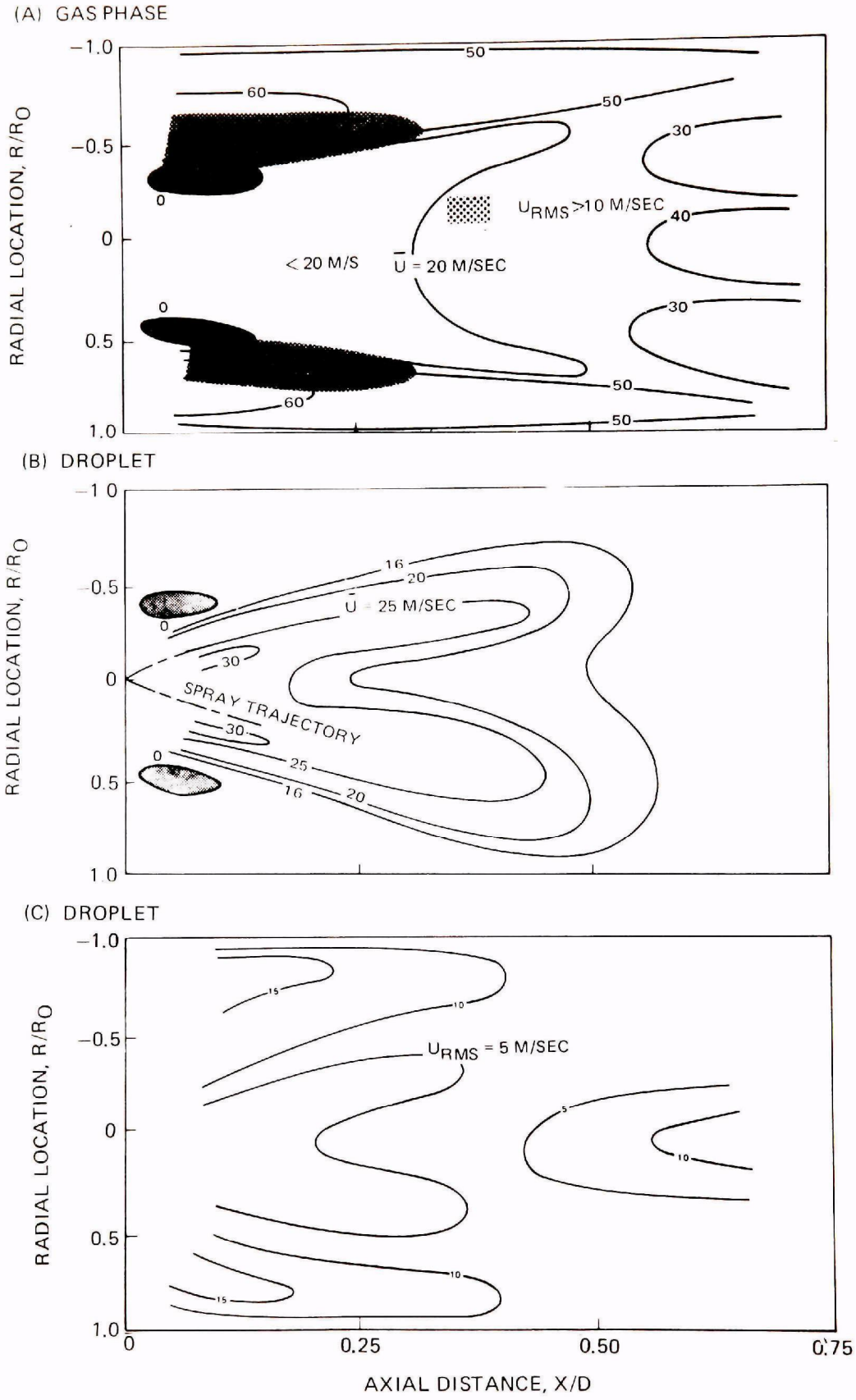

MEAN TANGENTIAL VELOCITY PROFILES

X/D = 0.123

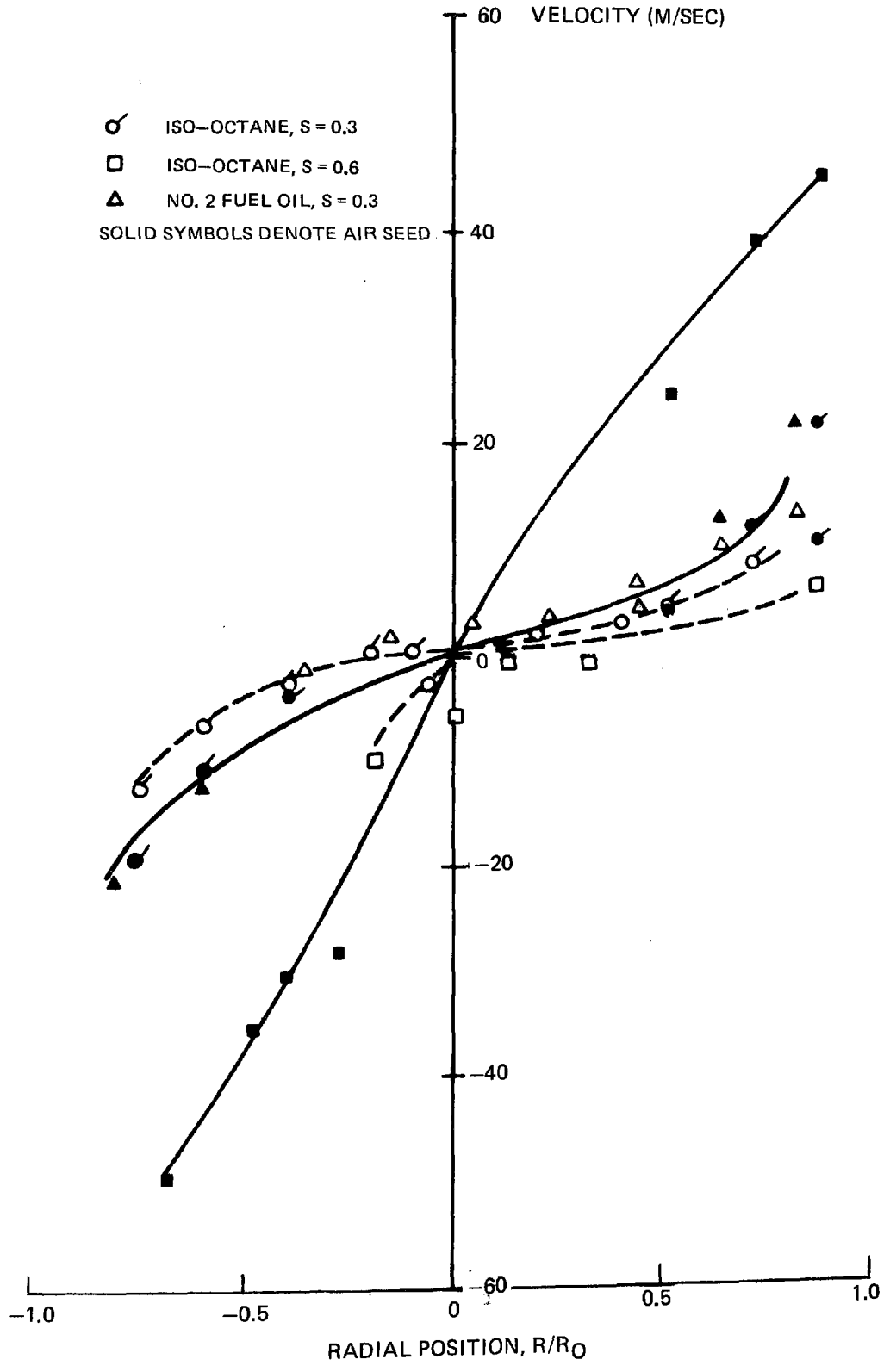

76–10–29–9

moderate swirl case vaporization of fuel spray should be enhanced by the large velocity differences which exist between the liquid and gas flow. Measurements taken at a second downstream station (X/D = 0.335 vs X/D = 0.123) indicate that a slight decay of the velocity difference between the gas and fuel droplets has occurred; however, the fuel and droplets still maintain distinctly different tangential velocities (Fig. 35).

To summarize these observations, the holographic and laser velocimeter measurements indicate that within the region close to the injector (within one combustor diameter downstream of the injector tip) the fuel spray was observed to maintain the structure of a hollow cone and to penetrate throughout the cross-section of the swirling airflow. Large differences between air and fuel time-mean velocities exist in this region as do large fluctuations in the local gas and droplet instantaneous velocities. These velocity field characteristics probably influence the vaporization and consumption of the smaller droplets in this region and thereby affect flame stability, but the impact of the velocity fluctuations on the larger droplets constituting the major portion of the fuel spray is undetermined. The phase-discriminating probe data indicate that significant amounts of liquid fuel exist for at least the first five combustor diameters, particularly near the outer radii of the combustor. The initial mean droplet size of the fuel oil spray is larger than that of the iso-octane spray; this together with the lower vapor pressure of the fuel oil would result in longer droplet burning times and hence are probably responsible for the greater concentrations of nitric oxides produced in some of the tests conducted with fuel oil.

MEAN TANGENTIAL VELOCITY PROFILES

X/D = 0.335

ISO–OCTANE, S = 0.3

ISO–OCTANE, S = 0.6

NO.2 FUEL OIL, S = 0.3

SOLID SYMBOLS DENOTE AIR SEED

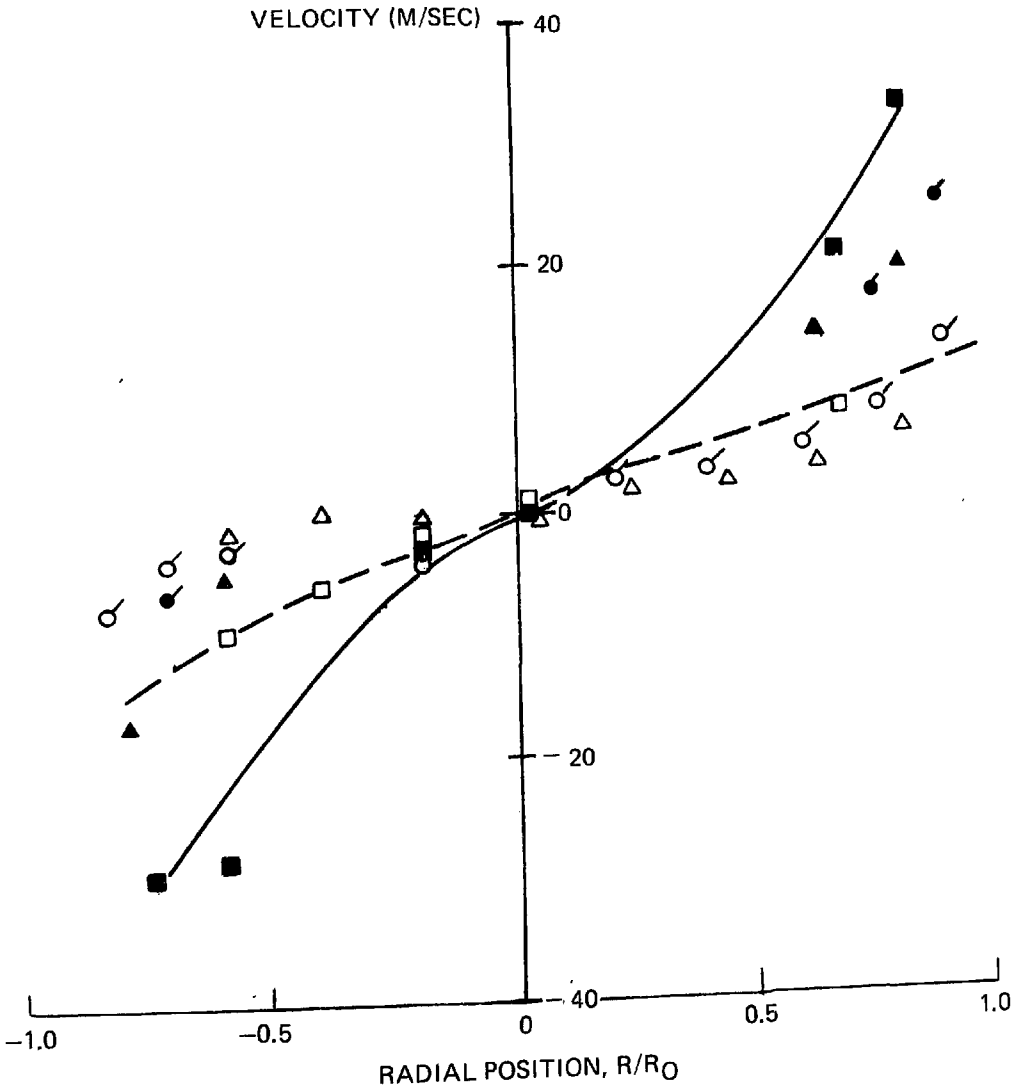

76–10–29–2

SECTION IV

RECOMMENDATIONS

The experimental investigations carried out under EPA contracts 68-02-1092 and 68-02-1873 have shown that variation in inlet conditions, e.g., pressure, inlet air swirl and inlet air temperature, produce major changes in the mean flow field, including vaporization and mixing rates, within a liquid fuel turbulent diffusion flame burner which result in subsequent changes in energy release rates and pollutant formation and destruction. The variation in pollutant emission trends with fuel type, found in the present investigation, serves to illustrate the difficulty in obtaining general relationships between pollutant emissions and inlet conditions in liquid fuel combustors. Pollutant formation and destruction are intimately connected with the flow field structure within the combustor and the structure depends on the spray pattern and on the interaction of the spray with the gas flow. The present data base is inadequate to permit definitive correlations of the flow field structure and pollutant emissions with burner inlet conditions.

Additional data on the effects of changes in inlet conditions on the mean and fluctuating flow field structure of liquid fuel turbulent diffusion flames and the subsequent effects on pollutant formation and destruction are required. Particular emphasis should be placed on determining spray characteristics, including droplet trajectories and size distributions, and in measuring fuel vaporization rates. Existing optical techniques for spray visualization in combusting flows should be refined to permit resolution of fuel droplets in the 5-50 μm range for spray particle densities of interest in real combustion devices to assist in these measurements. For each liquid fuel examined, separate fundamental experiments should be used to shed light on (a) the thermal decomposition of the fuel and (b) the combustion of droplet arrays. The complementary droplet combustion experiments would be particularly useful in examining the combustion characteristics of fuels containing bound nitrogen.

Recent studies of pollutant emissions from liquid fuel combustors have shown that changes in operating conditions which produce decreases in NO emissions generally result in significant increases in particulate emissions. Results from the present investigation followed similar trends. These observations suggest that future studies should be concerned with the effects of variation in operating conditions on formation and destruction of multiple pollutant species, including particulates (size, number density and composition) and various amine and cyano compounds.

APPENDIX A

DETAILS OF EXPERIMENTAL APPARATUS AND INSTRUMENTATION

Combustor Facility

A conventional pressure-atomizing swirl-type nozzle, Fig. A-1a, which produced a nominal 60 deg hollow-cone spray with a nominal droplet Sauter mean diameter of 100μm in quiescent air at atmospheric pressure was used for iso-octane and No. 2 distillate fuel. A tangential-feed pressure-atomizing nozzle, Fig. A-1b, with a similar spray angle and in which the full pressure drop occurred across the exit orifice was used with propane to maintain the fuel liquid to the point of injection. The direction of rotation imparted by the swirlers to both the fuel and the air streams were identical for each of the configurations tested.

The air swirl vane designs, shown together with the fuel injector assembly in Fig. A-2, are similar to those used previously in the gaseous fuel test program (Ref. 10). The swirl number, S, was computed from the injector geometry Z, and the angle of the swirl vanes, η, according to the following expression (Ref. 11):

$$S = \frac{1}{3}\frac{(1-Z^3)}{(1-Z^2)^{1.5}} \tan\eta \ . \qquad \text{(A-1)}$$

The swirl number is simply the ratio of the angular momentum flux to the axial momentum flux multiplied by an effective nozzle diameter.

The 12.23-cm diameter, 100-cm long instrumented combustor is divided into five water-cooled zones of approximately equal length. Water flow can be set independently in each zone, as needed, to keep wall temperature (∿500°K) roughly constant along the entire length of the combustor. Wall temperatures are set and monitored using thermocouples installed on the outer surface and at various depths in the combustor wall and cooling passages. Static pressure taps are also installed at several locations along the combustor. Flow exhausts from the combustor and extender sections to the facility exhaust stack. Combustor extender pieces, 33.4 cm in length, are inserted when required to fully contain the flame; the extender section consisted of two extender pieces during all of the current experimental effort.

Gas Sampling and Temperature Probes

Species concentration distributions within the combustor were measured using a traversing gas sampling probe, an exhaust gas sampling rake and a

PRESSURE ATOMIZING LIQUID FUEL INJECTORS

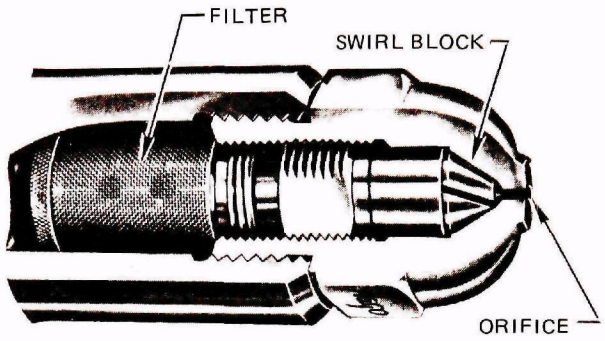

(a) AXIAL SWIRL

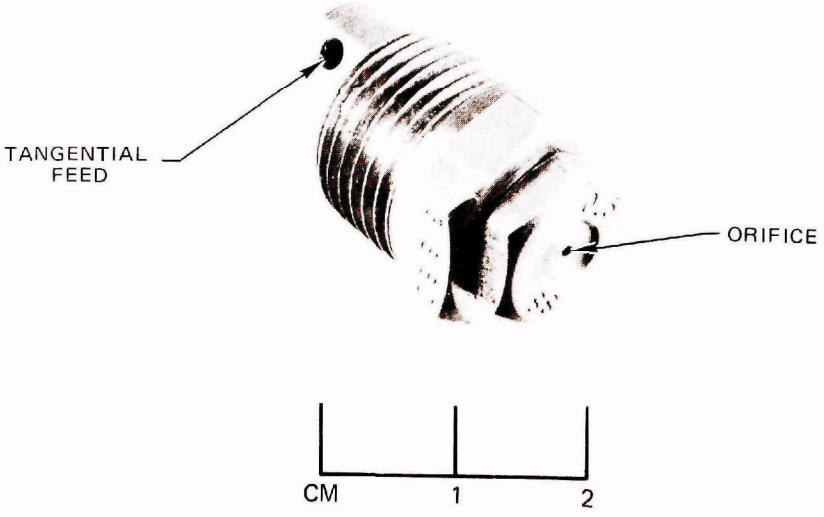

(b) RADIAL SWIRL

INJECTOR AND SWIRL VANE GEOMETRIES

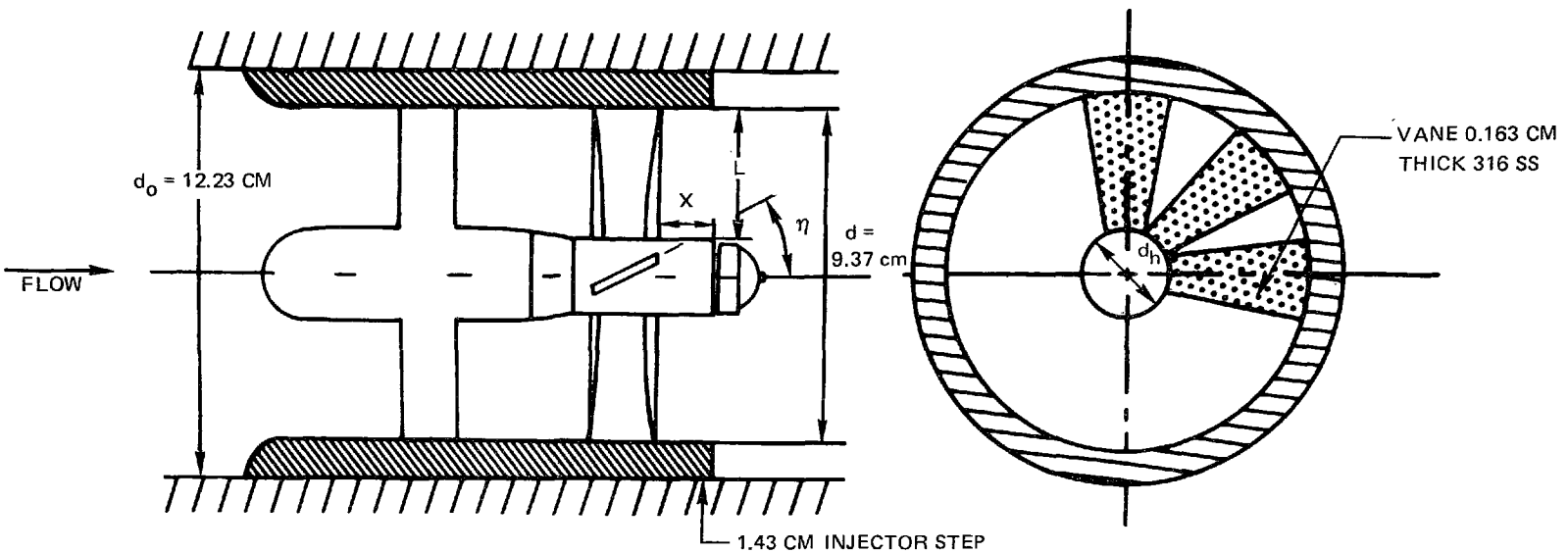

$Z = d_h/d$	L(CM)	S	η(DEG)	NO. OF VANES	X(CM)
0.203	3.732	0.3	40	12	2.24
		0.6	60	8	

FIG. A–2

phase-discriminating sampling probe. Composition information is determined on-line by aspirating flow through the cooled probes and analyzing the gas sample using a Scott Model 119 Exhaust Gas Analyzer and a heated discrete-sampling hydrocarbon analyzer. Pressurized hot water at 400°K was used as the probe coolant to minimize wall-catalyzed reactions and to prevent water and fuel condensation and loss of species within the sampling lines.

The exhaust probe rake, located at the exit of the extender section, consists of five identical probes centered on equal area annuli (Fig. A-3). The individual probes are manifolded downstream and a single mixed sample is transferred to the gas analyzer. Radial traverses are made at selected axial locations within the instrumented combustor section using a single gas sampling probe of similar design (Fig. A-4). The inlet flow into both sampling probes was maintained choked, resulting in aerodynamic cooling of the sample by means of a rapid internal expansion. This expansion combined with the wall cooling effect served to quench chemical reactions involving stable species.

Temperature profiles at the exhaust plane and within the combustor were measured by traversing a calibrated-heat-loss thermocouple probe across a combustor diameter. Although conventional thermocouple materials limit application of these sensors to temperatures below about 2000°K, cooling the exposed junction by conduction heat transfer extends the range of thermocouple utilization above the melting point of the material to the 2000-2500°K range. In order to obtain the local stream temperature, the measured stream thermocouple temperature must be corrected for conduction and radiation heat losses; therefore, calibration information is acquired simultaneously with the required temperature measurement. The probe consists of three thermocouples including an iridium - 10 percent rhodium/iridium thermocouple which protrudes from a water-cooled copper base into the reacting flow, and two platinum - 10 percent rhodium/platinum thermocouples installed on the ends of the iridium wire to record the base temperature and thereby permit calculation of the conduction heat loss (Fig. A-5). A thermocouple probe of this type was applied without difficulty in the combustion environment of the present program. Confidence in the accuracy of the temperature measurements was established in the previous contract effort by measurements made at identical test conditions using a conventional thermocouple probe and a double-sonic-orifice probe (Ref. 10).

Gas Sampling System

The gas samples withdrawn through the five-probe exhaust rake or the traversing probe are analyzed on-line to determine the time-averaged concentrations of carbon dioxide (CO_2), carbon monoxide (CO), oxygen (O_2), nitrogen oxides (NO, NO_2) and unburned hydrocarbons (THC). The samples are transferred to the analytical instruments through a teflon-coated, flexible line which is heated ($\sim$ 400°K)

EXHAUST SAMPLING PROBE RAKE

- PROBES CENTERED ON EQUAL AREAS
- FLOW FROM ALL PROBES MIXED BEFORE ON–LINE ANALYSIS

ALL DIMENSIONS IN CM
NOT TO SCALE

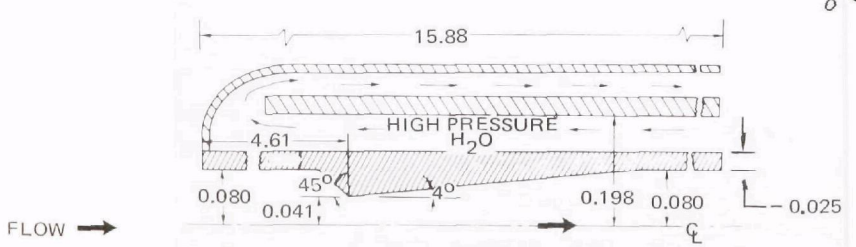

TIP DETAILS

FIG. A–3

76–05–79–4

TRAVERSING GAS SAMPLING PROBE

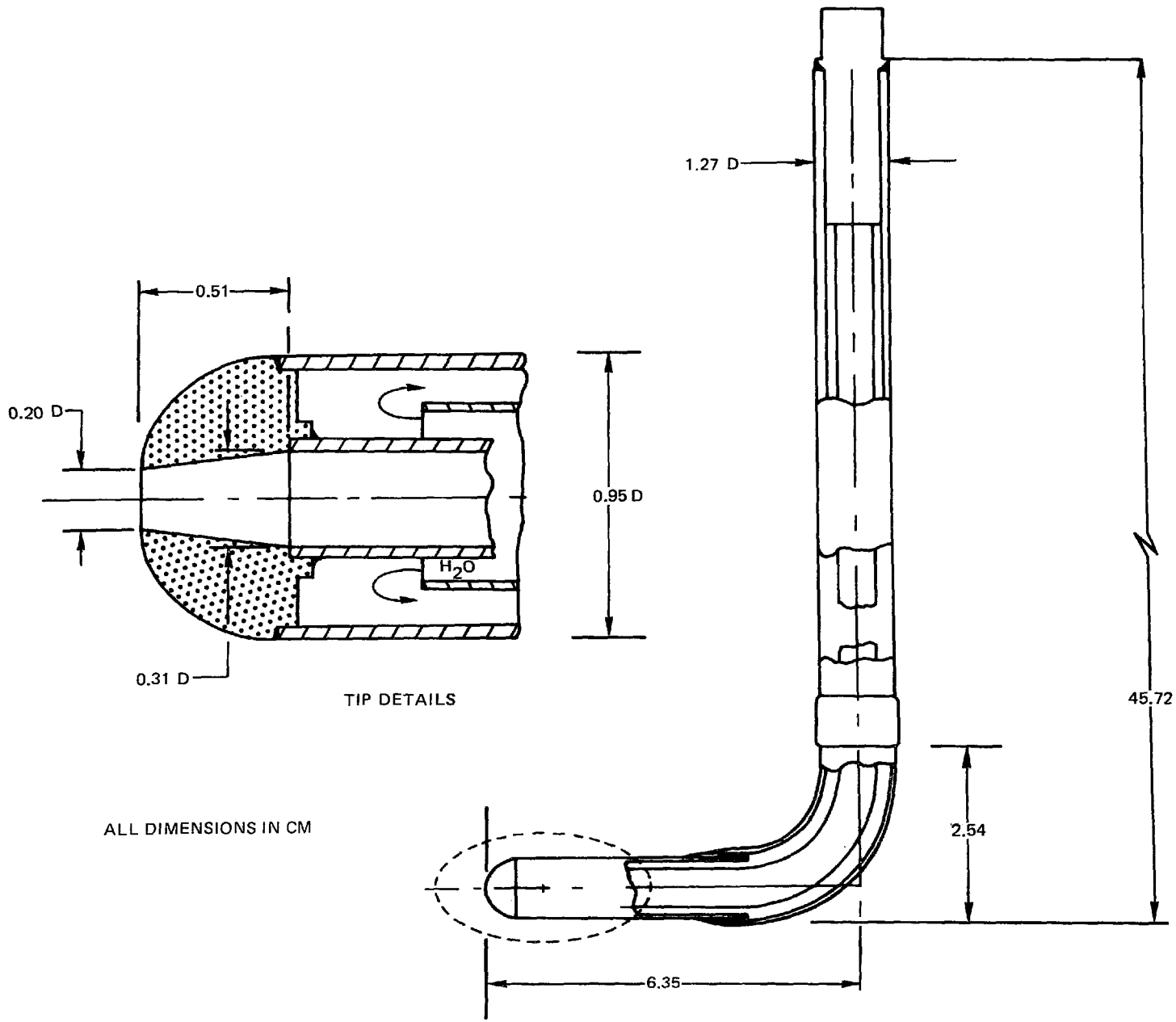

ALL DIMENSIONS IN CM

FIG. A-4

76-05-79-2

CALIBRATED–HEAT–LOSS THERMOCOUPLE PROBE

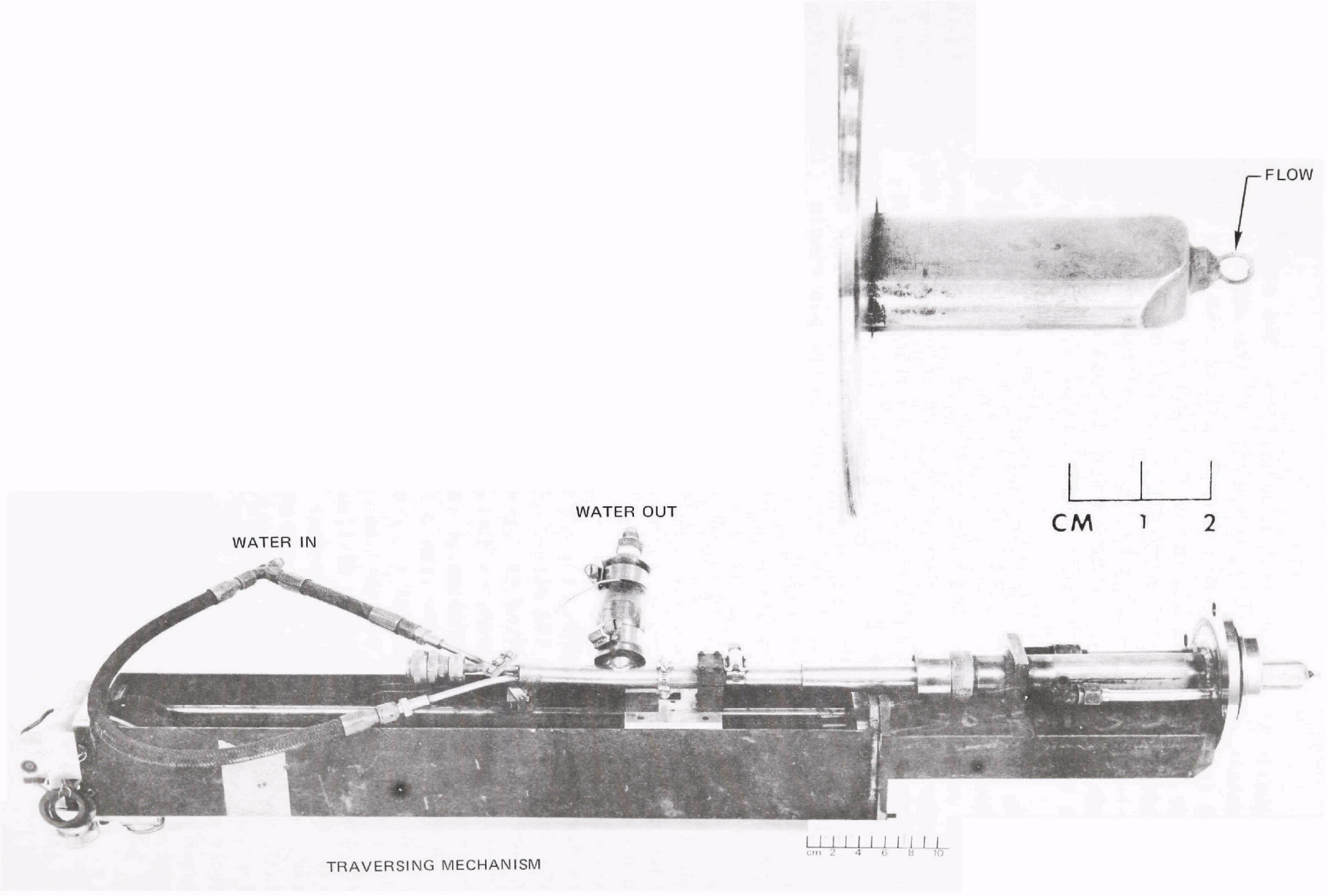

FIG. A-5

electrically to prevent water condensation. The sample is then directed through a condensate trap ($\sim$ 277°K), where most of the water is removed, and it is pumped through an unheated, teflon coated, aluminum line to a Scott Model 119 Exhaust Analyzer. A schematic diagram of the sampling system is shown in Fig. A-6. A stainless steel bellows pump increased the sample pressure from subatmospheric levels to 1 atm as required by the Exhaust Analyzer. The Analyzer, located in the combustion facility control room, approximately 10 m from the combustor, was used to measure the molar concentrations of CO, CO_2, O_2, NO, NO_2 and THC.

The Scott Model 119 Exhaust Analyzer, (Fig. A-7), is an integrated system, with flow controls for sample, zero and calibration gases conveniently located on the control panel. The incoming gas sample passes through a refrigeration condenser ($\sim$ 275°K), to remove residual water vapor. As the sample passes from the condenser, it is filtered to remove particulate matter. The Exhaust Analyzer is comprised of five different pieces of analytical instrumentation. Beckman Model 315B Nondispersive Infrared (NDIR) Analyzers were used to measure the CO and CO_2 concentrations (mole fractions) in the gas sample. Concentration ranges available on the CO analyzer were from 0-200 ppm to 0-15 percent on several scales. Concentration ranges available on the CO_2 analyzer were 0-4 percent and 0-16 percent. The accuracy of the NDIR analyzers is nominally $\pm$ 1 percent of full scale. A Scott Model 125 Chemiluminescence Analyzer was used to measure the NO and NO_2 concentrations in the gas sample. Concentration ranges available with this instrument were from 0-1 ppm to 0-10,000 ppm on several scales, with a nominal $\pm$ 1 percent of full scale accuracy. The thermal converter used in the chemiluminescent analyzer was stainless steel, and was operated at a temperature of approximately 1030°K. The converter efficiency (i.e., percent NO_2 dissociated) was determined using the method outlined in Refs. 10 and 15. In the present study a converter efficiency of 99 percent was measured, with an uncertainty in the measurement of 4 percent. A Scott Model 150 Paramagnetic Analyzer was used to measure the O_2 concentration in the gas sample. Concentration ranges available with this instrument were from 0-1 percent to 0-25 percent on several scales, with a nominal accuracy of $\pm$ 1 percent of full scale. A Scott Model 116 Total Hydrocarbon Analyzer was used to measure the hydrocarbon concentration in the gas sample. This analyzer utilizes an unheated flame ionization detection system to provide for measurement of hydrocarbons (as carbon) in concentration ranges from 0-1 ppm to 0-10 percent, with a nominal accuracy of $\pm$ 1 percent of full scale. The unheated analyzer was used to measure exhaust hydrocarbons only for propane. Output signals from the various analyzers are displayed on chart recorders. The Analyzer was calibrated prior to each test by flowing zero gases and calibration gas mixtures having compositions known to within one percent. Typically, at each test point, sampling data were acquired for a period of 2-4 min.

SCHEMATIC DIAGRAM OF ON–LINE GAS ANALYSIS SYSTEM

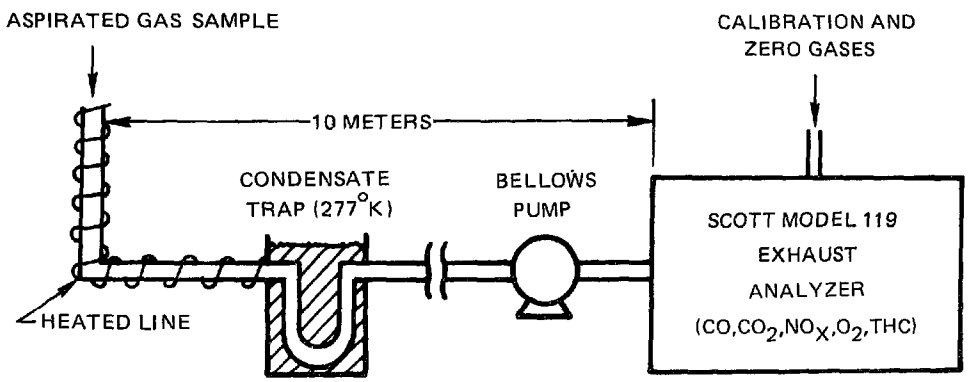

N12–161–1

EXHAUST GAS ANALYTICAL SYSTEM

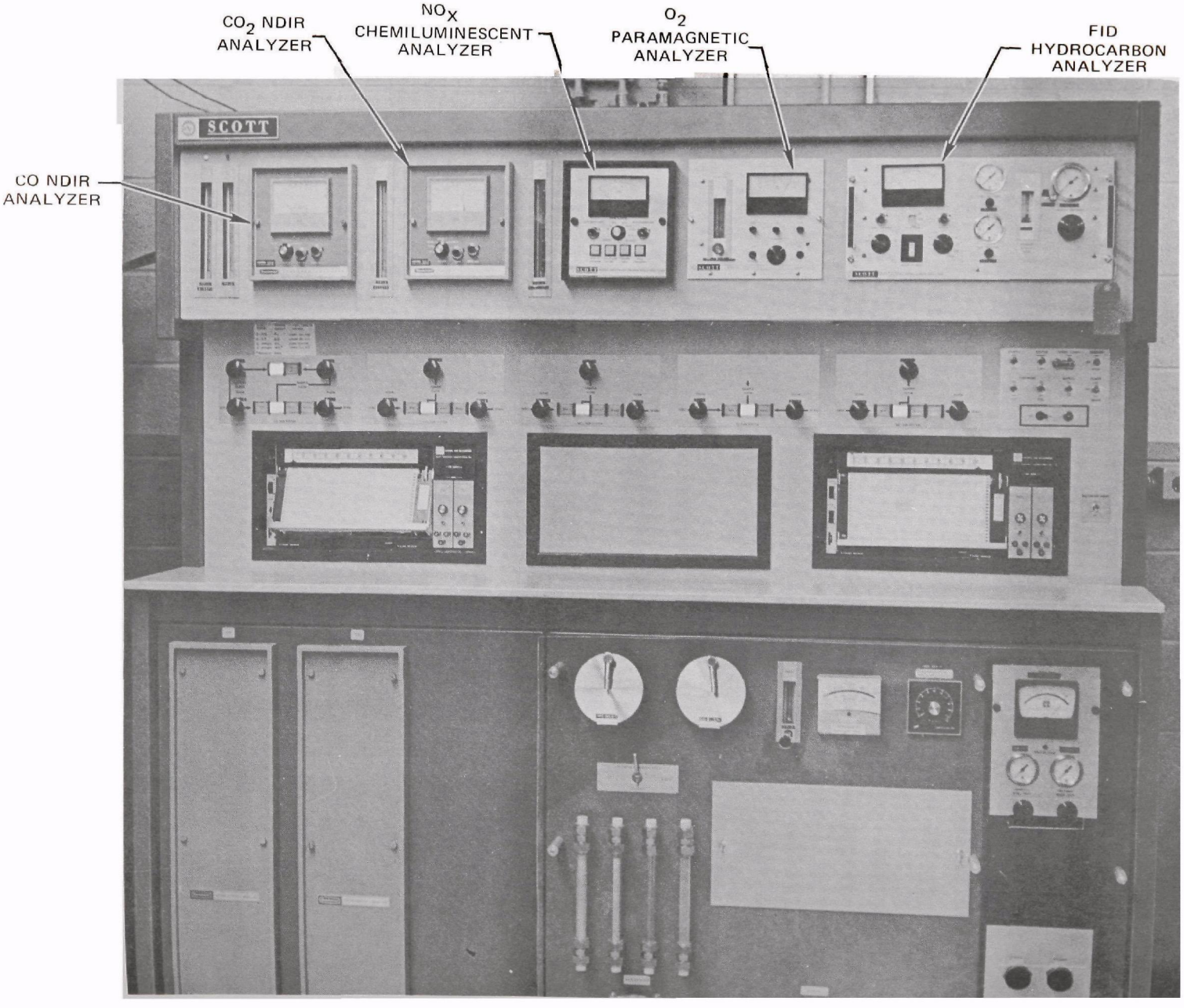

FIG. A-7

Phase-Discriminating Sampling Probe

The mole fractions of the vapor fuel and of the total (liquid + vapor) fuel within the combustor were measured by traversing a cooled phase-discriminating probe across the combustor diameter at selected axial locations downstream of the fuel nozzle. The probe designs employed were based on the work of Wadleigh and Oman (Ref. 16) who investigated the effects of the probe geometric design parameters and flow rates on the probe performance. Previously, uncooled phase-discriminating sampling probes have been designed, built and employed to measure the state of vaporization of nonburning fuel sprays (Ref. 17). The current study represents the first attempt to employ this probe design in a combusting flow field.

A schematic diagram showing the construction of the tip of the cooled phase-discriminating probe employed in this study is given in Fig. A-8. The central passage acts as a conventional gas sampling probe and collects the total (liquid + vapor) sample. Isokinetic flow is established within this passage by adjusting the flow rate through the tube so that the static pressure close to the tube lip is equal to the combustor static pressure. A tube oriented perpendicular to the axis of the total-sample tube is used to extract the vapor sample. A suction tube surrounding the vapor tube is used to purge any liquid which collects on the surface of the total-sample tube and which otherwise would spill over into the vapor sample tube and contaminate the vapor sample. Water jackets surround the sampling tubes so that the collected samples can be quickly quenched. Also, provisions were incorporated into the design for introducing a flow of nitrogen into the sample close to the probe tip in order to quench vaporization and chemical reaction. This purge feature was not employed in the present study. Water cooling also is required to ensure structural integrity of the probe. Heat transfer analyses of the probe design indicate that the probe tip can withstand gas temperatures of 2500^{o}K and pressures of 7 atmospheres for a water flow rate of 0.3 kilograms per second. A water supply pressure of 4 x 10^{5} Newtons/meter^{2} was adequate for providing this flow rate. It further is required that over-cooling of the probe be avoided since this would lead to condensation of the fuel vapor samples. Temperatures of the samples were monitored by a thermocouple inserted into the total-sample line at a location 15.2 cm from the probe tip (Fig. A-9). The probe coolant flow rate was regulated so that the measured temperature was maintained above 560^{o}K.

A photograph showing the phase-discriminating probe assembly is given in Fig. A-10. The probe is held in position by a water-cooled mounting plate which can be installed in any of the window ports in the combustor test section. The probe is traversed by a hydraulic actuating mechanism which is equipped with a slide wire probe position indicator.

SCHEMATIC DIAGRAM OF PHASE–DISCRIMINATING PROBE TIP

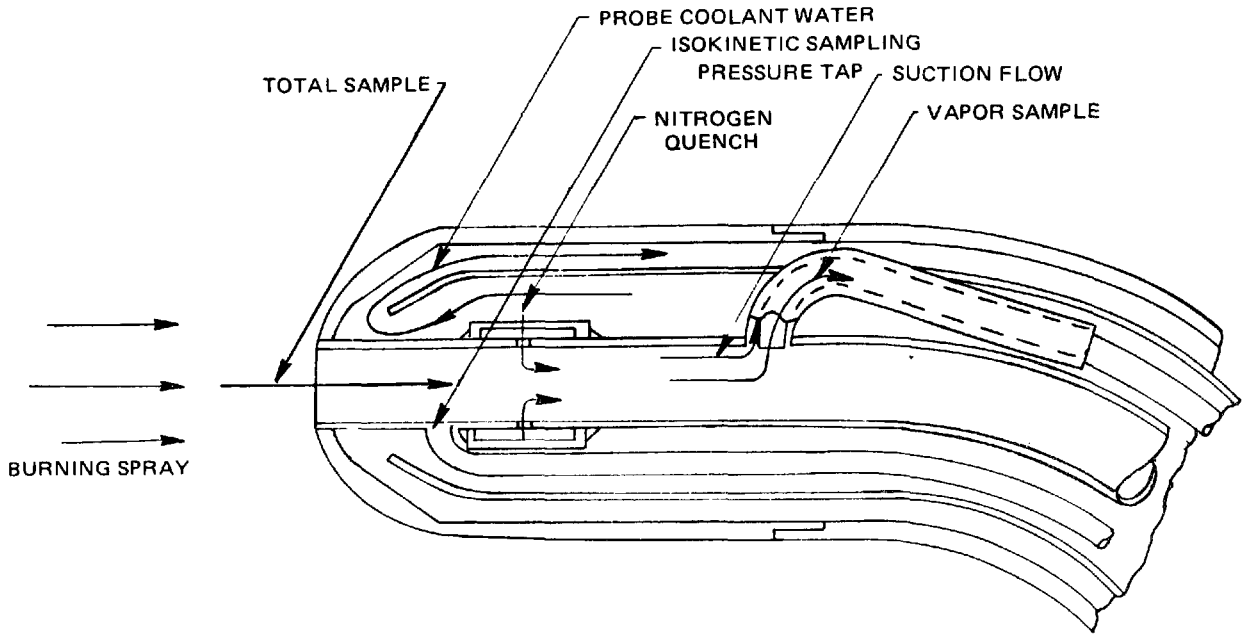

ALL DIMENSIONS IN CM

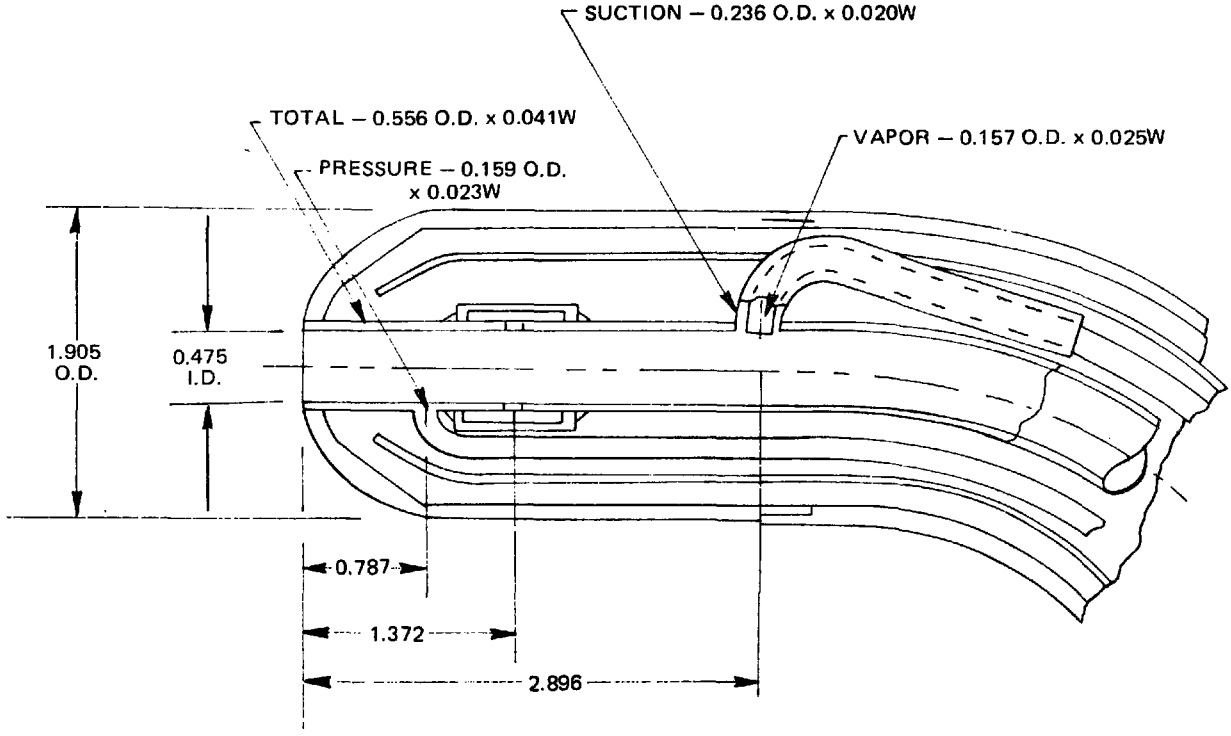

FIG. A–9

SCHEMATIC DIAGRAM OF PHASE DISCRIMINATING PROBE

ALL DIMENSIONS IN CM

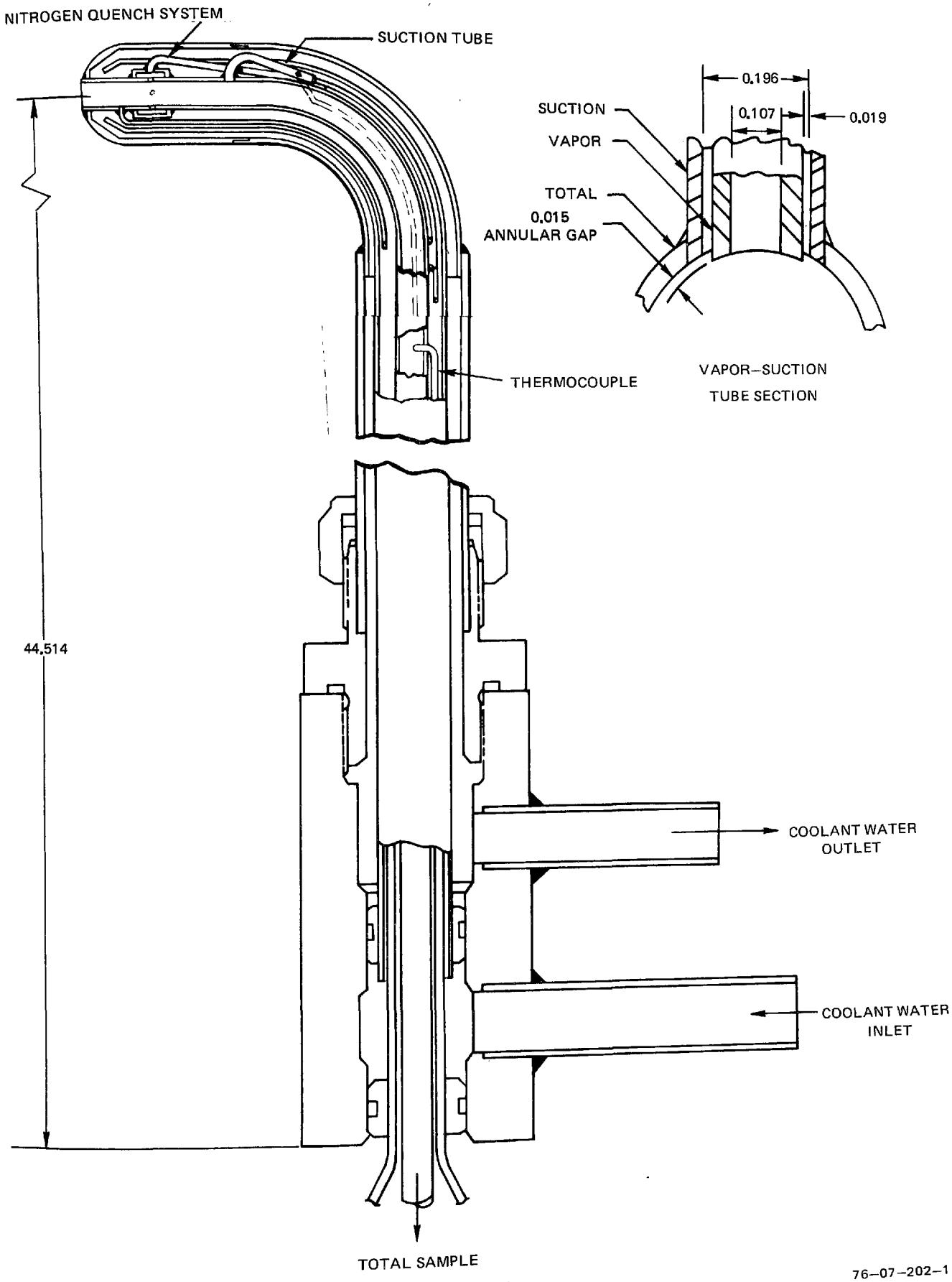

76–07–202–1

FIG. A-10

PHASE–DISCRIMINATING PROBE ASSEMBLY

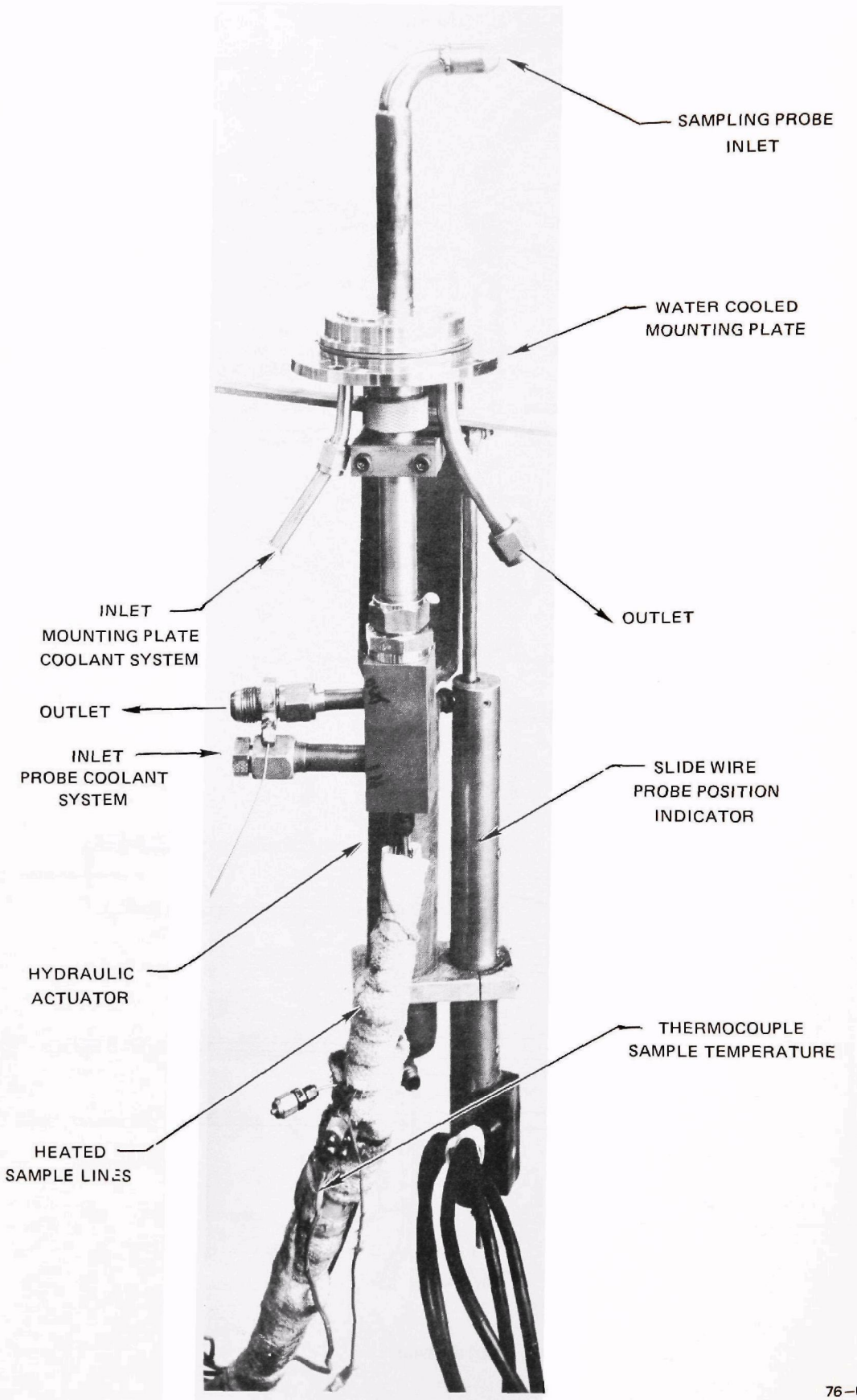

RL76–189–A

76–06–169–1

Fuel Analysis System

The concentration of fuel in the samples withdrawn by the phase-discriminating probe is obtained from on-line determinations of the hydrocarbon content using a flame ionization detector. A schematic diagram of the sampling system is shown in Fig. A-11. The sample is pumped from the probe through electrically-heated stainless steel lines, which maintain a sample temperature of approximately 500°K, and through glass wool particulate filters to the gas analysis equipment. Sample flow rates are controlled using electrically-operated throttling valves. Flow rates are determined from orifice pressure measurements. The pressures upstream and downstream of the orifices are measured by use of a Validyne DP7 Diaphragm Magnetic Reluctance Transducer employing a ± 3.4 atm diaphragm. The transducer used in establishing the pressure differential between the total sample tube and the combustor is a similar unit having a $\pm 7 \times 10^{-3}$ atm diaphragm. The flows then pass through MB-158 High Temperature Welded Bellows Pumps which increase the sample pressure from subatmospheric levels to one atm as required by the analyzer system. Stainless steel bellows pumps are used to prevent contamination of the samples. The metal bellows pumps are contained in ovens equipped with temperature limit switches which only permit operation of the pumps at the elevated temperatures required to prevent sample condensation. Because the flow fate in the total sample line required to ensure isokinetic conditions at the probe tip is greater than the flow capacity of the metal bellows pump, a bypass pump is connected to the total sample line upstream of the bellows pump. The flow rate through this GAST Model 0522 rotary vane vacuum pump is controlled by an electrically-operated throttling valve. Flow is passed around the metal bellows pumps when operating the combustor at above-atmospheric conditions. The vapor and total samples are passed to the ionization gauge via a ten-port sampling valve. Pressure relief valves having a 2×10^{-3} atm cracking pressure are installed in the lines upstream of the sampling valve in order to ensure atmospheric pressure in the ionization gauge. The flow in the suction line, which is not analyzed, is transferred to an exhaust line.

The ten-port sampling valve permits uninterrupted flow of a carrier gas, argon and gas samples through the ionization gauge (Fig. A-12). Conventional hydrocarbon analyzer systems employing flame ionization detectors provide a continuous sampling capability, but for the purposes of analyzing fuel sprays where locally high fuel/air ratios exist, a method of preventing saturation of the ionization gauge must be provided. The sampling valve employed in this system is designed to extract small discrete samples from either of the transfer lines and to dilute those samples with carrier gas prior to delivery to the ionization gauge. As shown in the figure, as the valve slide is repositioned a discrete amount of either the total fuel sample or vapor fuel is injected into the carrier gas for delivery to the ionization gauge. The peak concentration of the sample reaching the ionization gauge is determined by the length and size of the loops on the sampling valve and the length of the line between the sampling valve and the ionization gauge.

SCHEMATIC DIAGRAM OF PHASE DISCRIMINATING PROBE GAS ANALYSIS SYSTEM

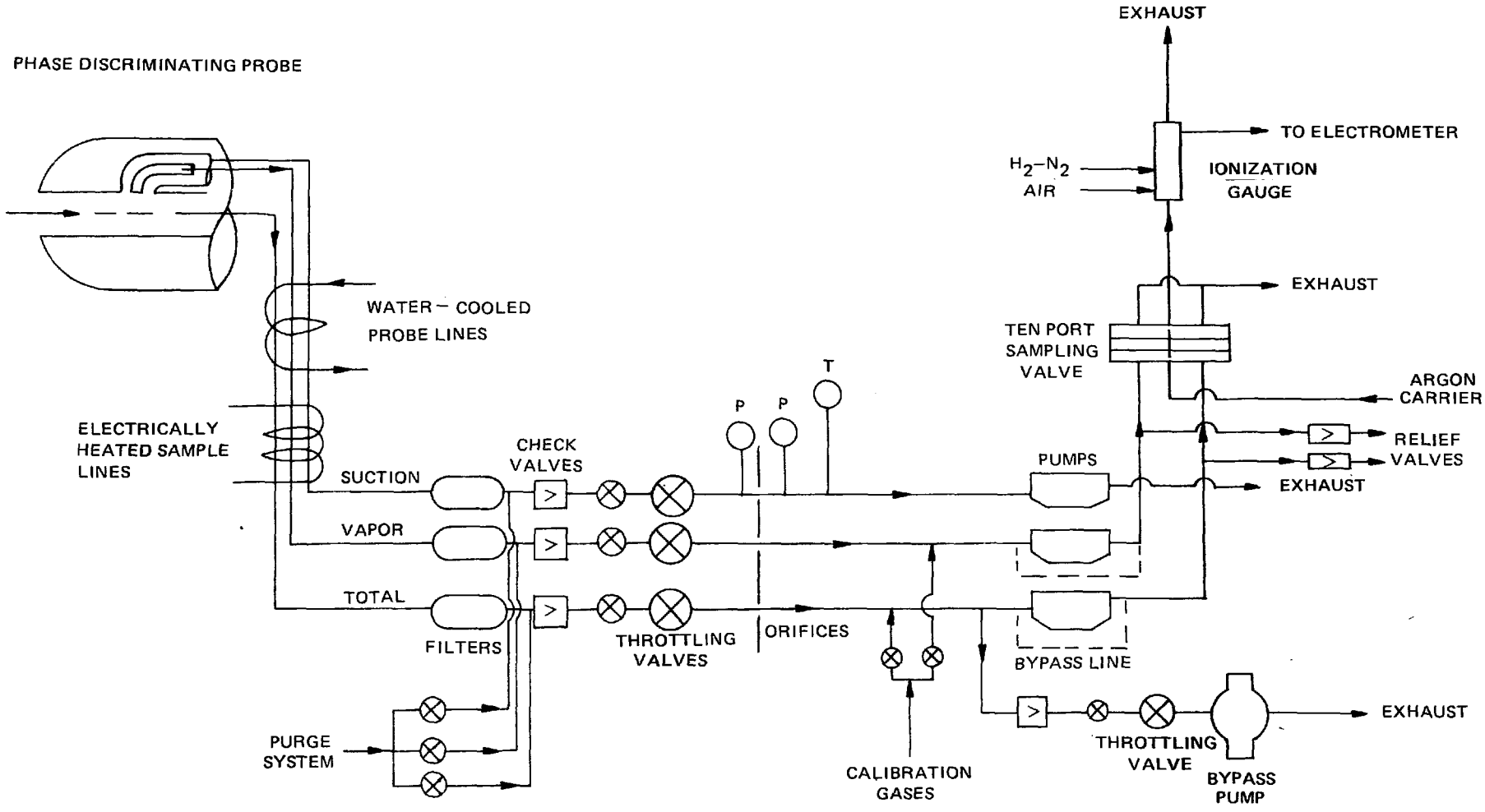

76-06-145-2

FIG. A-11

TEN PORT SAMPLING VALVE

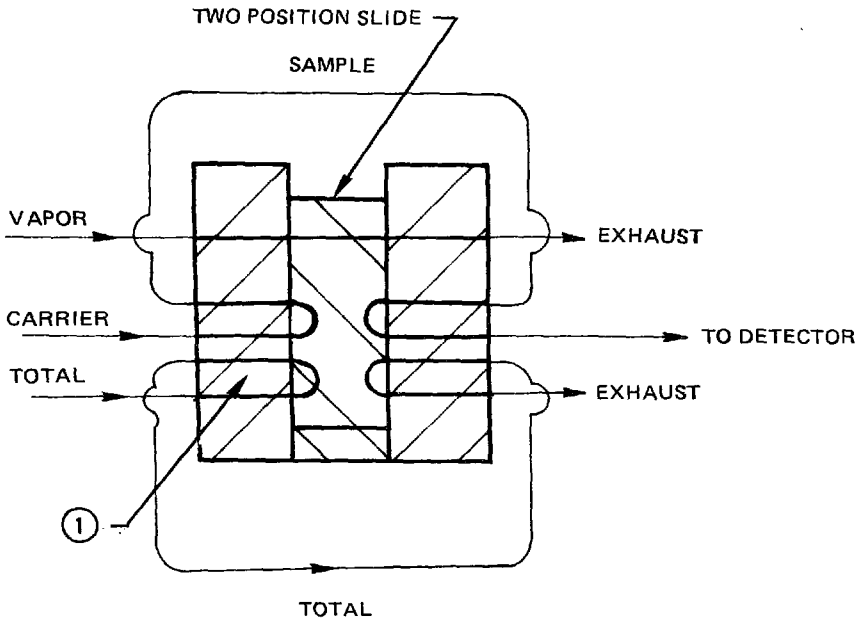

PORT (1) CONTAINS TOTAL SAMPLE TO BE INJECTED DURING NEXT SWITCHING OF SLIDES

a) SLIDE POSITION AFTER INJECTION OF VAPOR SAMPLE

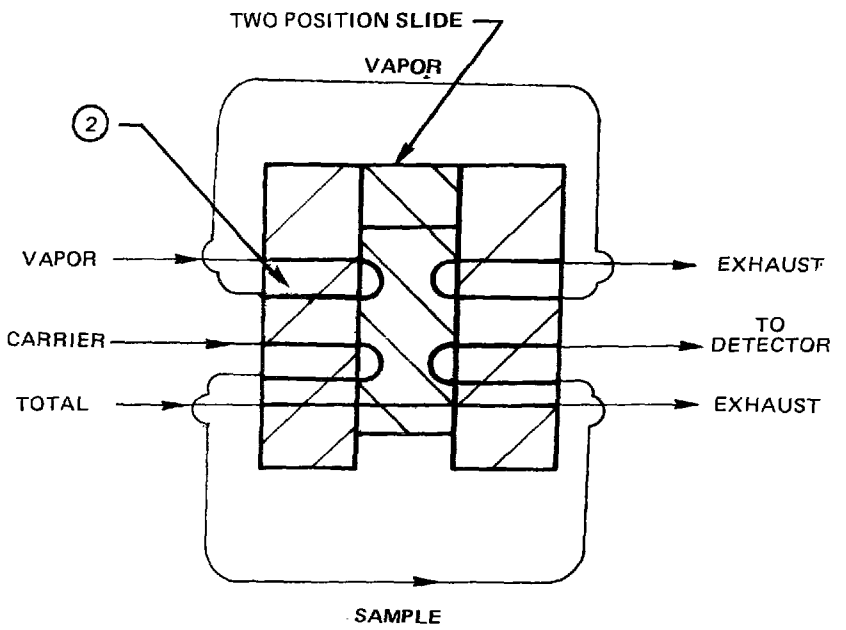

PORT (2) CONTAINS VAPOR SAMPLE TO BE INJECTED DURING NEXT SWITCHING OF SLIDES

b) SLIDE POSITION AFTER INJECTION OF TOTAL SAMPLE

FIG. A-12

76-06-145-6

A Gomac ionization gauge and signal conditioner (electrometer) are used to measure the hydrocarbon concentration in the gas samples. The ionization gauge is piloted with a hydrogen air flame using a 60/40 hydrogen/nitrogen fuel supply. A photograph showing the ionization gauge and ten-port sampling valve in a constant-temperature oven is given in Fig. A-13.

All of the components of the gas analysis system are installed on an instrumentation cart which was designed to withstand the harsh environment encountered in combustion facility test cells. A photograph showing installation of the equipment on the instrumentation cart is given in Fig. A-14. The instrumentation cart is located approximately 2 meters from the base of the probe. The probe hydraulic drive mechanism, flow control valves, and sampling valves are operated from a control room where the output of the ionization gauge is recorded on a strip chart recorder (Fig. A-15). The recorder displays the hydrocarbon concentration as a function of time and also mechanically integrates the concentration with respect to time. A typical trace is displayed in Fig. A-16. The system is capable of analyzing a gas sample every 30 seconds.

Laser Holographic System

A laser holographic system was developed and used to measure the spatial location of the fuel droplets and mean droplet size in liquid fuel sprays emanating from the fuel injector. A schematic diagram of the off-axis holographic system used to make these measurements is shown in Fig. A-17. The beam from a Q-switched ruby laser (Korad Model K-1QP) is separated into an object beam and a reference beam by a beam splitter. A Tropel Model 280 expander/collimator is used to expand the reference beam, which initially is less than five millimeters in diameter, to an approximately 12.5 cm diameter beam which strikes the holographic plate. The collimator is adjusted so that the wavefronts emanating from the lens of the collimator are plane. The reference beam is oriented so that the angle of the reference beam with respect to the object beam is approximately 45 deg. This angle is a compromise between larger angles which would cause the fringe patterns developed on the holographic plate to become very closed spaced, thereby reducing resolution, and smaller angles which would require the holographic plate to be moved away from the object. It is desirable to keep the holographic plate close to the object in order to maintain the high f-number optics required for good resolution and to permit the use of high f-number reconstruction optics which provide a short depth of focus.

The portion of the laser beam which is undeflected by the beam-splitter passes through a lens to a diffuser (ground glass plate). The diffuser causes the rays of light to be transmitted to the object (the spray over a large range of angles relative to the optical axis.) The light emanating from the spray is the true object beam, and consists of light transmitted through the transparent

HYDROCARBON ANALYZER

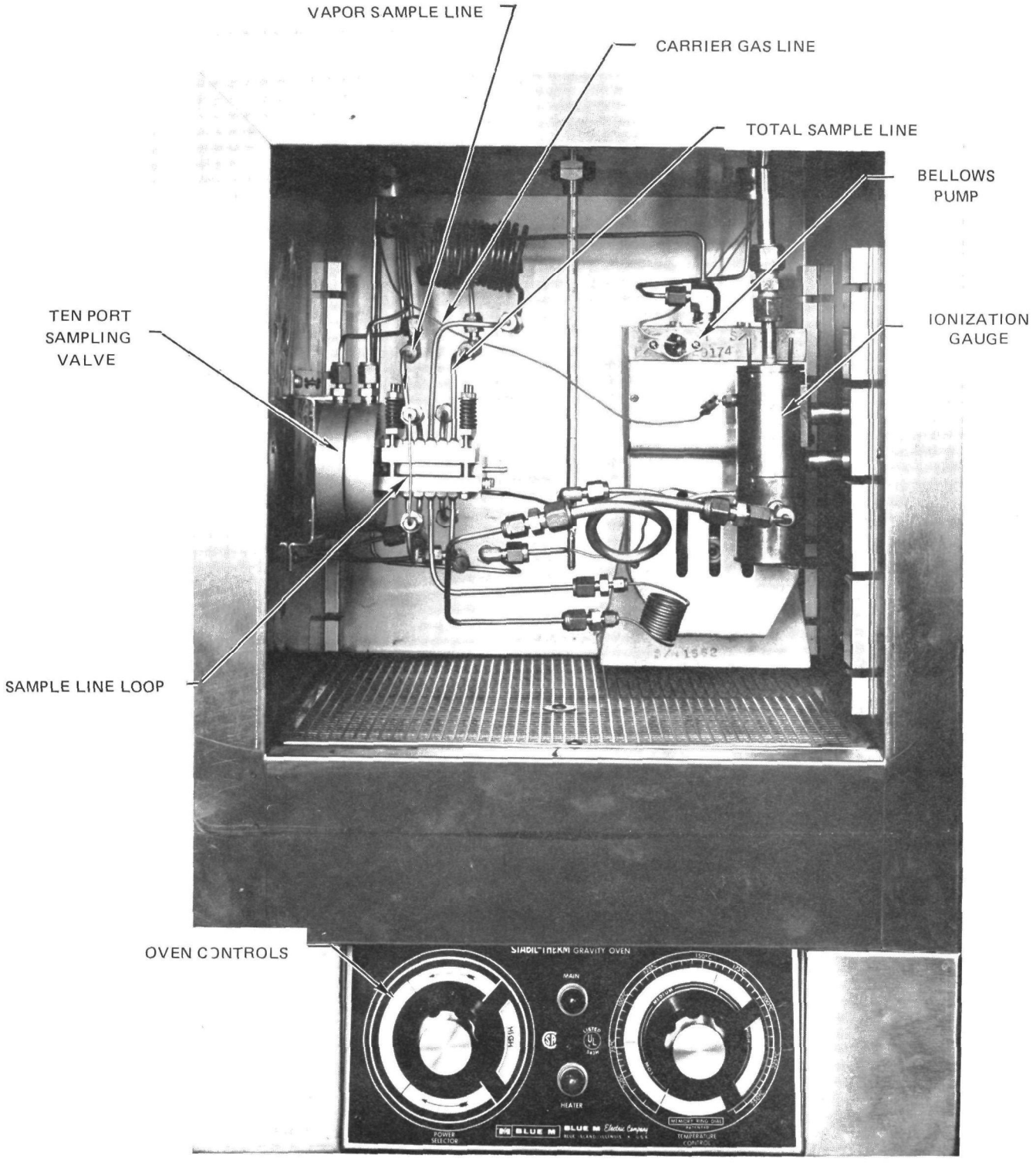

R76–189–B

76–06–169–2

PHASE DISCRIMINATING PROBE INSTRUMENT CART

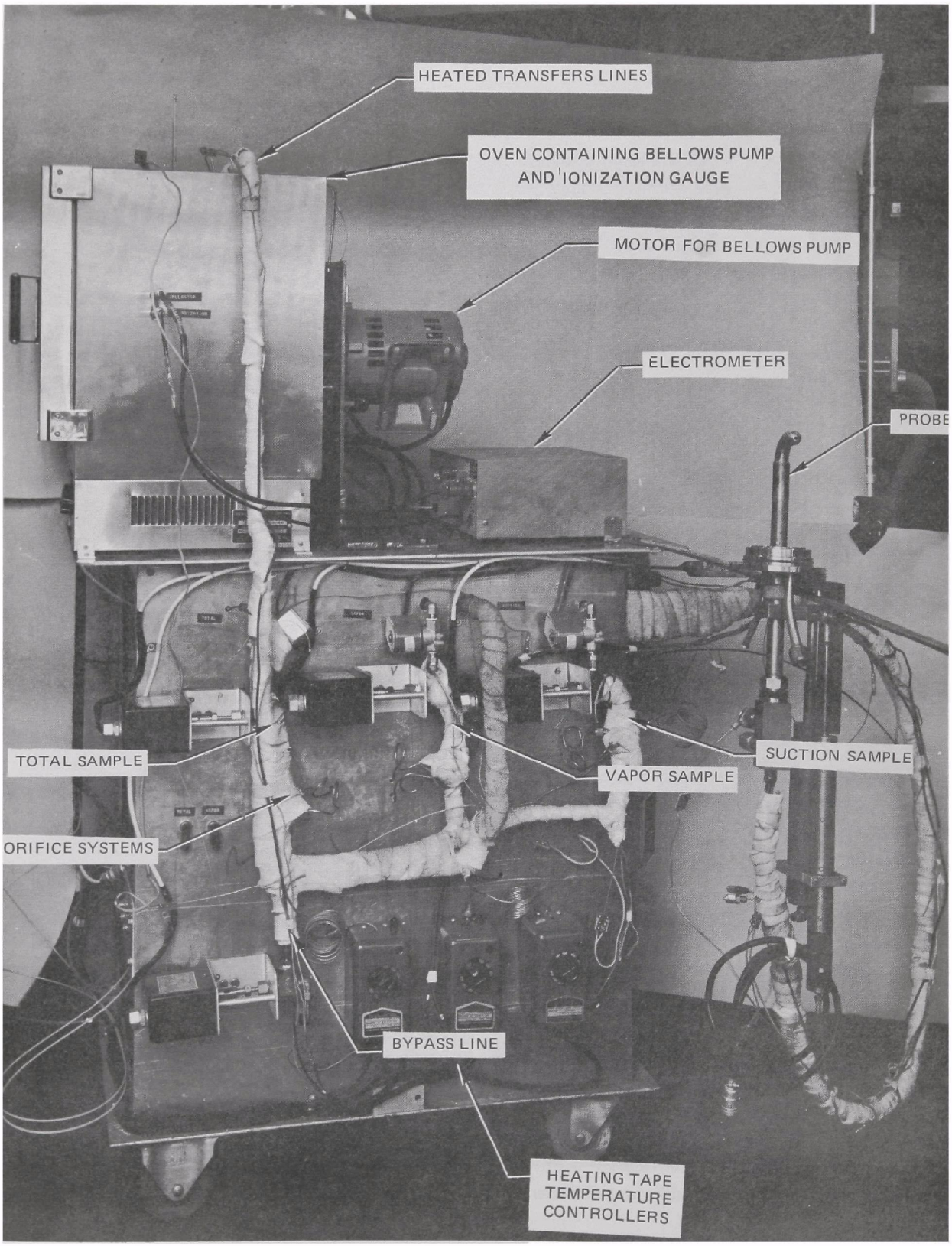

76-06-185-2

PHASE–DISCRIMINATING PROBE CONTROLS AND READ–OUT

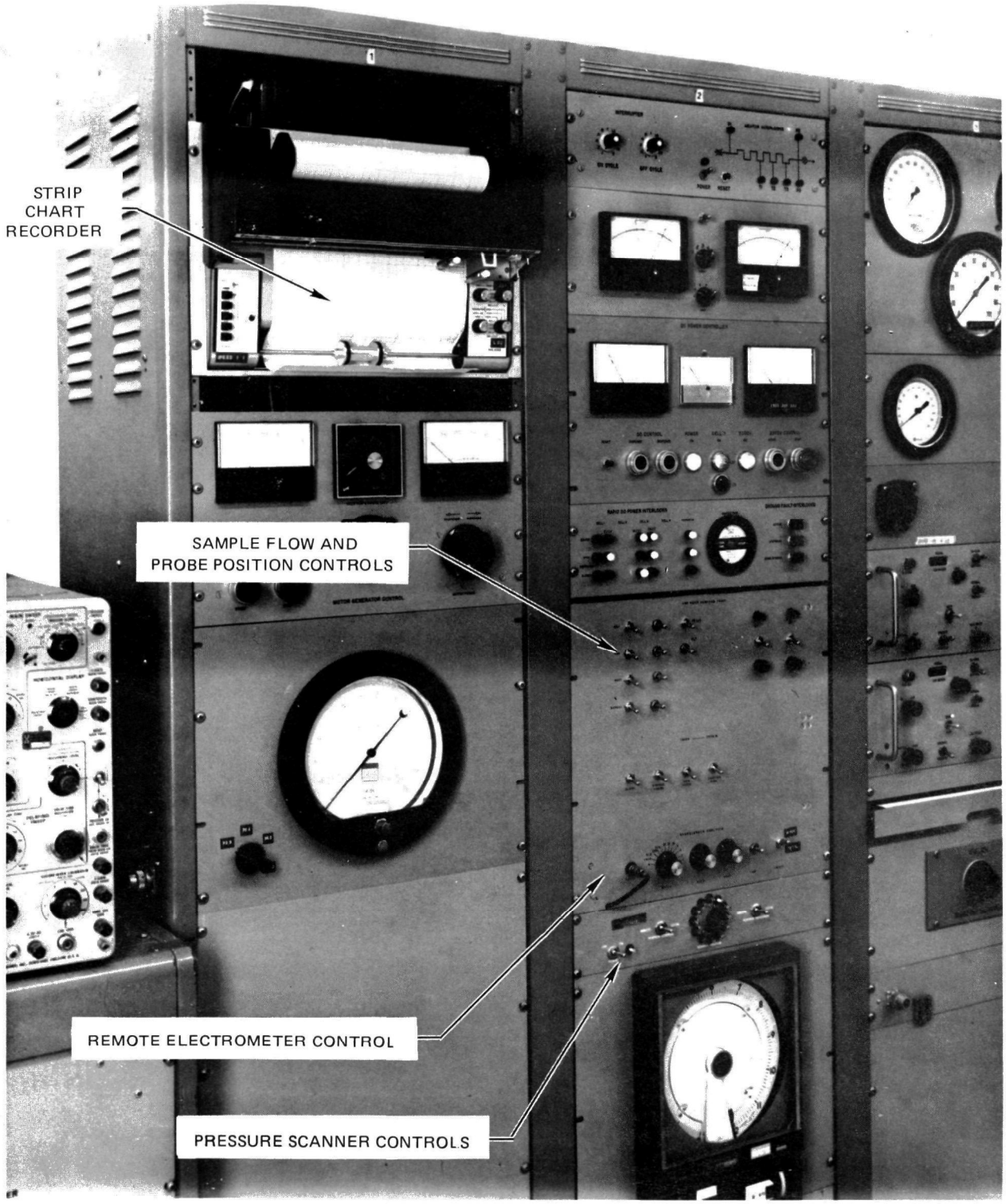

R76–189–D

76–06–169–3

TYPICAL EXPERIMENTAL TRACE FROM HYDROCARBON ANALYZER

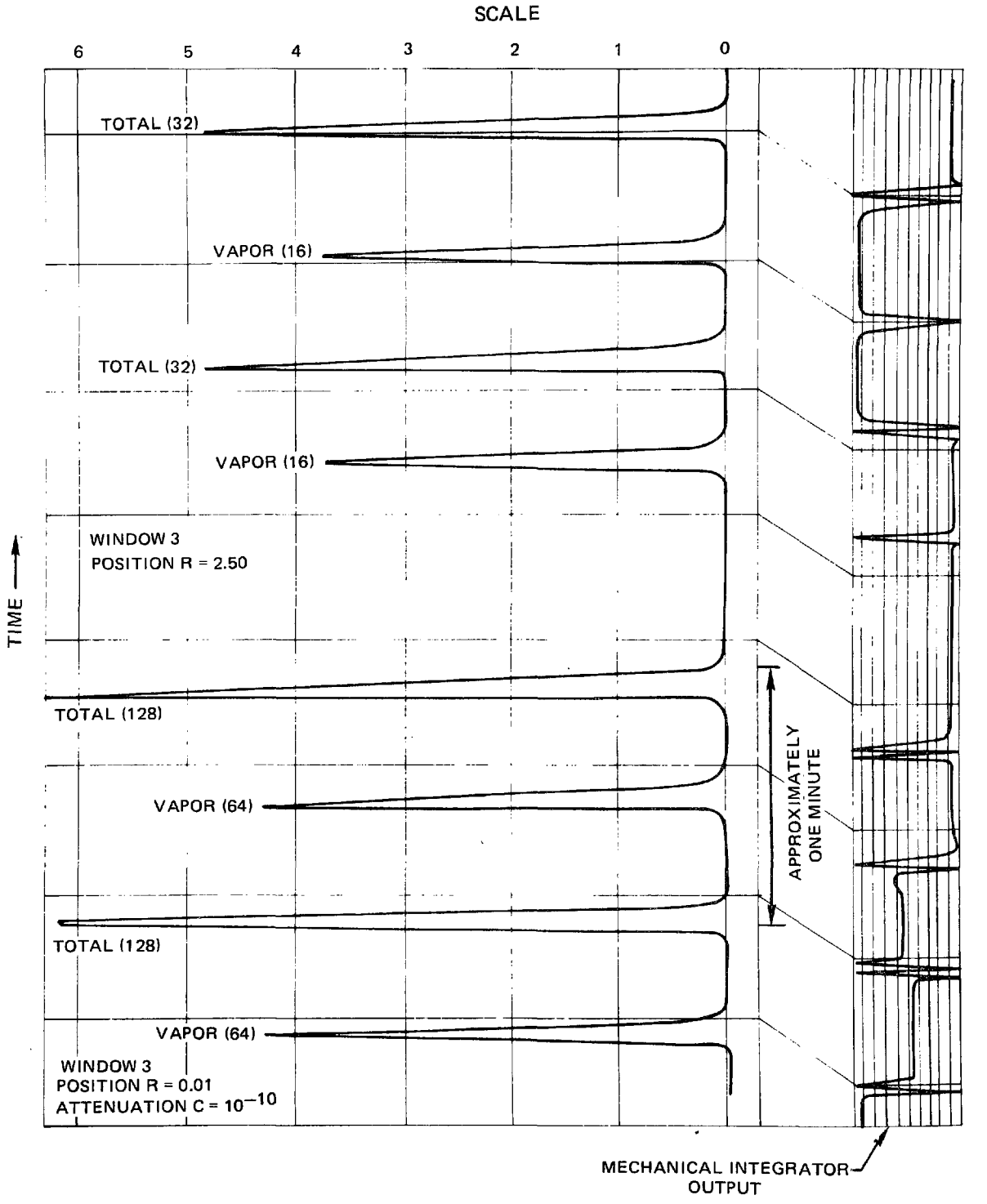

SCHEMATIC DIAGRAM OF LASER HOLOGRAPHY SYSTEM

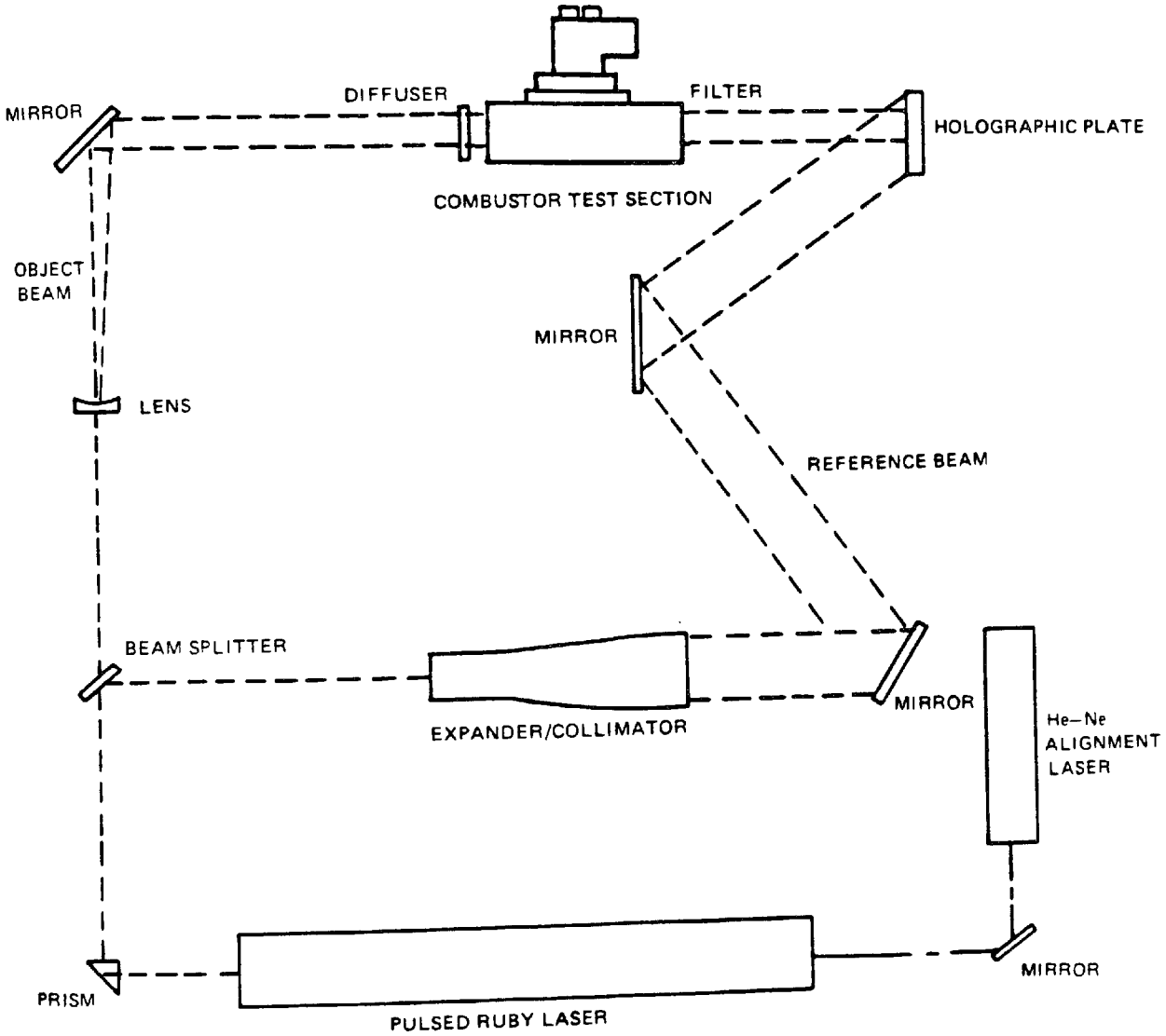

76-08-213-4

droplets, reflected from the surface of the droplet and refracted by the edges of the droplet. Light from each point in the spray reaches all points on the holographic plate thereby providing the information required to reconstruct a three-dimensional image of the spray. Depending on the distance traveled by the light emanating from the spray, the object beam will either interfere with or be reinforced by the reference beam, thereby producing fringes. The holography system employed is of the transmission type, since light from the diffuser is transmitted through the object to the holographic plate. With such systems the reconstructed images of the objects appear as silhouettes if the objects are opaque. In the case of a transparent droplet, the edge of the droplet appears dark because light at the edge is refracted out of the field of view of the holographic plate. Light that passes through the center of the droplet reaches the holographic plate and, therefore, the droplet image appears as a dark outer ring with a bright center. The dark outer edge represents the true dimension of the transparent droplet in the object field.

To reduce fogging of the holographic plate by light emitted from the hot combustion gases, a filter was installed between the test section window and the holographic plate. Both a gelatin filter (Kodak Wratten No. 29) and a high quality interference filter were employed. These filters, the transmission characteristics of which are shown in Fig. A-18, were equally effective in blocking the radiation emitted from the combustion gases. The holograms were recorded on Agfa Scienta Type 10E75 film on a 4 x 5 in. glass base. A remotely-controlled film magazine capable of holding eight film plates was utilized so that a series of holograms could be obtained without entering the test cell or disturbing the alignment of the optical components.

A schematic diagram showing the components used to reconstruct the holograms is given in Fig. A-19. A Spectra-Physics Stablite Model 124A helium-neon laser was used as the light source. The laser beam was expanded by a Tropel Model 280 expander/collimator to produce a beam of light approximately 12.5 cm in diameter. The light illuminated the holographic plate mounted in an articulated holder to facilitate precise orientation of the hologram relative to the incident laser beam. Light diffracted from the hologram formed a real image of the spray. This image was examined by eye using a 12-power loupe mounted on a tripod and rack-and-pinion mechanism so that the loupe could be translated in three-dimensions.

The traversing mechanisms were equipped with index scales having 1-mm divisions so that the coordinates of the object being viewed could be determined. The loupe was equipped with a reticle having square outlines ranging in size from 100 to 250 microns. This size range was comparable with the range of sizes of the larger droplets observed in the spray.

FILTER TRANSMISSION CHARACTERISTICS

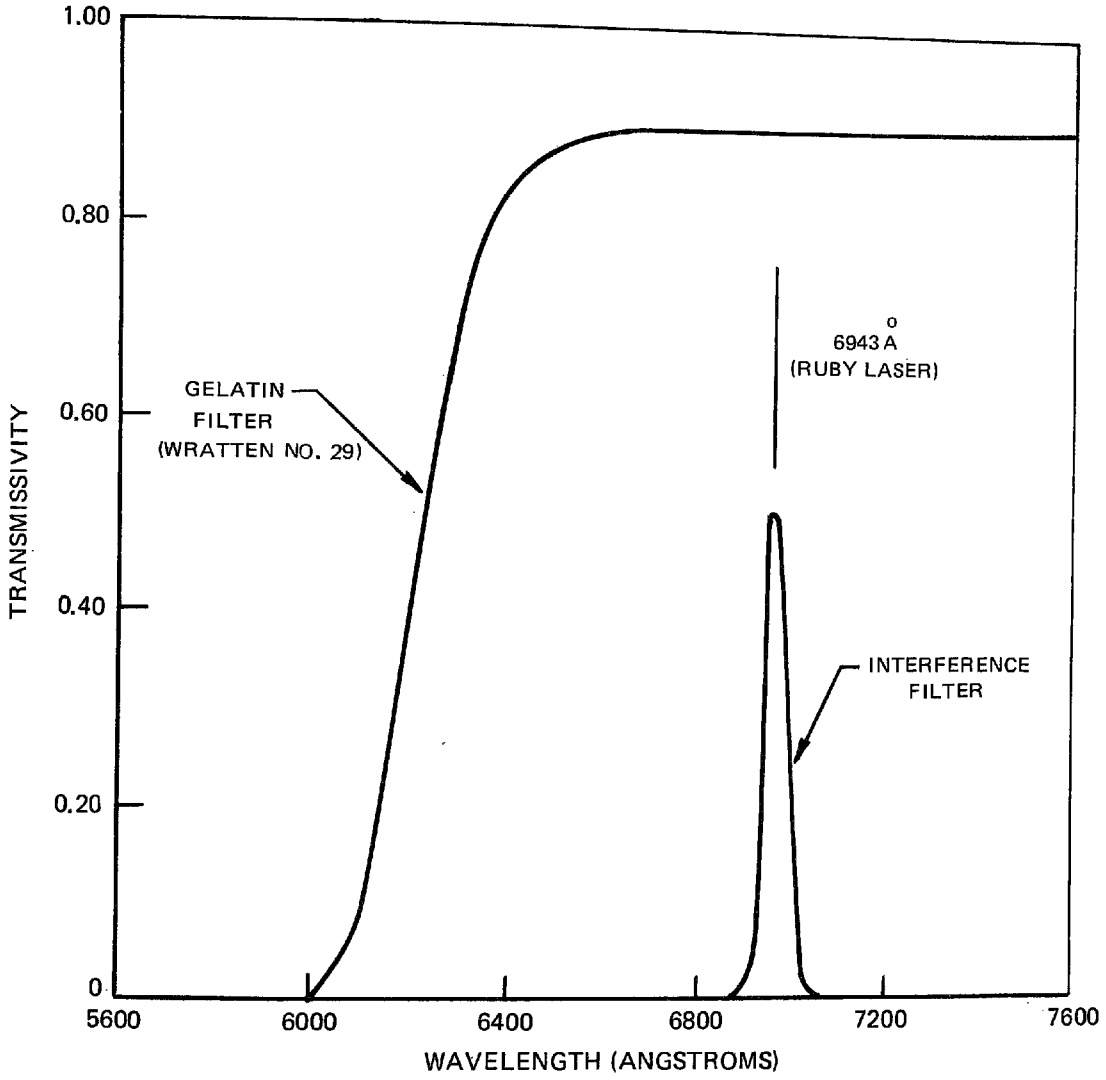

SCHEMATIC DIAGRAM OF HOLOGRAM RECONSTRUCTION APPARATUS

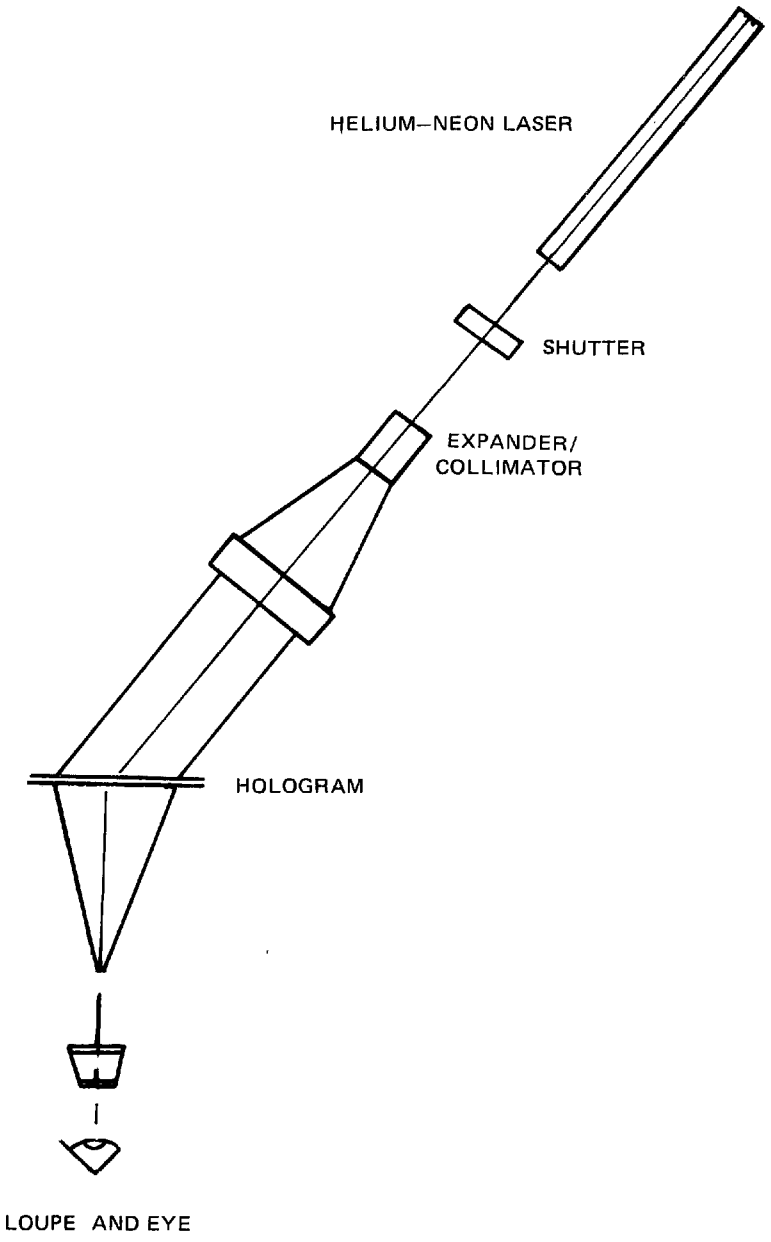

Laser Velocimeter

In the gaseous fuel test program (Ref. 10), a laser velocimeter was used to measure the mean and rms gas velocities in the initial regions of the reacting flow. It is desirable to obtain similar data in the liquid fuel program, and in addition it would be worthwhile to obtain data on droplet velocities and trajectories. However, in liquid fuel combustors the flow field immediately downstream from the fuel injector is complex, and the utility of laser velocimeter measurements in these flows is uncertain. Significant questions arise concerning the effect of the spray on the propagation of the laser beam within the combustor and concerning the ability of the laser velocimeter to discriminate between large fuel droplets, which generally have velocities different from the gas stream, and small droplets or seed particles, which move with the gas stream. Accordingly, a series of tests were carried out to evaluate the laser velocimeter as a velocity measuring technique in liquid-fuel turbulent flames and measurements of mean and rms gas and droplet velocities were obtained for several test conditions.

The laser velocimeter used in these tests was identical to the one employed in the gaseous fuel test program (Ref. 10). The measurements were made with a dual beam velocimeter utilizing an argon ion laser and a crystal Bragg cell which acted as a beam splitter and frequency shifted the first deflected beam. A schematic of the optics and signal processing instrumentation is shown in Figs. A-20 and A-21. The sensing volume determined by beam crossover volume, off-axis collection and photomultiplier pin hole size was elliptic with principal axes of 0.2 mm and 2.0 mm, respectively. The velocity component sensed with this optical arrangement lies in the plane of the two incident beams and is perpendicular to their bisector. Single particle, time domain signal processing was used to build up the velocity probability density distributions from which both the mean and rms velocities were obtained using the following equations:

$$\bar{U} = \sum_{i=1}^{N} \frac{U_i}{N} \tag{A-2}$$

$$\sigma = \sqrt{\overline{u^2}} = \left(\sum_{i=1}^{N} \frac{U_i^2}{N} - \bar{U}^2 \right)^{1/2} \tag{A-3}$$

In the present experiments, a minimum of 1000 instantaneous velocity determinations was used to build up the probability densities. This number of determinations results in a statistical error of less than 5 percent in the computer values of both the mean and variance with a confidence level of 95 percent (Ref. 10). On line signal processing to determine the local mean velocity, turbulent intensity and probability density function was achieved using the instrumentation shown

SCHEMATIC DIAGRAM OF THE LASER VELOCIMETER

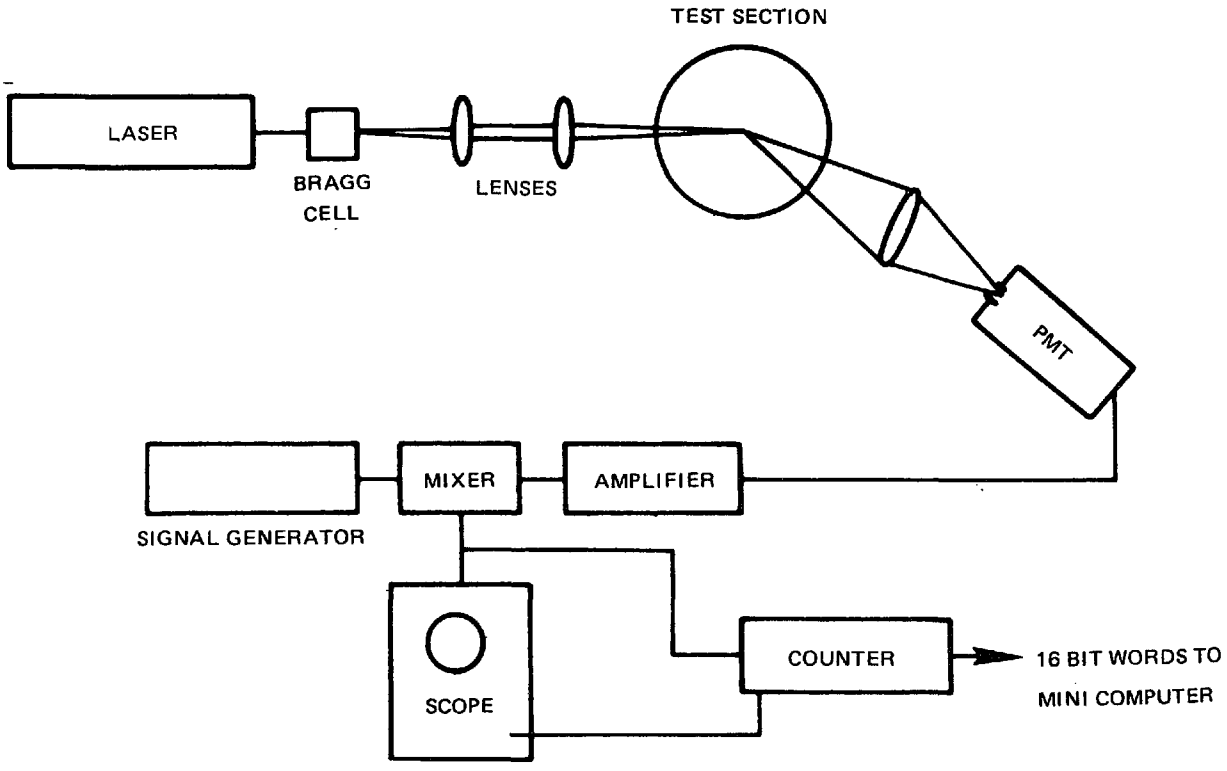

SCHEMATIC DIAGRAM OF THE LASER VELOCIMETER DATA PROCESSING EQUIPMENT

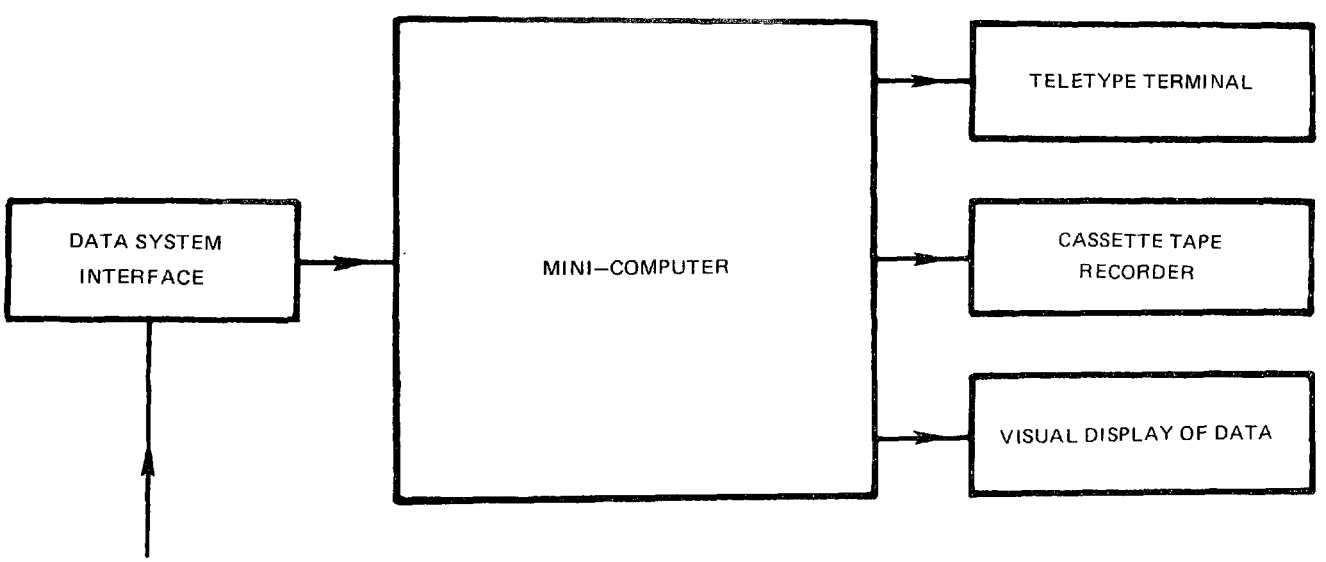

in Fig. A-21. A limited number of measurements of droplet velocity were made using a frequency-tracker. These measurements were limited to those regions of the burning spray where valid data rates were in excess of 20,000/sec.

The optical sensitivity of the forward scatter system used in the present study was such that naturally occurring submicron particles could be used for the gas velocity determinations in regions far from the fuel spray. However, to increase the signal to noise ratio and thus, increase the data acquisition rate in these regions, the air flow was seeded with micron sized particles dispensed from a fluidized bed. Since for these flows more than 95 percent of the turbulence energy is likely to be in scales corresponding to Eulerian frequencies below 25 kHz (turbulence scales less than 1/10 of the combustor dia), errors due to particle response (in the Lagrangian frame) should be negligible (Ref. 10). To determine gas velocity in regions of moderate fuel droplet concentration the air flow was selectively seeded as discussed later.

To avoid problems associated with directional ambiguity (which can result in data interpretation errors in highly turbulent and/or recirculating flows) (Ref. 18), zero velocity frequency offset was achieved by combining the primary and modulated beams at the detection volume where they generated moving fringes so that a stationary particle produced a Doppler frequency, f_o. Thus, in the flow field, moving particles generated Doppler frequencies of $f_o \pm f_D$ depending on their velocities normal to the moving fringes. Hence, the sign as well as the magnitude of the instantaneous velocities could be determined as follows:

$$U = \frac{(f_D - f_o)\lambda}{2\sin\theta/2} \tag{A-4}$$

where λ is the wavelength of the laser light and θ is the angle between the incident laser beams.

However, in the case of fuel droplet velocity studies there is another reason to use a moving fringe laser velocimeter system. Consider first a stationary fringe system where the peak to peak fringe spacing, d, is

$$d = \frac{\lambda}{2\sin\theta/2} \simeq \frac{\lambda}{\theta} \tag{A-5}$$

when θ is small.

Since the $(1/e^2)$ diameter of the focal region is given by

$$2b_o = \frac{4}{\pi}\lambda\frac{f}{2b} \tag{A-6}$$

where f is the focal length of the lens and 2b is the beam diameter at the focusing lens. The number of fringes contained within the probe volume is, therefore, given by

$$N = \frac{4}{\pi} \frac{D}{2b} \tag{A-7}$$

where D is the beam spacing at the focusing lens. Thus, the maximum number of fringes is independent of the focal length of the focusing lens and is determined solely by the ratio of input beam spacing to diameter ratio. Increasing the number of fringes will increase the accuracy of the velocity measurements by providing a greater number of signal cycles from which the average value may be determined. Since most commercial counting devices require a minimum of eight cycles this provides a lower fringe number limit. Unfortunately, most practical liquid fuel sprays have a size distribution over a wide range (up to 250 μm) with typical mean droplet sizes between 75 and 150 μm. So this minimum fringe number requirement may raise a problem of spatial resolution associated with stationary fringe systems, since optimum signal/noise requirements dictate that the fringe spacing should be greater than or equal to the maximum fuel droplet diameter. Thus, for 250 μm droplets, the focal volume diameter would be approximately 2 mm. Even with off-axis light collection the probe volume dimension limiting spatial resolution (i.e., $2b_o/\sin\theta/2$), which typically is an order of magnitude greater than the focal volume diameter ($\sim$ 2 cm), would render the spatial resolution of most optical systems open to question.

Fortunately, frequency biasing increases the number of effective fringes in the focal volume and hence, the number of cycles of useful information. Again, the fringe spacing is given by Eq. (A-5) but now the fringes are propagating with a velocity U_o given by

$$U_o = f_o d \tag{A-8}$$

thus, the actual number seen by a droplet is

$$N_s = N\left[f_o/f_D \pm 1\right] \tag{A-9}$$

In the present system $N_S \leq 45N$ so that sufficient fringe crossings can be achieved with adequate spatial resolution.

In the experiments using iso-octane, measurements were made using the green line (λ = 514.5 nm) from the laser. Because of the intense luminosity from the

No. 2 fuel oil flames, an improved signal-to-noise ratio could be obtained using the blue line (λ = 488.0 nm). However, a limited number of measurements on No. 2 fuel oil flames were made using the green line to verify the velocity data.

Laser Velocimeter Statistical Errors and Particle Dynamics

Statistical confidence levels within stated error limits in the determination of both the mean and variance of any quantity with a Gaussian probability variation may be defined according to Ref. 19 as

$$\text{Error} = P\left(|\bar{x} - \beta| < K\gamma \frac{S_x}{\sqrt{N}}\right) = \gamma_m \tag{A-10}$$

$$\text{Error} = P\left(|S_x^2 - \sigma^2| < K\gamma \sigma^2 \frac{\sqrt{2}}{N-1}\right) = \gamma_T \tag{A-11}$$

where x is a random variable; N is the number of samples;

$$\bar{x} = \frac{1}{N}\left(\sum_{i=1}^{N} x_i\right) = \text{calculated mean} \tag{A-12}$$

$$S_x^2 = \frac{1}{N}\left[\sum_{i=1}^{N} (x_i - \bar{x})^2\right] = \text{calculated variance} \tag{A-13}$$

β is the true mean and σ^2 is the true variance.

For the particular case of the laser velocimeter measurements let us replace the random variable, x, by the measured Doppler frequency (f_D). Then the confidence level for the mean velocity determinations may be written

$$\frac{|f_D - \beta_D|}{\bar{f}_D} < K\gamma \frac{S_f}{\bar{f}_D} \frac{1}{\sqrt{N}} = \gamma_m \tag{A-14}$$

since

$$\frac{S_f}{f_D} = \frac{\sqrt{\frac{1}{N}\left[\sum_{i=1}^{N}\left(f_i - \bar{f}_D\right)^2\right]}}{\bar{f}_D} \approx \frac{\sigma\mu}{\bar{U}} \qquad \text{(A-15)}$$

we see that

$$\frac{\left|\bar{f}_D - \beta_D\right|}{\bar{f}_D} < K_\gamma \left(\frac{\sigma\mu}{\bar{U}}\right)\frac{1}{\sqrt{N}} \qquad \text{(A-16)}$$

The confidence level for the standard deviation may be written as

$$\frac{\left|S_f^2 - \sigma_f^2\right|}{\sigma_f^2} \approx \frac{2\left|S_f - \sigma_f\right|}{\sigma_f} < K_\gamma \sqrt{\frac{2}{N-1}} = \gamma_T \qquad \text{(A-17)}$$

Now since s_f and f_D are functions of the same random variable (f_D), the error in $\sigma_u\sqrt{U}$ is the sum, not the square root of the sum of the squares of each error, i.e., the confidence level in $\sigma_u\sqrt{U} = \gamma_M + \gamma_T$.

For normal distribution functions, confidence levels may be calculated using the following table:

γ	0.5	0.68	0.9	0.95	0.98	0.99
K_γ	0.675	1.00	1.6	1.96	2.33	2.57

For example, if at a particular location, the local turbulence level was 1 percent and 100 instantaneous velocities were measured, 50 percent of the mean measurements would be in error by less than 0.0675 percent of the true value. Whereas only 1 point in a hundred would be in error by more than 0.257 percent.

For a spherical particle of diameter D_p suspended in a sinusoidally vibrated column of air and acted on by Stokes drag, the ratio of particle velocity to gas velocity can be expressed as (Ref. 20):

$$\frac{u_p}{u} = \left[1 + \left(\frac{2\pi f}{a}\right)^2\right]^{-1/2} \tag{A-18}$$

where

$$a = \frac{18\mu}{\rho_p D_p^2}\left(1 + \frac{K\ell}{D_p}\right)^{-1} \tag{A-19}$$

where u_p and u are the rms velocities of the particle and the gas ρ_p is the particle density, f is the vibration frequency, ℓ is the molecular mean free path of the gas and K is the Cunningham constant ($\approx$ 1.8 for air). Thus, a 5 μm phenolic resin microballoon in air at ambient conditions will follow velocity fluctuations up to 10 kHz within 10 percent. Power spectral density measurements in the shear layer of nonreacting jets (Ref. 20) indicate that for the reacting flows investigated in the present study more than 95 percent of the turbulence energy will be associated with Eulerian frequencies below 25 kHz. Hence, the scale of the smallest energy containing eddy will be on the order of

$$\lambda = u/f \approx 100\,\text{m/sec}/25\,\text{kHz} = 4\times10^{-3}\,\text{m} \tag{A-20}$$

In the Lagrangian frame, this scale corresponds to the frequency on the order of

$$f = (U - U_c)/\lambda \approx 20\,\text{m/sec}/4\times10^{-3}\,\text{m} = 5\,\text{kHz} \tag{A-21}$$

so that errors due to particle response should be negligible.

APPENDIX B

PHASE-DISCRIMINATING PROBE TEST PROCEDURES

Hydrocarbon Data

For each mapping test condition, a series of measurements was made by traversing the phase-discriminating sampling probe at various axial locations to obtain percent carbon as a function of radial distance. Before and after each test the calibration of the hydrocarbon analyzer was checked by using three different calibration gas compositions (100 percent, 4.5 percent and 0.09 percent methane). After the combustor airflow conditions were established, the probe was traversed to the desired radial position and the sampling line valves opened. Isokinetic conditions were established in the total sample line at the probe tip by adjusting the total sample flow rate to match the probe and combustor static pressures. The vapor-sample mass flux was set to between 10 and 20 percent of the total sample mass flux, and the suction flow rate was set to between 30 and 60 percent of the total-sample mass flux. The background level of hydrocarbons in the combustor flow was then measured to insure that no hydrocarbon contaminants were present. Combustor fuel flow was initiated, the flow was ignited, and steady state conditions were established within the combustor. Sample line flow rates were readjusted and the attenuation levels on the electrometer were adjusted to give reasonable concentration peak heights on the chart recorder. For most tests, two measurements of the hydrocarbon content of the total sample and two measurements of the vapor sample were obtained at each probe condition.

For each of the flow field mapping tests, see Table B-1, the phase discriminating probe was positioned at window port locations 3 through 6. The axial location of the probe tip at these four positions is given in Table B-1. For each sample, values of the integral of percent carbon versus time were obtained from the mechanical integrator output. This information was combined with the hydrocarbon analyzer calibration curve to obtain the local value of percent carbon. Tabulations of the experimental data are presented in Appendix H. The tables indicate the combustor test conditions and present data on the percent carbon in the total and in the vapor samples at various probe psotions.

To assist in interpretation of the experimental results, the data were reduced to isopleth form. To accomplish this, plots of percent carbon as a function of radial position were generated for each of the four axial positions (e.g., Fig. B-1), and data crossplotted to obtain the isopleths.

TABLE B–1: PHASE–DISCRIMINATING PROBE TEST MATRIX

TEST	FUEL	PRESSURE ATM	SWIRL	TEMP °K	AXIAL WINDOW 3	4	5	6
1	ISO–OCTANE	1	0.3	533	X	X	X	X
4	ISO–OCTANE	3.3	0.3	533				
5	ISO–OCTANE	1	0.6	533	X	X	X	X
6	NO. 2 FUEL OIL	1	0.3	533	X	X	X	X
8	NO. 2 FUEL OIL	1	0.3	755	X	X	X	X
11	PROPANE	1	0.3	533	X	X	X	X

PHASE–DISCRIMINATING PROBE TIP POSITION

$\phi = 0.65$

WINDOW	PROBE TIP LOCATION,* X(cm)	X/D
3	14.83	1.21
4	31.83	2.60
5	48.82	3.99
6	65.81	5.38

*FUEL INJECTOR TIP IS AT X = 0
D = 12.23 CM

76–06–145–1

FIG. B–1

TYPICAL RADIAL PROFILES OF PERCENT CARBON

ISO–OCTANE
TEMP = 533 °K
PRESS = 1.0 ATM
S = 0.3

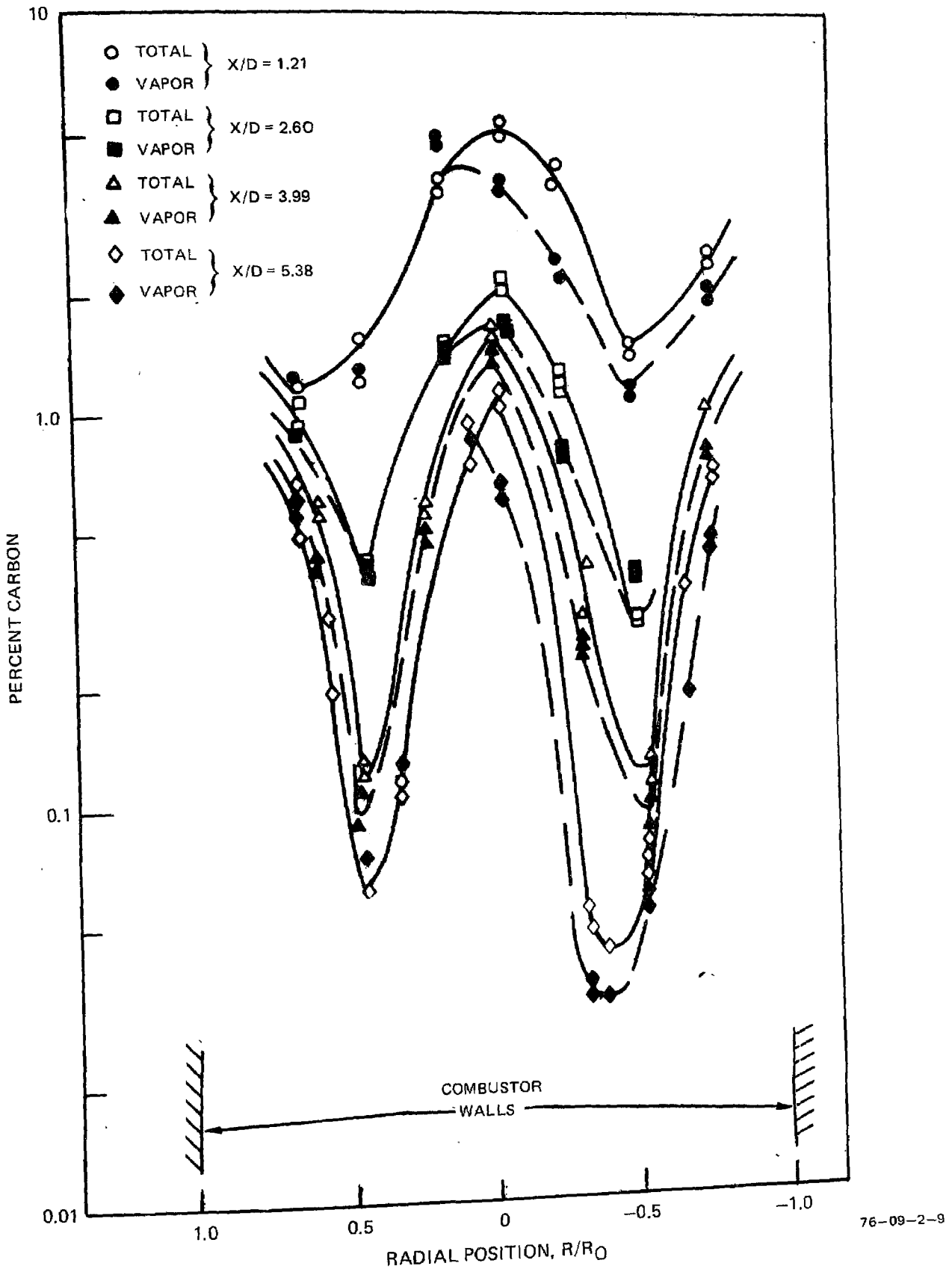

APPENDIX C

LASER VELOCIMETRY TEST PROCEDURES

The use of LDV in liquid-fuel combustor experiments presents unique problems because of the presence of the fuel droplets. The basic mechanism for LDV techniques is scattering of incident laser light by particles. If motion of the spray were the only phenomenon of interest, the potential problems would be limited to the effects of particles outside of the measuring volume on the signals. These effects (opaqueness, background luminosity, beam wander and divergence) were not apparent. Thorough investigation of combustor flows, however, requires knowledge of the gas velocities as well. To obtain such information, the air supply was seeded with particles. Two methods of data analysis were used to distinguish between gas and spray velocities. In regions where the spray droplet density was relatively low, testing with and without seeding in the air supply allowed the two velocities to be separated. In regions of high droplet density, a method based on relative signal (or visibility) was employed. Selective seeding of the air supply was used in regions of the flow where the gas and fuel droplet velocities were substantially different so that characteristic bi-modal velocity probability density functions were apparent, as illustrated in Fig. C-1. With seeding, the probability density function at $R/R_o = 0.75$ is heavily weighted toward the local gas velocity since the seen particle number density is much larger than the number of fuel droplets in this region. The situation is reversed as the point of measurement approaches the mean droplet spray trajectory ($R/R_o = 0.63$). The method used to separate the two mode velocities is illustrated in Fig. C-2, where probability densities obtained with and without airstream seeding are presented. Without seeding, the fuel droplet velocity distribution is determined directly since the natural particle data rate is small. This distribution is normalized by the total number of velocity determinations and then subtracted from the bi-modal distribution obtained at the same location with air seeding. The result represents the local gas velocity distribution from which the mean velocity and the variance can be determined.

Typical mean axial velocity profiles obtained with and without seeding are presented in Figs. C-3, C-4, and C-5. Close to the injector (X/D = 0.164) large differences between local fuel droplet and gas velocities occur and there is evidence of gas flow recirculation which is indicated by significant numbers of negative seed particle velocity occurrences close to the half radius locations. At X/D = -.409 there is agreement between velocity measurements obtained with and without seeding which could be interpreted to mean that, except in the wall region, the fuel droplets are following the local gas flow. However, away from the wall the velocity data acquisition rates showed no significant changes when seed particles were introduced; thus, it was apparent that fuel droplets were dominating

AXIAL VELOCITY PROBABILITY DENSITY FUNCTIONS WITH SEEDING

ISO–OCTANE/AIR
SWIRL = 0.6
1 ATM

$T_{AIR} = 533^{o}K$
$\phi = 0.65$
X/D = 0.164

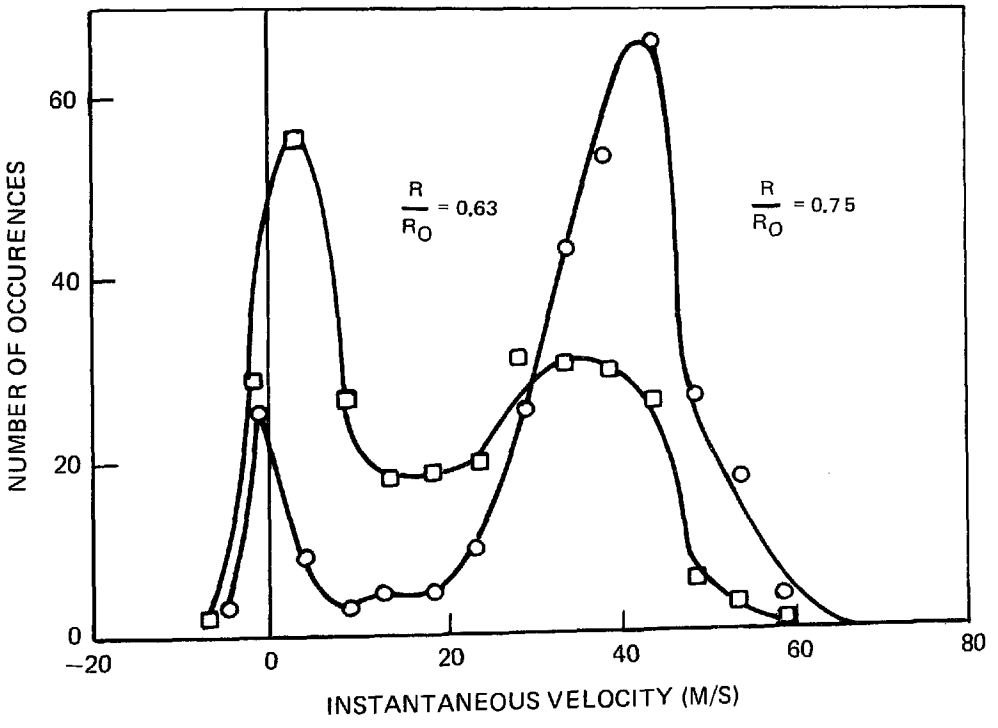

76–10–29–12

AXIAL VELOCITY PROBABILITY DENSITY FUNCTIONS WITH AND WITHOUT SEEDING

ISO–OCTANE/AIR
SWIRL = 0.6
1 ATM

$T_{AIR} = 533^{o}K$
$\phi = 0.65$
X/D = 0.164

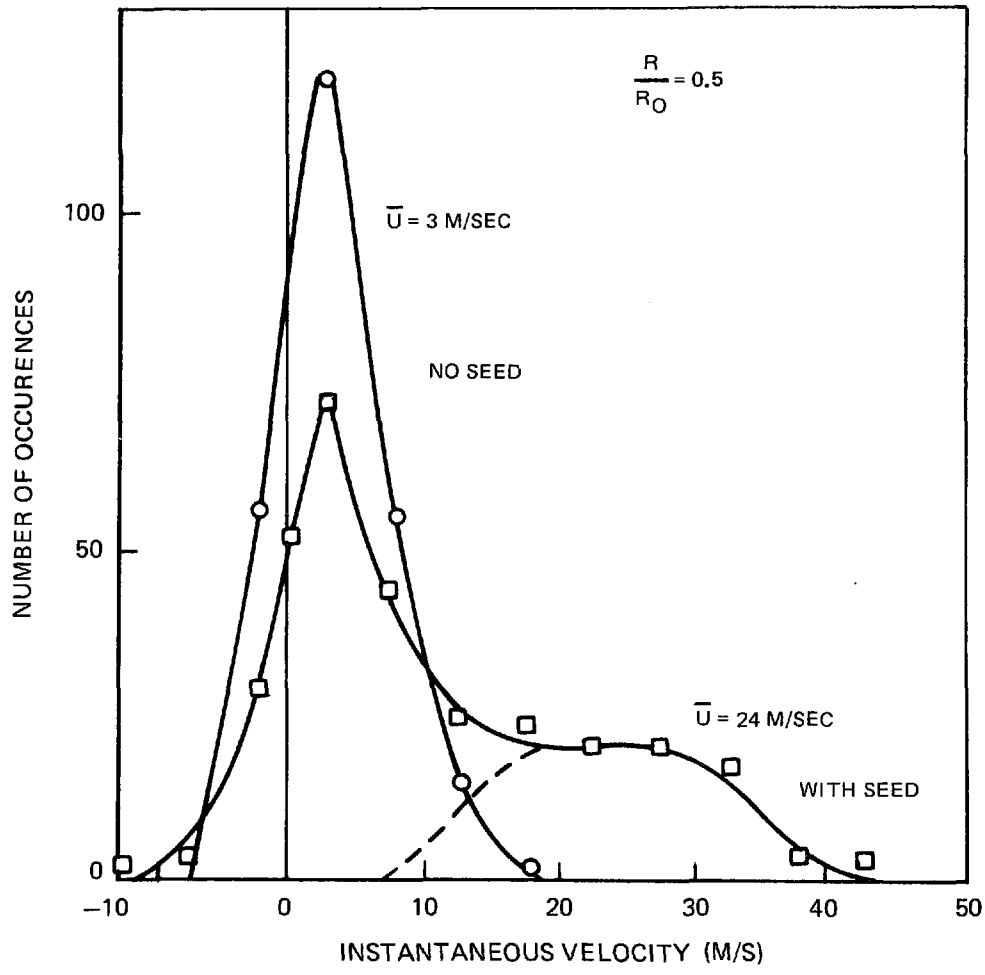

76–10–29–1

MEAN AXIAL VELOCITY PROFILE

ISO–OCTANE/AIR
SWIRL=0.3
1 ATM

$T_{AIR} = 533^{o}K$
$\phi = 0.65$
X/D = 0.164

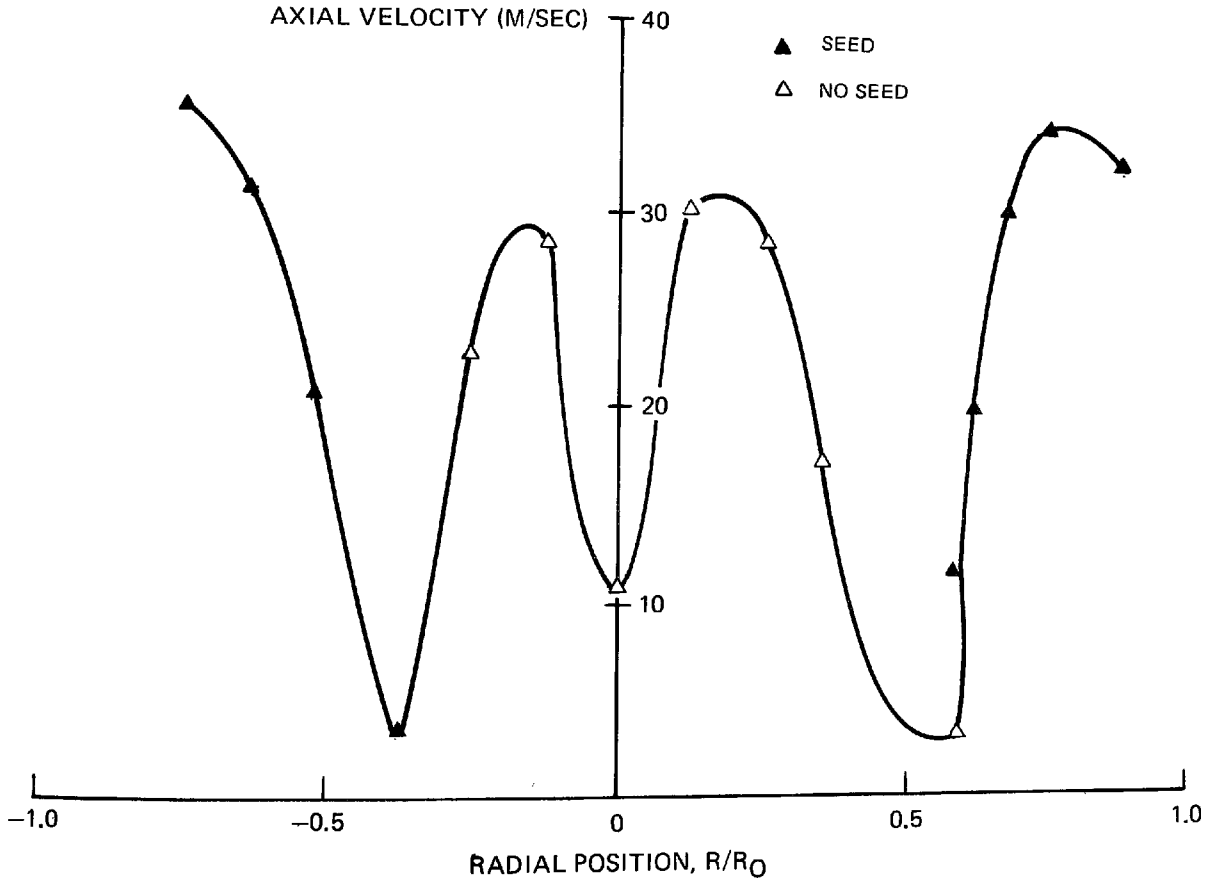

76–10–29–5

MEAN AXIAL VELOCITY PROFILE

ISO–OCTANE/AIR	$T_{AIR} = 533^{o}$ K
SWIRL = 0.3	$\phi = 0.65$
1 ATM	X/D = 0.409

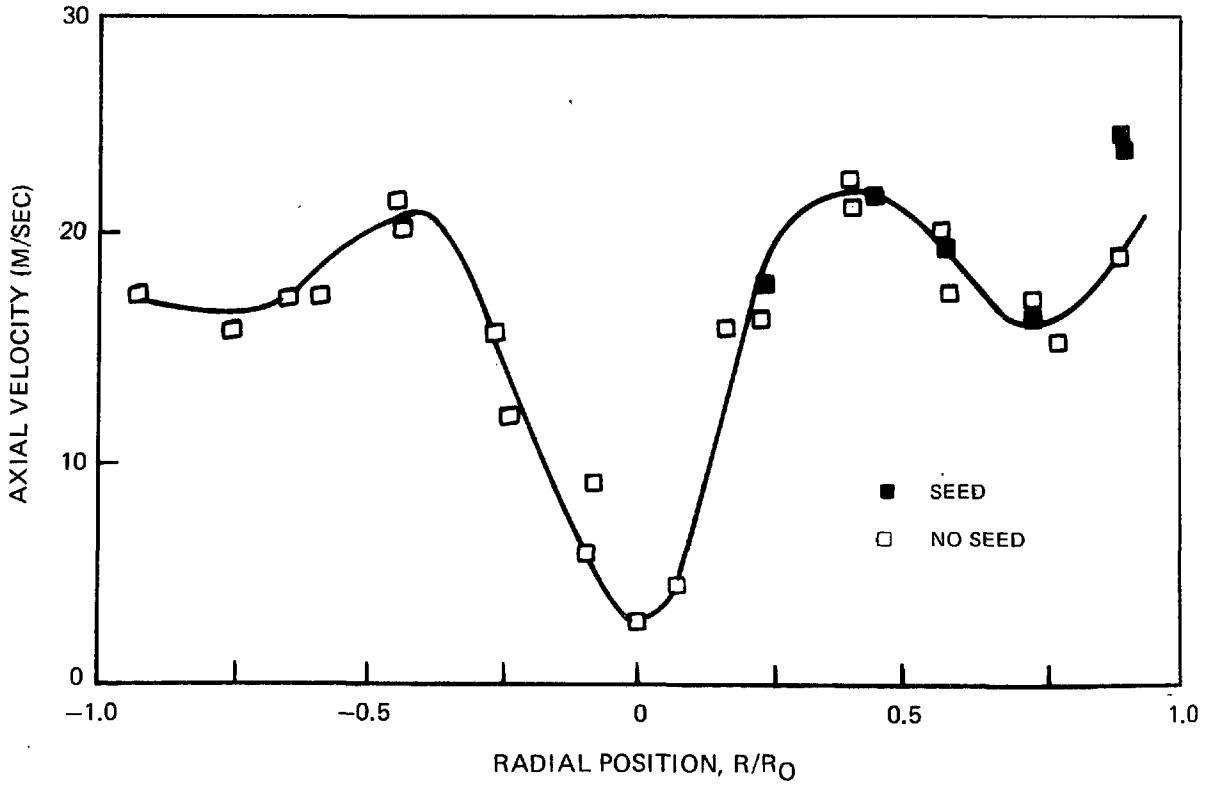

76–10–29–7

MEAN AXIAL VELOCITY PROFILE

ISO–OCTANE/AIR
SWIRL = 0.3
1 ATM

$T_{AIR} = 533^{o}K$
$\phi = 0.65$
X/D = 1.64

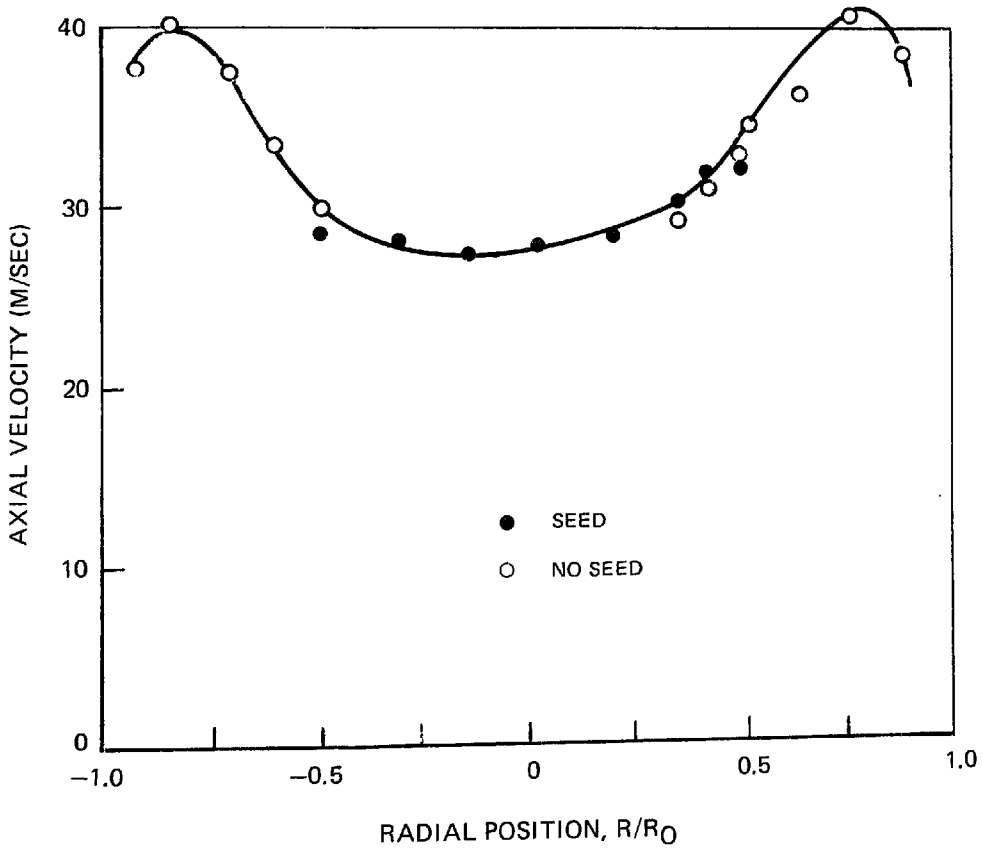

76–20–29–6

the velocity probability density distributions at this location. Except in the region close to the wall where a sufficiently high seed particle/fuel droplet number density ratio could be achieved, there was no evidence of bi-modal distributions and therefore gas velocity data could not be extracted. Farther downstream (X/D = 1.64) droplet concentrations are sufficiently reduced by evaporation and combustion so that the addition of seed material can once again influence the data acquisition rate. Thus, the agreement between the seeded and unseeded velocity measurements at this location shows that the fuel droplet and/or particulate combustion products are convected with the local gas velocity.

In regions of high droplet number density (X/D = 0.409 for example) an alternate method which utilizes particle visibility variations can be employed to infer local gas velocity. The visibility of the photomultiplier output signal which is a measure of the relative amount of oscillation in the signal, is defined for the current application as

$$V = \frac{I_{max} - I_{min}}{I_{max} + I_{min}} \qquad \text{(C-1)}$$

where I_{max} and I_{min} are the collected scattered intensities when a particle is centered in a bright and dark fringe, respectively.

The visibility is dependent on several factors: incident laser power, measuring volume dimensions, location within measuring volume of the particle, and electronics conversion factors. Incident laser power was monitored on the laser power supply and held constant. Fixing the incident and receiving optics for the entire test, the measuring volume dimensions were held constant, subject to beam wander due to temperature and spray effects on local index of refraction. This latter effect was deemed small, principally because of no noticable dropout which would occur if the volume produced by the incident beams did not coincide with the collecting volume. This is not a completely satisfactory argument, however, since the incident volume was necessarily large because of the small included angle between the incident beams. It is conceivable that the receiving volume could move relative to the incident volume producing apparent signal variations while maintaining essentially continuous signal output. The location within the measuring volume (defined by the overlap of the incident and receiving volumes) determines the incident power level since the Guassian intensity distribution of the incident beams results in an intensity distribution within the volume. This problem can be minimized by controlling the offset frequency. Careful selection of the value can limit the fraction of the incident volume over which the residence time of particles within the volume is sufficient to permit the counter processors to validate the data. Again, the relatively small included angle between the beams limits the effectiveness of this procedure. The electronics conversion factors convert a scattered light intensity to a signal voltage. Within the test period for the current effort, variations in these factors were negligible.

The use of the visibility, subject to the restrictions of the previous paragraph, is dependent upon the interaction of particles and gas in the following manner. For particles in an airstream, the velocity lag of the particle relative to the gas is a function of the drag on the particle. For simple models, the velocity lag is a function of the square of the particle diameter. For a limited range of particles, assumed spherical, the signal level or visibility can be considered linear with particle size. (Acutal Mie scattering is much more complicated.) The result is a dependence of velocity lag on the square of the visibility defined by Eq. C-1. An example is shown in Fig. C-6, where extrapolation to zero visibility coincides with the gas velocity (anticipated in this instance by the secondary peak noted on the histogram shown schematically). Visibility variations were achieved by altering the trigger level necessary for a signal from a particle to be input to the processor. Thus it is often possible to distinguish between spray and gas velocities in this manner.

Careful consideration should be given, however, to the various limitations and assumptions necessary for the procedure. For example, well inside the fuel spray, the variation of velocity with particle size was found to be the opposite of that for Fig. C-6. It is possible that this apparent lower gas velocity compared to the spray velocity is indicative of a gas recirculation region which has little influence on the spray with its relatively higher momentum. It is also possble that the mechanism is not applicable for this case. If the particle momentum is such that the spray droplets are not carried by the gas flow (with a velocity lag due to particle drag) but rather interact in some more complicated manner, the general dependence of velocity on visibility may change over the range tested.

In conclusion, therefore, the use of visibility as defined within this report, provides additional information subject to several restrictions and assumptions. The general application of the method would require more detailed attention to these procedural limitations; but in principle, the potential exists to not only extract local gas velocity but possibly also relative particle size distributions. This ultimate effect of the limitations on the accuracy of the results is unknown based on work to date.

A new method was used to determine droplet spray trajectory on the present work which provides a relatively simple and convenient means of trajectory documentation. The technique, which involves droplet velocity number density measurements, is illustrated in Fig. C-7 which shows the velocity data rate variation across the combustor at X/D = 0.164. The two peaks define the time-averaged hollow cone spray location. Measurements at a series of axial stations can then be used to determine the time-averaged spray trajectory.

The overall root-mean-square turbulent velocity measurement techniques applied in the program represent the simplest characterization of combustor turbulent flow field. Such measurements are therefore limited in the extent to which they may be used to obtain physical insight into the mixing process. Measurement of turbulent velocity length scales as a function of frequency and position would be desirable

INFLUENCE OF VISIBILITY ON MEASURED LOCAL MEAN VELOCITY

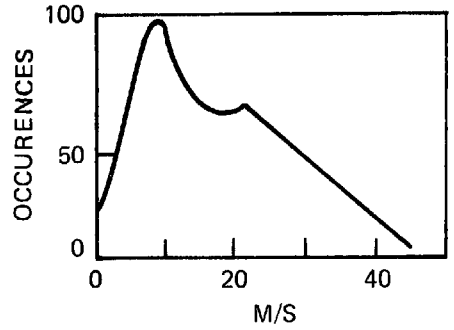

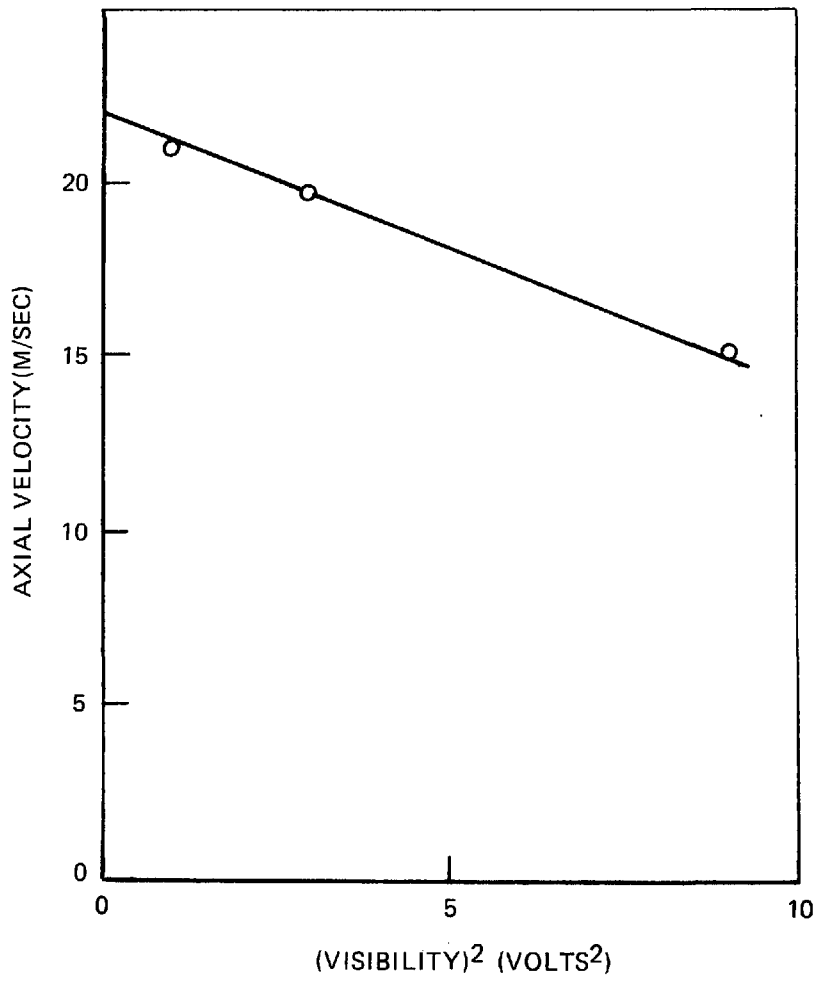

76-10-29-3

DROPLET NUMBER DENSITY PROFILE

ISO–OCTANE/AIR
SWIRL = 0.6
1 ATM

$T_{AIR} = 533^{o}K$
$\phi = 0.65$
X/D = 0.164

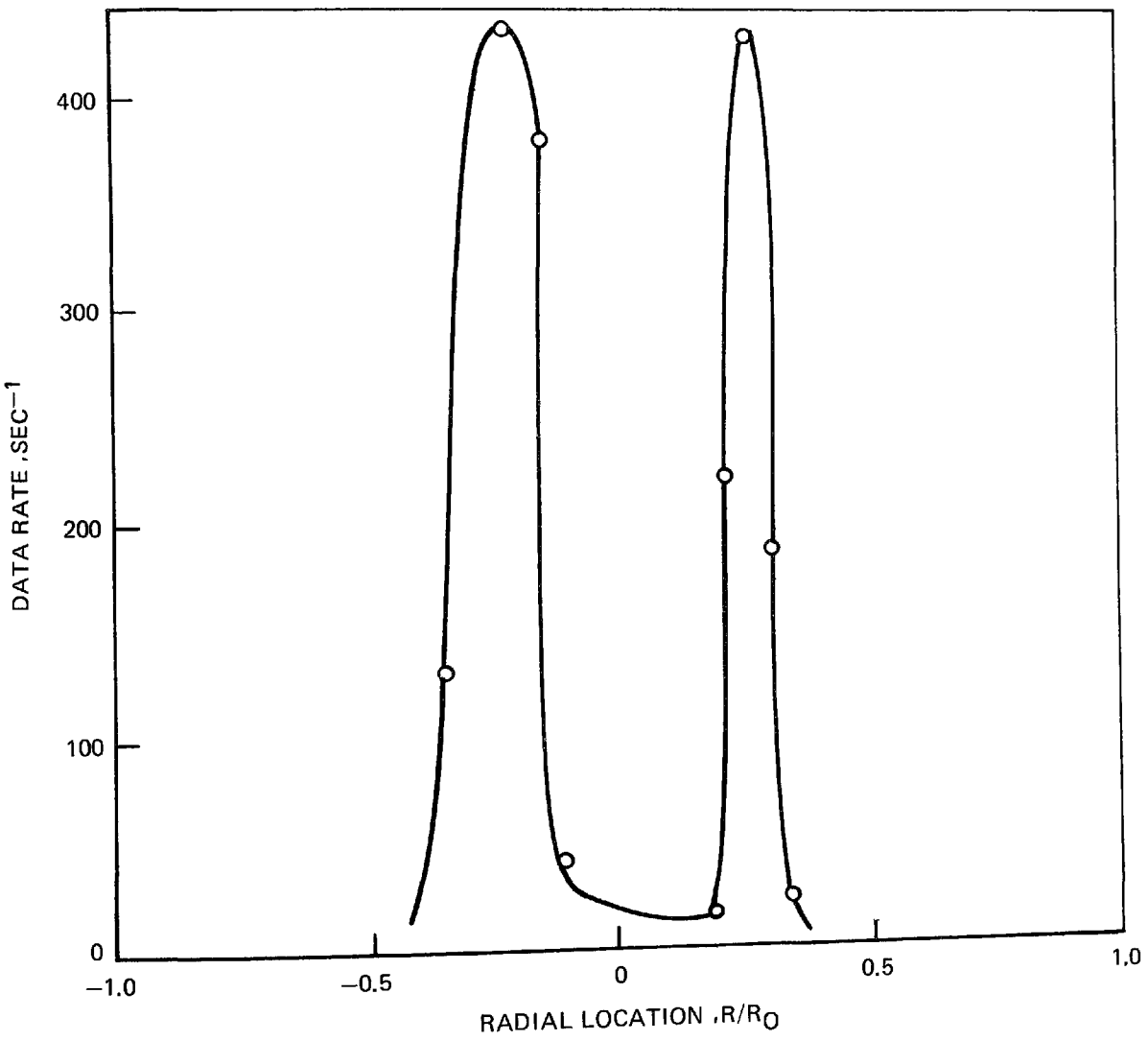

76–10–29–8

since they would assist in the understanding of the relative importance of varying length scales on the mixing process. For example, is the mixing process governed by the large eddy structure or do such eddies act as a gross transport mechanism with the mixing rate determined by small scale eddy interaction? In general, LV measurement of turbulent velocity cross-power spectral density, which would provide frequency dependent length scale information, does not appear practicable in combustor flows at this time. Two-point LV velocity correlations are possible, however, and these measurements would provide eddy convection velocity information and frequency integrated (overall) eddy length scales. From the behavior of the cross-correlation function sin space and time (i.e., zero time delay amplitude verses separation distance and amplitude versus delay time at fixed separation distance) it may be possible to obtain information concerning the various length scales and their associated convection velocities. Such two-point measurements are to be preferred to single point correlations (auto correlations) for which Taylor's hypothesis ("frozen-flow" assumption) must be invoked to infer length scales from Eulerian time scales. For the high turbulence levels encountered in a combustor, Taylor's hypothesis would be expected to be invalid.

Prior to performing such two-point LV correlations in a combusting flow, validation of the technique should be carried out in a cold flow simulation. In addition to establishing the ability to perform correlations when the data rate is insufficient to permit use of a tracker, such a simulation would provide correlation data of use in the planning of a combusting flow measurement program.

APPENDIX D

LASER HOLOGRAPHY TEST PROCEDURES

In the tests which employed the holographic system, the optical apparatus was aligned with the first window in the combustion rig so that the field of view included the region immediately downstream from the fuel injector, Fig. 1. A cylindrical ring containing calibration wire and having an internal diameter of 5 cm was installed in the window so that the unobstructed viewing area was defined by a 5-cm dia circle with a center located 4.2 cm downstream of the injector tip. Hence, the nozzle tip was outside the field-of-view.

During initial testing of the holographic system an interference filter, which was mounted adjacent to the quartz window in the test apparatus, failed due to overheating. To preclude further failures, the filter-holder was moved away from the window, cooling air was flowed over the surface of the filter, and the combustor was operated only for the time required to establish steady flow conditions.

To obtain the holographic data, the optical components were aligned and the magazine containing eight unexposed film plates was loaded. Airflow was initiated, the electric air heater was activated and the combustor was brought up to temperature as evidenced by a steady reading of the inlet air temperature. Fuel flow was initiated and a hologram was exposed to record the behavior of the spray in non-combusting flow. The duration of the fuel-on portion of this test was less than ten seconds. Holograms were not recorded during the first five seconds to insure that a steady fuel flow had been achieved prior to the recording of data. After fuel shut-off, hot air continued to flow for approximately one minute to purge the combustor of any accumulated fuel. The film magazine was advanced, fuel flow was initiated, the flow was ignited and after a period of approximately ten seconds a hologram was exposed to record the spray characteristics in combusting flow. The combustor was shut down and the interference filter was replaced with the gelatin filter and the test sequence repeated.

After development of the holographic plates, the reconstructed images of the holograms were examined and the better of the two holograms taken at each condition (one with the gelatin filter, one with the interference filter) was selected for detailed examination. The first step in the reconstruction process was alignment of the holographic plate relative to the incident reference beam. The tripod-mounted loupe was then placed so that the entire field-of-view could be examined by moving the rack-and-pinion traversing mechanisms. The surface coordinates of the hollow cone spray were determined by focusing on the far and near surfaces as illustrated in Fig. D-1. This technique was used rather than focusing on the upper and lower edges of the cone because those edges were generally outside the viewing area. The spray surface is, in fact, a diffuse layer of droplets of finite

METHOD USED TO ESTABLISH SPRAY SURFACE COORDINATES

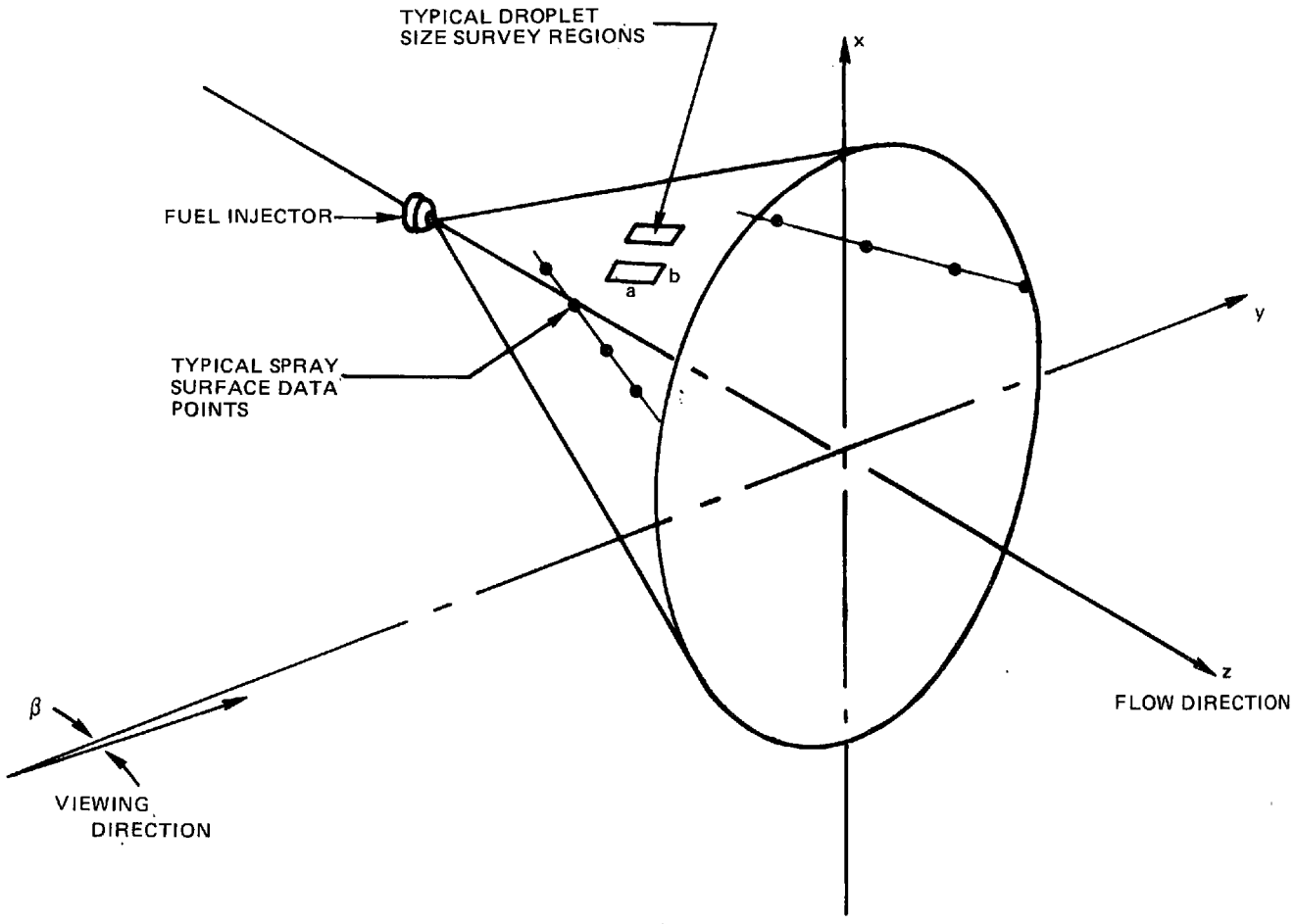

76–09–2–1

TYPICAL SPRAY COORDINATE DATA

ISO–OCTANE, NO COMBUSTION
T = 541 °K
S = 0.6
P = 1 ATM

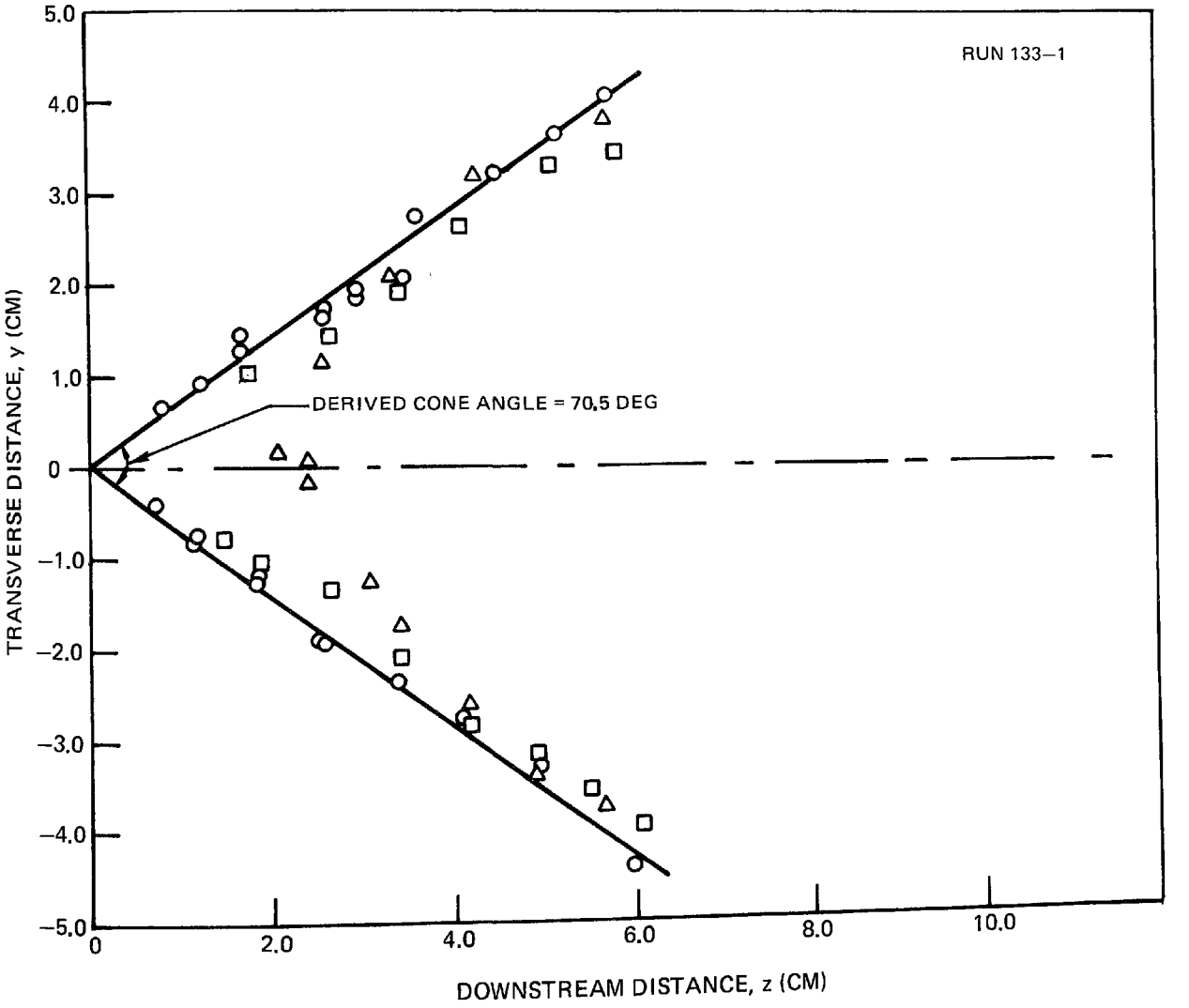

76–09–2–6

thickness; the "surface" coordinates recorded are the coordinates of the center of the region being viewed. The center was established by fixing the x and z coordinates and traversing along the y coordinate through the volume containing droplets. The image viewed was of a wave of droplets passing across the object field. The y coordinate was established by centering this wave in the object field.

Estimates of the mean droplet size in the spray were obtained by counting droplets of various diameters at several locations as shown in Fig. D-1. These regions were established at values of z in the range from 2.5 to 4.7 cm. The value of z could not be fixed at a specific value for all holograms because the location of the injector tip, which was not in the field of view, could only be estimated at the time of data acquisition. The volume of the individual regions examined for droplet size were defined by a 3.6 x 1.0 mm rectangle and a depth equal to the spray layer thickness. Typically, seven volumes were examined in each hologram.

Tabulated results giving the spray surface coordinates and the derived spray cone angle are presented in Appendix M. The spray coordinates given are for a transformed coordinate system in which the z axis lies along the centerline of the injector and the apex of the cone lies at the injector tip. The reported cone angle was obtained by determining the best fit between the data and the surface coordinate of a right circular cone by use of the regression analysis described in Appendix K. The estimated error in the derived cone angle was approximately 2 to 3 deg for most of the cases examined. A plot showing a typical distribution of data as projected on the y-z plane is shown in Fig. D-2. Data were not obtained in the x = 0 plane. The projected edges of the cone appear as boundaries for the data.

Measurements of the thickness of the spray cone and of the size of the observed droplets downstream of the injector tip also are given in Appendix M. The coordinates y_1 and y_2 represent the observed coordinates of the inner and outer edges of the spray on the side of the hollow-cone spray closest to the observer. The coordinate z gives the downstream distrance at which the measurements were obtained. Occasionally a droplet might be observed outside of these coordinates; however, it is estimated that over 90 percent of the observed droplets reside between y_1 and y_2 in any of the measurements. Because of the limited number of measurements made on spray thickness, the error in the spray thickness determined from the holograms is estimated to be approximately 30 percent. However, there is generally good agreement between the estimates of spray thickness obtained from the laser velocimeter data and the values obtained from the holograms. The droplet count tables give the number of droplets in a range of sizes from 2 mils to 10 mils in diameter. Conversion of the data into microns and application of the correction for the magnification caused by the fact that the holograms were reconstructed using a laser wavelength, different from the wavelength used to generate the hologram (by a factor of approximately 1.1) results in the numbers shown.

Droplet size could be measured with greater accuracy than required by the fineness of this classification schedule, however, a finer classification was not warranted for the study.

The Sauter mean diameter (SMD) generally is regarded as the appropriate diameter to be used to characterize a spray for use in analyses in which surface phenomena such as vaporization or combustion are of interest. The SMD is computed by the expression:

$$SMD = \frac{\sum_i n_i d_i^3}{\sum_i n_i d_i^2} \qquad \text{(D-1)}$$

where:

n_i - number of droplets of diameter d_i
d_i - droplet diameter

The SMD ranged from 100 to 150 microns for the holograms examined. In the table of reduced data, the quantity N-counted, which is determined by dividing the total mass of the counted droplets by the mass of the droplets having a diameter equal to the SMD is given. This quantity represents, on average, the number of droplets counted and is approximately 50 for most of the holograms examined. The quantity N-measured represents the number of droplets passing the plane per unit time at which the droplet measurements were made based on the number of droplets counted, the measured spray diameter, and an assumed value for the velocity of the droplets.

$$N\text{-measured} = N \text{ counted } x\frac{V}{b} \times \frac{\pi/4((D_S+t)^2 - (D_S-t)^2) \times b}{a \times b \times N_{block}} \qquad \text{(D-2)}$$

where:

D_S - Spray diameter
t - Spray thickness
a, b - Dimension of block
N_{block} - Number of blocks counted
V - Droplet velocity

The magnitude of the droplet velocity, V, was taken to be 19 m/sec, a value obtained from LDV measurements of the droplet velocity in an iso-octane spray at a location five centimeters downstream of the injector tip (Fig. C-4, Appendix C). The quantity N-calculated represents the number of droplets per unit time passing the plane as computed from the measured fuel flow and the derived mean droplet size;

$$N\text{ - calculated} = \frac{6 \times w_f}{\pi d_m^3 \rho} \qquad \text{(D-3)}$$

where

w_f - Fuel flow
ρ - Fuel density
d_m - Mean droplet diameter

In general it was found that the value of N-calculated was less than that of N-measured.

The value of the fuel flow rate as calculated from the measured droplet size, number density and velocity (as determined from the laser velocimeter measurements) was generally found to be one half the measured fuel flow rate. This discrepancy could arise from an under estimate of the mean droplet size, failure to account for the mass of the small droplets in the spray (which are not counted), the influence of vaporization or an under estimate of the velocity of the droplets. The fact that little change in the magnitude of the discrepancy occurred when changing from combusting to noncombusting flows suggests that the vaporization effects are not the cause. The laser velocimetry data indicates that it is unlikely that the spray velocity is significantly greater than the assumed value of 20 m/sec. For typical droplet size distributions obtained for pressure atomizing nozzles, droplets smaller than the SMD can account for as much as 20 percent of the mass flow; therefore, this factor could account for a portion of the discrepancy. Finally, because the cube of the SMD enters the calculations, an error of 17 percent in the droplet sizing measurements could result in the observed difference. It is probable that the latter two factors were major contributors to the observed difference.

Several observations of general interest were made during examination of the reconstructed holograms. First, no direct evidence of combustion could be observed in any of the holograms; i.e., there was no change in resolution or evidence of index of refraction gradients for the cases for which combustion was occurring. During testing, there was a large amount of radiation emitted from the gases in the region being examined by the holographic system, therefore combustion gases were certainly present in this region, at least on the time average.

The quality of the holograms was more or less independent of the type of filter used to block visible radiation from the combustor. It did not appear that the superior ability of the interference filter to block transmission of the combustion-generated radiation had a beneficial effect on hologram resolution, nor did the optical qualities of the filters appear to affect resolution (as determined from the noncumbusting flow cases). In each of the sprays, there were a few large droplets having diameters approximately 5 times the mean droplet

diameter, and the size of these droplets appeared to increase with distance from the injector. These observations suggest the occurrence of agglomeration of smaller droplets; however, there are insufficient data to substantiate this point.

APPENDIX E

TYPICAL PROPERTIES OF LIQUID FUELS

	Propane	Iso-Octane	No. 2 Oil
Specific gravity (@ 298 K)	-	0.70	0.85
H/C	2.67	2.25	1.75
Wgt. fraction N	0	0	$5\text{-}20 \times 10^{-6}$
Viscosity (CS @ 298 K)	-	0.8	5.3
Surface Tension (dynes/cm @ 298 K)	-	18	24
Initial Boiling Pt. (deg K)	231	373	454
End Boiling Pt. (deg K)	-	-	603
Specific Heat (Cal/gm K)	-	0.52	0.45
Heating Value (Cal/gm)	11064	10600	10570
Heat of Vaporization (Cal/gm)	102	65	153
Molecular Wgt.	44	114	195 (nominal)
Stoichiometric Ratio (by wgt.)	.064	.066	.069

APPENDIX F

COMBUSTOR HEAT BALANCE

A thermal balance was performed on the combustion system for a typical operating condition to evaluate the magnitude of the heat transferred to the combustor walls and to provide a check on the accuracy of the exhaust gas temperature measurements. The heat transferred from the system was determined from measurements of the flow-rate and the temperature rise of the cooling water. The results of the heat balance are summarized below:

Swirl No. = 0.3 — Iso-octane - Air

P = 1 atm — Equivalence Ratio = 0.65

$T_{air} = 533^{o}K$ — $\dot{m}_{air} = 0.137$ kg/sec

Q_{IN}

Air Heater	7.7 kg cal/sec	
Fuel:	61.9 kg cal/sec	69.6 kg cal/sec

Q_{OUT}

Combustion Products:	43.04 kg cal/sec	
Cooling Water:	17.90 kg cal/sec	
Unreacted Fuel:	0.72 kg ca/sec	61.6 kg cal/sec

$$\frac{Q_{IN} - Q_{OUT}}{Q_{IN}} = .115$$

APPENDIX G

TABULATED TEMPERATURE DATA

TABLE G-1. TEMPERATURE DISTRIBUTIONS - TEST NO. 1

Iso-Octane
$\Phi = 0.65 \pm .01$
Pressure = 1.0 atm

Inlet Air Swirl No. = 0.3
Inlet Air Temperature = $532 \pm 5^{\circ}$ K

R/R_o	Temperature, $^{\circ}$K					
	X/D=0.34	1.73	3.12	4.52	5.91	14.59
-0.88	--	1109	1334	1354	1265	--
-0.75	--	1431	1558	1557	1431	--
-0.67	--	--	--	--	--	1381
-0.62	--	1622	1718	1648	1582	1414
-0.50	--	1706	1830	1769	1708	1458
-0.37	--	1718	1864	1887	1815	1521
-0.25	--	1662	1779	1868	1761	1558
-0.12	--	1646	1754	1796	1721	1573
0.00	--	1690	1888	1910	1800	1550
0.13	--	1787	1870	1906	1847	1508
0.25	--	1701	1776	1809	1717	1459
0.38	--	1585	1608	1656	1587	1392
0.42	568	--	--	--	--	--
0.50	677	1347	1434	1535	1455	1327
0.58	692	--	--	--	--	--
0.63	--	1112	1233	1348	1310	1276
0.67	630	--	--	--	--	--
0.75	555	914	1056	1107	1134	1210
0.83	516	--	--	--	--	--
0.87	--	743	858	866	886	1105
0.92	476	--	--	--	--	--
1.00	411	466	434	426	458	540

TABLE G-2. TEMPERATURE DISTRIBUTIONS - TEST NO. 4

Iso-Octane
Φ = 0.65 ± .01
Pressure = 3.3 atm

Inlet Air Swirl No. = 0.3
Inlet Air Temperature = 529 ± 7° K

R/R_o	Temperature, °K				
	X/D=1.73	3.12	4.52	5.91	14.59
-0.89	1105	928	1197	753	--
-0.75	1449	1405	1453	1133	--
-0.68	--	--	--	--	1192
-0.62	1066	--	--	--	--
-0.50	--	--	--	1291	--
-0.45	--	--	--	--	1269
-0.37	836	876	888	--	--
-0.25	--	--	--	877	880
-0.12	771	810	860	787	--
-0.04	--	--	--	--	1107
0.00	702	786	1075	779	--
0.13	681	802	1180	1155	--
0.17	--	--	--	--	1296
0.25	690	1382	1395	1405	1234
0.38	1163	1636	1529	1584	1191
0.50	1214	1407	1405	1502	--
0.58	--	--	--	--	1095
0.63	1058	1055	1047	1270	--
0.75	725	857	810	990	--
0.79	--	--	--	--	983
0.87	613	769	713	774	--
1.00	582	678	641	660	638

TABLE G-4 TEMPERATURE DISTRIBUTIONS - TEST NO. 5

Iso-Octane
Φ = 0.65
Pressure = 1.0 atm

Inlet Air Swirl No. = 0.6
Inlet Air Temperature = 530 $\pm$ 50° K

R/R_o	Temperature, °K				
	X/D=1.73	3.12	4.52	5.91	14.59
-0.89	1488	1543	1168	1255	--
-0.75	1797	1908	1745	1679	--
-0.67	--	--	--	1809	--
-0.62	1766	1880	1858	1775	--
-0.58	--	--	--	1821	--
-0.50	1545	1678	1169	785	--
-0.37	1085	--	--	797	1046
-0.35	--	--	--	--	923
-0.25	1147	1122	1070	902	--
-0.18	--	--	--	--	1045
-0.12	1497	1476	1339	1101	--
0.00	1639	1610	1360	1241	1225
0.13	1724	1736	1605	1376	1597
0.25	1801	1869	1940	1832	--
0.31	--	--	--	--	1375
0.38	1747	1931	1898	1673	--
0.50	1478	1632	1479	1224	1225
0.63	1159	1256	1090	897	1129
0.75	941	893	564	718	--
0.81	--	--	--	--	1087
0.87	724	738	497	640	--
1.00	393	385	373	429	454

TABLE G-4. TEMPERATURE DISTRIBUTIONS - TEST NO. 6

No. 2 Oil
Φ = 0.67
Pressure = 1.0 atm

Inlet Air Swirl No. = 0.3
Inlet Air Temperature = 529 ± 6° K

R/R_o	Temperature, °K				
	X/D=1.73	3.12	4.52	5.91	14.59
-0.89	1088	1452	1546	1520	--
-0.75	1214	1523	1645	1611	--
-0.66	--	--	--	--	1439
-0.62	1343	1605	1711	1662	--
-0.50	1451	1684	1738	1719	1501
-0.37	1472	1726	1803	1771	--
-0.33	--	--	--	--	1538
-0.25	1447	1717	1764	1789	--
-0.17	--	--	--	--	1553
-0.12	1424	1669	1711	1763	--
0.00	1428	1720	1736	1764	1542
0.03	--	--	--	1711	--
0.13	1406	1723	1745	--	--
0.17	--	--	--	--	1486
0.25	1294	1639	1693	1654	--
0.33	--	--	--	--	1412
0.38	1195	1585	1653	1595	--
0.50	1081	1525	1579	1551	1347
0.63	1008	1466	1502	1489	--
0.67	--	--	--	--	1267
0.75	924	1400	1384	1410	--
0.83	--	--	--	--	1206
0.87	837	1290	1211	1276	--
1.00	623	685	739	762	496

TABLE G-5 . TEMPERATURE DISTRIBUTIONS - TEST NO. 8

No. 2 Oil
Φ = 0.67
Pressure = 1.0 atm

Inlet Air Swirl No. = 0.3
Inlet Air Temperature = 751 ± 40 K

R/R_o	Temperature, °K				
	X/D=1.73	3.12	4.52	5.91	14.59
-0.89	1440	1667	1649	1646	--
-0.75	1478	1797	1736	1693	--
-0.68	--	--	--	--	1489
-0.62	1524	1865	1819	1782	--
-0.50	1592	1918	1899	1890	1643
-0.37	1581	1918	1942	1925	--
-0.33	--	--	--	--	1721
-0.25	1559	1883	1863	1872	--
-0.16	--	--	--	--	1732
-0.12	1536	1842	1846	1876	--
0.00	1553	1903	1905	1879	1698
0.13	1550	1903	1926	1817	--
0.17	--	--	--	--	1594
0.25	1497	1857	1831	1716	--
0.33	--	--	--	--	1489
0.38	1421	1783	1752	1659	--
0.50	1364	1738	1671	1599	1383
0.63	1336	1639	1584	1553	--
0.67	--	--	--	--	1338
0.75	1341	1554	1455	1468	--
0.83	--	--	--	--	1235
0.87	1308	1417	1267	1303	--
1.00	1050	1048	687	695	613

TABLE G-6. TEMPERATURE DISTRIBUTIONS - TEST NO. 11

Propane
Φ = 0.65 ± .01
Pressure = 1.0 atm

Inlet Air Swirl No. = 0.3
Inlet Air Temperature = 536 ± 6° K

R/R_o	Temperature, °K				
	X/D=1.73	3.12	4.52	5.91	14.59
-0.88	334	1161	1024	868	--
-0.75	1195	1367	1392	1424	--
-0.68	--	--	--	--	1467
-0.62	1398	1030	1471	793	--
-0.50	1310	--	--	--	--
-0.45	--	996	865	759	1580
-0.37	1193	--	--	804	1658
-0.25	1127	1088	932	890	--
-0.16	--	--	--	--	1628
-0.12	1118	--	--	1019	--
-0.04	--	--	1084	--	--
0.00	1076	1265	--	1128	1696
0.13	1129	1387	--	1239	--
0.17	--	--	--	--	1691
0.25	1232	1561	1311	1545	--
0.33	--	--	--	--	1533
0.38	1379	1477	1491	1643	--
0.50	1324	1088	1529	1499	1396
0.63	997	720	989	1095	--
0.67	--	--	--	--	1260
0.75	677	554	570	693	--
0.83	--	--	--	--	1098
0.87	497	492	476	521	--
1.00	375	394	370	334	481

APPENDIX H

TABULATED PHASE-DISCRIMINATING PROBE DATA

TABLE H-1

PERCENT CARBON DISTRIBUTIONS AS DETERMINED BY
PHASE-DISCRIMINATING PROBE
TEST NO. 1

Iso-Octane

Φ = 0.65

Pressure = 1 atm

Inlet Swirl No. = 0.3

Inlet Air Temperature = 533°K

D = 12.23 cm

R_o = 6.17 cm

X/D = 1.21	Percent Carbon					
R/R_o	THC	VHC	THC	VHC	THC	VHC
.672	1.04	1.15	1.10	1.19	1.08	
.446	1.14	1.28	1.17	1.17	1.16	
.161	3.63	4.67	3.53	4.86		4.60
-.048	5.95	3.48	6.41	38.02	5.54	
-.257	3.93	2.15	3.58	2.34		
-.297	1.59	2.26	1.42	1.21		1.17
-.505	1.48	1.14	1.06	1.05	1.39	1.14
-.505	1.10					
-.795	2.16	1.89	2.48	1.94	2.27	
X/D = 2.60						
.673	.917	.868	.923	.860		
.457	.410	.388	.371	.387		
.148	1.36	1.47				
.141	1.50	1.44				
-.053	2.07	1.40	1.63	1.59	1.96	1.58
-.259	1.105	.740	1.24	.771	1.15	
-.508	.29	.39	.271	.369		

TABLE H-1 (Cont'd)

PERCENT CARBON DISTRIBUTIONS AS DETERMINED BY
PHASE-DISCRIMINATING PROBE

Iso-Octane

Φ = 0.65

Pressure = 1 atm

Inlet Swirl No. = 0.3

Inlet Air Temperature = 533°K

D = 12.23 cm

R_o = 6.17 cm

X/D = 3.99	Percent Carbon					
R/R_o	THC	VHC	THC	VHC	THC	VHC
.593	.564	.376	.54	.413	.528	.396
.475	.127	.106	.114	.0868		
.222	.537	.434	.553	.532		.513
-.023	1.5	1.31	1.44	1.32		
-.318	.296	.247	.382	.266		.235
-.550	.123	.0843	.0834	.103	.109	
-.785	.985	.670	1.02	.787		.766
X/D = 5.38						
.675	.471	.593		.556		.535
.572	.191		.292			
.454	.061	.0868	.0527	.0871		.0741
.336	.105	.129	.111			
.078	.722	.793	.862	.847		
-.026	1.08	.607	1.04	.658		
-.319	.0474	.0305	.0536	.0349		.034
-.360	.0405	.0317				
-.534	.0639	.0551	.07	.0596	.0762	
-.672	.342	.188	.349	.188		
-.779	.685	.462	.645	.447		

TABLE H-1 (Cont'd)

PERCENT CARBON DISTRIBUTIONS AS DETERMINED BY
PHASE-DISCRIMINATING PROBE

Iso-Octane

Φ = 0.65

Pressure = 1 atm

Inlet Swirl No. = 0.3

Inlet Air Temperature = 533°K

D = 12.23 cm

R_o = 6.17 cm

X/D = 5.38	Percent Carbon					
R/R_o	THC	VHC	THC	VHC	THC	VHC
.560	.013	.0155	.0077	.0275	.0187	.0235
.314	.013	.02	.0059	.014		
.04	.104	.056	.093	.058		
.021	.14	.086		.073		
.021	.113	.083	.11	.081	.16	.081
-.206	.36	.3	.36	.3		
-.599	2.25	1.2	1.58	1.25	1.81	

TABLE H-2

PERCENT CARBON DISTRIBUTIONS AS DETERMINED BY
PHASE-DISCRIMINATING PROBE
TEST NO. 5

Iso-Octane

Φ = 0.65

Pressure = 1 atm

Inlet Swirl No. = 0.6

Inlet Air Temperature = 533°K

D = 12.23 cm

R_o = 6.17 cm

X/D = 1.21	Percent Carbon					
R/R_o	THC	VHC	THC	VHC	THC	VHC
.671	.214	.063	.225	.059		.061
.617	.254	.155	.239	.135	.239	
.252	1.46	.455	5.49	.51		
-.287	.972	.097	.592			
-.614	.76	.566	.704	.51		
-.791	.373	.35	.376	.31		
X/D = 2.60						
.674	.204	.225		.236		.279
.674		.241				
.254	1.127	.45	1.06	.36		
.064	1.01	.326	.79	.344		.29
.064		.331				
-.238	.93	.247	1.01	.326		
-.470	.63	.335	.62	.362		
-.785	.67	.247		.344		.462

TABLE H-2 (Cont'd)

PERCENT CARBON DISTRIBUTION AS DETERMINED BY PHASE-DISCRIMINATING PROBE

Iso-Octane

Φ = 0.65

Pressure = 1 atm

Inlet Swirl No. = 0.6

Inlet Air Temperature = 533°K

D = 12.23 cm

R_o = 6.17 cm

X/D = 3.99	Percent Carbon					
R/R_o	THC	VHC	THC	VHC	THC	VHC
.564	.746	.421	.683	.429	.65	.405
.564		.396		.400		.405
.460	.62					
.323	.894	.797	.889	.822		
.050	.120	1.124	.718	1.02		
-.255	1.17	.858	1.13	.923		.997
-.5039		.204		.225		.454
-.5039	.437	.209		.196		
-.785	.986	1.44	1.41	1.44		.93
-.785		.97		1.06		
X/D = 5.38						
.669	.60	.60	.634	.634		
.363	.528	.53	.528	.528	.493	
.139	.613	.613	.669	.67		
.067	.775	.775	1.06	1.06		
-.026	1.197	1.20	1.13	1.1		
-.212	.915	.92	.986	.99		
-.299	.986	.98	.986	.98		
-.459						

TABLE H-3

PERCENT CARBON DISTRIBUTIONS AS DETERMINED BY
PHASE-DISCRIMINATING PROBE
TEST NO. 6

No. 2 Fuel Oil

Φ = 0.65

Pressure = 1 atm

Inlet Swirl No. = 0.3

Inlet Air Temperature = 533°K

D = 12.23 cm

R_o = 6.17 cm

X/D = 1.21	Percent Carbon					
R/R_o	THC	VHC	THC	VHC	THC	VHC
.673	.0809	.0396	.122	.0335		
.458	.36	.31	.307	.376		
.263	.67	.689	.808	.732	.748	
.168	1.36	.753	1.0	.739	1.18	.723
.040	1.79	1.68	1.89	1.5	1.54	1.60
-.155	1.68	1.48	1.84	1.33	1.65	
-.279	.895	.604	.781	.487	.774	
-.366	.918	.593	.827	.613	.749	
-.569	.542	.403	.478	.309		.340
-.786	.317	.274	.421	.282	.510	.322
-.786	.544					

TABLE H-3 (Cont'd)

PERCENT CARBON DISTRIBUTIONS AS DETERMINED BY
PHASE-DISCRIMINATING PROBE

No. 2 Fuel Oil

Φ = 0.65

Pressure = 1 atm

Inlet Swirl No. = 0.3

Inlet Air Temperature = 533°K

D = 12.23 cm

R_o = 6.17 cm

X/D = 2.60	Percent Carbon					
R/R_o	THC	VHC	THC	VHC	THC	VHC
.671	.288	.254	.38	.248	.39	.272
.671	.385					
.452	.185	.239	.148	.234	.191	.198
.452	.20	.254	.169			
.264	.313	.781	.293	.351		.426
.130	1.02	1.05	.87	1.12	.91	1.12
.130		1.05				
.056	1.31	1.48	1.37	1.29	1.25	1.32
-.045	1.59	1.43				
-.049	1.91	1.72	1.69	1.9		
-.158	1.08	1.29	1.08	1.25	1.12	1.16
-.158		1.26				
-.252	.512	.7	.512	.658	.523	.626
.252	.713	.596	.594	.582	.61	
-.582	.434	.348	.388	.322	.322	.298
-.766	.569	.405	.778	.521	.87	.585
-.766	.753	.537	.735	.534		

TABLE H-3 (Cont'd)

PERCENT CARBON DISTRIBUTIONS AS DETERMINED BY
PHASE-DISCRIMINATING PROBE

No. 2 Fuel Oil

Φ = 0.65

Pressure = 1 atm

Inlet Swirl No. = 0.3

Inlet Air Temperature = 533°K

D = 12.23 cm

R_o = 6.17 cm

X/D = 3.99	Percent Carbon					
R/R_o	THC	VHC	THC	VHC	THC	VHC
.666	.304	.0739	.118	.109	.195	.116
.425	.0713	.0361		.0462		
.246	.145	.137	.11	.126		
.242	.092	.13				
0		.115		.858		
-.004	.968	.902				
-.175	.487	.426	.42	.41		
-.425	.0593	.0536	.0241			
-.448	.0531					
-.571	.169	.136	.109	.156		
-.798	1.52	1.11	1.81	1.25	1.47	3.11
-.798	1.42	1.24				
X/D = 5.38						
.676	.214	.133	.293	.149	.243	.162
.449	.0821	.0858	.065	.072	.0646	
.322	.0154	.0292	.0118	.0253		
.088	.435	.363		.296		
.027		.352				
.010	.38	.598	.34	.666		.572
.010		.683				
-.149	.343	.249	.221	.211		
-.326	.0232	.0213	.0194	.0171		
-.548	.258	.0894	.182	.064	.154	.0515
-.788	.367	.127	.402	.144		

TABLE H-4

PERCENT CARBON DISTRIBUTIONS AS DETERMINED BY PHASE-DISCRIMINATING PROBE

Test No. 8

No. 2 Fuel Oil

Φ = 0.65

Pressure = 1 atm

Inlet Swirl No. = 0.3

Inlet Air Temperature = 755°K

D = 12.23 cm

R_o = 6.17 cm

X/D = 1.21	Percent Carbon					
R/R_o	THC	VHC	THC	VHC	THC	VHC
.675	.31	.281		.326		.323
.675		.333				
.464	.27	.257		.262		.32
.252	.817	.844	.784	.710	.637	.726
.252	.614					
.135	1.48	1.46	1.51			
.060	3.43	3.07	3.07	3.14	3.05	
-.055	3.14	3.08	3.10	2.92		
-.158	2.53	2.89	2.50	2.71		2.72
-.261	1.32	1.105	1.09	1.09		
-.373	.255	.158	.187	.174	.206	.166
-.373	.185					
-.460	.671	.356	.485	.323		
-.579	.119	.133	.12	.112	.169	
-.674	.946	.503	.771	.428		
-.787	1.44	.668	.987	.656	1.24	.669
-.787	1.406	.656	1.41			

TABLE H-4 (Cont'd)

PERCENT CARBON DISTRIBUTIONS AS DETERMINED BY
PHASE-DISCRIMINATING PROBE

No. 2 Fuel Oil

Φ = 0.65

Pressure = 1 atm

Inlet Swirl No. = 0.3

Inlet Air Temperature = 755°K

D = 12.23 cm

R_o = 6.17 cm

X/D = 2.60	Percent Carbon					
R/R_o	THC	VHC	THC	VHC	THC	VHC
.664	.312	.166	.313	.204		
.471	.061	.141	.0916	.139	.0787	.226
.471	.098					.158
.271	.137	.379	.133	.375		
.271		.265		.258		.218
.044	1.01	1.04	.98	1.1	1.08	
-.076	1.26	1.31				
-.082	1.15	1.25	1.11			
-.175	.896	.68	.895	.752	.88	.838
-.251	.41	.446	.463	.528	.46	.58
-.251	.447	.486				
-.388	.09	.183	.061	.156		
-.569	.218	.223	.199	.212		
-.783	.524	.268	.566	.344		.38

TABLE H-4 (Cont'd)

PERCENT CARBON DISTRIBUTIONS AS DETERMINED BY
PHASE-DISCRIMINATING PROBE

No. 2 Fuel Oil

Φ = 0.65

Pressure = 1 atm

Inlet Swirl No. = 0.3

Inlet Air Temperature = 755° K

D = 12.23 cm

R_o = 6.17 cm

X/D = 3.99

R/R_o	Percent Carbon					
	THC	VHC	THC	VHC	THC	VHC
.672	.0124	.0124	.0144	.0202	.0158	.0196
.466	.00298	.0035	.00266			
.211	.145	.137	.153	.128	.129	.120
.211		.117				
.028	.653	.639	.596	.523	.566	
-.062	.29	.273				
-.192	.235	.182		.184		
-.218	.235	.189				
-.232	.172	.21				
-.390	.0063	.00681	.00636	.00836	.00888	
-.390	.00675					
-.596	.00434	.0045	.00417	.00466		
-.794	.154	.103	.15	.115		

TABLE H-4 (Cont'd)

PERCENT CARBON DISTRIBUTIONS AS DETERMINED BY
PHASE-DISCRIMINATING PROBE

No. 2 Fuel Oil

Φ = 0.65

Pressure = 1 atm

Inlet Swirl No. = 0.3

Inlet Air Temperature = 733°K

D = 12.23 cm

R_o = 6.17 cm

X/D = 5.38

R/R_o	Percent Carbon					
	THC	VHC	THC	VHC	THC	VHC
.676	.00075	.00425		.00294		
.449	.00188	.00188				
.246	.00573	.014		.0128		
.213	.0063	.0132	.00883			
.113	.513	.401				
.033	.23	.355				
-.028	.23	.309		.273		
-.125	.358	.375		.278		
-.205	.102	.107		.065		
-.389	.00171	.00276	.00134	.00251		
-.574	.00349	.0048	.00243	.00593		.0057
-.786	.0264	.0384	.0232	.0470	.0235	.0484
-.786	.0186					

TABLE H-5

PERCENT CARBON DISTRIBUTIONS AS DETERMINED BY
PHASE-DISCRIMINATING PROBE
TEST NO. 11

Propane

Φ = 0.65

Pressure = 1 atm

Inlet Swirl No. = 0.3

Inlet Air Temperature = 533°K

D = 12.23 cm

R_o = 6.17 cm

X/D = 1.21	Percent Carbon					
R/R_o	THC	VHC	THC	VHC	THC	VHC
.674	.429	.144	3.61	.0387	.257	
.435	12.83	5.09	9.86	5.56		
.250	36.77	26.43	27.34	27.17	28.655	27.34
.150	40.55	34.42	41.32	31.17		
.057	35.51	32.89	37.36	33.16	36.55	32.62
-.362	35.19	32.57	31.03	28.74		
-.575	15.37	13.98	12.16	7.22		12.95
-.783	.268	.08	.118	.273	.0868	.118
X/D = 2.60						
.676	.133	.374	1.02	.280	.131	
.676	.123					
.635	.387	.57	.729	.68		
.580	2.81	1.57	1.66	2.49	1.38	
.456	8.32	5.08	8.11	7.64		7.97
.267	12.12	10.14	12.67	9.27		
.041	13.74	10.22	11.84	11.01		
-.166	15.21	12.67	15.96	12.12	15.37	
-.360	12.04	9.35	15.01	10.46		
-.462	11.13	7.93		7.95		
-.577	1.63	1.37	2.13	1.39		1.25
-.669	0.0	.0169	.0103	0.0		

TABLE H-5 (Cont'd)

PERCENT CARBON DISTRIBUTIONS AS DETERMINED BY
PHASE-DISCRIMINATING PROBE

Propane

Φ = 0.65

Pressure = 1 atm

Inlet Swirl No. = 0.3

Inlet Air Temperature = 533°K

D = 12.23 cm

R_o = 6.17 cm

X/D = 3.99	Percent Carbon					
R/R_o	THC	VHC	THC	VHC	THC	VHC
.641	.0168	.026				
.554	.19	.3	.0365	.2	.044	.0281
.374	4.02		3.64		2.704	
.263	2.29	1.43	3.05	.84		
.026		.075		.075		
-.014	9.93		10.26			
-.170	5.1	.075	5.25		4.94	
-.365	7.25		7.74		7.69	
-.365	6.67		6.44		6.76	
-.705	.486	.098	.503	.0709	.439	.0709
-.705	.439	.098	.451			

TABLE H-5 (Cont'd)

PERCENT CARBON DISTRIBUTIONS AT DETERMINED BY
PHASE-DISCRIMINATING PROBE

Propane

Φ = 0.65

Pressure = 1 atm

Inlet Swirl No. = 0.3

Inlet Air Temperature = 533°K

D = 12.23 cm

R_o = 6.17 cm

X/D = 5.38	Percent Carbon					
R/R_o	THC	VHC	THC	VHC	THC	VHC
.634	.113	.09	.0497		.0677	
.634	.054		.0549		.0452	
.634	.0491					
.571	.87	1.01	.68	1.04		
.445	4.58	4.56	.449	3.97	.447	.462
.445		3.471				
.429	4.483	3.394	4.66	3.799		4.02
.240	6.01	5.35	6.15	5.77	5.99	
.033	7.98	7.59	7.68	6.79		7.18
-.152	7.3	5.81	7.02	5.77		
-.370	4.08	3.53	3.95	3.52		
-.465	3.24	2.72	2.80			
-.582	1.17	1.07	1.228	1.24	1.67	
-.684	.105	.159	.109	.156		
-.782	.0232	.0387	.0287	.0383	.0321	.0389

APPENDIX I

TABULATED SPECIES CONCENTRATION DATA

TABLE I-1. SPECIES CONCENTRATION DISTRIBUTIONS - TEST NO. 1

Iso-Octane
$\phi = 0.65 \pm .01$
Pressure = 1.0 atm

Inlet Air Swirl No. = 0.3
Inlet Air Temperature = $530 \pm 3^{\circ}K$

	NO, ppm			
R/R_o	X/D = 1.21	2.60	4.00	5.38
-0.80	3	1	6	-
-0.58	23	22	44	-
-0.48	41	-	-	-
-0.38	58	91	101	-
-0.17	75	127	146	167
0.04	71	112	116	133
0.24	70	127	158	172
0.45	42	68	101	73
0.66	6	145	26	13
0.85	1	-	3	3
0.88	-	3	-	-

	NO_x, ppm			
R/R_o	X/D = 1.21	2.60	4.00	5.38
-0.80	5	13	24	-
-0.58	36	46	66	-
-0.48	-	-	-	-
-0.38	-	119	127	-
-0.17	-	-	-	-
0.04	71	-	165	-
0.24	-	-	-	186
0.45	69	89	111	104
0.66	23	35	45	38
0.85	8	-	14	13
0.87	-	13	-	-

TABLE I-1. SPECIES CONCENTRATION DISTRIBUTIONS
(Continued)

R/R_o	CO, Mole %			
	X/D = 1.21	2.60	4.00	5.38
-0.80	0.90	0.56	0.54	-
-0.58	3.00	1.18	0.85	-
-0.48	5.80	-	-	-
-0.38	8.10	3.50	2.10	-
-0.17	11.40	7.50	6.80	5.60
0.04	12.20	10.00	10.20	10.00
0.24	10.6	5.95	5.30	3.90
0.45	6.20	2.10	1.80	0.75
0.66	1.80	0.80	0.80	0.48
0.85	0.78	-	0.50	0.38
0.87	-	0.60	-	-

R/R_o	CO_2, Mole %			
	X/D = 1.21	2.60	4.00	5.38
-0.80	2.3	3.4	5.3	-
-0.58	6.5	7.9	8.1	-
-0.48	7.6	-	-	-
-0.38	7.6	9.4	10.2	-
-0.17	7.6	9.0	9.4	10.0
0.04	7.2	8.0	8.0	8.6
0.24	7.6	9.4	10.2	10.7
0.45	7.4	9.0	10.0	9.4
0.66	5.0	6.2	7.0	6.2
0.85	1.8	-	3.4	3.3
0.87	-	3.5	-	-

R/R_o	O_2, Mole %			
	X/D = 1.21	2.60	4.00	5.38
-0.80	16.85	15.86	14.00	-
-0.58	9.00	10.14	8.15	-
-0.48	4.68	-	4.34	-
-0.38	2.42	3.77	-	-
-0.17	0.65	0.78	0.95	1.15
0.04	0.52	0.29	0.26	0.40
0.24	1.22	1.17	1.03	1.65
0.45	4.81	5.59	4.43	6.75
0.66	11.96	11.57	10.20	12.13
0.85	7.50	-	16.	16.20
0.87	-	14.43	-	-

TABLE I-2. SPECIES CONCENTRATION DISTRIBUTIONS - TEST NO. 4

Iso-Octane
ϕ = 0.66
Pressure = 3.3 atm

Inlet Air Swirl No. = 0.3
Inlet Air Temperature = 533 ± 4°K

R/R_o	NO, ppm			
	X/D = 1.21	2.60	4.00	5.38
-0.84	3	-	2	-
-0.80	-	10	-	3
-0.66	58	47	66	18
-0.57	92	-	-	-
-0.45	-	90	76	73
-0.28	68	-	-	-
-0.24	-	74	55	66
-0.04	70	58	54	50
0.17	63	-	60	53
0.38	81	91	75	79
0.58	90	94	71	45
0.69	71	-	-	-
0.76	12	-	-	15
0.80	7	6	6	-

R/R_o	NO_x, ppm			
	X/D = 1.21	2.60	4.00	5.38
-0.84	13	-	10	-
-0.80	-	-	-	10
-0.66	74	60	91	32
-0.57	-	-	-	-
-0.45	-	-	-	-
-0.28	-	-	-	-
-0.24	-	-	-	-
-0.04	-	-	-	-
0.17	-	-	-	-
0.38	-	-	-	-
0.58	-	109	12	70
0.69	-	-	-	-
0.76	17	-	-	29
0.80	12	-	-	-

TABLE I-2. SPECIES CONCENTRATION DISTRIBUTIONS
(Continued)

R/R_o	CO, Mole %			
	X/D = 1.21	2.60	4.00	5.38
-0.84	0.00	-	0.25	-
-0.80	-	0.12	-	0.05
-0.66	2.10	0.80	3.40	0.40
-0.57	7.30	-	7.30	-
-0.45	-	5.5	-	4.6
-0.28	9.8	-	-	-
-0.24	-	8.85	8.5	7.4
-0.04	9.6	9.44	8.6	8.4
0.17	10.05	-	7.75	8.1
0.38	8.70	7.55	6.9	5.92
0.58	7.00	3.15	4.2	1.62
0.69	3.35	-	-	-
0.76	0.36	-	-	3.50
0.80	0.40	0.12	0.30	-

R/R_o	CO_2, Mole %			
	X/D = 1.21	2.60	4.00	5.38
-0.84	0.5	-	2.1	-
-0.80	-	1.95	-	0.85
-0.66	7.3	6.0	8.8	4.1
-0.57	7.95	-	-	-
-0.45	-	8.6	8.0	10.2
-0.28	6.1	-	-	-
-0.24	-	6.95	7.42	8.4
-0.04	5.9	6.7	7.5	7.25
0.17	5.9	-	8.0	7.75
0.38	6.3	7.75	8.45	9.3
0.58	8.15	8.85	9.4	8.75
0.69	8.1	-	-	-
0.76	2.6	-	-	3.65
0.80	3.25	1.6	2.45	-

TABLE I-2. SPECIES CONCENTRATION DISTRIBUTIONS
(Continued)

R/R_o	O_2, Mole %			
	X/D = 1.21	2.60	4.00	5.38
-0.84	20.38	-	18.23	-
-0.80	-	18.39	-	19.61
-0.66	7.83	11.80	3.00	15.05
-0.57	0.37	-	-	-
-0.45	-	0.87	0.18	0.63
-0.28	0.07	-	-	-
0.24		0.25	0.26	0
0.04	0	0.12	0.13	0.25
0.17	0	-	0.13	0.06
0.38	0.13	0.37	0.13	0.18
0.58	0.75	2.98	1.78	6.37
0.69	4.72	-	-	-
0.76	16.6	-	-	15.56
0.80	17.27	19.14	17.69	-

TABLE I-3. SPECIES CONCENTRATION DISTRIBUTIONS - TEST NO. 5

Iso-Octane
ϕ = 0.65
Pressure = 1.0 atm

Inlet Air Swirl No. = 0.6
Inlet Air Temperature = 530 ± 5°K

	NO, ppm			
R/R_o	X/D = 1.21	2.60	4.00	5.38
-0.85	3	4	4	8
-0.66	42	35	12	39
-0.45	87	27	23	187
-0.24	71	22	103	99
-0.04	65	16	76	72
0.17	63	19	81	80
0.38	-	25	160	127
0.48	90	-	-	-
0.58	50	86	55	79
0.80	1	5	3	4

	NO_x, ppm			
R/R_o	X/D = 1.21	2.60	4.00	5.38
-0.85	18	10	10	14
-0.66	72	44	22	44
-0.45	-	-	-	-
-0.24	-	-	-	-
-0.04	-	-	-	-
0.17	-	-	-	-
0.38	-	-	-	-
0.48	-	-	195	-
0.58	-	87	65	83
0.80	18	7	14	6

	CO, Mole %			
R/R_o	X/D = 1.21	2.60	4.00	5.38
-0.85	0.3	0.45	0.42	0.40
-0.66	2.0	1.00	0.50	0.25
-0.45	9.55	6.6	5.2	5.7
-0.24	11.1	9.7	12.6	12.5
-0.04	11.25	11.25	13.5	11.7
0.17	11.25	11.4	13.2	13.2
0.38	-	9.0	8.9	11.1
0.48	8.15	-	2.1	-
0.58	4.7	1.45	4.0	0.15
0.80	0.35	0.43	0.4	0.45

TABLE I-3. SPECIES CONCENTRATION DISTRIBUTIONS
(Continued)

R/R_o	CO_2, Mole %			
	X/D = 1.21	2.60	4.00	5.38
-0.85	1.35	2.6	2.45	3.5
-0.66	8.0	7.45	5.45	6.6
-0.45	7.5	7.9	9.8	9.95
-0.24	6.7	7.0	7.3	7.05
-0.04	6.4	6.05	6.8	6.3
0.17	6.55	6.6	6.85	6.7
0.38	-	7.6	8.65	7.5
0.48	8.1	-	10.75	-
0.58	8.3	8.5	7.0	9.5
0.80	1.9	3.5	2.6	3.8

R/R_o	O_2, Mole %			
	X/D = 1.21	2.60	4.00	5.38
-0.85	18.84	17.33	17.46	16.26
-0.66	5.47	8.78	13.69	11.59
-0.45	0.05	1.27	1.14	0.51
-0.24	0.00	1.01	0.05	0.18
-0.04	0.00	1.14	0.02	2.40
0.17	0.00	1.39	0.02	0.08
0.38	-	1.27	0.25	0.63
0.48	0.38	-	2.5	-
0.58	3.31	5.95	9.0	9.33
0.80	18.33	16.02	17.43	15.75

TABLE I-4. SPECIES CONCENTRATION DISTRIBUTIONS - TEST NO. 8

No. 2 Fuel Oil
ϕ = 0.67
Pressure = 1.0 atm

Inlet Air Swirl No. = 0.3
Inlet Air Temperature = 755 K

	NO, ppm			
R/R_o	X/D = 1.21	2.60	4.00	5.38
-0.84	14	-	-	103
-0.80	-	23	39	-
-0.66	31	-	-	157
-0.57	-	49	101	-
-0.45	47	-	-	209
-0.38	-	83	143	-
-0.24	79	-	-	295
-0.17	-	154	196	-
-0.04	108	-	-	290
0.04	-	188	201	-
0.17	108	-	-	280
0.25	-	188	203	-
0.38	56	-	-	225
0.45	-	135	151	-
0.58	41	-	-	-
0.66	-	83	119	157
0.80	14	-	-	-
0.84	-	55	84	-

	NO_x, ppm			
R/R_o	X/D = 1.21	2.60	4.00	5.38
-0.84	19	-	-	-
-0.80	-	32	73	-
-0.66	38	-	-	-
-0.57	-	57	105	-
-0.45	64	-	-	-
-0.38	-	95	146	-
-0.24	-	-	-	-
-0.17	-	-	-	-
-0.04	-	-	-	-
0.04	-	-	-	-
0.17	56	-	-	-

TABLE I-4. SPECIES CONCENTRATION DISTRIBUTIONS
(Continued)

R/R_o	NO_x, ppm			
	X/D = 1.21	2.60	4.00	5.38
0.25	-	-	-	-
0.38	83	-	-	225
0.45	-	135	-	-
0.58	-	-	-	-
0.66	-	83	119	157
0.80	27	-	-	-
0.84	-	-	-	-

R/R_o	CO, Mole %			
	X/D = 1.21	2.60	4.00	5.38
-0.84	1.47	-	-	0.38
-0.80	-	0.86	0.77	-
-0.67	1.11	-	-	0.34
-0.58	-	0.87	0.62	-
-0.45	1.9	-	-	0.8
-0.38	-	1.21	1.06	-
-0.24	3.99	-	-	2.6
-0.17	-	3.0	3.43	-
-0.04	6.19	-	-	5.88
0.04	-	7.18	8.46	-
0.17	6.05	-	-	4.06
0.25	-	5.18	4.43	-
0.38	2.82	-	-	1.25
0.45	-	1.65	1.46	-
0.58	1.52	-	-	-
0.66	-	0.83	0.77	0.65
0.80	0.97	-	-	-
0.84	-	0.63	0.55	-

TABLE I-4. SPECIES CONCENTRATION DISTRIBUTIONS
(Continued)

R/R_o	CO_2, Mole %			
	X/D = 1.21	2.60	4.00	5.38
-0.84	4.01	-	-	7.43
-0.80	-	6.14	7.39	-
-0.67	5.07	-	-	8.3
-0.58	-	6.95	8.24	-
-0.45	6.07	-	-	9.0
-0.38	-	7.85	8.96	-
-0.24	7.81	-	-	9.74
-0.17	-	8.25	9.7	-
-0.04	7.92	-	-	9.28
0.04	-	8.73	8.65	-
0.17	7.98	-	-	9.53
0.25	-	9.3	9.25	-
0.38	7.4	-	-	9.3
0.45	-	8.44	8.87	-
0.58	5.79	-	-	-
0.66	-	7.1	8.49	8.56
0.80	4.7	-	-	-
0.84	-	6.1	7.41	-

I-4. SPECIES CONCENTRATION DISTRIBUTIONS
(Continued)

R/R_o	O_2, Mole %			
	X/D = 1.21	2.60	4.00	5.38
-0.84	14.7	-	-	10.1
-0.80	-	12.4	9.8	-
-0.67	13.3	-	-	8.0
-0.58	-	10.8	8.15	-
-0.45	10.8	-	-	6.2
-0.38	-	8.7	6.1	-
-0.24	5.3	-	-	2.5
-0.17	-	3.7	1.7	-
-0.04	2.9	-	-	1.1
0.04	-	1.1	0.38	-
0.17	3.2	-	-	2.0
0.25	-	1.7	2.1	-
0.38	7.4	-	-	5.1
0.45	-	6.9	5.9	-
0.58	12.0	-	-	-
0.66	-	10.5	7.5	7.4
0.80	14.2	-	-	-
0.84	-	12.4	9.7	-

TABLE I-5. SPECIES CONCENTRATION DISTRIBUTIONS - TEST NO. 6

No. 2 Oil
ϕ = 0.67
Pressure = 1.0 atm

Inlet Air Swirl No. = 0.3
Inlet Air Temperature = 529 $\pm$ 6°K

R/R_o	NO, ppm			
	X/D = 1.21	2.60	4.00	5.38
-0.84	-	-	-	39
-0.80	-	19	37	-
-0.66	-	-	-	62
-0.58	-	29	66	-
-0.45	-	-	-	119
-0.38	-	52	95	-
-0.24	-	-	-	132
-0.17	-	97	120	-
-0.04	87	-	-	132
0.04	-	112	103	-
0.17	83	101	-	119
0.25	-	93	105	-
0.38	46	-	-	110
0.45	51	42	86	-
0.58	21	-	-	102
0.66	30	21	53	-
0.80	5	-	-	65
0.84	15	17	45	-

TABLE I-5. SPECIES CONCENTRATION DISTRIBUTIONS
(Continued)

R/R_o	NO_x, ppm			
	X/D = 1.21	2.60	4.00	5.38
-0.84	-	-	-	-
-0.80	-	32	41	-
-0.66	-	-	-	66
-0.58	-	36	69	-
-0.45	64	-	-	-
-0.38	-	58	-	-
-0.24	-	-	-	-
-0.17	-	-	-	-
-0.04	-	-	-	-
0.04	-	-	-	-
0.17	-	-	-	-
0.25	-	-	-	-
0.38	66	-	-	-
0.45	-	48	-	-
0.58	38	-	-	-
0.66	-	26	-	-
0.80	19	-	-	-
0.84	-	23	-	-

R/R_o	CO, Mole %			
	X/D = 1.21	2.60	4.00	5.38
-0.84	1.46	-	-	0.62
-0.80	-	1.28	1.08	-
-0.66	1.3	-	-	0.66
-0.58	-	1.17	0.97	-
-0.45	2.82	-	-	1.44
-0.38	-	1.49	1.23	-
-0.24	5.07	-	-	2.6
-0.17	-	3.47	3.79	-
-0.04	6.57	-	-	4.5
0.04	-	7.48	5.83	-
0.17	5.82	4.3	-	3.36
0.25	-	2.8	3.7	-
0.38	2.97	-	-	1.39
0.45	-	1.09	1.51	-
0.58	1.52	-	-	1.03
0.66	-	0.89	1.10	-
0.80	0.99	-	-	0.55
0.84	-	1.13	1.22	-

TABLE I-5. SPECIES CONCENTRATION DISTRIBUTIONS
(Continued)

R/R_o	CO_2, Mole %			
	X/D = 1.21	2.60	4.00	5.38
-0.84	3.01	-	-	6.6
-0.80	-	5.47	6.53	-
-0.66	5.11	-	-	8.06
-0.58	-	6.14	7.73	-
-0.45	6.94	-	-	9.36
-0.38	-	7.48	8.92	-
-0.24	8.35	-	-	9.65
-0.17	-	9.12	9.62	-
-0.04	8.45	-	-	9.45
0.04	-	8.87	8.87	-
0.17	8.44	8.86	-	9.24
0.25	-	8.96	9.39	-
0.38	7.33	-	-	9.05
0.45	-	7.15	8.87	-
0.58	5.43	-	-	8.73
0.66	-	5.65	7.98	-
0.80	3.17	-	-	7.28
0.84	-	5.31	6.95	-

R/R_o	O_2, Mole %			
	X/D = 1.21	2.60	4.00	5.38
-0.84	15.9	-	-	11.7
-0.80	-	12.6	11.6	-
-0.66	13.1	-	-	8.8
-0.58	-	11.9	9.2	-
-0.45	8.5	-	-	4.9
-0.38	-	9.1	6.3	-
-0.24	3.2	-	-	3.3
-0.17	-	4.0	2.2	-
-0.04	1.7	-	-	1.9
0.04	-	0.89	2.5	-
0.17	2.9	-	-	3.3
0.25	-	-	3.58	-
0.38	7.8	-	-	5.7
0.45	-	10.1	5.9	-
0.58	12.6	-	-	6.6
0.66	-	13.0	8.4	-
0.80	16.4	-	-	10.6
0.84	-	13.4	10.4	-

TABLE I-6. SPECIES CONCENTRATIONS DISTRIBUTIONS - TEST NO. 11

Propane
$\phi = 0.64 \pm .01$
Pressure = 1.0 atm

Inlet Air Swirl No. = 0.3
Inlet Air Temperature = $521 \pm 8°$ K

R/R_o	NO, ppm			
	X/D = 1.21	2.60	4.00	5.38
-0.80	5	3	14	4
-0.58	8	20	75	16
-0.38	47	70	75	84
-0.17	55	70	74	64
0.04	54	71	68	61
0.24	48	69	70	78
0.45	23	68	-	78
0.59	-	-	72	-
0.66	2	7	-	10
0.70	-	-	10	-
0.85	1	3	2	3

R/R_o	NO_x, ppm			
	X/D = 1.21	2.60	4.00	5.38
-0.80	-	-	23	4
-0.58	11	-	-	-
-0.38	-	-	-	31
-0.17	-	-	-	-
0.04	-	-	-	-
0.24	-	-	-	-
0.45	-	-	-	-
0.59	-	-	-	-
0.66	3	20	-	14
0.70	-	-	14	-
0.85	4	5	4	7

Table I-6. SPECIES CONCENTRATIONS DISTRIBUTIONS (Continued)

R/R_o	CO, Mole %			
	X/D = 1.21	2.60	4.00	5.38
-0.80	0.1	-	1.07	0.03
-0.58	2.4	2.36	9.37	0.8
-0.38	7.4	-	10.52	2.28
-0.17	7.3	9.3	10.71	2.4
0.04	7.3	9.4	10.72	1.0
0.24	7.4	9.08	10.6	2.38
0.45	6.25	8.58	-	2.2
0.59	-	-	7.52	-
0.66	0.55	2.8	-	0.18
0.70	-	-	0.65	-
0.85	0.0	0.22	0.02	0.01

R/R_o	CO_2, Mole %			
	X/D = 1.21	2.60	4.00	5.38
-0.80	0.9	0.4	2.75	1.05
-0.58	5.05	4.84	8.6	6.15
-0.38	6.15	-	7.85	6.35
-0.17	5.55	5.92	7.9	5.65
0.04	5.55	5.92	7.7	5.65
0.24	5.6	5.99	7.7	5.85
0.45	5.8	6.47	-	6.5
0.59	-	-	7.05	-
0.66	1.8	5.51	-	3.00
0.70	-	-	4.5	-
0.85	0.15	0.93	1.0	0.50

R/R_o	O_2, Mole %			
	X/D = 1.21	2.60	4.00	5.38
-0.80	19.71	20.4	15.4	19.53
-0.58	10.94	11.5	0.76	-
-0.38	1.00	0.85	0.25	9.82
-0.17	0.2	0.35	0.56	1.12
0.04	0.37	0.3	0.58	1.12
0.24	1.12	0.45	0.61	1.12
0.45	2.98	0.85	-	1.32
0.59	-	-	2.2	-
0.66	17.99	10.1	-	16.65
0.70	-	-	16.2	-
0.85	20.73	19.8	19.8	20.31

TABLE I-7. EXHAUST SPECIES CONCENTRATIONS (ISO-OCTANE)

Test No.	Swirl No.	Pressure (atm)	Inlet Air Temperature (^{o}K)	Φ	ΔP_{inj} (atm)
1	0.3	1.0	740	0.89	-
	0.3	1.0	746	0.65	-
	0.3	1.0	746	0.57	-
	0.3	1.0	744	0.73	-
	0.3	1.0	746	0.81	-
	0.3	1.0	765	0.96	-
2	0.3	1.0	749	0.73	7.71
	0.3	1.0	747	0.65	-
	0.3	1.0	637	0.65	-
	0.3	1.0	638	0.72	7.65
	0.3	1.0	530	0.57	-
	0.3	1.0	528	0.61	-
	0.3	1.0	527	0.72	7.64
	0.3	1.0	533	0.80	9.99
	0.3	1.0	524	0.88	12.72
3	0.3	3.5	527	0.65	-
4	0.3	3.5	532	0.65	-
5	0.6	1.0	530	0.65	-
	0.6	1.0	535	0.62	-
	0.6	1.0	525	0.67	-

TABLE I-7. EXHAUST SPECIES CONCENTRATIONS (ISO-OCTANE)
(Continued)

Test No.	O_2 (Mole %)	CO_2 (Mole %)	CO (Mole %)	NO ppm	NO_x ppm
1	4.2	9.6	0.98	218	235
	9.6	7.3	0.12	156	169
	11.8	5.9	0.11	101	110
	7.6	8.1	0.25	183	198
	6.0	8.8	0.62	200	210
	3.3	9.9	1.30	230	250
2	6.6	9.0	0.30	185	207
	9.4	8.0	0.10	147	185
	9.4	8.0	0.15	91	117
	7.5	9.0	0.21	125	147
	12.1	6.4	0.18	20	48
	9.5	7.8	0.17	50	76
	7.6	8.8	0.38	72	93
	5.9	9.6	0.80	90	113
	4.6	10.0	1.35	102	117
3	10.8	7.1	0.37	31	44
4	10.2	7.5	0.25	39	47
5	10.9	6.7	0.3	46	52
	11.6	6.1	0.7	27	40
	10.4	6.9	0.2	55	64

TABLE I-8. EXHAUST SPECIES CONCENTRATIONS (NO. 2 OIL)

Test No.	Swirl No.	Pressure (atm)	Inlet Air Temperature (°K)	Φ	ΔP_{inj} (atm)
1	0.6	1.0	530	0.65	-
	0.6	1.0	537	0.63	-
	0.6	1.0	532	0.67	-
2	0.3	1.0	522	0.57	-
	0.3	1.0	532	0.64	-
	0.3	1.0	526	0.72	8.73
	0.3	1.0	530	0.79	10.84
	0.3	1.0	525	0.87	13.22
3	0.3	1.0	748	0.64	7.09
4	0.3	3.5	533	0.65	-
				0.57	-
				0.74	-
5	0.3	1.0	533	0.65	-
	0.3	1.0	533	0.57	-
	0.3	1.0	533	0.74	-
6	0.3		644	0.65	-
	0.3		644	0.57	-
	0.3		644	0.74	-

Test No.	O_2 (Mole %)	CO_2 (Mole %)	CO (Mole %)	NO ppm	NO_x ppm
1	7.7	8.9	0.007	66	72
	8.1	8.6	0.006	62	66
	7.2	9.0	0.01	78	82
2	9.6	7.9	0.001	52	58
	7.5	8.8	0.18	84	85
	6.1	9.1	0.52	103	105
	4.9	9.4	1.11	115	115
	3.9	9.5	1.81	125	-
3	7.7	9.0	0.04	166	167
4	6.8	10.4	0.06	116	116
	8.8	9.3	0.04	104	-
	5.2	11.2	0.10	111	-
	6.6	9.9	0.14	108	109
	8.9	9.2	0.06	80	-
	5.8	10.7	0.46	119	-
6	8.8	-	0.08	120	120
	8.8	-	0.02	94	94
	5.7	-	0.22	152	152

Table I-9. EXHAUST SPECIES CONCENTRATIONS (PROPANE)

Test No.	Swirl No.	Pressure (atm)	Inlet Air Temperature (^{o}K)	Φ	ΔP_{inj} (atm)
1	0.6	1.0	533	0.64	10.90
	0.6	1.0	538	0.61	9.20
	0.6	1.0	539	0.66	7.84
2	0.3	1.0	533	0.57	-
	0.3	1.0	533	0.65	-
	0.3	1.0	533	0.74	-
	0.3	1.0	533	0.82	-
	0.3	1.0	533	0.90	-
3	0.3	1.0	644	0.65	-
4	0.3	1.0	755	0.65	-
5	0.3	3.5	533	0.65	-
				0.57	-
				0.74	-
6	0.3	1.0	526	0.28	8.52
	0.3	1.0	529	0.32	8.66
	0.3	1.0	531	0.36	9.54
	0.3	1.0	525	0.40	11.92
	0.3	1.0	525	0.32	7.16
	0.3	1.0	529	0.44	12.67

Test No.	O_2 (Mole %)	CO_2 (Mole %)	CO (Mole %)	NO ppm	NO_x ppm	HC ppm C
1	11.7	6.4	0.19	47	67	
	12.4	0.0	0.245	36	61	
	10.9	6.8	0.145	60	82	
2	12.8	6.5	0.26	52	52	461
	11.0	6.9	0.26	63	63	461
	8.6	8.8	0.29	83	83	471
	7.3	9.2	0.44	91	91	451
	7.2	10.0	0.76	108	108	531
3	10.9	7.6	0.18	87	89	336
4	11.5	7.1	0.08	110	113	241
5	8.1	7.3	0.02	94	94	186
	10.0	8.1	0.04	81	81	193
	5.5	10.2	0.10	-	107	227
6	17.9	2.4	0.03	12	16	
	17.2	3.1	0.01	18	23	
	16.6	3.4	0.01	22	24	
	16.2	3.7	0.02	26	32	
	17.2	2.9	0.01	17	25	
	15.8	4.1	0.09	31	38	

APPENDIX J

TABULATED VELOCITY DATA

TABLE J-1. AXIAL VELOCITY DATA (M/SEC) - TEST NO. 1

Iso-Octane/Air
ϕ = 0.65
Pressure = 1 atm

Inlet Air Swirl = 0.3
Inlet Air Temperature = 533°K

X/D = 0.123

R/R_O	$\bar{U}$	U'_{RMS}
-0.86	32.7	13.7
-0.86	34.1	14.9
-0.68	12.39	15.4
-0.68	21.5	19.8
-0.50	-3.1	7.6
0.00	7.4	15.8
0.31	25.6	6.2
0.47	-0.8	7.4
0.80	23.9	15.3
0.80	24.9	15.7
0.88	14.8	12.2
0.88	16.5	14.4
0.80	21.6	14.2
0.80	33.5	15.1
0.72	19.9	13.5
0.72	33.2	16.6
0.58	6.4	8.0
0.58	8.9	11.6
0.47	4.2	4.0
0.39	2.4	4.0
0.31	8.6	5.1
0.15	29.3	3.9
-0.88	18.1	14.9
-0.88	29.3	14.9
-0.75	19.2	17.4
-0.75	33.5	20.2
-0.63	6.3	12.3
-0.63	13.2	17.3
-0.50	-2.1	8.9
-0.40	-3.99	6.7
-0.28	14.8	9.6
-0.18	26.1	6.1
-0.04	13.3	14.9
0.06	23.7	5.3

TABLE J-1. AXIAL VELOCITY DATA (M/SEC) - TEST NO. 1
(continued)

X/D = 0.336

R/R_O	$\bar{U}$	U'_{RMS}
-0.88	22.1	16.6
-0.88	16.4	13.0
-0.88	21.7	16.9
-0.88	41.3	17.5
-0.71	9.0	9.3
-0.71	8.7	7.4
-0.71	15.8	17.7
-0.55	9.5	7.8
-0.55	9.6	6.9
-0.55	9.9	6.7
-0.38	12.8	12.6
-0.38	17.7	8.2
-0.38	19.1	8.2
-0.18	13.9	10.9
-0.18	17.7	10.3
0.02	7.3	13.0
0.23	18.8	9.5
0.23	22.6	7.3
0.43	19.8	5.5
0.43	18.2	6.2
0.64	12.5	5.4
0.64	13.5	4.5
0.64	12.9	5.6
0.76	13.8	5.9
0.76	13.7	7.3
0.76	16.3	10.8
0.93	20.9	11.0
0.93	24.7	11.0

TABLE J-1. AXIAL VELOCITY DATA (M/SEC) - TEST NO. 1
(continued)

X/D = 0.524 R/R_o	$\bar{U}$	U'_{RMS}
-0.81	18.8	5.2
-0.81	18.8	5.1
-0.59	17.1	6.1
-0.59	17.3	6.8
-0.38	14.4	9.9
-0.18	13.1	13.1
0.00	8.7	10.1
0.23	12.8	11.6
0.43	16.9	8.4
0.64	17.1	5.0
0.84	18.9	5.A

TABLE J-2. AXIAL VELOCITY DATA (M/SEC) - TEST NO. 5

Iso-Octane/Air
ϕ = 0.6
Pressure = 1 atm

Inlet Air Swirl = 0.6
Inlet Air Temperature = 533°K

X/D = 0.123

R/R_0	$\bar{U}$	U'_{RMS}
-0.88	63.20	16.3
-0.88	67.30	22.9
-0.71	36.90	22.6
-0.55	0.00	12.5
-0.38	31.80	5.4
-0.38	32.80	4.8
-0.18	31.10	3.4
0.02	30.10	3.5
0.23	24.50	7.8
0.43	13.50	24.0
0.64	57.60	13.8
0.64	65.70	14.4
0.84	43.20	18.3
-0.79	66.70	16.3
-0.63	35.90	21.8
-0.49	1.30	12.1
-0.28	31.40	4.0
0.08	29.50	3.4
0.13	28.50	3.1
0.33	20.70	10.1
0.33	2.98	8.1
0.54	33.50	25.6
0.74	61.50	14.8
-0.38	30.60	5.1

TABLE J-2. AXIAL VELOCITY DATA (M/SEC) - TEST NO. 5
(continued)

X/D = 0.336

R/R_0	$\bar{U}$	U'_{RMS}
-0.59	29.3	5.6
-0.38	27.7	4.1
-0.18	24.4	5.3
0.00	22.6	7.7
0.23	26.4	4.4
0.43	22.5	5.0
0.72	7.2	10.7
0.64	12.0	8.7
0.47	22.3	5.4
0.31	25.0	4.2
0.15	22.3	6.2
0.00	17.9	6.1
-0.18	23.3	6.0
-0.34	26.3	4.6
-0.51	25.6	6.7
-0.67	22.6	9.9

TABLE J-2. AXIAL VELOCITY DATA (M/SEC) - TEST NO. 5
(continued)

X/D = 0.524

R/R_0	$\bar{U}$	U'_{RMS}
0.68	16.3	5.4
0.56	17.2	5.6
0.39	16.3	6.6
0.23	15.7	5.9
0.23	11.7	8.8
0.06	17.9	4.8
0.06	17.2	6.7
-0.10	16.2	4.2
-0.10	17.7	6.7
-0.26	14.0	5.9
-0.26	17.7	6.0
-0.26	15.1	-
-0.43	18.8	5.8
-0.43	20.2	-
-0.59	18.9	5.9
-0.59	21.7	-
-0.75	19.2	5.5
-0.75	21.6	3.7
0.23	11.9	8.8

TABLE J-2. AXIAL VELOCITY DATA (M/SEC) - TEST NO. 5
(continued)

X/D = 1.64

R/R_O	$\overline{U}$	U'_{RMS}
-0.88	44.7	7.9
-0.88	47.3	9.1
-0.69	37.8	7.5
-0.51	26.4	7.3
-0.30	29.1	11.4
-0.10	44.0	12.8
0.11	37.3	12.3
0.33	21.4	7.4
0.52	26.0	7.6
0.72	50.2	6.9
0.72	46.8	10.3
0.84	52.8	7.3
0.84	53.7	8.7
0.64	33.5	9.7
0.02	47.1	12.4

TABLE J-3. AXIAL VELOCITY DATA (M/SEC) - TEST NO. 6

No. 2 Fuel Oil/Air
ϕ = 0.65
Pressure = 1 atm

Inlet Air Swirl = 0.3
Inlet Air Temperature = 533°K

X/D = 0.123

R/R_0	$\bar{U}$	U'_{RMS}
.8770	35.7	13.9
.6926	12.3	12.0
.5082	-2.5	5.6
.3033	9.3	9.3
.0984	19.5	5.9
.1066	21.7	2.8
.3115	-3.4	4.9
.5164	1.2	6.9
0	20.0	7.6
.2295	-0.9	4.7
.1270	4.9	6.3
.0656	16.0	5.7
.8770	20.4	12.7
.8770	32.2	14.5
.6926	11.3	6.7
.6926	12.3	-
.1803	22.9	3.2
.0779	21.5	4.0
.0246	23.5	3.4

TABLE J-3. AXIAL VELOCITY DATA (M/SEC) - TEST NO. 6
(continued)

X/D = 0.336

R/R_0	$\bar{U}$	U'_{RMS}
.8361	14.7	12.5
.8361	41.3	12.2
.6311	19.7	6.8
.6311	19.9	7.1
.4262	20.8	3.5
.2213	20.0	2.6
0	20.6	6.1
.2008	20.0	4.0
.3934	14.8	6.8
.5984	4.3	5.6
.8033	22.4	13.8
.8033	11.1	11.9
.7951	11.2	7.8
.7951	39.4	9.5
.5902	21.4	4.3
.3852	21.4	-
.0246	22.7	-
.8443	26.4	-
.5164	15.7	-
.6373	6.7	5.5

TABLE J-3. AXIAL VELOCITY DATA (M/SEC) - TEST NO. 6
(continued)

λ = 514.5 nm

X/D = 0.336

R/R_o	$\bar{U}$	U'_{RMS}
.8770	18.8	10.2
.8770	27.0	18.4
.7131	22.3	5.7
.5492	22.9	4.6
.3852	22.7	5.9
.2213	14.5	8.3
.1885	17.8	3.9
.3934	15.8	6.2
.1803	20.8	5.0
0	8.2	8.7
-.1885	18.7	5.9
-.3934	16.5	5.2
-.5984	8.2	6.2
-.5984	14.6	13.1
-.1803	20.7	6.3
-.5902	3.1	6.3
-.5902	4.3	6.4
-.3852	15.3	7.8
-.8770	14.7	9.3
-.5902	6.2	6.5

TABLE J-3. AXIAL VELOCITY DATA (M/SEC) - TEST NO. 6
(continued)

X/D = 0.524

R/R_0	$\bar{U}$	U'_{RMS}
.9180	14.6	4.8
.9180	25.1	10.2
.7131	16.1	3.8
.5082	16.5	4.2
.2623	12.8	6.9
.3115	17.4	8.6
.0082	8.2	7.4
-.2295	10.1	5.8
-.4344	15.2	4.3
-.6393	13.3	3.4
-.8443	12.8	3.2
-.3525	15.3	-

TABLE J-3. AXIAL VELOCITY DATA (M/SEC) - TEST NO. 6
(continued).

λ = 514.5 nm

X/D = 0.524

R/R_O	$\bar{U}$	U'_{RMS}
.8770	18.8	4.7
.8770	21.3	10.2
.6721	16.4	3.9
.4918	18.0	4.4
.3320	22.0	4.1
.1803	11.3	7.6
-.0164	11.1	6.3
-.2295	12.7	6.1
-.4344	16.9	4.9
-.5984	18.5	3.5
-.7623	19.5	4.8

TABLE J-4. TANGENTIAL VELOCITY DATA (M/SEC) - TEST NO. 1

Iso-Octane/Air
ϕ = 0.65
Pressure = 1 atm

Inlet Air Swirl = 0.3
Inlet Air Temperature = 533°K

X/D = 0.123

R/R_0	$\bar{W}$	w'_{RMS}
-0.88	11.20	5.4
-0.88	22.20	8.1
-0.71	8.80	6.0
-0.71	12.00	9.2
-0.51	4.20	3.9
-0.51	4.20	3.8
-0.39	3.40	3.3
-0.18	1.99	2.6
0.13	0.10	2.5
0.23	0.30	2.5
0.43	-3.50	2.8
0.43	-3.80	2.8
0.64	-7.00	4.8
0.64	-11.30	8.3
0.80	-13.50	6.5
0.80	-20.00	9.7
0.23	0.02	3.3

TABLE J-4. TANGENTIAL VELOCITY DATA (M/SEC) - TEST NO. 1
(continued)

X/D = 0.336

R/R_0	$\bar{W}$	w'_{RMS}
-0.90	13.70	8.3
-0.90	22.60	8.3
-0.90	23.00	9.7
-0.75	8.10	6.3
-0.75	8.10	6.8
-0.75	14.50	11.6
-0.59	4.50	4.1
-0.59	4.80	4.2
-0.38	3.10	3.0
-0.38	3.00	3.0
-0.18	3.00	3.9
-0.18	2.90	3.3
0.00	-4.10	6.1
0.23	-4.02	4.1
0.43	-1.48	3.3
0.64	-3.60	3.7
0.64	-3.00	3.2
0.76	-4.60	3.6
0.76	-6.10	5.9
0.76	-3.90	3.5
0.88	-7.20	5.1
-0.88	11.40	7.7
-0.88	13.50	9.8
-0.90	13.80	9.5

TABLE J-5. TANGENTIAL VELOCITY DATA (M/SEC) - TEST NO. 5

Iso-Octane/Air
ϕ = 0.6
Pressure = 1 atm

Inlet Air Swirl = 0.6
Inlet Air Temperature = 533°K

X/D = 0.123

R/R_0	$\bar{W}$	ω'_{RMS}
-0.88	6.6	15.0
-0.88	46.0	14.2
-0.11	39.6	14.8
-0.51	25.2	9.2
-0.30	-1.1	3.2
-0.10	-2.3	4.2
0.11	-5.7	2.5
0.31	-28.0	7.3
0.52	-35.0	11.7
0.72	-49.8	10.5
0.43	-30.2	7.8
0.23	-10.7	3.9

TABLE J-5. TANGENTIAL VELOCITY DATA (M/SEC) - TEST NO. 5
(continued)

X/D = 0.336

R/R_0	$\bar{W}$	ω'_{RMS}
-0.82	33.2	9.0
0.64	-19.0	6.9
0.64	-28.6	18.5
0.80	-29.6	7.8
0.00	-0.7	3.0
0.00	-0.9	5.2
-0.67	7.7	8.2
-0.67	21.2	15.1
0.43	-6.3	2.8
0.23	-1.5	2.8
0.23	-1.3	2.7

TABLE J-6. TANGENTIAL VELOCITY DATA (M/SEC) - TEST NO. 6

No. 2 Fuel Oil/Air
ϕ = 0.65
Pressure = 1 atm

Inlet Air Swirl = 0.3
Inlet Air Temperature = 533°K

X/D = 0.123

R/R_0	$\bar{W}$	ω'_{RMS}
.8361	13.8	4.9
.8361	13.4	5.6
.6311	13.2	7.8
.6311	22.3	9.5
.4262	4.3	4.1
.4262	7.1	5.5
.2213	2.9	3.0
.2213	3.5	3.1
.0164	3.2	1.8
-.1885	1.8	2.1
-.3934	-1.7	2.5
-.6393	-12.0	7.2
-.8443	-21.5	6.6

TABLE J-6. TANGENTIAL VELOCITY DATA (M/SEC) - TEST NO. 6
(continued)

X/D = 0.336

R/R_0	$\bar{W}$	w'_{RMS}
.8115	5.9	6.4
.8115	19.8	5.6
.6311	3.1	3.1
.6311	14.4	8.1
.4262	1.6	2.2
.2213	1.6	2.1
0.	0.	2.2
-.2295	-.7	2.0
-.4344	-.4	1.9
-.6393	-1.7	2.0
-.8443	-4.5	3.9
-.8443	-16.8	5.5
-.6393	-4.5	6.1

TABLE J-7. RADIAL VELOCITY DATA

ϕ = 0.65
Pressure = 1 atm

Inlet Air Temperature = 533°K
X/D = 0.336

Fuel	Swirl No.	Distance From ℄ (ins)	V
Iso-octane	0 = .6	+.2	-4.0
		-.1	+1.9
		-.4	+4.5
		-.7	+10.9
		+.5	-7.1
		+.7	-13.3
		+1.1	-16.1
	0.3	+.8	-10.0
		+.2	- 2.1
		-.4	+8.1
		-.8	+14.5
		-.8	+14.4
No. 2 Fuel	0.3	+0.3	-6.5
		+0.9	-12.4
		-0.5	+ 7.0

Note: Mean flow is radially outward from centerline.

APPENDIX K

DETERMINATION OF SPRAY CONE ANGLE FROM HOLOGRAPHIC DATA

The method used to derive the spray cone angle from the spray surface coordinates involves a "best fit" of the measured data to the surface coordinates of right circular cones.

The coordinate system used in the analysis of the data is shown in Fig. K-1a. The center line of the conical surface is parallel to the z axis and the vertix of the cone lies at an arbitrary point. In general a slight deviation of angle β existed between the viewing direction, y' and the y coordinate axis. This deviation produced a slight rotation of the transformed coordinate system (in which the centerline is parallel to the z axis) and the raw data coordinate system (Fig. K-1b)). The first step in the data analysis was to assume a value of the angle of rotation, β, so that the measured data were transformed from the (x, y', z) system to the (x, y, z) system:

$$y = y' \cos\beta - z' \sin\beta \tag{K-1}$$

and

$$z = y' \sin\beta + z' \cos\beta \tag{K-2}$$

Such a transformation was made for several assumed values of β. The angle, β, was varied over an appropriate range as determined from estimates obtained from raw data plots.

The data in the transformed coordinate system (x, y, z) was assumed to lie on the surface of the cone whose apex was located at the point (x_o, y_o, z_o) and whose vertex angle was θ (see Fig. K-1a). The unknowns $(x_o, y_o, z_o, \theta, \beta)$ were determined using a technique in which three parameters (x_o, y_o, β) were varied parametrically and the remaining variables (z_o, θ) were obtained by means of a multiple, linear regression analysis. The set of unknowns yielding the highest value of the computed coefficient of determination was considered to be the best fit of the data. Details of this procedure follow.

Any cross-section perpendicular to the z-axis is a circle whose radius is given by

$$s = \sqrt{(x - x_o)^2 + (y - y_o)^2} \tag{K-3}$$

COORDINATE SYSTEMS EMPLOYED FOR SPRAY CONE ANGLE DATA ANALYSIS

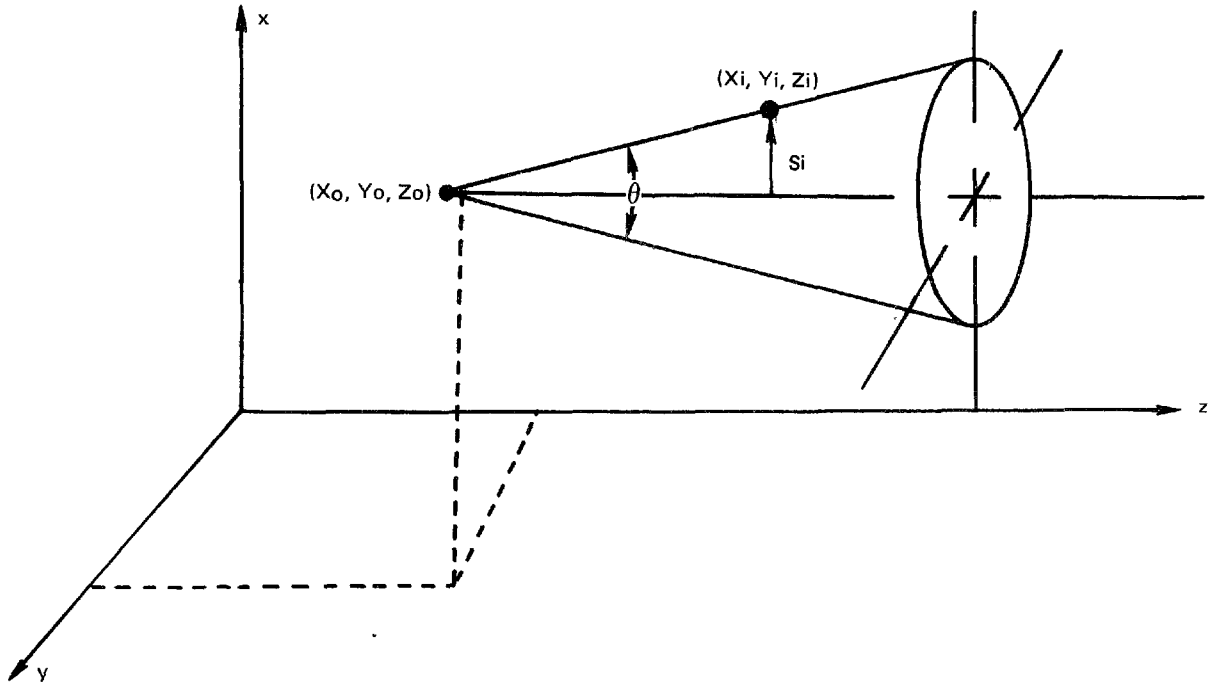

a) CONE ORIENTATION IN ROTATED COORDINATE SYSTEM

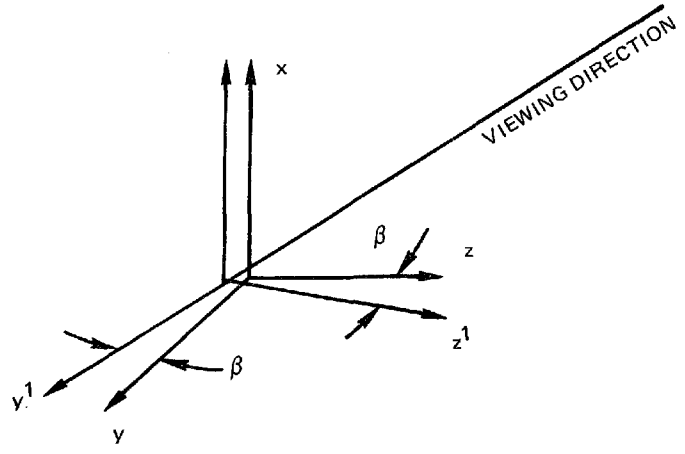

b) ROTATION OF COORDINATE SYSTEM

76–09–2–8

This radius is related to the axial coordinate and vertex angle by:

$$\frac{s}{z - z_o} = \tan \theta/2 \tag{K-4}$$

Combining these two equations, squaring both sides of the result, and rearranging yields the working equation:

$$z_c = z_o + \alpha \sqrt{(x - x_o)^2 + (y - y_o)^2} \tag{K-5}$$

where the variable, z_c, indicates that this equation is used to estimate the measured value of z for each data point from the measured values (x, y) and the unknowns (x_o, y_o, z_o, θ, β). The variable, a, is introduced for convenience and is defined by:

$$\alpha \equiv \frac{1}{\tan \theta/2} \tag{K-6}$$

so that the unknowns are now (x_o, y_o, z_o, a, β).

The quantitative measure of how well Eq. (K-5) approximates the measured values of the axial coordinate, z_m, is given by the coefficient of determination, r^2

$$r^2 = 1.0 - \frac{\sum_{i=1}^{N} (z_{mi} - z_{ci})^2}{\sum_{i=1}^{N} (z_{mi} - \bar{z}_m)^2} \tag{K-7}$$

where $\bar{z}_m$ is the average of the measured values of z. The numerator of the ratio within the expression represents the variation in z_m that is not accounted for by Eq. (K-5) and the denominator represents the total variation in the data. The difference between the denominator and numerator represents the variation in the data that is accounted for by the working equation. (This difference is often called the associated variation.) In other words:

$$r^2 = \frac{\text{ASSOCIATED VARIATION}}{\text{TOTAL VARIATION}}$$

Thus, the coefficient of determination is the ratio of the amount of variation in the data accounted for by the working equation to the total variation in the data. The objective of the analysis of the data was to maximize r^2 which is equivalent to minimizing the quantity:

$$e(x_o, y_o, z_o, \alpha, \beta) \equiv \sum_{i=1}^{N} (Z_{mi} - Z_{ci})^2 \tag{K-8}$$

Minimization of e requires differentiating Eq. (K-8) with respect to the unknowns (x_o, y_o, z_o, a, β), setting these five derivatives to zero, and solving the five equations simultaneously. However, the system of equations is nonlinear (because of the form of Eq. (K-7)). To avoid elaborate solution techniques, a parametric approach was used in this study. The unknowns (x_o, y_o, β) were varied parametrically and the unknowns (z_o, a) were calculated from a set of linear equations. These two equations are:

$$\frac{\partial e}{\partial \alpha} = 0 \tag{K-9}$$

and

$$\frac{\partial e}{\partial z} = 0 \tag{K-10}$$

Using Eq. (K-7) in Eq. (K-8) and applying Eqs. (K-9) and (K-10) yields the two equations:

$$\sum_{i=1}^{N} \left\{ Z_{mi} - (Z_o + \alpha s_i) \right\} = 0 \tag{K-11}$$

$$\sum_{i=1}^{N} \left\{ (Z_{mi} - (Z_o + \alpha s_i)) s_i \right\} = 0 \tag{K-12}$$

where

$$s_i = \sqrt{(x_i - x_o)^2 + (y_i - y_o)^2} \tag{K-13}$$

has been introduced for convenience. These equations are linear in z_o and a so that:

$$\alpha = \frac{N \sum_{i=1}^{N} (s_i Z_{mi}) - \sum_{i=1}^{N} s_i \sum_{i=1}^{N} Z_{mi}}{N \sum_{i=1}^{N} s_i^2 - \left(\sum_{i=1}^{N} s_i \right)^2} \tag{K-14}$$

and

$$\theta_i = 2\tan^{-1}\left(\frac{s_i}{Z_{mi} - Z_o}\right) \tag{K-15}$$

For each set (x_o, y_o, z_o, a, β), the coefficient of determination, r^2, was calculated. The best fit of the data occurred for the highest value of r^2.

Of the five unknowns, four of these (x_o, y_o, z_o, β) were used to transform the raw data to the coordinate system in which the cone vertex lies at the origin and the cone centerline lies on the z axis; data in the table in Appendix M conforms to this coordinate system. The remaining unknown, θ, is a property of the injector spray. After determining the best set of (x_o, y_o, z_o, θ, β), it was necessary to estimate the precision with which the spray angle, θ, had been determined.

It was assumed that (x_o, y_o, z_o, β) were fixed at the values giving the best fit to the data. It was then assumed that a "spray" angle could be calculated for each data point by applying Eq. (K-4) as follows:

$$Z_o = \frac{\sum_{i=1}^{N} Z_{mi} - \alpha \sum_{i=1}^{N} s_i}{N} \tag{K-16}$$

where

$$s_i = \sqrt{(x_i - x_o)^2 + (y_i - y_o)^2} \tag{K-17}$$

Two standard errors of estimate were defined. In the first definition, values of θ_i are referenced to the average value of θ_i determined using Eq. (41):

$$\sigma_{\bar{\theta}} = \sqrt{\frac{\sum_{i=1}^{n} (\theta_i - \bar{\theta})^2}{n-2}} \tag{K-18}$$

where

$$\bar{\theta} = \frac{1}{n} \sum_{i=1}^{n} \theta_i \tag{K-19}$$

The factor n-2 indicates that the regression analysis had been used to calculate two of the unknowns. In the second definition, the spray angle determined in the regression analysis is used so that:

$$\sigma_{\bar{\theta}} = \sqrt{\frac{\sum_{i=1}^{n}(\theta_i - \theta)^2}{n-2}} \qquad \text{(K-20)}$$

The results produced by Eq. (K-18) and Eq. (K-20) did not differ significantly. Since each set of data consisted of a large number of measurements, the standard error of estimate is an excellent approximation of the more familiar standard deviation. Thus, approximately 95 percent of the data lies within two standard deviations of the spray angle θ.

APPENDIX L

GAS ANALYZER CALIBRATION PROCEDURES

The flame ionization detector output is related to the number of carbon atoms released by the breaking of carbon-hydrogen bonds as the test gas passes through the detector. By operating the analyzer at fixed temperature and pressure (400K, 1 atm) the output can be interpreted as being proportional to the mole fraction of unburned hydrocarbon in the flame. For example, the mole fractions of fuel in a stoichiometric mixture of propane and air is 0.04; because there are three carbon atoms/mole, the output of the analyzer in percent carbon (PC) for the mixture would be 12. Likewise, for stoichiometric mixtures of high molecular weight fuels of the form C_nH_{2n} would be 14.1

The gas analysis system was calibrated by passing gases of known composition through the analyzer and comparing the percent carbon output to the values. Various concentrations of methane, ethane, propane and butane were used in this calibration procedure. The composition of the calibration gases, supplied by Scott Research Laboratories, were guaranteed to within two percent of specifications. The calibration gases were injected into the previously evacuated gas analysis stream upstream of the ten-port sampling valve as shown in Fig. L-1.

The calibration of the ionization gauge was carried out over five orders of magnitude from 100 ppm methane to 100 percent butane. The resultant calibration curve is shown in Fig. L-2. The abscissa is the percent carbon, PC, and the ordinate is the integrated area (Ac) under the recorded concentration vs time curves.

Expressions of the form

$$\ln PC = A + B \ln A_c \qquad \text{(L-1)}$$

were fit to the data using a multiple linear regression analysis. The coefficients were:

$A = -3.12$

$B = .691$

for $.0001 < PC < .02$

and

HYDROCARBON ANALYZER CALIBRATION SYSTEM

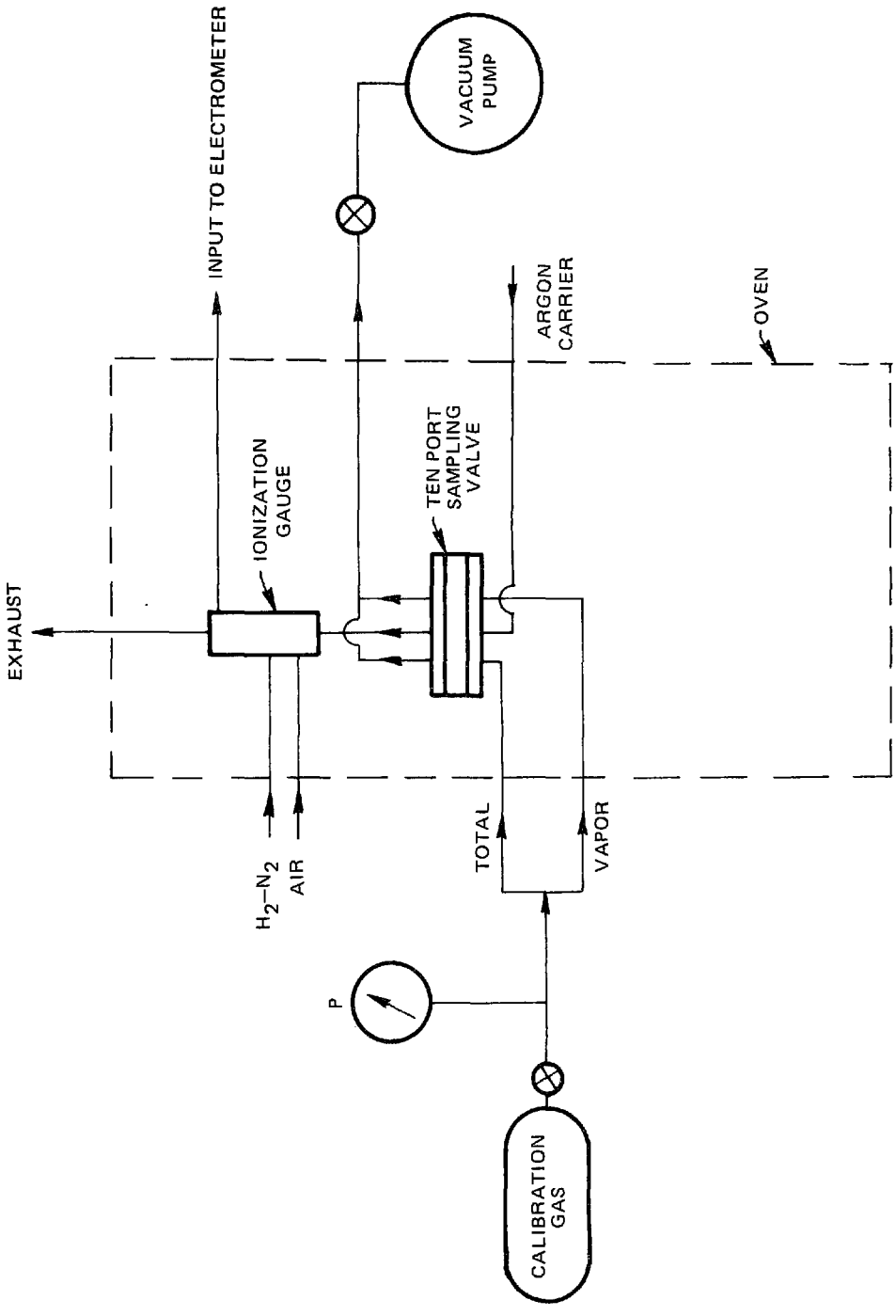

76-06-145-4

HYDROCARBON ANALYZER CALIBRATION CURVE

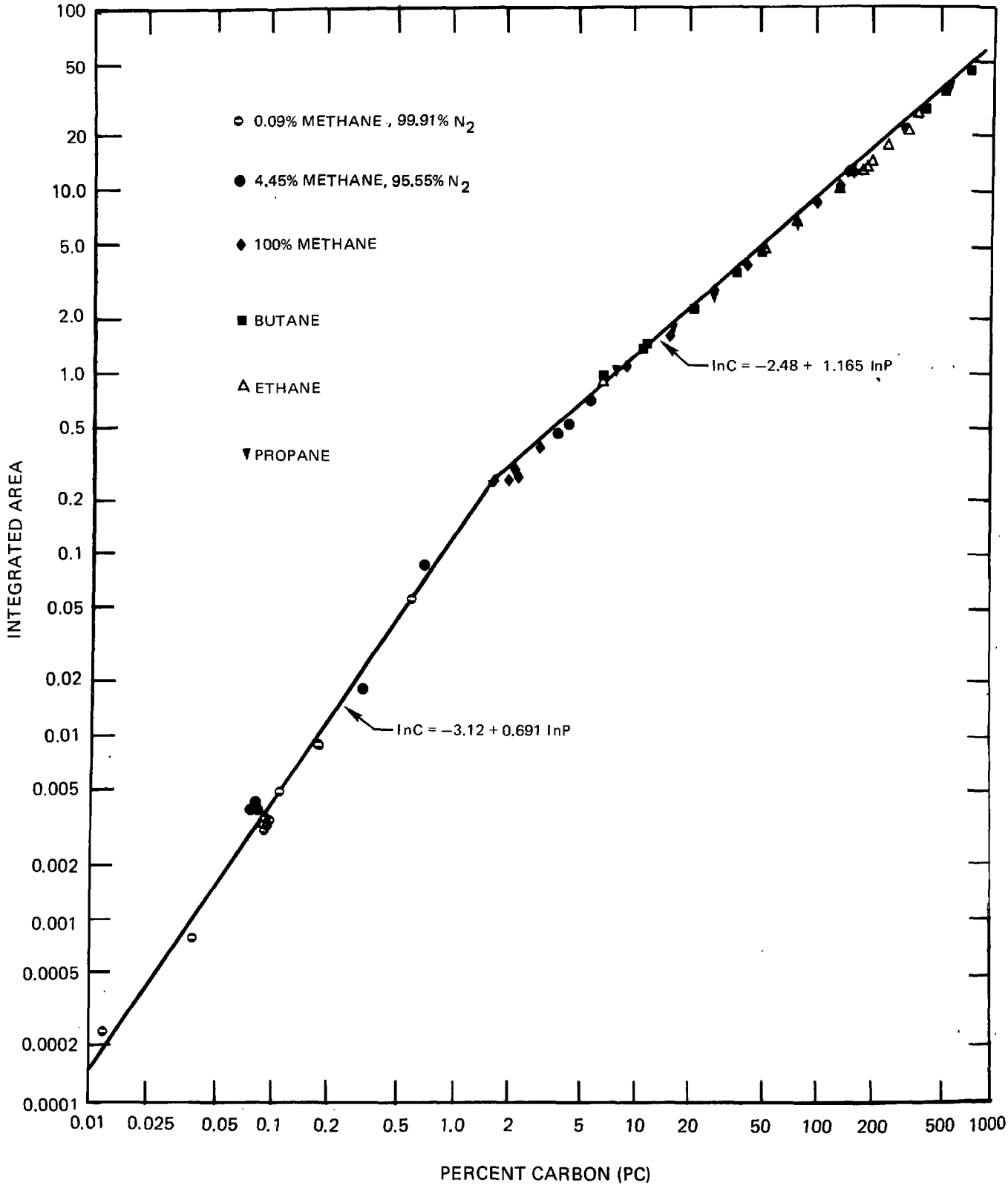

76–06–167–1

$A = -2.48$

$B = 1.165$

for $.0001 < C < 8$

The standard deviation of the data about the curve is 0.116 in units of ln PC.

APPENDIX M

TABULATED HOLOGRAPHIC DATA

This appendix contains the following data for each of the holographic tests:

1) Spray surface coordinate data - see Fig. D-1 for definition of coordinate directions.

2) Spray thickness data - coordinates y_1 and y_2 give the locations of the inner and outer surfaces of the hollow cone spray at the indicated values of x and z.

3) Droplet diameter data - the number of droplets in a given size range within a series of survey regions (see Fig. D-1) are tabulated. The coordinates of the position of survey region are given in the table of spray thickness data.

4) Reduced data - the Sauter mean diameter and spray thickness is reported and the flow rate calculated from the droplet count, droplet size and droplet velocity (from LV measurements) is compared with the metered fuel flow rate.

TABLE M-1 HOLOGRAPHIC RESULTS FOR RUN 129-7

Combusting Flow
Pressure (atm): 0.99
Swirl No.: 0.3
Equivalence Ratio: 0.66

Fuel Type: Iso-octane
Inlet Temp. (K): 574
Fuel Flow (Kg/sec): 0.006
Airflow (Kg/sec): 0.137

Cone Angle: 69.4 ± 2.0 deg

Associated Data Variation, R^2:0.96

Spray Surface Coordinates(cm)

Point	x	y	z	Point	x	y	z
1	.77	1.49	2.06	32	1.65	1.98	3.94
2	.77	-1.14	1.97	33	1.65	2.09	3.95
3	.77	1.22	2.05	34	1.65	-2.19	3.80
4	.77	-1.47	1.96	35	1.65	2.14	3.95
5	.77	-2.06	3.14	36	1.65	2.88	4.91
6	.77	-2.06	3.14	37	1.65	2.88	4.91
7	.77	-1.97	3.15	38	1.65	-2.99	4.70
8	.77	-2.81	4.21	39	1.65	-2.99	4.70
9	.77	-2.81	4.21	40	1.65	-3.74	5.72
10	.77	-3.56	5.29	41	1.65	-3.79	5.72
11	.77	-3.67	5.28	42	.00	-3.96	5.71
12	.77	-4.15	6.36	43	.00	-4.01	5.71
13	.77	-4.15	6.36	44	.00	-4.59	6.51
14	.77	-2.78	6.41	45	.00	-4.92	6.50
15	.77	4.63	6.67	46	.00	-3.67	5.28
16	.77	4.01	5.55	47	.00	-3.61	5.28
17	.77	3.84	5.54	48	.00	-2.92	4.21
18	.77	3.90	5.55	49	.00	-3.08	4.21
19	.77	2.95	4.42	50	.00	-2.39	3.13
20	.77	3.17	4.42	51	.00	-2.28	3.14
21	.77	2.11	3.29	52	.00	-1.82	2.60
22	.77	2.11	3.29	53	.00	-1.93	2.60
23	.77	1.69	2.72	54	.00	-1.52	1.90
24	.77	1.80	2.73	55	.00	-1.63	1.90
25	1.65	1.73	3.22	56	.00	1.44	2.00
26	1.65	-1.40	3.11	57	.00	1.55	1.90
27	1.65	-.90	3.13	58	-.55	-4.14	6.25
28	1.65	1.45	3.21	59	-.55	-4.14	6.25
29	1.65	1.45	3.21	60	-.55	-3.72	5.28
30	1.65	-1.01	3.12	61	-.55	-3.78	5.28
31	1.65	-2.25	3.80	62	-.55	-2.86	4.21

TABLE M-1. HOLOGRAPHIC RESULTS FOR RUN 129-7 (Cont'd)

Spray Surface Coordinates (cm)

Point	x	y	z	Point	x	y	z
63	-.55	-2.81	4.21	93	-1.65	-2.42	4.23
64	-.55	-2.17	3.14	94	-1.65	-2.42	4.23
65	-.55	-2.11	3.14	95	-1.65	-3.34	5.29
66	-.55	-1.71	2.61	96	-1.65	-3.40	5.29
67	-.55	-1.82	2.60				
68	-.55	-1.58	2.06				
69	-.55	1.49	2.17				
70	-.55	1.33	2.16				
71	-.55	2.05	3.29				
72	-.55	2.11	3.29				
73	-.55	2.89	4.41				
74	-.55	2.84	4.41				
75	-.55	3.62	5.54				
76	-.55	3.73	5.54				
77	-.55	4.41	6.66				
78	-.55	4.46	6.66				
79	-1.65	4.30	6.49				
80	-1.65	4.19	6.49				
81	-1.65	3.24	5.52				
82	-1.65	3.57	5.54				
83	-1.65	2.45	4.40				
84	-1.65	2.51	4.40				
85	-1.65	1.29	3.26				
86	-1.65	.37	2.68				
87	-1.65	.70	2.69				
88	-1.65	-.72	2.64				
89	-1.65	-.72	2.64				
90	-1.65	1.45	3.27				
91	-1.65	-1.40	3.17				
92	-1.65	-1.40	3.17				

TABLE M-1. HOLOGRAPHIC RESULTS FOR RUN 129-7 (Cont'd)

Spray Thickness Data (cm)

Pos.	x	y_1	y_2	z
1	1.6	2.0	3.3	4.4
2	1.3	2.1	3.6	4.4
3	.8	2.2	3.9	4.4
4	.4	2.3	3.5	4.4
5	.0	2.5	3.1	4.4
6	-.5	2.1	3.3	4.4
7	-1.1	2.1	3.6	4.4
8	-1.6	1.4	3.4	4.4
9	-2.2	.9	2.3	4.4

Spray Droplet Diameter Data (microns)
(Table entry is number of droplets observed)

Pos.	55	83	111	139	167	195	222	250	278
1	3	3	2	0	0	0	0	0	0
2	0	4	2	1	0	0	0	0	0
3	0	3	0	1	1	0	0	0	0
4	2	8	0	0	0	0	0	0	0
5	2	4	0	0	0	0	0	0	0
6	0	7	1	1	0	0	0	0	0
7	0	5	2	0	0	0	0	0	0
8	0	5	1	2	1	0	0	0	0
9	0	5	5	0	0	0	0	0	0

Reduced Data

SMD	4.1 MILS
SMD	105 MICRONS
AVE. THICKNESS	1.2 CENTIMETERS
AVE. Z	4.4 CENTIMETERS
N-COUNTER	58
N-MEASURED	15.7×10^6
N-CALCULATED	12.3×10^6
AVE. THICKNESS	1.2 CENTIMETERS
STD. ERROR OF T	.4 CENTIMETERS

TABLE M-2. HOLOGRAPHIC RESULTS FOR RUN 129-8

Non-combusting Flow
Pressure (atm): 1.0
Swirl No.: 0.3
Equivalence Ratio: 0.66

Fuel Type: Iso-octane
Inlet Temp. (K): 576
Fuel Flow (Kg/sec): 0.006
Airflow (Kg/sec): 0.137

Cone Angle: 81.4 $\pm$ 2.6

Associated Data Variation, R^2: 0.96

Spray Surface Coodinates(cm)

Point	x	y	z	Point	x	y	z
1	.11	1.26	1.41	32	1.43	4.17	5.30
2	.11	-1.48	1.41	33	1.43	4.17	5.30
3	.11	1.26	1.41	34	1.43	2.14	3.11
4	.11	-1.37	1.41	35	1.43	2.14	3.11
5	.11	1.76	2.01	36	1.43	.99	2.01
6	.11	1.70	2.01	37	1.43	1.32	2.01
7	.11	2.58	3.11	38	1.15	.22	1.13
8	.11	2.69	3.11	39	-1.32	2.30	2.83
9	.11	3.68	4.20	40	-1.32	2.25	2.83
10	.11	3.29	4.20	41	-1.32	2.91	3.66
11	.11	3.18	4.20	42	-1.32	2.63	3.66
12	.11	4.44	4.97	43	-1.32	3.73	4.75
13	.11	-4.55	4.97	44	-1.32	3.73	4.75
14	.11	-4.55	4.97	45	-1.32	4.39	5.41
15	.11	-3.95	4.20	46	-1.32	-4.06	5.41
16	.11	-3.90	4.20	47	-1.32	-2.85	4.20
17	.11	-2.96	3.11	48	-1.32	-2.74	4.20
18	.11	-2.96	3.11	49	-1.32	-1.97	3.11
19	.11	-1.76	2.01	50	-1.32	-2.30	3.11
20	.11	-1.92	2.01	51	-.88	-1.76	2.01
21	.11	-.93	1.13	52	-.88	1.81	2.01
22	.11	-.93	1.13	53	-.88	1.81	2.01
23	1.43	-1.10	2.34	54	-.88	-1.21	2.01
24	1.43	-.88	2.34	55	-.88	-1.26	2.01
25	1.43	-1.87	3.11	56	-.88	-1.26	2.01
26	1.43	-2.14	3.11	57	-.88	-1.37	2.01
27	1.43	-3.40	4.20	58	-.88	1.76	2.01
28	1.43	-3.24	4.20				
29	1.43	-4.50	5.30				
30	1.43	3.29	4.20				
31	1.43	3.18	4.20				

TABLE M-2. HOLOGRAPHIC RESULTS FOR RUN 129-8 (Cont'd)

Spray Thickness Data (cm)

Pos.	x	y_1	y_2	z
1	1.3	1.4	2.2	3.1
2	.9	1.9	2.5	3.1
3	.4	2.1	2.9	3.1
4	.0	1.8	2.9	3.1
5	2.4	-.9	3.2	3.1
6	-1.0	1.5	2.6	3.1
7	-1.7	1.9	2.9	3.1

Spray Droplet Diameter Data (microns)
(Table entry is number of droplets observed)

Pos.	55	83	111	139	167	195	222	250	278
1	0	0	0	2	2	0	0	0	0
2	0	0	4	2	0	0	0	0	0
3	0	0	6	0	0	0	0	0	0
4	0	6	2	1	0	0	0	0	0
5	0	6	4	1	0	0	0	0	0
6	0	0	5	2	0	0	0	0	0
7	0	5	2	0	0	0	0	0	0

Reduced Data

SMD	4.7 MILS
SMD	118 MICRONS
AVE. THICKNESS	.9 CENTIMETERS
AVE. Z	3.1 CENTIMETERS
N-COUNTED	44
N-MEASURED	4.43×10^6
N-CALCULATED	8.7×10^6
AVE. THICKNESS	.9 CENTIMETERS
STD. ERROR OF T	.3 CENTIMETERS

TABLE M-3. HOLOGRAPHIC RESULTS FOR RUN 130-3

Non-combusting Flow
Pressure (atm): 1.0
Swirl No.: 0.3
Equivalence Ratio: 0.69

Fuel Type: No. 2 Fuel Oil
Inlet Temp. (K): 739
Fuel Flow (Kg/sec): 0.006
Airflow (Kg/sec): 0.137

Cone Angle: 67.5 ± 3.2

Associated Data Variation, R^2: 0.94

Spray Surface Coordinates (cm)

Point	x	y	z	Point	x	y	z
1	-.55	1.22	1.51	33	-.55	-3.48	5.21
2	-.55	1.33	1.53	34	-.55	-3.48	5.21
3	-.55	-.61	1.17	35	-.55	-4.18	6.59
4	-.55	-.69	1.16	36	-.55	-4.18	6.59
5	-.55	-.61	1.17	37	.55	-.09	1.38
6	-.55	-1.29	1.83	38	.55	-.20	1.36
7	-.55	-1.08	1.87	39	.55	.99	1.58
8	-.55	-1.08	1.87	40	.55	1.20	1.62
9	-.55	1.62	2.37	41	.55	1.82	2.79
10	-.55	1.51	2.35	42	.55	1.82	2.79
11	-.55	2.02	3.22	43	.55	-1.15	2.24
12	-.55	2.18	3.25	44	.55	-1.20	2.23
13	-.55	2.18	3.25	45	.55	-1.20	2.23
14	-.55	2.85	4.16	46	.55	-1.31	2.21
15	-.55	2.69	4.13	47	.55	2.41	3.85
16	-.55	2.80	4.15	48	.55	2.41	3.85
17	-.55	-2.36	3.19	49	.55	-2.12	3.01
18	-.55	-2.22	3.22	50	.55	-2.07	3.02
19	-.55	-2.16	3.23	51	.55	-2.23	2.99
20	-.55	-1.45	2.24	52	.55	-3.03	3.96
21	-.55	-1.43	2.25	53	.55	-2.97	3.97
22	-.55	-2.81	4.00	54	.55	-2.92	3.98
23	-.55	-2.81	4.00	55	.55	-3.17	4.71
24	-.55	3.34	5.14	56	.55	-3.17	4.71
25	-.55	3.56	5.18	57	.55	-3.13	5.72
26	-.55	3.34	5.14	58	.55	3.97	5.37
27	-.55	3.83	5.51	59	.55	2.75	4.08
28	-.55	3.72	5.49	60	.55	2.75	4.08
29	-.55	-2.75	4.29	61	.55	1.73	2.66
30	-.55	-2.64	4.31	62	-1.54	-1.47	3.08
31	-.55	-2.64	4.31	63	-1.54	-1.20	3.13
32	-.55	-3.48	5.21	64	-1.54	-1.31	3.11

TABLE M-3. HOLOGRAPHIC RESULTS FOR RUN 130-3 (Cont'd)

Spray Surface Coordinates (cm)

Point	x	y	z	Point	x	y	z
65	-1.54	1.77	3.68				
66	-1.54	1.88	3.70				
67	-1.54	2.69	4.74				
68	-1.54	2.80	4.76				
69	-1.54	-1.79	3.91				
70	-1.54	-1.84	3.90				
71	-1.54	-2.24	5.16				
72	-1.54	-2.24	5.16				
73	-1.54	3.53	6.23				
74	-1.54	3.69	6.26				

TABLE M-3. HOLOGRAPHIC RESULTS FOR RUN 130-3 (Cont'd)

Spray Thickness Data (cm)

Pos.	x	y_1	y_2	z
1	1.5	1.5	1.5	4.2
2	1.1	1.3	1.3	4.1
3	1.9	.2	.2	3.9
4	.2	2.2	2.2	4.3
5	-.2	2.1	2.1	4.3
6	-.5	2.2	2.2	4.3
7	-.8	1.8	1.8	4.2
8	-1.1	1.5	1.5	4.2
9	-1.4	1.8	1.8	4.2

Spray Droplet Diameter Data (microns)
(Table entry is number of droplets observed)

Pos.	55	83	111	139	167	195	222	250	278
1	0	3	2	1	0	0	0	0	0
2	0	0	1	1	2	0	0	0	0
3	0	0	4	3	0	0	0	0	0
4	0	0	0	5	0	1	0	0	0
5	0	0	3	1	1	1	0	0	0
6	0	0	3	1	1	0	1	0	0
7	0	0	5	0	0	0	0	0	0
8	0	0	3	0	1	0	0	0	0
9	0	0	2	0	1	0	0	0	0

Reduced Data

SMD	5.7 MILS
SMD	144 MICRONS
AVE. THICKNESS	.0 CENTIMETERS
AVE. Z	4.2 CENTIMETERS
N-COUNTED	40
N-MEASURED	3.8×10^6
N-CALCULATED	4.8×10^6
AVE. THICKNESS	.0 CENTIMETERS
STD. ERROR OF T	.0 CENTIMETERS

TABLE M-4. HOLOGRAPHIC RESULTS FOR RUN 130-4

Combusting Flow
Pressure (atm): 1.0
Swirl No.: 0.3
Equivalence Ratio: 0.66

Fuel Type: No. 2 Fuel Oil
Inlet Temp. (K): 758
Fuel Flow (Kg/sec): 0.006
Airflow (Kg/sec): 0.138

Cone Angle: 56.5 ± 2.1

Associated Data Variation, R^2: 0.92

Spray Surface Coordinates (cm)

Point	x	y	z	Point	x	y	z
1	-.55	1.43	2.83	33	-1.65	.82	3.48
2	-.55	-1.34	2.49	34	-1.65	.58	3.45
3	-.55	1.35	2.82	35	-1.65	.58	3.45
4	-.55	-1.40	2.48	36	-1.65	-.50	3.31
5	-.55	-1.70	3.16	37	-1.65	-.78	3.28
6	-.55	-1.65	3.17	38	-1.65	-.50	3.31
7	-.55	1.67	3.58	39	-1.65	-.99	3.64
8	-.55	1.67	3.58	40	-1.65	-1.53	3.57
9	-.55	-1.76	3.16	41	-1.65	-1.64	3.56
10	-.55	-2.18	4.05	42	-1.65	1.25	3.91
11	-.55	-2.33	4.03	43	-1.65	1.35	3.93
12	-.55	2.65	4.64	44	-1.65	1.19	3.91
13	-.55	2.49	4.62	45	-1.65	1.85	4.87
14	-.55	-2.45	4.01	46	-1.65	1.85	4.87
15	-.55	-2.36	4.02	47	-1.65	1.74	4.86
16	-.55	2.49	4.62	48	-1.65	-1.96	4.40
17	-.55	3.01	5.57	49	-1.65	-1.75	4.43
18	-.55	3.09	5.58	50	-1.65	-1.64	4.44
19	-.55	-2.63	4.87	51	.77	3.21	5.92
20	-.55	-2.69	4.87	52	.77	3.78	7.10
21	-.55	-2.79	4.85	53	.77	3.84	7.11
22	-.55	-3.03	5.88	54	.77	-3.26	7.34
23	-.55	-3.19	5.86	55	.77	-3.12	7.36
24	-.55	-3.19	5.86	56	.77	-2.78	6.13
25	-.55	3.65	6.70	57	.77	-2.78	6.13
26	-.55	3.70	6.70	58	.77	-2.83	5.18
27	-.55	3.83	7.60	59	.77	-2.51	5.22
28	-.55	3.94	7.62	60	.77	-2.05	4.17
29	-.55	-3.57	6.69	61	.77	-1.99	4.18
30	-.55	-3.79	6.67	62	.77	-1.99	4.18
31	-.55	-3.84	6.66	63	.77	-1.42	3.14
32	-.55	-3.68	6.68	64	.77	-1.37	3.15

TABLE M-4. HOLOGRAPHIC RESULTS FOR RUN 130-4 (Cont'd)

Spray Surface Coordinates (cm)

Point	x	y	z	Point	x	y	z
65	.77	-.67	2.41				
66	.77	-.72	2.40				
67	-1.65	-1.91	4.41				
68	-1.65	1.70	5.63				
69	-1.65	2.46	5.72				
70	-1.65	2.52	5.73				
71	-1.65	-2.06	5.17				
72	-1.65	-2.11	5.16				
73	-1.65	-2.74	6.19				
74	-1.65	-2.74	6.19				
75	-1.65	3.14	6.91				
76	-1.65	3.29	6.93				
77	-1.65	3.27	7.65				
78	-1.65	-3.15	6.86				
79	-1.65	-3.31	6.84				
80	.77	-1.21	2.62				
81	.77	-1.21	2.62				
82	.77	1.97	3.01				
83	.77	1.89	3.00				
84	.77	2.17	4.03				
85	.77	2.17	4.03				
86	.77	2.17	4.03				
87	.77	2.74	4.82				
88	.77	2.74	4.82				
89	.77	3.32	5.94				
90	.77	3.32	5.94				
91	.77	-2.73	5.19				

TABLE M-4. HOLOGRAPHIC RESULTS FOR RUN 130-4 (Cont'd)

Spray Thickness Data (cm)

Pos.	x	y_1	y_2	z
1	1.6	1.5	2.9	4.7
2	1.1	2.6	2.0	4.7
3	.7	2.7	3.1	4.8
4	.0	2.6	3.1	4.8
5	-.3	3.1	2.6	4.8
6	-.8	2.4	3.0	4.8
7	-1.3	2.1	2.6	4.7
8	-1.9	1.0	3.2	4.7
9	-2.2	.5	-1.2	4.4

Spray Droplet Diameter Data (microns)
(Table entry is number of droplets observed)

Pos.	55	83	111	139	167	195	222	250	278
1	0	0	5	5	2	0	0	0	0
2	0	0	2	3	0	0	0	0	0
3	0	0	4	2	1	0	0	0	0
4	0	0	2	0	0	0	0	0	0
5	0	0	0	1	1	0	0	0	0
6	0	0	3	0	0	0	0	0	0
7	0	0	2	1	0	0	0	0	0
8	0	4	2	1	4	0	0	0	0
9	0	0	4	2	0	1	0	0	0

Reduced Data

SMD	5.4 MILS
SMD	137 MICRONS
AVE. THICKNESS	.6 CENTIMETERS
AVE. Z	4.7 CENTIMETERS
N-COUNTED	46
N-MEASURED	3.2×10^6
N-CALCULATED	5.5×10^6
AVE. THICKNESS	.6 CENTIMETERS
STD. ERROR OF T	.4 CENTIMETERS

TABLE M-5. HOLOGRAPHIC RESULTS FOR RUN 130-7

Non-combusting Flow
Pressure (atm): 1.0
Swirl No.: 0.3
Equivalence Ratio: 0.67

Fuel Type: No. 2 Fuel Oil
Inlet Temp. (K): 523
Fuel Flow (Kg/sec): 0.0063
Airflow (Kg/sec): 0.137

Cone Angle: 75.1 ± 3.2

Associated Data Variation, R^2: 0.95

Spray Surface Coordinates

Point	x	y	z	Point	x	y	z
1	-.63	-.52	1.19	33	-.63	2.74	3.82
2	-.63	1.01	1.19	34	-.63	3.68	4.75
3	-.63	-.53	1.19	35	-.63	3.59	4.75
4	-.63	1.10	1.19	36	-.63	3.62	4.75
5	-.63	-.44	1.19	37	-.63	3.57	4.75
6	-.63	1.21	1.19	38	-.63	-3.51	4.75
7	-.63	1.43	1.79	39	-.63	-3.40	4.75
8	-.63	-.99	1.79	40	-.63	-3.49	4.75
9	-.63	1.57	1.79	41	-.63	-3.40	4.75
10	-.63	-1.24	1.79	42	-.63	-4.06	5.47
11	-.63	1.40	1.79	43	-.63	-4.19	5.47
12	-.63	-1.04	1.79	44	-.63	-4.14	5.47
13	-.63	-1.15	2.56	45	-.63	4.17	5.47
14	-.63	2.00	2.56	46	-.63	4.17	5.47
15	-.63	-1.65	2.56	47	-.63	4.28	5.47
16	-.63	2.30	2.56	48	-2.12	-1.54	3.00
17	-.63	-1.65	2.56	49	1.62	-1.54	3.00
18	-.63	1.92	2.56	50	1.59	-1.54	3.00
19	-.63	2.19	3.22	51	.66	1.26	1.79
20	-.63	-2.19	3.22	52	.66	1.15	1.79
21	-.63	2.36	3.22	53	.66	1.21	1.79
22	-.63	-2.63	3.22	54	.66	-1.54	1.79
23	-.63	2.30	3.22	55	.66	-1.87	1.79
24	-.63	2.74	3.82	56	.66	-2.30	2.50
25	-.63	-3.13	3.82	57	.66	-2.14	2.50
26	-.63	2.74	3.82	58	.66	-2.19	2.50
27	-.63	-2.74	3.82	59	.66	1.59	2.50
28	-.63	-3.07	3.82	60	.66	1.70	2.50
29	-.63	-3.02	3.82	61	.66	1.65	2.50
30	-.63	3.24	3.82	62	.66	2.52	3.44
31	-.63	2.74	3.82	63	.66	2.36	3.44
32	-.63	2.69	3.82	64	.66	2.52	3.44

TABLE M-5. HOLOGRAPHIC RESULTS FOR RUN 130-7 (Cont'd)

Spray Surface Coordinates

Point	x	y	z	Point	x	y	z
65	.66	2.36	3.44	91	-1.54	2.03	3.44
66	.66	-2.58	3.44	92	-1.54	3.13	4.37
67	.66	-2.50	3.44	93	-1.54	3.18	4.37
68	.66	-2.63	3.44	94	-1.54	-2.96	4.37
69	.66	-2.63	3.44	95	-1.54	-3.07	4.37
70	.66	2.63	3.44				
71	.66	2.41	3.44				
72	.66	3.24	4.50				
73	.66	3.18	4.50				
74	.66	3.29	4.50				
75	.66	-3.40	4.50				
76	.66	-3.68	4.50				
77	.66	-3.51	4.50				
78	-1.54	.38	1.73				
79	-1.54	-1.21	2.50				
80	-1.54	-.66	2.50				
81	-1.54	-1.37	2.50				
82	-1.54	-1.32	2.50				
83	-1.54	1.26	2.50				
84	-1.54	1.21	2.50				
85	-1.54	1.43	2.50				
86	-1.54	-2.19	3.44				
87	-1.54	-2.19	3.44				
88	-1.54	-2.19	3.44				
89	-1.54	1.43	3.44				
90	-1.54	1.97	3.44				

Note: Spray thickness and droplet size data were not available for Run 130-7

TABLE M-6. HOLOGRAPHIC RESULTS FOR RUN 130-8

Combusting Flow
Pressure (atm): 1.0
Swirl No.: 0.3
Equivalence Ratio: 0.66

Fuel Type: No. 2 Fuel Oil
Inlet Temp. (K): 532
Fuel Flow (Kg/sec): 0.006
Airflow (Kg/sec): 0.137

Cone Angle: 64.8 ± 5.2

Associated Data Variation, R^2: 0.93

Spray Surface Coordinates

Point	x	y	z	Point	x	y	z
1	.00	.58	.59	33	.00	-3.79	5.42
2	.00	.44	.59	34	.00	-3.62	5.42
3	.00	.33	.59	35	.00	3.29	5.42
4	.00	-.66	.59	36	.00	3.29	5.42
5	.00	-.71	.59	37	1.65	3.29	4.73
6	.00	-.66	.59	38	1.65	3.07	4.73
7	.00	-1.32	1.14	39	1.65	-2.30	4.73
8	.00	-1.21	1.14	40	1.65	-2.19	4.73
9	.00	.66	1.14	41	1.65	-1.43	3.89
10	.00	.77	1.14	42	1.65	-1.21	3.89
11	.00	.66	1.14	43	1.65	-1.32	3.89
12	.00	.60	1.14	44	1.65	-1.43	3.89
13	.00	1.10	1.75	45	1.65	2.08	3.89
14	.00	.93	1.75	46	1.65	2.08	3.89
15	.00	.93	1.75	47	1.65	1.10	3.08
16	.00	-1.50	1.75	48	1.65	1.10	3.08
17	.00	-1.54	1.75	49	1.65	1.10	3.08
18	.00	-1.76	2.46	50	1.65	-.11	3.08
19	.00	-1.72	2.46	51	1.65	.99	3.08
20	.00	-1.72	2.46	52	1.65	-.33	3.08
21	.00	1.68	2.46	53	1.65	-.33	3.08
22	.00	1.54	2.46	54	-1.32	.44	2.35
23	.00	1.97	3.06	55	-1.32	.44	2.35
24	.00	2.08	3.06	56	-1.32	-.44	2.35
25	.00	-1.92	3.06	57	-1.32	-.44	2.35
26	.00	-1.97	3.06	58	-1.32	1.26	3.10
27	.00	-2.03	3.06	59	-1.32	1.43	3.10
28	.00	-2.63	3.85	60	-1.32	1.18	3.10
29	.00	-2.60	3.85	61	-1.32	-1.43	3.10
30	.00	2.41	3.85	62	-1.32	-1.32	3.10
31	.00	2.30	3.85	63	-1.32	1.81	3.89
32	.00	2.41	3.85	64	-1.32	1.97	3.89

TABLE M-6. HOLOGRAPHIC RESULTS FOR RUN 130-8 (Cont'd)

Spray Surface Coordinates

Point	x	y	z	Point	x	y	z
65	-1.32	1.87	3.89				
66	-1.32	-1.97	3.89				
67	-1.32	-1.97	3.89				
68	-1.32	-2.47	4.98				
69	-1.32	-2.41	4.98				
70	-1.32	-2.58	4.98				
71	-1.32	2.85	4.98				
72	-1.32	3.18	4.98				
73	-1.32	2.85	4.98				

TABLE M-6. HOLOGRAPHIC RESULTS FOR RUN 130-8 (Cont'd)

Spray Thickness Data (cm)

Pos.	x	y_1	y_2	z
1	1.5	.2	.2	2.5
2	1.4	.7	.7	2.5
3	.8	1.5	1.5	2.5
4	.4	1.9	1.9	2.5
5	.0	1.9	1.9	2.5
6	-.4	1.5	1.5	2.5
7	-1.3	.5	.5	2.5

Spray Droplet Diameter Data (microns)
(Table entry is number of droplets observed)

Pos.	55	83	111	139	167	195	222	250	278
1	0	0	3	4	1	0	0	0	0
2	0	0	6	1	1	0	0	0	0
3	0	1	6	1	1	1	0	0	0
4	0	0	6	8	1	0	0	0	0
5	0	0	4	1	0	0	0	0	0
6	0	0	4	4	2	0	0	0	0
7	0	0	0	4	0	0	1	0	0

Reduced Data

SMD	5.5 MILS
SMD	139 MICRONS
AVE. THICKNESS	.0 CENTIMETERS
AVE. Z	2.5 CENTIMETERS
N-COUNTED	54
N-MEASURED	3.2×10^6
N-CALCULATED	5.2×10^6
AVE. THICKNESS	.0 CENTIMETERS
STD. ERROR OF T	.0 CENTIMETERS

TABLE M-7. HOLOGRAPHIC RESULTS FOR RUN 132-4

Combusting Flow
Pressure (atm): 3.046
Swirl No.: 0.3
Equivalence Ratio: 0.64

Fuel Type: Iso-octane
Inlet Temp. (K): 528
Fuel Flow (Kg/sec): 0.006
Airflow (Kg/sec): 0.139

Cone Angle: 66.9 ± 3.1

Associated Data Variation, R^2: 0.97

Spray Surface Coordinates

Point	x	y	z	Point	x	y	z
1	-.11	1.65	2.51	33	1.26	3.56	5.86
2	-.11	1.70	2.52	34	1.26	3.28	5.83
3	-.11	2.20	3.51	35	1.26	4.37	7.04
4	-.11	3.12	4.71	36	1.26	-2.75	4.47
5	-.11	3.18	4.71	37	1.26	-2.75	4.47
6	-.11	4.05	5.91	38	1.26	-3.59	5.10
7	-.11	3.88	5.89	39	1.26	-3.48	5.12
8	-.11	4.45	6.83	40	1.26	-3.48	5.12
9	-.11	-2.79	4.25	41	1.26	-1.66	3.54
10	-.11	-2.84	4.25	42	1.26	-1.66	3.54
11	-.11	-2.82	4.08	43	1.26	-1.11	2.50
12	-.11	-2.49	3.56	44	-1.76	-.46	2.62
13	-.11	-2.44	3.57	45	-1.76	-1.40	3.13
14	-.11	-2.05	3.06	46	-1.76	-2.34	4.24
15	-.11	-2.05	3.06	47	-1.76	-2.91	5.40
16	-.11	-1.56	2.56	48	-1.76	-3.36	6.07
17	-.11	-1.72	2.54	49	-1.76	3.72	6.87
18	-.11	-1.28	2.04	50	-1.76	3.45	5.84
19	-.11	-1.39	2.03				
20	-.11	-.68	1.55				
21	-.11	1.19	1.63				
22	-.11	-.49	.80				
23	-.11	-.44	.80				
24	-.11	.93	.95				
25	-.11	.93	.95				
26	1.26	.83	2.42				
27	1.26	.88	2.43				
28	1.26	1.71	3.45				
29	1.26	1.71	3.45				
30	1.26	1.88	3.47				
31	1.26	2.80	4.67				
32	1.26	2.85	4.68				

TABLE M-7. HOLOGRAPHIC RESULTS FOR RUN 132-4 (Cont'd)

Spray Thickness Data (cm)

Pos.	x	y_1	y_2	z
1	1.7	2.0	3.0	4.6
2	1.4	1.9	3.2	4.6
3	1.2	2.1	3.2	4.7
4	.5	2.1	3.7	4.7
5	-.2	2.6	3.5	4.7
6	-.7	2.3	3.9	4.7
7	-1.3	2.3	3.8	4.7
8	-2.0	1.4	3.1	4.6
9	-2.6	1.0	2.4	4.6

Spray Droplet Diameter Data (microns)
(Table entry is number of droplets observed)

Pos.	55	83	111	139	167	195	222	250	278
1	6	1	0	1	0	0	0	0	0
2	0	5	3	0	1	0	0	0	0
3	0	0	3	0	1	0	0	0	0
4	0	3	4	0	1	0	0	0	0
5	0	7	1	1	0	0	0	0	0
6	4	3	0	0	0	0	0	0	0
7	0	6	6	0	0	0	0	0	0
8	7	3	0	0	0	0	0	0	0
9	7	2	1	0	0	0	0	0	0

Reduced Data

SMD	4.1 MILS
SMD	104 MICRONS
AVE. THICKNESS	1.2 CENTIMETERS
AVE. Z	4.7 CENTIMETERS
N-COUNTED	57
N-MEASURED	5.1×10^6
N-CALCULATED	12.5×10^6
AVE. THICKNESS	1.2 CENTIMETERS
STD. ERROR OF T	.3 CENTIMETERS

TABLE M-8. HOLOGRAPHIC RESULTS FOR RUN 133-1

Non-combusting Flow
Pressure (atm): 1.0
Swirl No.: 0.6
Equivalence Ratio: 0.67

Fuel Type: Iso-Octane
Inlet Temp. (K): 541
Fuel Flow (Kg/sec); 0.006
Airflow (Kg/sec): 0.137

Cone Angle: 70.5 $\pm$ 2.4

Associated Data Variation, R^2: 0.97

Spray Surface Coordinates

Point	x	y	z	Point	x	y	z
1	-.22	1.07	1.41	33	1.15	-4.34	6.66
2	-.22	-.84	1.24	34	1.15	3.69	5.55
3	-.22	.86	1.39	35	1.15	3.63	5.54
4	-.22	-.89	1.24	36	1.15	3.83	6.39
5	-.22	.68	.88	37	1.15	2.90	4.49
6	-.22	-.47	.78	38	1.15	2.24	3.77
7	-.22	-1.40	2.02	39	1.15	2.08	3.75
8	-.22	-1.29	2.03	40	1.15	1.61	2.89
9	-.22	-2.13	2.84	41	1.15	1.14	1.91
10	-.22	-2.13	2.84	42	-1.59	-1.30	3.35
11	-.22	-2.59	3.68	43	-1.59	.09	2.59
12	-.22	-3.05	4.46	44	-1.59	-.13	2.57
13	-.22	-3.68	5.40	45	-1.59	-1.88	3.74
14	-.22	-3.84	5.38	46	-1.59	-2.94	4.53
15	-.22	-4.88	6.51	47	-1.59	-3.68	5.34
16	-.22	4.01	5.63	48	-1.59	-4.08	6.19
17	-.22	4.50	6.28	49	-1.59	4.18	6.25
18	-.22	3.52	4.93	50	-1.59	3.54	4.65
19	-.22	3.04	4.17	51	-1.59	2.31	3.66
20	-.22	2.12	3.26	52	-1.59	1.29	2.75
21	-.22	2.01	3.25	53	-1.59	.12	2.26
22	-.22	1.80	2.52				
23	-.22	1.86	2.52				
24	-.22	1.40	1.82				
25	-.22	1.59	1.84				
26	1.15	-.87	1.62				
27	1.15	-1.18	2.04				
28	1.15	-1.48	2.89				
29	1.15	-2.32	3.70				
30	1.15	-3.11	4.51				
31	1.15	-3.46	5.36				
32	1.15	-3.90	6.04				

TABLE M-8. HOLOGRAPHIC RESULTS FOR RUN 133-1 (Cont'd)

Spray Thickness Data (cm)

Pos.	x	y_1	y_2	z
1	1.3	1.1	2.4	3.2
2	.8	1.4	2.2	3.2
3	.3	1.5	2.7	3.3
4	-.1	1.4	2.6	3.2
5	-.5	1.3	2.6	3.2
6	-1.0	.7	2.6	3.2
7	-1.5	-.6	1.8	3.1

Spray Droplet Diameter Data (microns)
(Table entry is number of droplets observed)

Pos.	55	83	111	139	167	195	222	250	278
1	0	0	5	2	2	0	0	0	0
2	0	0	2	2	2	0	0	0	0
3	0	3	1	0	0	0	0	0	0
4	0	0	3	2	0	0	0	0	0
5	0	1	3	1	0	0	0	0	0
6	0	3	9	2	1	0	0	0	0
7	0	0	5	3	0	0	0	0	0

Reduced Data

SMD	5.0 MILS
SMD	128 MICRONS
AVE. THICKNESS	1.1 CENTIMETERS
AVE. Z	3.2 CENTIMETERS
N-COUNTED	46
N-MEASURED	4.4×10^6
N-CALCULATED	6.8×10^6
AVE. THICKNESS	1.1 CENTIMETERS
STD. ERROR OF T	.3 CENTIMETERS

TABLE M-9. HOLOGRAPHIC RESULTS FOR RUN 133-3

Combusting Flow
Pressure (atm): 1.0
Swirl No.: 0.6
Equivalence Ratio: 0.66

Fuel Type: Iso-Octane
Inlet Temp. (K): 537
Fuel Flow (Kg/sec): 0.006
Airflow (Kg/sec): 0.136

Cone Angle: 63.8 ± 3.0

Associated Data Variation, R^2: 0.94

Spray Surface Coordinates

Point	x	y	z	Point	x	y	z
1	.16	-1.65	1.95	33	1.54	-1.04	3.70
2	.16	.99	1.95	34	-1.21	.33	1.89
3	.16	.99	1.95	35	-1.21	.88	2.44
4	.16	.55	1.02	36	-1.21	1.43	3.21
5	.16	1.43	2.33	37	-1.21	2.03	3.87
6	.16	1.92	3.21	38	-1.21	2.30	4.53
7	.16	2.52	3.87	39	-1.21	3.07	5.08
8	.16	3.13	4.86	40	-1.21	2.80	6.72
9	.16	3.62	5.62	41	-1.21	4.17	6.72
10	.16	3.84	5.90	42	-1.21	-4.33	6.72
11	.16	-3.51	5.90	43	-1.21	-4.66	7.49
12	.16	-4.11	6.72	44	-1.21	-3.51	6.01
13	.16	-4.39	7.27	45	-1.21	-2.85	5.35
14	.16	-3.24	5.62	46	-1.21	-2.52	4.53
15	.16	-3.07	4.97	47	-1.21	-1.97	3.76
16	.16	-2.52	4.14	48	-1.21	-1.48	2.99
17	.16	-2.08	3.27	49	-1.21	-1.15	2.50
18	.16	-1.87	2.33	50	-1.21	.49	1.95
19	.16	-1.21	1.89				
20	.16	-.77	1.02				
21	1.54	-.22	2.22				
22	1.54	.88	2.94				
23	1.54	2.08	3.43				
24	1.54	2.52	4.31				
25	1.54	2.91	5.19				
26	1.54	3.07	6.06				
27	1.54	2.91	6.06				
28	1.54	3.62	6.94				
29	1.54	-4.06	6.94				
30	1.54	-3.13	5.95				
31	1.54	-2.41	5.24				
32	1.54	-1.87	4.53				

TABLE M-9. HOLOGRAPHIC RESULTS FOR RUN 133-3 (Cont'd)

Spray Thickness Data (cm)

Pos.	x	y_1	y_2	z
1	-.1	.9	2.0	3.7
2	-.5	.9	2.1	3.7
3	-1.2	.4	1.3	3.7
4	-1.8	-.4	2.0	3.7

Spray Droplet Diameter Data (microns)
(Table entry is number of droplets observed)

Pos.	55	83	111	139	167	195	222	250	278
1	0	2	2	2	0	0	0	0	0
2	0	2	4	2	0	0	0	0	0
3	4	3	1	1	0	0	0	0	0
4	0	0	7	2	1	0	0	0	0

Reduced Data

SMD	4.7 MILS
SMD	119 MICRONS
AVE. THICKNESS	.9 CENTIMETERS
AVE. Z	3.7 CENTIMETERS
N-COUNTED	27
N-MEASURED	4.4×10^6
N-CALCULATED	8.3×10^6
AVE. THICKNESS	.9 CENTIMETERS
STD. ERROR OF T	.3 CENTIMETERS

REFERENCES

1. Norster, E. R. and A. H. Lefebvre: Effects of Fuel Injection Method on Gas Turbine Combustor Emissions. Emissions from Continuous Combustion Systems, Cornelius, W. and W. G. Agnew (eds.), New York, Plenum Press, pp. 255-278, 1972.

2. Grobman, J. S.: Effect of Operating Variables of Pollutant Emissions from Aircraft Turbine Engine Combustors. Emissions from Continuous Combustion Systems, Cornelius, W. and W. G. Agnew (eds.), New York, Plenum Press, pp. 279-303, 1972.

3. Tuttle, J. H., R. A. Altenkirch and A. M. Mellor: Emissions From and Within an Allison J-33 Combustor. II. The Effect of Inlet Air Temperature. Comb. Sci. Technol. 7: 125-134, 1973.

4. Pompei, F. and J. B. Heywood: The Role of Mixing in Burner-Generated Carbon Monoxide and Nitric Oxide. Comb. Flame 19: 407-418, 1972.

5. Mellor, A. M.: Simplified Physical Model of Spray Combustion in a Gas Turbine Engine. Comb. Sci. Technol. 8: 101-109, 1973.

6. Bowman, C. T. and L. S. Cohen: Influence of Aerodynamic Phenomena on Pollutant Formation in Combustion. Environmental Protection Agency, Research Triangle Park, N. C., Publication Number 650/2-75=061a, p. 159, July 1975.

7. Tuttle, J. H., M. B. Colket, R. W. Bilger and A. M. Mellor: Characteristic Times for Combustion and Pollutant Formation in Spray Combustion. Paper presented at the 16th Symposium (International) on Combustion. Cambridge, Mass., August 1976.

8. Appleton, J. P. and J. B. Heywood: The Effects of Imperfect Fuel-Air Mixing in a Burner on NO Formation from Nitrogen in the Air and the Fuel. Fourteenth Symposium (International) on Combustion. Pittsburgh, PA. The Combustion Institute, pp. 77-786, 1973.

9. Spadaccini, L. J., F. K. Owen and C. T. Bowman: Influence of Aerodynamic Phenomena on Pollutant Formation in Combustion of Gaseous Fuels. Environmental Protection Agency, Research Triangle Park, NC, Publication Number 600/2-76-247a, September 1976.

10. Kerr, N. M. and D. Fraser: Swirl. Part I, Effect on Axisymmetrical Turbulent Jets. J. Inst. Fuel 38: 519:538, 1965.

11. Bowman, C. T. and L. S. Cohen: Influence of Aerodynamic Phenomena on Pollutant Formation in Combustion. Environmental Protection Agency, Research Triangle Park, NC, Publication Number EPA 650/2-75-061a, July 1975.

12. Tuttle, J. H., R. A. Altenkirch and A. M. Mellor: Emissions From an Within an Allison J-33 Combustor II. The Effect of Inlet Air Temperature. Comb. Sci. Technol. 7: 125-134, 1973.

13. Beer, T. M. and N. A. Chigier: Combustion Aerodynamics, J. Wiley & Sons, p. 142 (1972).

14. Tuttle, J. H., R. A. Shisler and A. M. Mellor: Nitrogen Dioxide Formation in Gas Turbine Engines. Measurements and Measurement Methods. Comb. Sci. Technol. 9: 261-271, 1975.

15. Wadleigh, R. R. and R. A. Oman: Instrumentation to Measure Composition and Temperature of High-Velocity, Two-Phase, Two-Component Flows. MIT Dept. of Mech. Engrg. Gas Turbine Laboratory, July 1956.

16. Kennedy, J. B. and J. B. McVey: An Experimental Study of Fuel Spray Vaporization Rates. United Technologies Research Center Report UAR-N139, September 27, 1974 and Eleventh JANNAF Combustion Meeting, Vol. II, CPA, Publication Number 261, pp. 387-406, December 1974.

17. Owen, F. K.: Laser Velocimeter Measurements of a Confined Turbulent Diffusion Flame Burner. United Technologies Research Center, Fourteenth AIAA Aerospace Sciences Meeting, Washington, D.C., p.10, 1976.

18. Lindgren, B. W. and G. W. McAlrath: Introduction to Probability and Statistics, New York, Macmillan, p. 165, 1959.

19. Becker, H. A., H. C. Hottel and G. C. Williams: On the Light-Scatter Technique for the Study of Turbulence and Mixing. J. Fluid Mech. 30: 259-284, 1967.

NOMENCLATURE

A = Area, cm^2

d = Outer diameter or air annulus, cm, or
Peak to peak fringe spacing

d_h = Inner diameter of air annulus, cm

d_i = Measured droplet diameter, microns

d_m = Calculated mean droplet diameter, microns

D = Combustor diameter, m

D_p = Particle diameter

D_s = Spray diameter, cm

f = Frequency, Hz, or
Lens focal length

f_D = Doppler frequency, Hz

f_o = Offset frequency, Hz

K = Cunningham constant 1.8

K_γ = Defined by Appendix A

ℓ = Mean free path, cm

L = Height of air annulus, cm

M = Mass flow rate, kg/sec

n_i = Number of droplets of diameter, d_i

N = Total number of samples

P = Error as defined by Eqs. (14) and (15)

r^2 = Coefficient of determination as defined by Eq. (32)

R = Radius, m

R_o = Combustor radius, m

S = Swirl number as defined by Eq. (1), or
Displacement

SMD = Sauter Mean Diameter

S_x = Calculated variance in the variable x as defined in Eq. (17)

t = Spray thickness, cm

T = Temperature, ^oK

u_p = Rms particle velocity, m/sec

U_c = Convective velocity, m/sec

U_i = Instantaneous axial velocity, m/sec

u' = Axial velocity fluctuation, m/sec

V = Droplet velocity, m/sec

V_{ref} = Combustor reference velocity, m/sec

$\bar{W}$ = Mean tangential gas velocity, m/sec

w' = Tangential velocity fluctuation, m/sec

w_f = Fuel flow rate, kg/sec

x = Random variable

X = Axial distance, m

Z = Swirler hub-to-tip ratio

Z_m = Axial coordinate

β = True mean of the variable x, or
Angle of rotation

γ = Directional intermittency

γ_m = Error in the mean as defined by Eq. (14)

γ_T = Error in the variance as defined by Eq. (15)

η = Swirl vane angle, deg

θ = Angle, deg

λ = Wavelength, m

μ = Viscosity, gm/cm-sec

ρ = Density, gm/cc

ρ_p = Particle density, gm/cc

σ = Rms velocity, m/sec

σ_θ = Error of estimate as defined by Eq. (20)

$\bar{\sigma_\theta}$ = Effor of estimate as defined by Eq. (18)

Φ = Overall fuel-air equivalence ratio = $(\dot{m}_{fuel}/\dot{m}_{air})/(\dot{m}_{fuel}/\dot{m}_{air})_{stoich}$

TECHNICAL REPORT DATA
(Please read Instructions on the reverse before completing)

1. REPORT NO.	2.	3. RECIPIENT'S ACCESSION NO.
EPA-600/7-79-003		

4. TITLE AND SUBTITLE	5. REPORT DATE
Influence of Aerodynamic Phenomena on Pollutant Formation in Combustion (Phase II. Liquid Fuels)	January 1979
	6. PERFORMING ORGANIZATION CODE

7. AUTHOR(S)	8. PERFORMING ORGANIZATION REPORT NO.
L. J. Spadaccini, John McVey, Jan Kennedy, A. S. Kesten, F. K. Owen, and C. T. Bowman	

9. PERFORMING ORGANIZATION NAME AND ADDRESS	10. PROGRAM ELEMENT NO.
United Technologies Research Center 300 Main Street East Hartford, Connecticut 06108	EHE624A
	11. CONTRACT/GRANT NO. 68-02-1873

12. SPONSORING AGENCY NAME AND ADDRESS	13. TYPE OF REPORT AND PERIOD COVERED
EPA, Office of Research and Development Industrial Environmental Research Laboratory Research Triangle Park, NC 27711	Final; 8/76 - 10/77
	14. SPONSORING AGENCY CODE EPA/600/13

15. SUPPLEMENTARY NOTES IERL-RTP project officer is W. Steven Lanier, MD-65, 919/541-2432. EPA-600/2-76-247a was the Phase I report.

16. ABSTRACT The report gives results of an experimental investigation of the effects of the interaction between physical and chemical processes on pollutant formation and destruction in a liquid-fuel, turbulent-diffusion flame burner. The effects of fuel type, inlet air swirl, inlet air temperature, and combustor pressure on the spray characteristics and the time-mean and fluctuating flow field structure were determined, using probing and optical techniques. Changes in the spray and flow field structure were correlated with changes in pollutant emissions from the burner. The investigation showed that varying these operating parameters produces major changes in spray dynamics, vaporization rates, and time-averaged fuel/air distribution within the burner which significantly influence energy release rates and pollutant formation and destruction. Significant differences were found between the mean velocities of the gas and fuel droplets which likely influence droplet vaporization rates and mixing of the vaporized fuel and air.

17. KEY WORDS AND DOCUMENT ANALYSIS

a. DESCRIPTORS		b. IDENTIFIERS/OPEN ENDED TERMS	c. COSATI Field/Group	
Air Pollution	Flames	Air Pollution Control	13B	21B
Nitrogen Oxides	Kinetics	Stationary Sources	07B	20K
Carbon Monoxide	Aerodynamics	Liquid Fuels		20D
Oxygen	Spraying	No. 2 Fuel Oil		07A
Propane	Lasers	Iso Octane	07C	20E
Fuel Oil	Holography		21D	
Speed Indicators			14B	

18. DISTRIBUTION STATEMENT	19. SECURITY CLASS *(This Report)*	21. NO. OF PAGES
Unlimited	Unclassified	
	20. SECURITY CLASS *(This page)* Unclassified	22. PRICE

EPA Form 2220-1 (9-73)